

**LASER-BASED HYBRID PROCESS FOR MACHINING
HARDENED STEELS**

A Thesis
Presented to
The Academic Faculty

by

SATYANARAYANAN RAGHAVAN

In Partial Fulfillment
of the Requirements for the Degree
MASTER OF SCIENCE in the
School of MECHANICAL ENGINEERING

Georgia Institute of Technology
MAY 2012

**LASER-BASED HYBRID PROCESS FOR MACHINING
HARDENED STEELS**

Approved by:

Dr. MELKOTE, SHREYES, Advisor
School of Mechanical Engineering
Georgia Institute of Technology

Dr. LIANG, STEVEN
School of Mechanical Engineering
Georgia Institute of Technology

Dr. DANYLUK, STEVEN
School of Mechanical Engineering
Georgia Institute of Technology

Date Approved: December 09, 2011

[This page is intentionally left blank]

To
Amma and Appa

ACKNOWLEDGEMENTS

First, I wish to thank my advisor, Professor. Shreyes N. Melkote for the mentorship and the research experience. He encouraged me in getting this work to shape provided invaluable guidance for presenting this thesis. I extend my thanks to my reading committee Dr. Steven Danyluk, and Dr. Steven Liang for their time and support.

Thanks to Mr. Steven Sheffield for helping me build the laser lab. His support and assistance helped me during various stages of the build. Thanks to Mr. John Graham, Mr. Kyle French, Mr. Anh Nguyen, Ms. Pamela Rountree, Ms. Melissa Raine, Ms. Glenda Johnson for their continuous support.

Thanks to all the lab members for the refreshing chats, cup cakes, and fun discussions throughout my time at Georgia Tech. Thanks to all my friends, who have constantly shown their interest and belief in my endeavors.

Lastly, but I should admit as the foremost, I would like to thank my mother, and my wife, Ranjani for all their love, care, endurance, and support in my pursuits. Also, I wish to thank my entire family for providing a cherishing environment for us.

TABLE OF CONTENTS

	Page
ACKNOWLEDGEMENTS	v
LIST OF TABLES	viii
LIST OF FIGURES	x
LIST OF SYMBOLS	xix
SUMMARY	xxii
CHAPTER	
1 INTRODUCTION	1
1.1 Background and Motivation	1
1.2 Research Goals and Objectives	9
1.3 Thesis Outline	9
2 LITERATURE REVIEW	11
2.1 Overview of Hard Turning	11
2.2 Cutting Tool	12
2.3 Tool Wear in Hard Turning	18
2.4 Thermally Enhanced Machining Processes	24
2.5 Laser Based Processes	27
2.6 Modeling of Laser Based Process	35
2.7 Summary	38
3 LASER TEMPERING BASED HYBRID TURNING PROCESS	40
3.1 Limitations of Thermally Enhanced Hard Turning Process	40
3.2 Process Description	41
3.3 Experimental Setup for Laser Tempering	48
3.4 Summary	56

4	LASER TEMPERING MODEL	57
	4.1 Introduction	57
	4.2 Physical and Mathematical Description	59
	4.3 Implementation	71
	4.4 Summary	84
5	MODEL VALIDATION	85
	5.1 Validation Procedure	85
	5.2 Microstructure and Phase Analysis	87
	5.3 Prediction of Hardness	105
	5.4 Summary	109
6	HARD TURNING APPLICATION	111
	6.1 Experimental Work	111
	6.2 Process Parameter Selection	114
	6.3 Experimental Procedure	117
	6.4 Results and Discussion	124
	6.5 Summary	142
7	CONCLUSIONS AND RECOMMENDATIONS	144
	7.1 Conclusions	144
	7.2 Recommendations	149
8	APPENDIX	150
	8.1 Equipments	150
	8.2 Micrographs of Tempered Subsurface Region	160
	8.3 Composition of Phases Using X-ray Diffraction	164
9	REFERENCES	186

LIST OF TABLES

	Page
Table 2.1: Comparison of laser systems [Dumitrescu et al. 2006]	28
Table 3.1: Specification of Nuvonyx ISL-1000M laser system	51
Table 3.2: Specification of Precitec YW50	52
Table 4.1: Heat distribution profile of laser beam	63
Table 4.2: Chemical composition and physical properties of AISI 52100 steel	71
Table 4.3 : Comparison of constants with similar alloy steels	83
Table 5.1: Peak intensities and diffraction angle for α -iron and γ -iron	101
Table 5.2: Composition of phases in hardened AISI 52100 steel (no laser treatment) from x-ray diffraction analysis	102
Table 5.3: Composition of phases in laser-treated AISI 52100 steel samples (laser power: 800 W, spot size: 2 mm)	104
Table 6.1: Kennametal CBN and ceramic turning inserts - nomenclature	112
Table 6.2: Experiment matrix	117
Table 6.3: Surface roughness parameters	123
Table 8.1.1: Specifications of fiber optics system	151
Table 8.1.2: Specifications of a linear stage	152
Table 8.1.3: Specifications of Leica microscope	153

Table 8.1.4: Specifications of Hardinge Conquest lathe	155
Table 8.1.5: Specifications of Kistler force dynamometer	157
Table 8.1.6: Specifications for Zygo NewView200	158
Table 8.3.1: Specifications of x-ray diffractometer	168

LIST OF FIGURES

	Page
Figure 1.1: 2010 steel usage by industry	1
Figure 1.2: High strength steel structure in Mercedes-Benz passenger car	2
Figure 1.3: Large bearings for wind turbine	3
Figure 1.4: Titanium components for medical application	3
Figure 1.5: Large turbine shafts for aerospace application	3
Figure 1.6: Gear production - grinding vs. hard turning	4
Figure 1.7: Cost - grinding vs. hard turning	5
Figure 1.8: Development of cutting tools	7
Figure 1.9: US budget for cutting tools	7
Figure 1.10: Hardness distribution for bearing steel scanned with 1.4 kW CO ₂ rectangular laser beam under different overlapping conditions: hardness along the width of laser-treated surface for 16.4 μm/sec and 26.2 μm/sec scanning speeds	8
Figure 1.11: Thesis outline	10
Figure 2.1: Orthogonal cutting model	11
Figure 2.2: Tool angles of single-point cutting tool	12
Figure 2.3: Hardness vs. toughness of tool material	13
Figure 2.4: Hot hardness of tool material	14
Figure 2.5: Cutting edge preparation	16
Figure 2.6: Cutting tool wear pattern	17
Figure 2.7: Representative flank wear	18

Figure 2.8: Comparison of CBN and ceramic tools in hard turning 100Cr6 [Konig et al. 1990]	22
Figure 2.9: Comparison of power consumption in plasma-arc assisted machining over conventional machining. (cemented carbide inserts, cutting speed: 100 m/min, feed : 0.088 mm/rev (SS10) and, 0.175 mm/rev (alloy steel)) [Madhavulu et al. 1994]	26
Figure 2.10: Comparison of flank wear (top-left), surface finish (top-right), cutting force (bottom) in hybrid plasma machining (HM) over plasma enhanced machining (PEM) and conventional machining. (tungsten carbide inserts, depth of cut: 0.76 mm, feed: 0.109 mm/rev (Conventional), 0.127 mm/rev (PEM & HM), cutting speed: 5.2 m/sec [Wang et al. 1994]	26
Figure 2.11: Operational regimes of laser based manufacturing processes [Ohse et al. 1988, Steen 1998]	28
Figure 2.12: Illustration of laser machining (LM) process (a) LM for machining cavities (b) gas flow at the erosion front [Leidinger et al. 1995]	30
Figure 2.13: Five-axis laser machining center precision processes a ring used in a power-generation turbine	31
Figure 2.14: Laser-assisted hard turning	32
Figure 2.15: Flank wear vs. cutting time in laser assisted hard turning of silicon nitride [Lei et al. 2001]	34
Figure 3.1: Laser tempering based hybrid turning process	43
Figure 3.2: Illustration of non-overlapping laser scan in laser tempering based hybrid turning process	44
Figure 3.3: Illustration of overlapping laser scans in laser tempered hybrid turning process	45
Figure 3.4: Illustration of turning in laser tempered hybrid turning process	46
Figure 3.5: Schematic of the experimental setup	48

Figure 3.6: Nuvonyx ISL-1000M laser system	50
Figure 3.7: Precitec laser head	52
Figure 3.8: Schematic of laser head optics [Precitec]	53
Figure 3.9: Laser treatment – overall layout	54
Figure 3.10: Laser treatment – experimental setup	55
Figure 3.11: Laser system power levels	56
Figure 4.1: Schematic of laser tempering	60
Figure 4.2: Block diagram representation of model	61
Figure 4.3: Fe-C diagram [Li et al. 1986]	68
Figure 4.4: AISI 52100: yield strength vs. temperature [Gustavo 2002]	72
Figure 4.5: AISI 52100: specific heat vs. temperature [Touloukian 1970]	73
Figure 4.6: AISI 52100: thermal conductivity vs. temperature [Umbrello et al. 2004, Podgornik B et al. 2001]	73
Figure 4.7: AISI 52100: coefficient of thermal expansion vs. temperature [Guo et al. 2002].	74
Figure 4.8: Transformation diagram of AISI 52100 steel: (a) Time-Temperature Transformation, (b) Continuous Cooling Transformation. [Voort 1991]	76
Figure 4.9: Schematic of the thermal model	78
Figure 4.10: Finite element model, showing mesh, application of first thermal load	79
Figure 4.11: Temperature distribution thermal model at time, $t =$ (a) t , (b) $(t + \Delta t)$, (c) $(t + 2\Delta t)$. (spot size: 2 mm, power: 694 W, scan speed: 17.95 m/min)	81
Figure 4.12: Isothermal tempering of AISI 52100 steel	82

Figure 5.1: Illustration (front view of the longitudinal cross section of irradiated sample) of single, non-overlapping laser scan	87
Figure 5.2: Microstructure (longitudinal cross-section of AISI 52100 steel sample) of a single non-overlapping laser scan (laser power: 800 W, spot size: 2 mm, scan rate: 17.95 m/min)	89
Figure 5.3: Absorptivity calibration of white layer depth in single, non-overlapping laser scan (AISI 52100, laser power: 800 W, spot size: 2 mm, scan speed: 17.95 m/min)	90
Figure 5.4: White layer characterization as a function of laser power: (a) depth, and (b) width of white layer. (AISI 52100, spot size: 2 mm, scan speed: 17.95 m/min)	91
Figure 5.5: Simulated peak temperature (model) vs. depth from surface at different laser powers in single, non-overlapping scans. (spot size: 2 mm, scan speed: 17.95 m/min)	93
Figure 5.6: Peak surface temperature (model) vs. scan speed at different laser beam intensity in single, non-overlapping scans. (AISI 52100, spot size: 2 mm, scan speed: 17.95 m/min)	94
Figure 5.7: Microstructure (longitudinal cross-section of AISI 52100 steel sample) of overlapping laser scan (laser power: 800 W, spot size: 2 mm, scan speed: 17.95 m/min, overlap: 93.58%)	95
Figure 5.8: Microstructure (longitudinal cross-section of AISI 52100 steel sample) of overlapping laser scan (laser power: 800 W, spot size: 2 mm, scan speed: 35.90 m/min, overlap: 93.58 %)	97
Figure 5.9: Microstructure (longitudinal cross-section of AISI 52100 steel sample) of overlapping laser scan (laser power: 800 W, spot size: 2 mm, scan speed: 17.95 m/min, overlap: 75.76 %)	98
Figure 5.10: Depth of tempered white layer in overlapping laser scans as a function of overlap ratio (AISI 52100, laser power: 800 W, spot size: 2 mm, scan speed: 17.95 m/min).	99
Figure 5.11: X-ray diffraction patterns of laser-treated AISI 52100 steel (laser	105

power: 800 W, spot size: 2 mm, scan speed: 17.95 m/min, overlap: 93.58 %)

Figure 5.12: Surface and sub-surface hardness of longitudinal cross-section of AISI 52100 steel at laser scanning conditions: laser power: 800 W, spot size: 2 mm, and (a) overlap: 93.58 %, scan speed: 17.95 m/min (b) overlap: 87.22 %, scan speed: 17.95 m/min (c) overlap: 75.76 %, scan speed: 17.95 m/min (d) overlap: 93.58 % scan speed: 35.90 m/min	109
Figure 6.1: Kennametal CBN double-tipped turning insert	112
Figure 6.2: Kennametal ceramic turning insert	113
Figure 6.3: Experimental setup for turning	114
Figure 6.4: Predicted hardness vs. depth from surface for varying scan speeds (m/min) and overlap ratios (%) at constant laser intensity (laser power: 800 W, spot size: 2 mm)	116
Figure 6.5: Laser treatment of AISI 52100 steel workpiece	118
Figure 6.6: Rake face of CBN tool (top view)	119
Figure 6.7: Rake face of ceramic tool (top view)	119
Figure 6.8: Tool wear characterization: arc length and flank wear	121
Figure 6.9: Representative cutting force profiles	121
Figure 6.10: Representation of surface roughness profile	122
Figure 6.11: CBN tool wear (a. arc length, b. flank wear) progression in laser tempering based hybrid turning (LT) and conventional hard turning (Conv). Error bars represent 1 std. dev. of the wear measurements. (depth of cut: 0.3 mm, cutting speed: 180 m/min, feed: 0.10 mm/rev)	125
Figure 6.12: CBN tool wear in laser tempering based hybrid turning (LT) and conventional hard turning (Conv) after (a) ~22 s, (b) ~151 s, (c) ~235 s, of machining. (depth of cut: 0.3 mm, cutting speed: 180 m/min, feed: 0.10 mm/rev).	127

Figure 6.13: CBN tool wear in laser tempering based hybrid turning (LT) after 526 s of machining (depth of cut: 0.3 mm, cutting speed: 180 m/min, feed: 0.10 mm/rev)	128
Figure 6.14: Tool wear (a. arc length, b. flank wear) progression in laser tempering based hybrid turning (LT) and in conventional hard turning (Conv). Error bars represent 1 std. dev. of the wear measurements. (depth of cut: 0.3 mm, cutting speed: 130 m/min, feed: 0.10 mm/rev)	130
Figure 6.15: Ceramic tool wear in laser tempering based hybrid turning (LT) and CBN tool wear in conventional hard turning (Conv): (a) ~29 s, (b) ~84 s, (c) ~115 s, (d) ~170 s, of machining. (depth of cut: 0.3 mm, cutting speed: 130 m/min, feed: 0.10 mm/rev)	132
Figure 6.16: Ceramic tool wear in laser tempering based hybrid turning (LT) after ~639 s of machining. (depth of cut: 0.3 mm, cutting speed: 130 m/min, feed: 0.10 mm/rev)	133
Figure 6.17: Tool wear (a. arc length, b. flank wear) progression in laser tempering based hybrid turning (LT) and conventional hard turning (Conv). Error bars represent 1 std. dev. of the wear measurements. (depth of cut: 0.2 mm, cutting speed: 130 m/min, feed: 0.10 mm/rev)	135
Figure 6.18: Ceramic tool wear in laser tempering based hybrid turning (LT) and CBN tool wear in conventional hard turning (Conv): (a) ~25 s, (b) ~245 s, (c) ~643 s, (d) ~1264 s, of machining. (depth of cut: 0.2 mm, cutting speed: 130 m/min, feed: 0.10 mm/rev)	137
Figure 6.19: Progression of cutting forces - depth of cut: 0.3 mm, cutting speed: 180 m/min, feed: 0.10 mm/rev (Conv: conventional hard turning with CBN tool, LT: laser tempering based hybrid turning with CBN tool)	138
Figure 6.20: Progression of cutting forces. (a) depth of cut: 0.3 mm, cutting speed: 130 m/min, feed: 0.10 mm/rev, (b) depth of cut: 0.2 mm, cutting speed: 130 m/min, feed: 0.10 mm/rev (Conv: conventional hard turning with CBN tool, LT: laser tempering based hybrid turning with ceramic tool)	140
Figure 6.21: Machined roughness (R_a and R_t) results - cutting speed: 180 m/min, feed: 0.10 mm/rev, depth of cut: 0.3 mm. Error bars represent 1 std. dev. of the measurements. (Conv: conventional hard turning with CBN tool, LT: laser tempering based hybrid turning with ceramic tool)	141

Figure 6.22: Surface roughness (R_a and R_t) results - cutting speed: 130 m/min, feed: 0.10 mm/rev. Error bars represent 1 std. dev. of the measurements. (Conv: conventional hard turning with CBN tool, LT: laser tempering based hybrid turning with ceramic tool, 0.3: depth of cut: 0.3 mm, 0.2: depth of cut: 0.2 mm)	142
Figure 8.1.1: Fiber optics system	150
Figure 8.1.2: X-Y precision linear stage	151
Figure 8.1.3: Motor drive	152
Figure 8.1.4: Leica DMRM microscope	153
Figure 8.1.5: Hardinge Conquest CNC lathe	154
Figure 8.1.6: Kennametal MCGNL-124B tool holder	155
Figure 8.1.7: Kennametal MCGNL-124B tool geometry	156
Figure 8.1.8: Kistler force dynamometer	157
Figure 8.1.9: Zygo NewView200 setup	158
Figure 8.1.10: Principle of interferometry	159
Figure 8.2.1: Microstructure (longitudinal cross-section) of AISI 52100 steel samples after a single, non-overlapping laser scan (laser power: 580 W, spot size: 2 mm, scan rate: 17.95 m/min)	160
Figure 8.2.2: Microstructure (longitudinal cross-section) of AISI 52100 steel samples after a single, non-overlapping laser scan (laser power: 694 W, spot size: 2 mm, scan rate: 17.95 m/min)	161
Figure 8.2.3: Microstructure (longitudinal cross-section) of AISI 52100 steel samples after a single, non-overlapping laser scan (laser power: 879 W, spot size: 2 mm, scan rate: 17.95 m/min)	162
Figure 8.2.4: Microstructure (longitudinal cross-section) of AISI 52100 steel samples after a single, non-overlapping laser scan (laser power: 947 W, spot size: 2 mm, scan rate: 17.95 m/min)	163

Figure 8.3.1: Definition of crystal structure	164
Figure 8.3.2 (a) Diffraction of x-rays in crystalline material [Cullity 1956], (b) Beam interference patterns [Cullity 1956]	166
Figure 8.3.3: PANanalytical X'Pert Pro MPD	168
Figure 8.3.4: (a) Goniometer of PANanalytical X'Pert Pro MPD, (b) Schematic of the goniometer	170
Figure 8.3.5: X-ray diffraction patterns of hardened AISI 52100 steel sample (~63 HRC), no laser treatment	171
Figure 8.3.6: X-ray diffraction patterns of laser-treated AISI 52100 steel sample - depth from surface: 0 μm (laser power: 800 W, scan speed: 17.95 m/min, overlap: 93.58 %)	172
Figure 8.3.7: X-ray diffraction patterns of laser-treated AISI 52100 steel sample - depth from surface: ~7 μm (laser power: 800 W, scan speed: 17.95 m/min, overlap: 93.58 %)	173
Figure 8.3.8: X-ray diffraction patterns of laser-treated AISI 52100 steel sample - depth from surface: ~42 μm (laser power: 800 W, scan speed: 17.95 m/min, overlap: 93.58 %)	174
Figure 8.3.9: X-ray diffraction patterns of laser-treated AISI 52100 steel sample - depth from surface: ~77 μm (laser power: 800 W, scan speed: 17.95 m/min, overlap: 93.58 %)	175
Figure 8.3.10: X-ray diffraction patterns of laser-treated AISI 52100 steel sample - depth from surface: ~109 μm (laser power: 800 W, scan speed: 17.95 m/min, overlap: 93.58 %)	176
Figure 8.3.11: X-ray diffraction patterns of laser-treated AISI 52100 steel sample - depth from surface: ~152 μm (laser power: 800 W, scan speed: 17.95 m/min, overlap: 93.58 %)	177
Figure 8.3.12: X-ray diffraction patterns of laser-treated AISI 52100 steel sample - depth from surface: ~242 μm (laser power: 800 W, scan speed: 17.95 m/min, overlap: 93.58 %)	178
Figure 8.3.13: X-ray diffraction patterns of laser-treated AISI 52100 steel sample - depth from surface: ~456 μm (laser power: 800 W, scan speed: 17.95 m/min,	

overlap: 93.58 %)

179

Figure 8.3.14: X-ray diffraction patterns of laser-treated AISI 52100 steel sample
- depth from surface: ~ 0 μm (laser power: 800 W, scan speed: 35.90 m/min,
overlap: 93.58 %)

180

Figure 8.3.15: X-ray diffraction patterns of laser-treated AISI 52100 steel sample
- depth from surface: ~ 12 μm (laser power: 800 W, scan speed: 35.90 m/min,
overlap: 93.58 %)

181

Figure 8.3.16: X-ray diffraction patterns of laser-treated AISI 52100 steel sample
- depth from surface: ~ 27 μm (laser power: 800 W, scan speed: 35.90 m/min,
overlap: 93.58 %)

182

Figure 8.3.17: X-ray diffraction patterns of laser-treated AISI 52100 steel sample
- depth from surface: ~ 0 μm (laser power: 800 W, scan speed: 17.95 m/min,
overlap: 75.76 %)

183

Figure 8.3.18: X-ray diffraction patterns of laser-treated AISI 52100 steel sample
- depth from surface: ~ 11 μm (laser power: 800 W, scan speed: 17.95 m/min,
overlap: 75.76 %)

184

Figure 8.3.19: X-ray diffraction patterns of laser-treated AISI 52100 steel sample
- depth from surface: ~ 82 μm (laser power: 800 W, scan speed: 17.95 m/min,
overlap: 75.76 %)

185

LIST OF SYMBOLS

t	time (sec)
X, Y, Z	coordinate representation
A_1	eutectoid temperature of the steel (K)
A_{CM}	A_{CM} temperature of steel (K)
C_C	critical carbon concentration, 0.05 %
C_o	carbon concentration in ferrite before laser hardening (wt. %)
C_γ^c	carbon content in austenite in equilibrium with cementite (wt. %)
C_c^γ	carbon content in cementite in equilibrium with austenite (wt. %)
C_m	mean carbon content in martensite (wt. %)
$C_p(T)$	specific heat ($\text{Jm}^{-1}\text{K}^{-1}$)
D	laser spot diameter (m)
D_o	pre-exponential for diffusion of carbon ($\text{m}^2 \text{s}^{-1}$)
D_t	frequency factor for tempering (s^{-1})
F_f	feed force (N)
F_t	tangential force (N)
F_r	radial force (N)
f	volume fraction of carbon
h	lumped convection coefficient ($\text{W m}^{-2} \text{K}^{-1}$)
H	hardness of the surface (HV)
H_o	hardness of as-quenched state (HV)
H_a	hardness of annealed state (HV)
H_v	hardness of tempered state (HV)
$I(t)$	kinetic strength of the heat cycle
$k(T)$	thermal conductivity ($\text{J s}^{-1} \text{m}^{-1} \text{K}^{-1}$)
K	supersaturation parameter
K_c	critical carbon concentration factor

m	ageing exponent of the material
M_s	martensite start temperature (K)
M_f	martensite finish temperature (K)
P	output power of the laser source (W)
P_i	incident laser power (W)
$P_{a(x,y,z)}$	power distribution at location X, Y, Z (W)
ρ	density (Kg m^{-3})
Q	activation energy for diffusion of carbon (J mol^{-1})
\dot{Q}	rate of heat generation (W m^{-3})
R	universal gas constant, 8.314 ($\text{J mol}^{-1} \text{K}^{-1}$)
R_t^c	instantaneous radius of the particle (m)
R_a	surface roughness height (μm)
R_t	surface roughness peak-to-valley height (μm)
r_i	average initial radius of cementite particle (m)
$2r_e$	average spacing of adjacent cementite particles (m)
$T(t)$	subsurface temperature (K)
$\tau_v(t)$	tempering ratio
T_{melt}	melting point of the material (K)
T_n	nose temperature of the material, obtained from the material transformational diagrams (K)
T_o	ambient temperature (K)
ΔT	undercooling temperature (K)
V_y	laser scan speed (m sec^{-1})
$C, Cu, Cr, Fe, As,$ Mo, Mn, Ni, Si, V, W	alloying constituents of the steel (carbon, copper, chromium, iron, arsenium, molybdenum, manganese, nickel, silicon, vanadium, tungsten, respectively)
$f_m, f_p, f_{ce}, f_{ra}, f_f, f_\epsilon$	volume fraction of martensite, pearlite, cementite, retained austenite, ferrite, ϵ -carbide, respectively
$H_m, H_{ce}, H_f, H_\epsilon$	hardness of martensite, cementite, ferrite, ϵ -carbide, respectively (HV)
λ	wavelength of incident radiation

ϵ	emissivity of the material
η	efficiency of laser source
2θ	diffraction angle (deg)
K_α	characteristic lines of x-ray diffraction patterns
d	interplanar spacing of atoms (μm)
n_b	integral multiple (Bragg's law)
MRR	material removal rate (mm^3/min)
VB	flank wear (μm)

SUMMARY

Cost-effective machining of hardened steel (>60 HRC) components such as a large wind turbine bearing poses a significant challenge. This thesis investigates a new laser tempering based hybrid turning approach to machine hardened AISI 52100 steel parts more efficiently and cost effectively. The approach consists of a two-step process involving laser tempering of the hardened workpiece surface followed by conventional machining at higher material removal rates using lower cost ceramic tooling to efficiently cut the laser tempered material.

The specific objectives of this work are to: (a) study the characteristics of laser tempering of hyper-eutectoid 52100 hardened steel, (b) model the laser tempering process to determine the resulting hardness, and (c) conduct machining experiments to evaluate the performance of the laser tempering based hybrid turning process in terms of forces, tools wear and surface finish.

First, the microstructure alterations and phase content in the surface and subsurface layers are analyzed using metallography and x-ray diffraction (XRD) respectively. Laser tempering produces distinct regions consisting of - a tempered white layer and a dark layer- in the heat affected subsurface region of the workpiece. The depth of the tempered region is dependent on the laser scanning conditions. Larger overlap of laser scans and smaller scan speeds produce a thicker tempered region. Furthermore, the tempered region is composed of ferrite and martensite and weak traces of retained austenite (~ 1 %).

Second, a laser tempering model consisting of a three dimensional analytical model to predict the temperature field generated by laser scanning of 52100 hardened steel and a phase change based hardness model to predict the hardness of the tempered region are developed. The thermal model is used to evaluate the temperature field

induced in the subsurface region due to the thermal cycles produced by the laser scanning step. The computed temperature histories are then fed to the phase change model to predict the surface and subsurface hardness. The laser tempering model is used to select the laser scanning conditions that yield the desired hardness reduction at the maximum depth. This model is verified through laser scanning experiments wherein the hardness changes are compared with model predictions. The model is shown to yield predictions that are within 20 % of the measured hardness of the tempered region.

Using the laser scanning parameters determined from the laser tempering model, cutting experiments using Cubic Boron Nitride (CBN) tools and low cost alumina ceramic tools are conducted to compare the performance of laser tempering based hybrid turning with the conventional hard turning process. The machining experiments demonstrate the possibility of higher material removal rates, lower cutting forces, improved tool wear behavior, and consequently improved tool life in the laser tempering based process. In addition, the laser tempered based hybrid turning process produce is shown to yield lower peak-to-valley surface roughness height than the conventional hard turning process. Furthermore, it is found that lower cost ceramic tools can be used in place of CBN tools without compromising the material removal rate.

[This page is intentionally left blank]

CHAPTER 1

INTRODUCTION

1.1 Background and Motivation

Many industries including aerospace and automobile, energy, tool and die, metal machinery require components that have high load carrying capacity, high hardness, high toughness, good tempering properties, resistance to corrosion, fatigue and wear, and are able to operate under intense loading and extreme conditions. These applications require the use of high strength materials such as hardened steels, tool steels, stainless steels, and other superalloys with unique metallurgical properties to meet the demands of extreme applications. These high strength steels are replacing the conventional steels in various sectors (Figure 1.1). The consumption of steel accounts for 1 billion tons in 2010 [AISI].

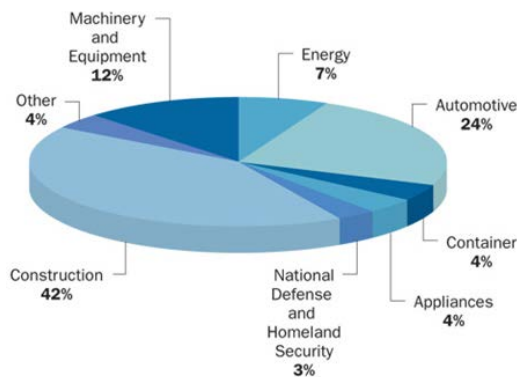


Figure 1.1: 2010 steel usage by industry [courtesy: American Iron and Steel Institute (AISI)].

In the construction sector, high strength steels are used from rails to bridges, towers to warehouses for superior toughness and low maintenance requirements. In the automobile sector, it is estimated that about 50 % of steels used to make vehicles today, did not exist ten years ago [AISI]. Industry analysts estimate that these materials have grown in usage in auto manufacturers by 44 % over the last decade because they provide

a superior combination of high strength, crash energy management, excellent formability and dent resistance, and make automobiles safer and more fuel-efficient [Ducker International 2009]. Figure 1.2 is Mercedes-Benz E-class structure that has about 72 % of body panels made of such ultra-high-strength steel alloys. In the tooling industry, the ultra-high-strength alloys, which have almost three to four times the tensile strength of conventional steels, are used where the material is exposed to exceptionally high stress. Figure 1.3 shows large (2 m diameter) turbine bearing that is used in wind energy applications. Figures 1.4 and 1.5 show titanium components used in medical applications, and large turbine shafts used in aerospace applications, respectively. Furthermore, high strength martensitic stainless steels are used in thermal and nuclear power plants due to its ability to retain properties at high temperatures [Klueh et al. 2001].



Figure 1.2: High strength steel structure in Mercedes-Benz passenger car
[courtesy: Daimler AG].



Figure 1.3: Large bearings for wind turbine [courtesy: The Timken Company].



Figure 1.4: Titanium components for medical application [courtesy: Alphaomegaswiss].



Figure 1.5: Large turbine shafts for aerospace application [courtesy: Science photo library].

On the other hand, materials that are harder and tougher are more difficult to machine. Manufacturers are constantly striving for lower cost solutions including innovative processes to process these high strength materials and at the same time, meet demands on productivity, sustainability, energy, and waste reduction.

Conventional machining methods such as hard turning have gained industrial acceptance because of the higher material removal rates that are possible with the use of hard, wear resistant tools and the quality of machined surfaces comparable to grinding [Technology assessment - AMT 2006]. From a processing time and cost standpoint, hard turning has considerable advantages (see Figures 1.6 and 1.7) than grinding [Tonshoff et al. 1995, Hasan 1998].

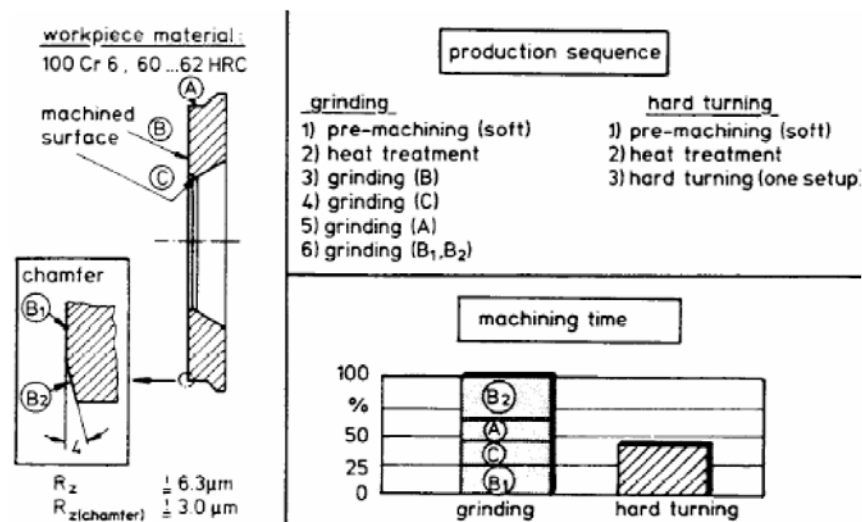


Figure 1.6: Gear production - grinding vs. hard turning [Tonshoff et al. 1995].

The developments in hard turning technology can be broadly classified as: (a) increasing the quality of the cutting tool materials, and (b) hot machining. In the former classification, the advent of CBN and tough ceramic tools and special cutting edge preparations on these tools have enabled longer tool life when machining these difficult-to-machine materials. On the other hand, hot machining gained importance for machining difficult-to-machine materials because they lower the hardness of the region of the

material to be removed without affecting the bulk material. It is well-known that with an increase in temperature there is a drop in the flow stress and strain-hardening rate of the material.

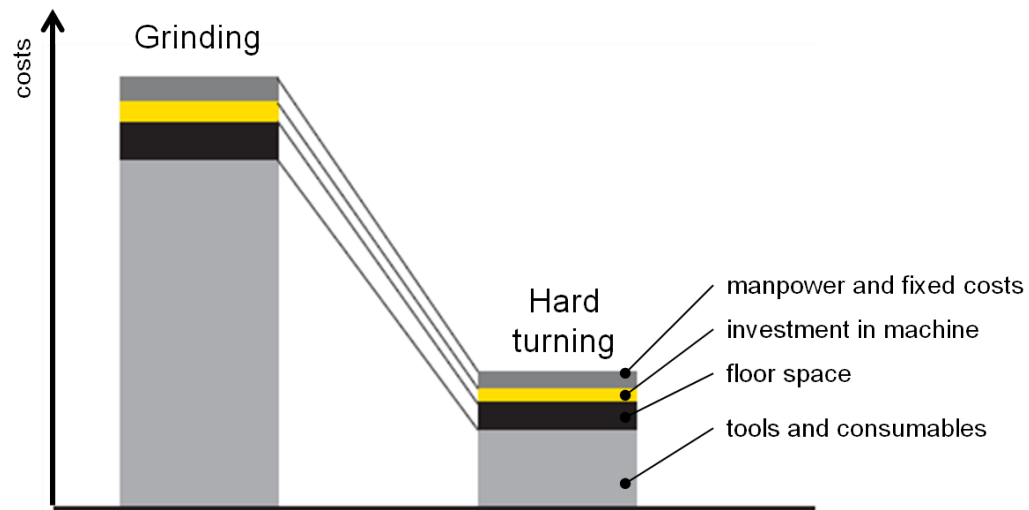


Figure 1.7: Cost - grinding vs. hard turning [Hasan et al. 1998, Sandvik 2005].

Among several methods for imparting heat to the work material, machining with the assistance of a laser beam has been studied since the 1960s when powerful pulse generators of monochromatic radiation were built. Konig et al. [Konig et al. 1993] noted that for hot machining to be most effective there needs to be sufficiently large heat transferred to a small, focused area directly in front of the cutting tool. CO₂ and Nd:YAG high power lasers have become well-accepted as machining tools in industrial manufacturing over the last two decades. The higher initial investment cost, size and complexity of CO₂ and Nd:YAG laser systems were overcome by the introduction of high power diode lasers that combine high performance with a compact design, which can be used in many applications due to their power, wavelength, spectral and beam quality. In addition, these high power lasers can be controlled in terms of positioning and timing and therefore, have become a flexible tool for various manufacturing processes.

In Laser-Assisted Machining (LAM), a laser is used as the heat source with its beam focused on the workpiece directly in front of the cutting tool. The induced temperatures are sufficiently high to cause reduction in hardness in the surface layer of the material. The cutting action of the tool is then by ductile deformation rather than brittle fracture for hard materials [Rajagopal et al. 1982, Klocke et al. 1997, Anderson et al. 2006]. Although this process can enhance the machinability of these materials, it has certain limitations when it comes to practical implementation. These include the physical and safety challenges associated with integrating a laser into a machine tool and the requirement of a relatively high power laser to induce sufficient thermal softening in order to achieve practical material removal rates. The latter limitation often constrains the maximum cutting speeds, feeds and depths of cut that can be achieved in the process. In addition, tool materials that can withstand sufficiently high temperatures without losing their strength (e.g. CBN) are needed for this process.

The focus for the development of the cutting tool has always been to scale productivity (see Figure 1.8). While existing laser based hard turning technologies have shown the way to work high strength materials, they fall short from a productivity standpoint due to low material removal rates. In addition, lower cost tools such as alumina tools cannot be employed in existing laser based processes. Figure 1.9 shows the tooling budget of the U.S. manufacturing companies, with a significant proportion of tools used for hard turning applications.

Further, it is estimated that if advancements in hard turning technology bring down manufacturing costs by up to 30 %, U.S. industry could reap annual gains of up to \$6 billion [NIST 2000].

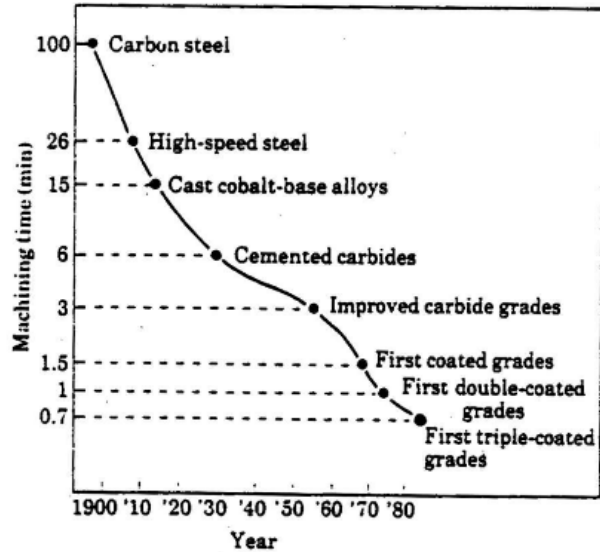


Figure 1.8: Development of cutting tools [Colding 1980].

What is your 2009 budget for cutting tools?

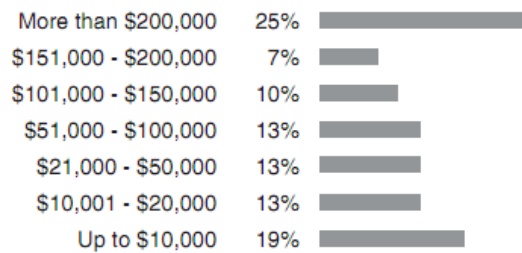


Figure 1.9: US budget for cutting tools [Tooling and Production 2009].

It is well-known from the laser hardening literature [Devgun et al. 1990] that overlapping laser scans can cause a reduction in the material hardness in the overlap region due to a tempering effect (see Figure 1.10). In addition, it was shown that, by appropriately choosing laser scanning conditions, it is possible to control the extent of tempering in the subsurface of the workpiece material. This material behavior can be used to increase both the material removal rates in difficult-to-machine materials and the

performance of the tool or alternatively lower tooling cost via the use of less expensive tool material.

While laser surface hardening has been studied extensively, laser surface tempering has not yet received wide industrial attention. It is necessary to investigate the laser surface tempering process in order to achieve controlled reduction in the subsurface hardness of through-hardened steel. A relationship between the laser process parameters and the variation in subsurface hardness needs to be established. Through-hardened steel can then be case-tempered without affecting the harder bulk material. From a machining standpoint, the tempering behavior can be used to enhance the machinability (i.e., higher material removal rate) of difficult-to-machine materials. In addition, a tempered subsurface region in the cutting zone implies higher material removal rate without significantly diminishing tool life. Furthermore, low cost ceramic tools can be used in place of expensive CBN tools that are used in conventional hard turning. It is therefore necessary to investigate the possibility of higher material removal rates, and improved tooling performance with the new hybrid turning approach proposed for machining hardened steel parts.

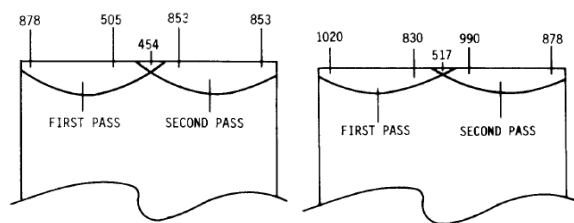


Figure 1.10: Hardness distribution for bearing steel scanned with 1.4 kW CO₂ rectangular laser beam under different overlapping conditions: hardness along the width of laser-treated surface for 16.4 μm/sec (left) and 26.2 μm/sec (right) scanning speed [Devgun et al. 1990].

1.2 Research Goals and Objectives

The goals of this thesis work are to investigate the possibility of using laser tempering to enhance the machinability of hardened surface steel (AISI 52100, ~63 HRC) through higher material removal rates and lower cost tooling. The goal is achieved through the following specific objectives:

1. Model the laser tempering process to aid in selecting the laser scanning conditions necessary to lower the hardness of a predefined volume of the workpiece material.
2. Design and build an experimental setup for laser tempering of difficult-to-machine material.
3. Analyze the microstructure and phase transformation of the laser tempered subsurface region.
4. Conduct machining experiments to compare the tool life, cutting forces, and surface finish obtained in laser tempering based hybrid process and conventional hard turning process.

1.3 Thesis Outline

Figure 1.11 illustrates the outline of this thesis. In Chapter 2, prior work in the field of hard turning and laser based approaches are discussed. In Chapter 3, the new laser based hybrid process and the experimental setup used for laser-treating the hardened steel samples is presented. In Chapter 4, a phase change model is formulated to simulate the laser tempering process. The model predicts the subsurface temperature field due to laser irradiation and uses this information to predict the tempered subsurface hardness of the hyper-eutectoid steel (AISI 52100 steel). In Chapter 5, the microstructure and composition of phases in the subsurface of the sample subjected to laser tempering under different laser scanning conditions are presented. Then, the results from the calibrated model are compared with the measured values obtained from laser tempering experiments. In Chapter 6, the model is used to select laser scanning conditions that yield

a large depth of tempered layer. The selected laser parameters are used to treat the AISI 52100 steel workpiece and machining experiments were carried out to compare the laser tempering based hybrid turning process with conventional hard turning. Machinability metrics used for comparison are tool wear, cutting force, and machined surface finish. Finally, in Chapter 7, the main conclusions and contributions of this thesis and possible future research directions are discussed.

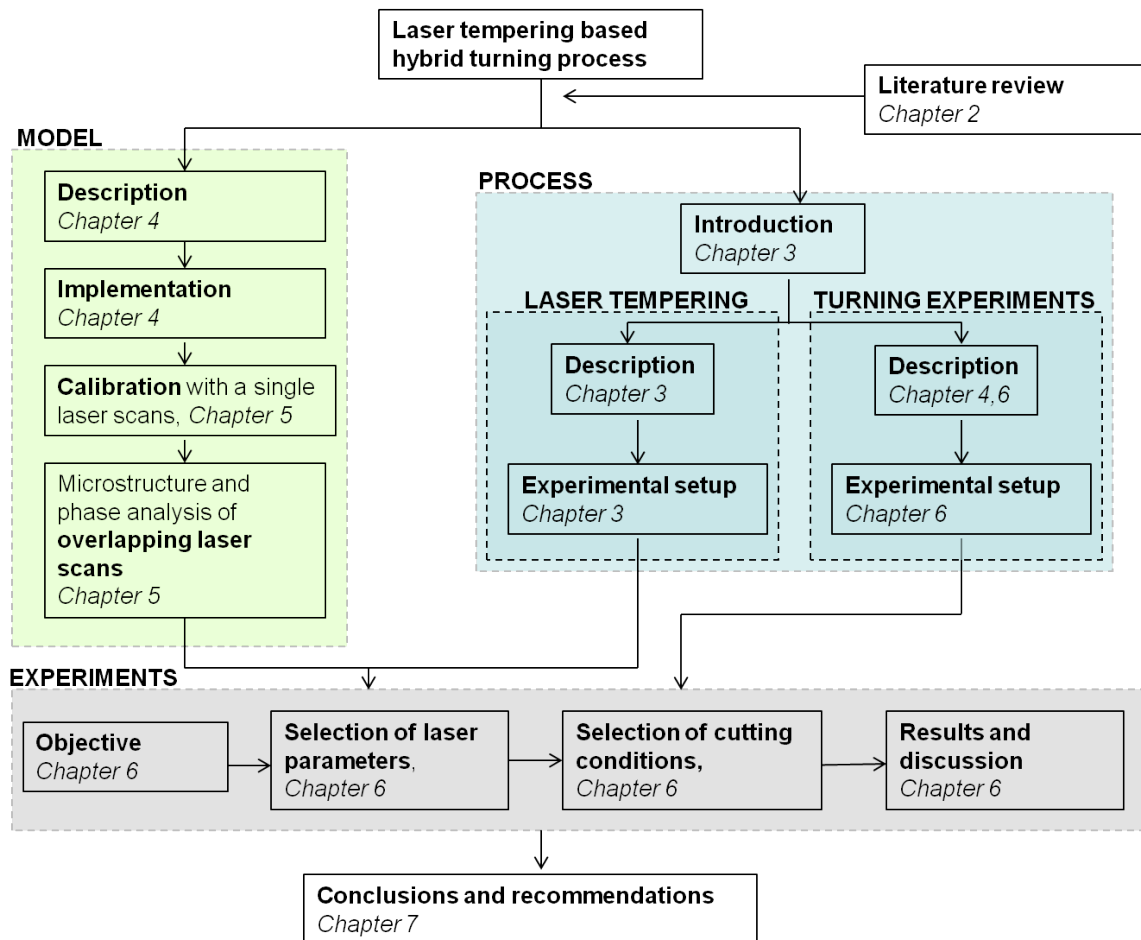


Figure 1.11: Thesis outline.

CHAPTER 2

LITERATURE REVIEW

2.1 Overview of Hard Turning

Hard turning is a material removal process involving plastic deformation of the workpiece (of hardness greater than 45 HRC) due to the action of cutting tool. For successful machining of hard materials, a very hard and tough tool material with appropriate cutting tool geometry and edge preparation, proper selection of cutting conditions is deemed. The energy used in cutting is converted to heat - about 80 % of this is carried away in the chip and rest is taken by the cutting tool.

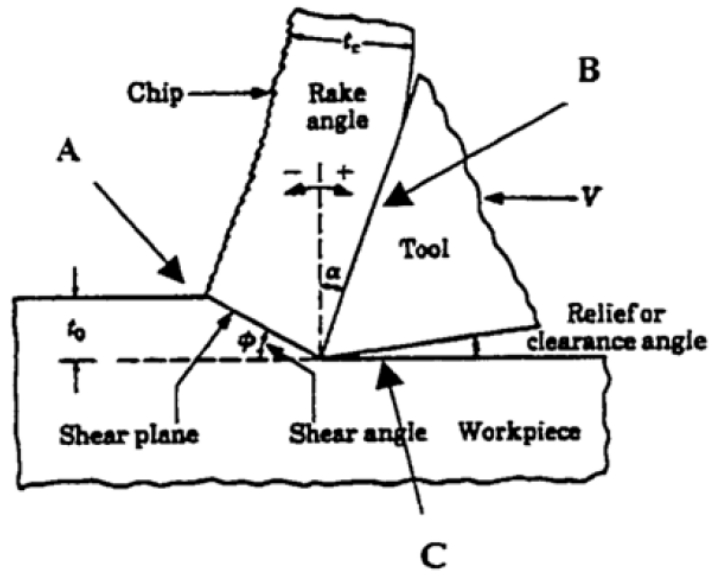


Figure 2.1: Orthogonal cutting model (t_0 : undeformed chip thickness, t_c : chip thickness, V : cutting speed, A: shear plane, B: chip-tool interface, C: interface between the tool face and the machined surface) [Boothroyd 1996].

Machining processes can be represented by two cutting models depending on the tool geometry and tool orientation, (a) orthogonal cutting, and (b) oblique cutting. In orthogonal cutting, the cutting edge is orthogonal to the cutting speed direction.

Consequently, the chip flow is always perpendicular to the cutting edge at all points along the cutting edge. Although, common machining processes, such as turning, are complex oblique cutting processes, these processes can be represented by two-dimensional geometry as shown in Figure 2.1. Several geometry in the cutting plane influence the cutting action. For instance, high shear plane angle leads to smaller shear plane which means lower shear force, cutting forces, power, and temperature.

High strain rates in the primary shear zone and elevated temperatures at the tool/chip interaction zone, frictional interaction between the chip and the tool in the secondary shear zone makes the process a complex thermo-mechanical phenomena.

2.2 Cutting Tool

2.2.1 Cutting Tool Geometry

Cutting tool geometry is one of the critical parameters in hard turning. The geometry of the single point cutting tool is described by the tool angles that influence the performance of the cutting tool (see Figure 2.2). Negative rake angle tools and inserts with custom edge geometry are used in hard turning to resolve stresses into the tool such that loading occurs primarily in compression [G.E. Superabrasives 1997].

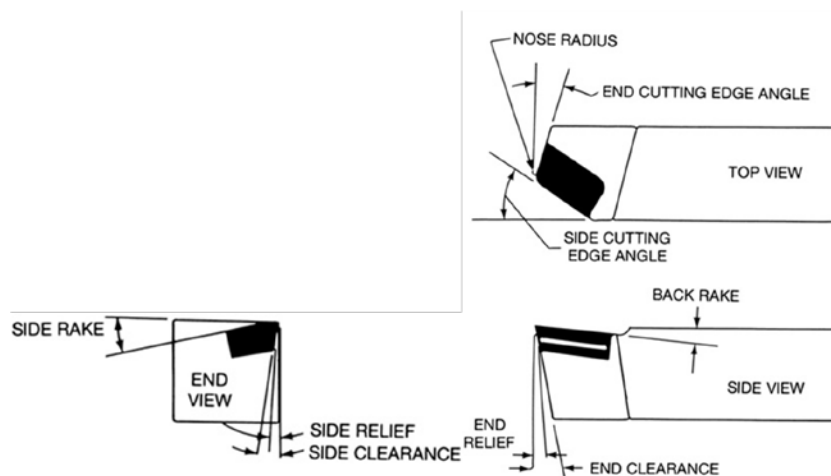


Figure 2.2: Tool angles of single-point cutting tool [Shaw 1984].

2.2.2 Cutting Tool Material

The cutting tools used for hard turning require high hardness, inertness to ferrous materials, chemical stability at elevated temperatures, high temperature stability, high expansion coefficient, high compressive strength and wear resistance, oxidation resistance.

Following materials listed in the order of increasing hardness are generally used for turning applications: (1) high speed steels, (2) cast alloys (e.g., stellites), (3) cermets, (4) ceramics, (5) silicon nitride, (6) cubic boron nitride (CBN), and (7) polycrystalline diamond [Trent et al. 2000]. Figures 2.3 and 2.4 represent the hardness, toughness, and hot hardness characteristics of the cutting tool material. Polycrystalline diamond cannot be used for machining steel because of its solubility and the catalytic effect of iron which causes graphitization of the diamond. Only polycrystalline Cubic Boron Nitride (CBN) and ceramic cutting tools are stable at temperatures $>1000\text{ }^{\circ}\text{C}$ for machining hardened ferrous or alloy steels of hardness $>45\text{ HRC}$ [Abrao et al. 1995a]. However, ceramic tools are attributed to poor shock resistance and low fracture toughness..

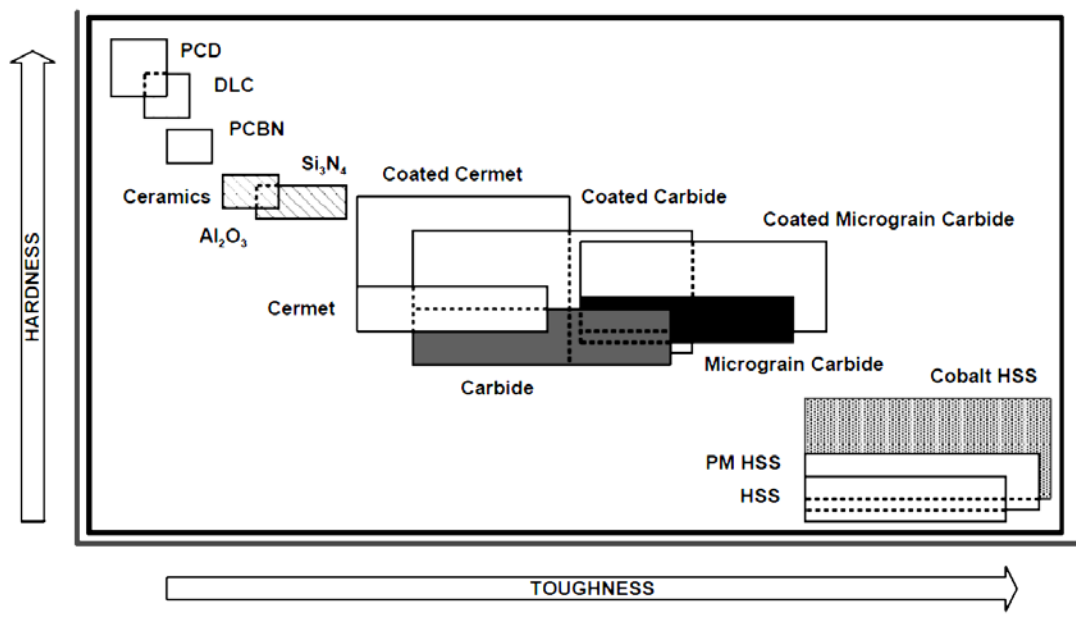


Figure 2.3: Hardness vs. toughness of tool material [Tool Materials - ASM 2005].

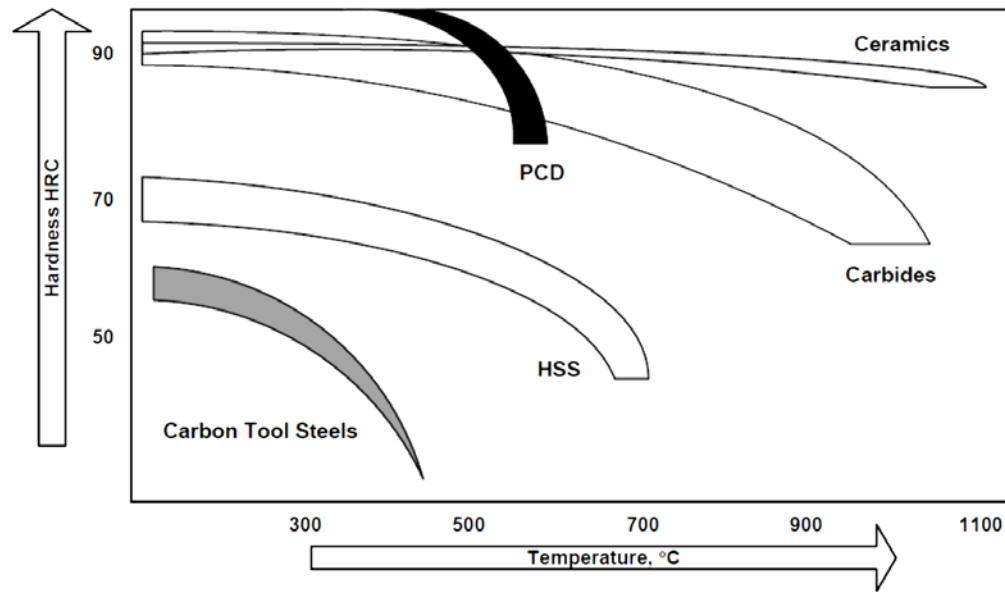


Figure 2.4: Hot hardness of tool material [Tool Materials, ASM 2005].

CBN tools are manufactured from the boron nitride hexagonal crystals using a high temperature (>1400 °C) and high pressure (>60 kilobars) process. The polycrystalline CBN crystals are either sintered with a binder phase or integrally bonded to a tungsten-carbide (TiC) or titanium-nitride (TiN) substrate. The addition of bonding material reduces the thermal conductivity of the resulting compound. CBN tools are classified based on the volume fraction of CBN grains in the tool. The selection of particular CBN grade is highly dependent on the workpiece material system and particular machining application [Chou et al. 1995].

Ceramic tools are primarily molded and sintered with alumina (Al_2O_3) and silicon nitride (Si_3N_4) in high pressure, high temperature process. Alumina is chemically stable at temperatures up to 1200 °C and has a low or zero tendency for diffusion wear when machining steels. The white Al_2O_3 based ceramics contain a sintering aid 2-5 % Zirconia (ZrO_2), which improves its fracture toughness by transformation toughening or crack deflection mechanism but decreases its thermal conductivity [Lange et al. 1982, Claussen et al. 1985]. Al_2O_3 ceramic tool are reinforced with TiC or TiN to improve thermal

conductivity, hardness, toughness without seriously degrading its chemical stability. In whisker reinforced alumina ceramic cutting tools, the SiC whiskers are reinforced in the aluminum oxide matrix to increase the fracture toughness, hardness of the composite [Kim et al. 1994]. Si_3N_4 based ceramics have whisker-like grain structure that possesses excellent hot hardness, thermal shock resistance and toughness.

2.2.2 Cutting Tool Edge Preparation

In order to improve the quality and reliability of the cutting tool and the workpiece, the cutting edge of the tool is prepared (see Figure 2.5). Cutting edge preparation consists of generating the cutting edge geometry, modifying the microtopography of the edge, changing the roughness and texture of the tool surfaces in the vicinity of the edge, eliminating the edge defects, and improving the strength [Rodriguez 2009]. Experimental works of [Johnson 1967, Liu et al. 1982, Jang et al. 1996, Thiele et al. 1999] have shown the importance of edge preparation for single-point turning tool. Thiele [Thiele et al. 2000] showed that, in hard turning, the cutting edge geometry had significant impact on the surface integrity and the residual stress. Large hone radius tools produced more compressive stresses, but left white layers on the machined surface.

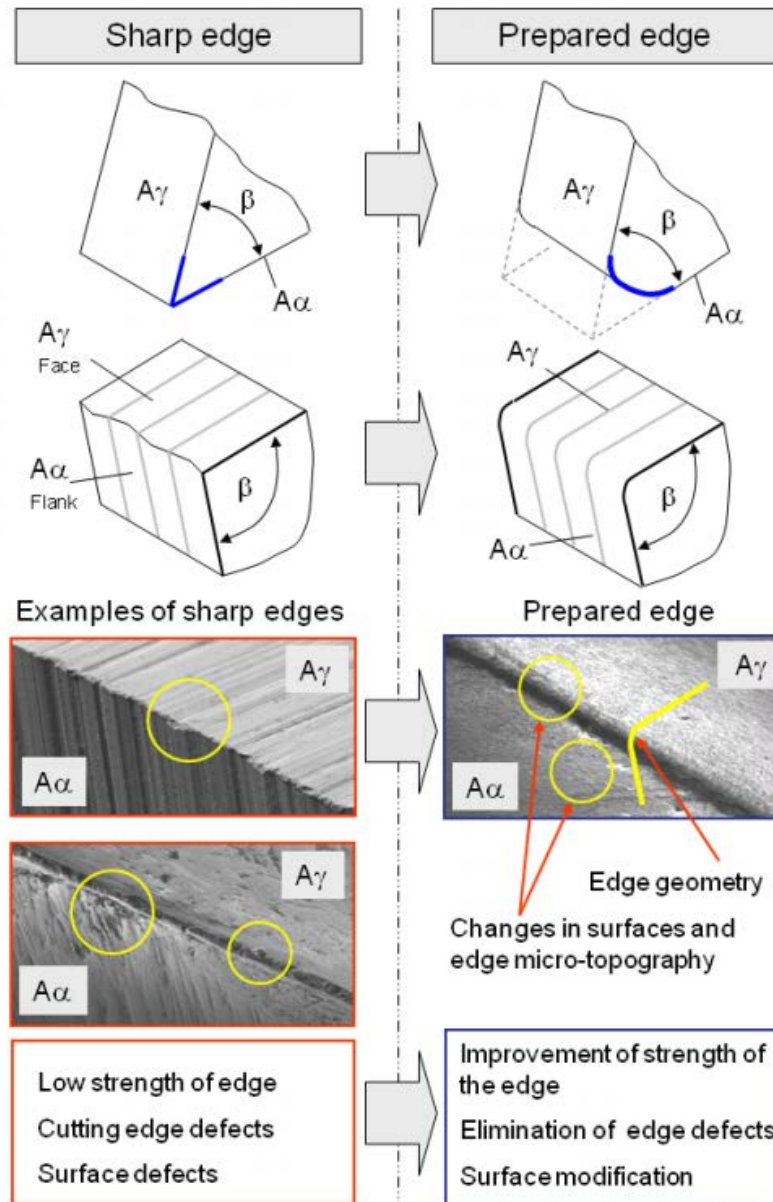


Figure 2.5: Cutting edge preparation [Rodriguez 2009].

2.2.3 Cutting Tool Wear

The high contact stress and high temperature between the tool rake-face and the chip, and between the tool flank face and the workpiece causes severe friction, leading to tool wear. Wear depends on the materials properties of the tool and the workpiece (physical, mechanical, thermal properties, tool geometry) and the cutting conditions

(cutting speed, feed rate, depth of cut). The types of wear on a tool depend on the relative roles of these variables. The result is a variety of wear mechanisms and patterns observed at the rake face and the flank face of the tool.

An irregular material flow and non-uniform tool/workpiece contact causes different wear mechanisms [Trent et al. 2000, Stephenson et al. 2006]: (a) abrasion, (b) adhesion, (c) diffusion/dissolution, (d) plastic deformation, (e) tribochemical wear.

Cutting tool has three modes of failure: (a) fracture failure, (b) thermal failure, and (c) gradual failure. The first two failures are premature failures that occur when the cutting temperature and cutting forces becomes excessive or if the cutting conditions are inappropriate for the tool/workpiece combination leading to brittle failure. Gradual failure (see Figure 2.6) occurs due to the gradual wear of the tool due to the high mechanical and thermal stresses as a result of tool/workpiece interaction. The various regions of wear [Armarego 1969, Kumar et al. 2006] are: (a) flank wear, (b) crater wear, (c) notch wear, and (d) nose radius wear. A representative flank wear is shown in Figure 2.7.

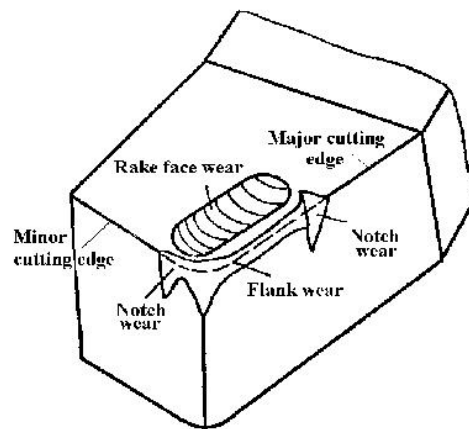


Figure 2.6: Cutting tool wear pattern [Armarego 1969].

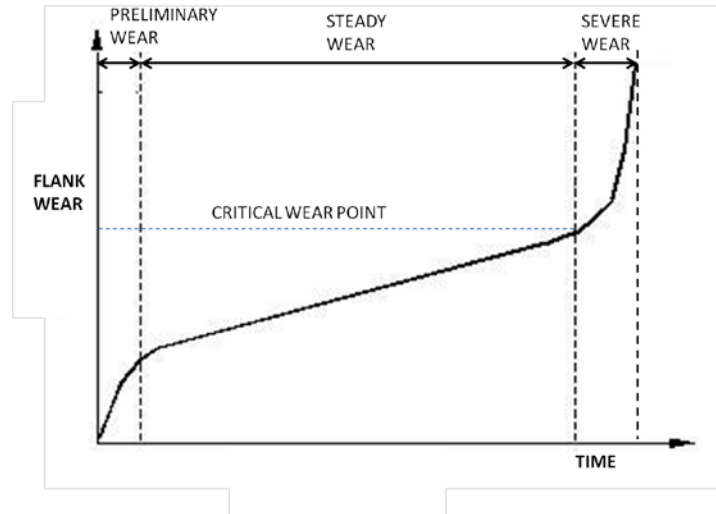


Figure 2.7: Representative flank wear [Groover 2007].

2.3 Tool Wear in Hard Turning

During hard-turning, the geometry of the cutting tool continuously changes due to wear of the tool. A number of researchers have studied the wear mechanisms and the performance of the CBN and ceramic tools in hard turning.

2.3.1 CBN

The wear in CBN tool has been attributed to many factors - composition, hardness and microstructure of the workpiece [Barry et al. 2001], tool geometry [Zhou et al. 2003] and cutting conditions [Arsecularatne et al. 2006]. High pressure and temperature at the tool/workpiece interface lead to micro-cracks and micro-fractures in CBN tool. The polycrystalline tool edge regenerates constantly during cutting and the sharp crystals emerging from the deeper layers of the flank of the tool ensure its continued sharpness and cutting ability. The wear resistance of the tool is high, because the micro-cracks are shallow and the grain boundaries localize [Mamalis et al. 2002].

Narutaki [Narutaki et al. 1979] investigated CBN tools on workpiece with wide hardness range (10-66 HRC). When machining softer steels, they observed that a low CBN content tool has less flank wear compared to the high content CBN tool. This

behavior was attributed to lower attrition wear due to greater bonding strength of the tool. On the other hand, high CBN content tool performed better when machining hardened tool steels, case hardened steels. This was attributed to the abrasive resistance of high content CBN.

Klimenko [Klimenko et al. 1996] observed the formation of built-up layer at the workpiece/flank interface which was attributed to the chemical interactions of tool with the work material and atmosphere. Chou [Chou et al. 1999] suggested the possibility of different dominant wear modes at different cutting condition – mechanical wear at low cutting speed and thermal wear at high cutting speeds. Poulachon [Poulachon et al. 2003] observed the wear of low CBN content tool is due to the abrasion of the tool/binder by hard carbide particles in the steel work materials. Farhat [Farhat et al. 2003] studied low CBN content tool in machining P20 tool steel and found that diffusion to be the dominant wear mechanism based on the worn flank topography.

2.3.2 Ceramic

When machining hardened steels, alumina based ceramic cutting tools are subjected to flank wear, crater wear and notch wear.

Brandt [Brandt et al. 1986] studied the flank and crater wear mechanisms of alumina ceramic to cut SS 2541 (HB 320) steel. It was observed that the flank wear in ceramic tool is predominantly due to lateral cracks and intergranular fracture mechanism. Crack initiation was attributed to the dislocation pile-ups at the grain boundaries as a result of thermally activated plastic deformation. On the other hand, crater wear was due to the plastic deformation of the thin layer leading to ductile or brittle fracture of small pieces from the asperities on the tool rake face.

Brandt et al. [Brandt et al. 1990] studied the wear mechanisms of alumina, silicon carbide and silicon nitride based ceramic tools when machining a heat resistant SS2541 (HB 320) and Inconel 718 alloy (HB 370). They observed that the dominant wear

mechanism for alumina and silicon carbide based ceramic tools was notch wear, while that for silicon nitride based ceramics was flank wear. Workpiece elements diffuse into the less chemically stable *SiN* based composite tool leading to higher flank wear rate. Due to the strong bonding formed as a result of chemical reaction between the tool and workpiece, individual grains or agglomerates were removed from the tool materials leading to edge line chipping. However, in the *SiC* ceramic composites, the flank wear mechanism was due to the preferential attack of the silicon carbide whiskers which was accentuated only at higher cutting speeds. Thangaraj et al. [Thangaraj et al. 1992] studied the wear behavior of *SiC* whisker reinforced alumina ceramic tools when machining Inconel 718 alloy. Flank wear played a dominant role at lower cutting speed and notch wear played a dominant role at higher cutting speed.

Recently, Kumar [Kumar et al. 2006] studied the wear behavior of alumina based ceramic tools on machining martensitic stainless steel - grade 410 (60 HRC) and EN 24 steel (45 HRC). They observed that flank wear, crater wear and notch wear are higher on machining martensitic stainless steel than that on machining hardened steel, which is due to the higher hardness of martensitic stainless steel than that of EN24 steel. They concluded that, *Ti[C,N]* mixed alumina ceramic cutting tool performs better than *SiC* whisker reinforced alumina ceramic cutting tool on machining martensitic stainless steel and hardened steel.

2.3.3 CBN vs. Ceramic Tools

Ceramic tools possess excellent thermal and chemical stability, however the ceramic tool lacks PCBN's toughness and hardness. Softer workpiece (< 45 HRC) tend to produce long, stringy chips that propagate crater wear on the PCBN tool and shortens its life to the point where it is no longer cost- effective compared to conventional tooling. For these softer workpiece, ceramic is the better tool-material choice [Clarius et al. 1995]. On the other hand, high temperatures are generated in hard turning. PCBN has therefore

been the preferred choice because of its hot hardness characteristics [Diniz et al. 2008]. In addition, the tool with higher thermal conductivity will allow the heat to flow out of the cutting region, leading to lower cutting temperatures near the tool edge [Stephenson et al. 1996]. The abrasive wear rate of the tool increases with the decrease in the thermal conductivity of the tool. The thermal conductivity of the CBN is higher in comparison to that of ceramic tools leading to relatively slower wear rate with CBN tools.

Konig [Konig et al. 1990] compared the tool lives of cutting tool materials in finish turning hardened roller bearing steel AISI 52100 (100Cr6). The tools chosen for comparison were conventional $Al_2O_3 + TiC$ ceramic composite tool, high-CBN content tool, CBN-based material with a high percentage of metal carbides with 60 % lower thermal conductivity. In addition, a comparison of CBN-based carbide tools with different edge preparation was done. The CBN tools with carbides proved significantly superior to the conventional CBN and ceramic composite (see Figure 2.8) tools. It was observed that mixed ceramic suffered from severe cracking and chipping of its brittle cutting edge, leading to development of peak-to-valley heights and cutting forces. Though the tools had comparable tool lives, it was noted that the sharp edged tool produced better machined surface quality over chamfered CBN tools.

In industries, the cost per edge of CBN is one of the ultimate considerations. The cost of CBN inserts is 5 - 7 times that of ceramic inserts [Kennametal]. Supporting the results of [Konig et al. 1990], several works [Silva et al. 1999, Brandt et al. 1999] showed that mixed alumina ceramic tool exhibited better performance than some PCBN tools. When successfully applied, ceramic cutting tools can increase the metal removal rate by several times over that obtained with conventional tool materials [Kumar et al. 2006].

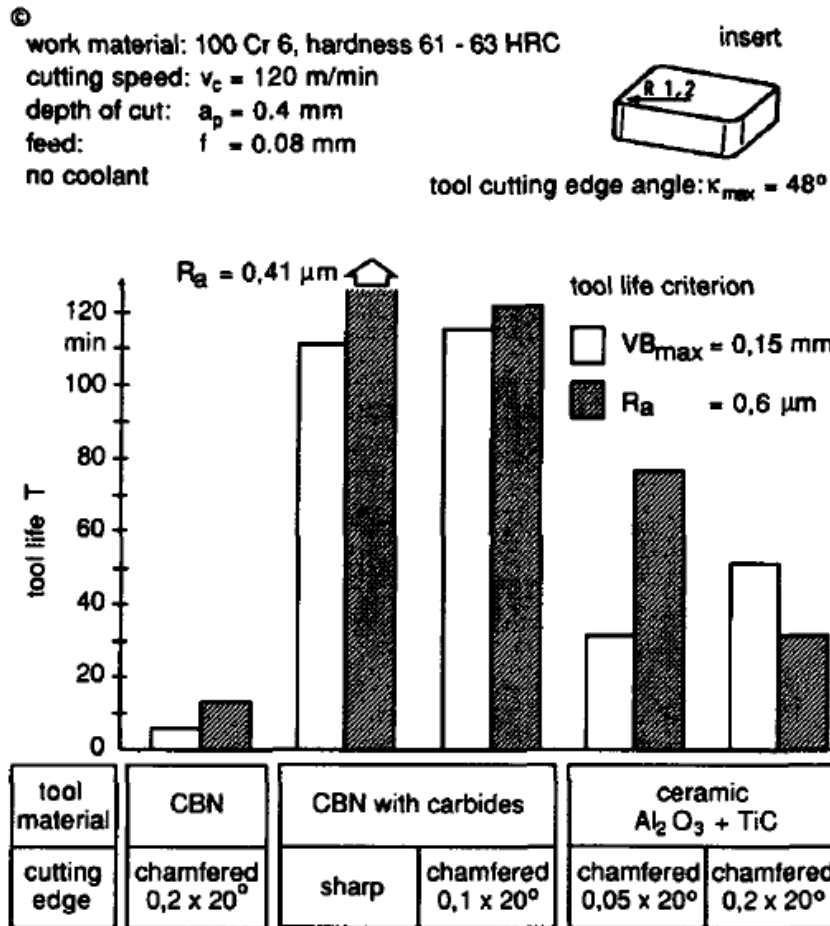


Figure 2.8: Comparison of CBN and ceramic tools in hard turning 100Cr6 [Konig et al. 1990].

2.3.5 Influence of Workpiece Microstructure

Several researchers evaluated the tool wear from microstructure of the workpiece standpoint. [Sin et al. 1979, Narukati et al. 1979] studied the correlation of carbides in the workpiece to the CBN content of the tool. They observed that the resistance to wear monotonically decreases with the CBN grain size. Evans [Evans et al. 1991] suggested that abrasive wear of the CBN tool is minimized in a highly refined workpiece microstructure. [Chryssolouris et al. 1982, Takatsu et al. 1983] showed that the CBN tool wear is dependent on the percentage of martensite content and the type, size and composition of hard phases in the cutting region. [Poulachon et al. 2003] observed

hardened D2 tool steel to induce high wear rates due to presence of massive carbides of hardness 2400 HV about three times that of martensite, in the material.

The tool wear evaluations guided several changes in the manufacturing processes for the workpiece – control of initial ingot size, powder metallurgy (atomization of liquid metal into droplets prior to solidification), and control of cooling rates [Chou et al. 1997].

2.3.6 Cutting Forces and Surface Finish

The continuous change in the geometry has undesirable effects on the process performance, workpiece surface quality. Both flank wear and crater wear of the cutting tool and the surface finish of the workpiece was considered as tool life criterion by researchers [Shintani et al. 1987, Abrao et al. 1995b, Benga et al. 2003].

Tool wear due to abrasion and high temperature in machining of hard materials increases the cutting forces. Due to the deterioration of the cutting edge, there is an increase in the cutting forces leading to deterioration in process stability, part accuracy and part surface finish. Kobayashi [Kobayashi et al. 1960] related the linear increase in the cutting forces with the increase in the wearland width and the growth of plastic flow region. The flank-wear land contact consists of both plastic flow region and elastic region [Waldorf et al. 1998]. Several researchers [Wang et al. 1999, Smithey et al. 2000, Smithey et al. 2001] reported that the chip formation forces depend on wear-land geometry and the cutting conditions.

Surface roughness is one of the important indicators of the surface integrity of machined components. The tool cutting edge and its topography deteriorates with the increase in the wear rate, which is reflected in the workpiece surface. Tool nose geometry and feed rate strongly affect surface roughness values in the turning process. The experimental results of Chou [Chou et al. 2004] showed that tool nose radius had considerable effect of the workpiece surface quality.

2.4 Thermally Enhanced Machining Processes

Advanced materials (tool steels, heat treated steels, alloy steels) are increasingly being used in many engineering applications due to their toughness, high strength at elevated temperatures and superior wear and fatigue resistance. With the increase in hardness (>60 HRC) of the workpiece, two factors mainly affect the cutting mechanism: (a) increase in the yield stress of the workpiece material that results in higher cutting forces, (b) increase in the heat generated at the tool/workpiece interface because of the higher stress. Conventional machining methods suffer from poor machinability, poor quality of machined surfaces and poor process reliability. Further, the life of the tool is shorter because of rapid wear rates.

The concept of hot machining began with induction heating and electric arc heating. In induction heating, the workpiece was heated in a furnace, while in electric arc heating, an electrical resistance was developed between the tool and the workpiece. An electric current of several hundred amps made it possible to decrease the cutting forces by approximately 10 % [Kainith et al. 1980]. However, the power densities in these processes were insufficient to be industrially accepted.

Several researchers proposed the non-abrasive, electrical discharge machining process [Petrofes et al. 1988, Lee et al. 1991] for materials with electrical resistivity less than 100 Ω -cm. Hahn [Hahn et al. 1993] used the abrasive, ultrasonic machining for fabricating ceramic parts. Induced vibration combined with abrasive slurry performs the material removal. Though complex shapes and high surface finish can be achieved in ultrasonic machining, the process is limited by the cost and wear of the sonotrodes used. Abrasive water jet machining [Freist et al. 1989] is another machining technique that involves the forceful impingement of abrasive particles to achieve surface material removal [Ozler et al. 2000].

Arc plasma and lasers were known to produce concentrated, rapid heat transfer, high-power density energy beam, capable of heating the material to >1000 °C to increase

the workability of the material. The intense beam produces hot spots in the exposed material. By positioning the cutting tool behind the source, it is possible to machine the thermally affected region in the material. It is well-known that with an increase in temperature there is a drop in the flow stress and strain-hardening rate of the material. Higher material removal temperatures yield higher reduction in hardness. From a machining standpoint, this thermal softening implies lower cutting forces.

A plasma arc consists of high velocity, high temperature stream of ionized gas capable of supporting a high-current, low-voltage electric arc. Kitagawa [Kitagawa et al. 1988] used plasma heating in machining experiments of high hardness metals such as 18 % *Mn* steel and 2.25 % *Cr* cast iron with tungsten carbide inserts and reported 50 % reduction in cutting cost due to reduced chipping and tool wear rates. König [König et al. 1990] used plasma enhanced machining in turning hard coatings made of cobalt alloys with PCBN inserts. It was noted that the relief face tool wear reduced by 40 % in comparison to that in conventional hard turning. Madhavulu [Madhavulu et al. 1994] performed plasma enhanced turning experiments using cemented carbides to machine alloy steels and stainless steel SS410 and noted low power requirements (see Figure 2.9) in plasma arc assisted machining over conventional hard turning.

Though plasma enhanced machining improved the machining performance, the process suffered due to the heating effect of the tool cutting edge. The heat flow inevitably increases the temperature in the cutting zone and leads to increase in tool wear. Wang [Wang et al. 2003] proposed a hybrid machining process that utilizes plasma arc for thermally softening the cutting region of the workpiece and additionally, uses low nitrogen to keep the tool cutting edge at lower temperature. Tungsten carbide inserts, WG-300 were used to machine Inconel 718 alloy and it was shown that plasma assisted machining process had advantages in surface roughness, cutting forces, flank wear, and consequently the tool life (see Figure 2.10).

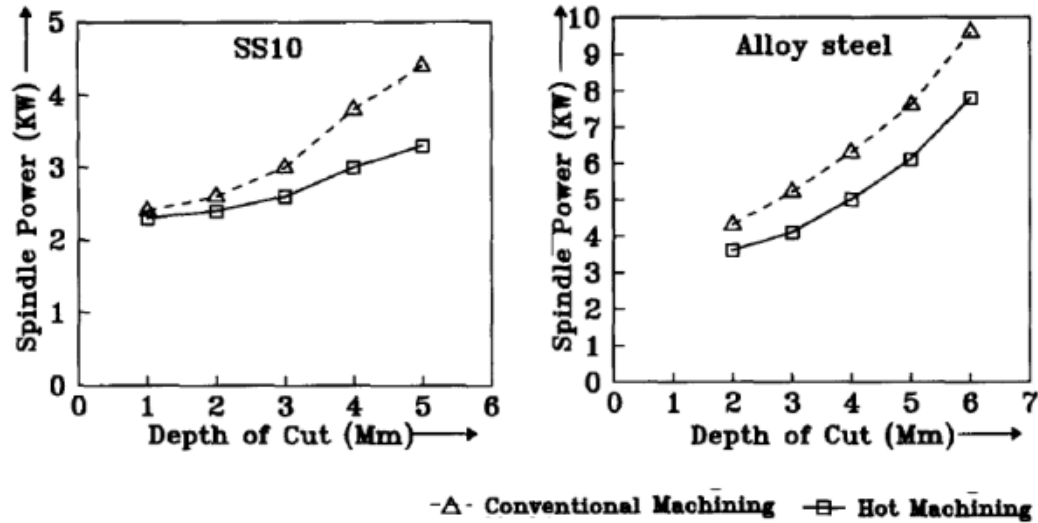


Figure 2.9: Comparison of power consumption in plasma-arc assisted machining over conventional machining. (cemented carbide inserts, cutting speed: 100 m/min, feed : 0.088 mm/rev (SS10) and, 0.175 mm/rev (alloy steel)) [Madhavulu et al. 1994].

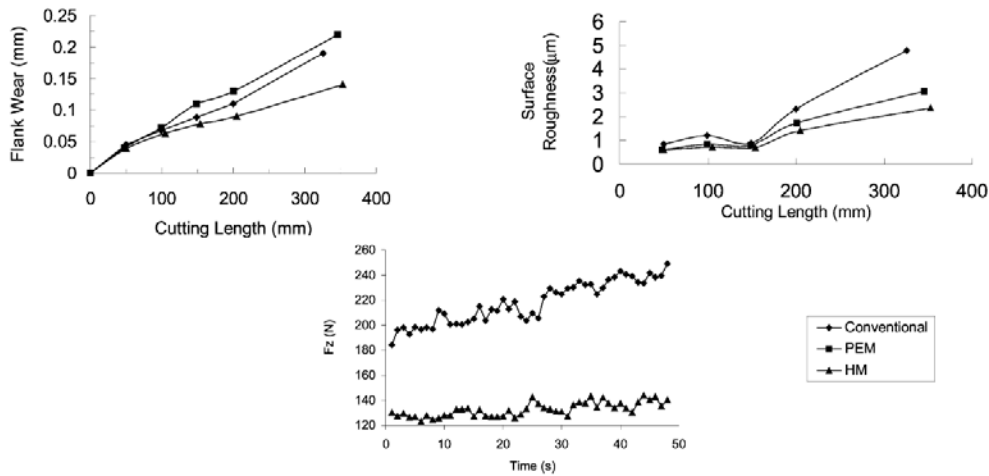


Figure 2.10: Comparison of flank wear (top-left), surface finish (top-right), cutting force (bottom) in hybrid plasma machining (HM) over plasma enhanced machining (PEM) and conventional machining. (tungsten carbide inserts, depth of cut: 0.76 mm, feed: 0.109 mm/rev (Conventional), 0.127 mm/rev (PEM & HM), cutting speed: 5.2 m/sec [Wang et al. 1994].

In spite of the advantages in the process capabilities, plasma enhanced machining had difficulties with larger spot size and consequently, lower energy density. Furthermore, the difficulties in accurately controlling the size of the heated area led to a layer with microstructure alteration that remained in the machined surface [Sun et al. 2010]. On the other hand, the advancement of laser technology provided better control of the spot size and higher energy density of the heated spot with smaller spot size.

2.5 Laser Based Processes

Different methods of beam generation (continuous wave, pulsed), multiple beam wavelengths (from tenths to fractions of a tenth of μm), and wide range of power intensity levels (10^9 W/sq.cm to greater than 10^{15} W/sq.cm) has attracted many manufacturing processes to embrace the laser technology (see Figure 2.11). During high energy beam-material interaction, a certain portion of the incident light energy is absorbed by the material (photon absorption) and high temperature is developed in the vicinity of the beam spot, resulting in heating, burning, melting, evaporation, local yielding or material softening.

CO₂ lasers and Nd:TAG lasers have lower energy conversion efficiency and lower investment costs, but the advantage of transmitting the radiation through optical fibers have significantly benefitted various applications. Table 2.1 compares the different laser system.

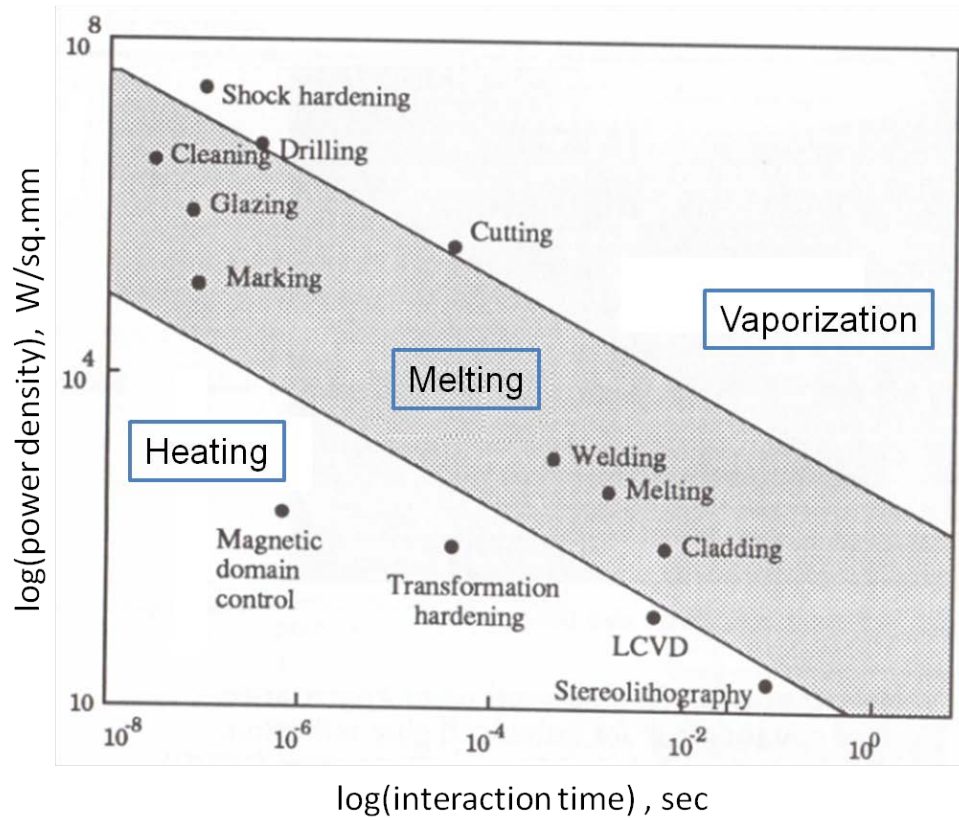


Figure 2.11: Operational regimes of laser based manufacturing processes [Ohse et al. 1988, Steen 1998].

Table 2.1: Comparison of laser systems [Dumitrescu et al. 2006].

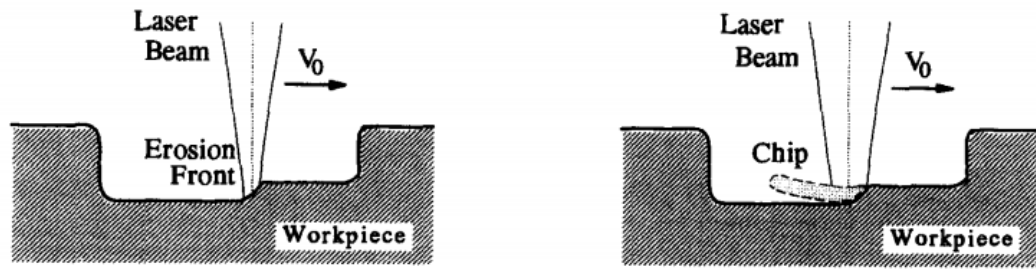
	<i>CO</i> ₂	Nd:YAG	HPDL
wavelength (μm)	10.6	1.06	0.8–1.0
metal absorption (%)	5–10	25–35	30–40
efficiency (%)	10–15	3–5	30–50
laser head size (cm ³ /W)	1000	10	1
maximum power (kW)	40	4	10
maximum power intensity (W/cm ²)	108	109	106
capital cost (\$/W)	150–300	200–600	100–300

2.5.1 Laser Machining

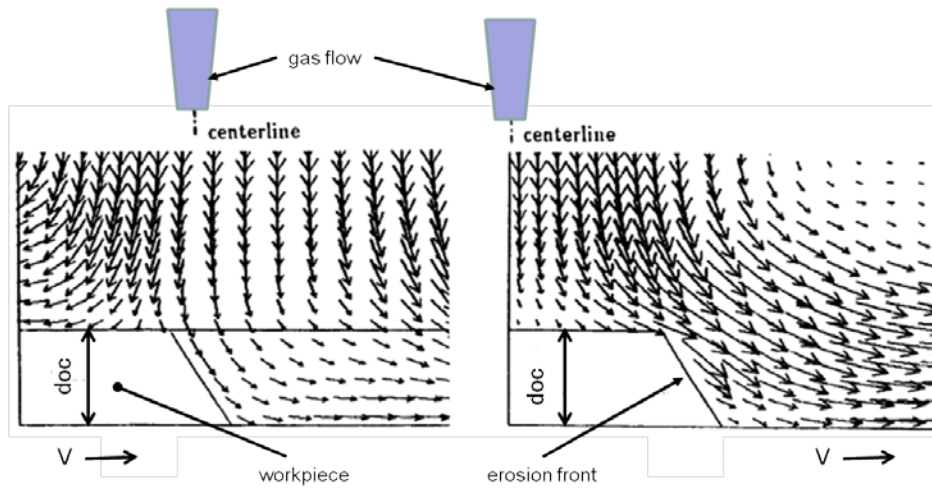
Laser machining is a localized, non-contact, force-free machining process that transports photon energy into the target material in the form of thermal energy or photochemical energy to remove material by melting or blowing away and/or direct vaporization. Melting of the surface, followed by evaporation of the liquid solution characterize the material removal process in laser machining.

A high energy laser beam is focused on the workpiece surface. When the energy intensity is high enough, the bonds of the lattice structure give up instantly without having time to transfer their energy to their neighboring lattice element. The removal of the molten material is accelerated by the forced stream (see Figure 2.12) of non-reactive supersonic gas jet, such that the major part of the liquid metal is ejected from the workpiece. In Figure 2.13, a ring gear is machined in a five axis laser machining center.

Unlike the traditional machining processes, laser machining process showed a number of advantages such as the absence of tool, absence of mechanically induced material damage and can be used to machine a variety of materials including metals, ceramics, glass, plastics and composites [Chryssolouris et al. 1988, Chrrsolouris et al. 1991]. However, laser machining processes involves material evaporation, which in turn induces surface micro-cracking and alters material composition in the heat affected zone necessitating additional finish machining. Furthermore, the process is sensitive to laser beam properties – the cutting depth is limited by the power of the laser source. In addition to the high intensity laser beam requirement, multiple passes were required for larger material removal rates.



(a)



(b)

Figure 2.12: Illustration of laser machining (LM) process (a) LM for machining cavities
(b) gas flow at the erosion front [Leidinger 1995].



Figure 2.13: Five-axis laser machining center precision processes a ring used in a power-generation turbine [courtesy: LAI International].

2.5.2 Laser-assisted Machining

Laser-assisted hard turning process replaced the laser machining process to overcome drawbacks of the latter process. In laser-assisted hard turning, the laser is employed only as an intense heat source to change the deformation behavior of the material from brittle to ductile. Laser-assisted machining process is a dry machining process, making it an environmentally friendly process.

2.5.2.1 Process Description

In laser-assisted hard turning, laser heating and material removal both occur simultaneously. Figure 2.14 illustrates this approach. The laser beam and the workpiece are positioned such that heating caused by laser irradiation precedes the cutting tool by a specified short distance. At higher temperatures, the tensile strength and yield strength of the material drops down based on the temperature dependent material properties. The laser irradiated region of the workpiece is thermally softened and is removed by the cutting tool that follows immediately behind. In this process, the tool is in contact with softened workpiece material at an elevated temperature as it is being removed.

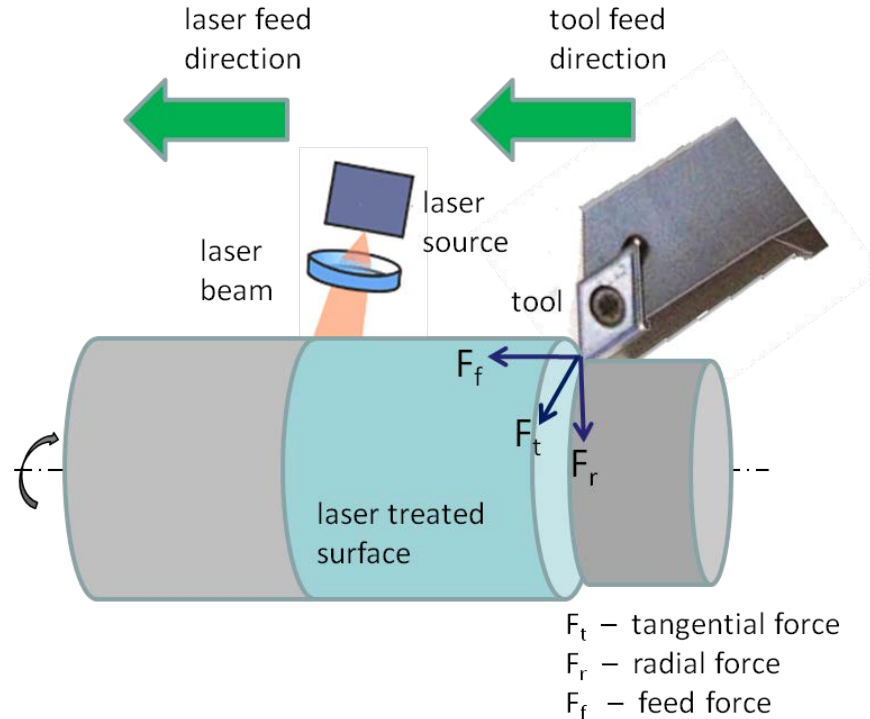


Figure 2.14: Laser-assisted hard turning.

Work materials that are well suited to laser-assisted hard turning include: (i) hard and brittle materials such as ceramics that can otherwise be subject only to abrasive processing [Klocke et al. 1997, Lei et al. 2001, Bowman et al. 2002, Pfefferkorn et al. 2004, Chang et al. 2007, Samant et al. 2009], (ii) heat resistant materials like nickel

alloys [Wang et al. 2003, Germain et al. 2008, Shi et al. 2008], (iii) metal matrix composites [Dandekar et al. 2010, Pramanik et al. 2008], and (iv) materials with a propensity to significant strain hardening like austenitic stainless steels [Anderson et al. 2006, Ding et al. 2010], (v) titanium alloys [Yang et al. 2009, Dandekar et al. 2010], (vi) cast iron [Armitage et al. 2005, Skvarenina et al. 2006].

In addition, laser pre-heating technique has been successfully integrated with planning of Al_2O_3 [Chang et al. 2007], dressing and truing [Zhang et al. 2002], burnishing [Tian et al. 2007], and grinding [Westkamper et al. 1995].

2.5.2.2 Process Performance

The earliest works of [Bass et al. 1978, Jau et al. 1980, Rajagopal et al. 1982] showed the feasibility of hot spot laser machining using 1.4 kW, 1060 nm CO_2 laser for difficult-to-machine materials. They suggested that process efficiency can be increased by efficient coordination of the cutting speed and the laser beam location. Gratias [Gratias et al. 1993] characterized the effect of laser power and laser-tool lead distance in the machining of hardened XC42 steel. It was shown that the cutting forces were reduced by 70 %. In the experimental work of [Germain et al. 2007], it was shown that the compressive residual stresses in the axial and tangential direction are smaller in laser assisted hard turning of bearing steel (100Cr6) than those machined conventionally. Dumitrescu [Dumitrescu et al. 2006] studied the chip morphology in laser-assisted process. At constant cutting speed, continuous chip was formed in the laser-assisted process whereas a saw-tooth chip was produced in the conventional hard turning process. It was noted that the change in chip morphology is because the material shears by plastic deformation at elevated temperatures in laser assisted hard turning process.

Lei [Lei et al. 2001] investigated the tool wear of PCBN tool insert at different material removal temperatures in laser assisted machining of silicon nitride. A cutting speed of 0.4 m/sec, feed rate of 0.02 mm/rev, 1 mm depth of cut was used at material

removal temperatures 1260 °C, 1410 °C, 1570 °C. It was observed that the tool wear (see Figure 2.15) decreases with the increase in material removal temperature. As the temperature increases, the strength decreases, however there is optimal temperature, beyond which the additional heat retained within the workpiece leads to accelerated wear.

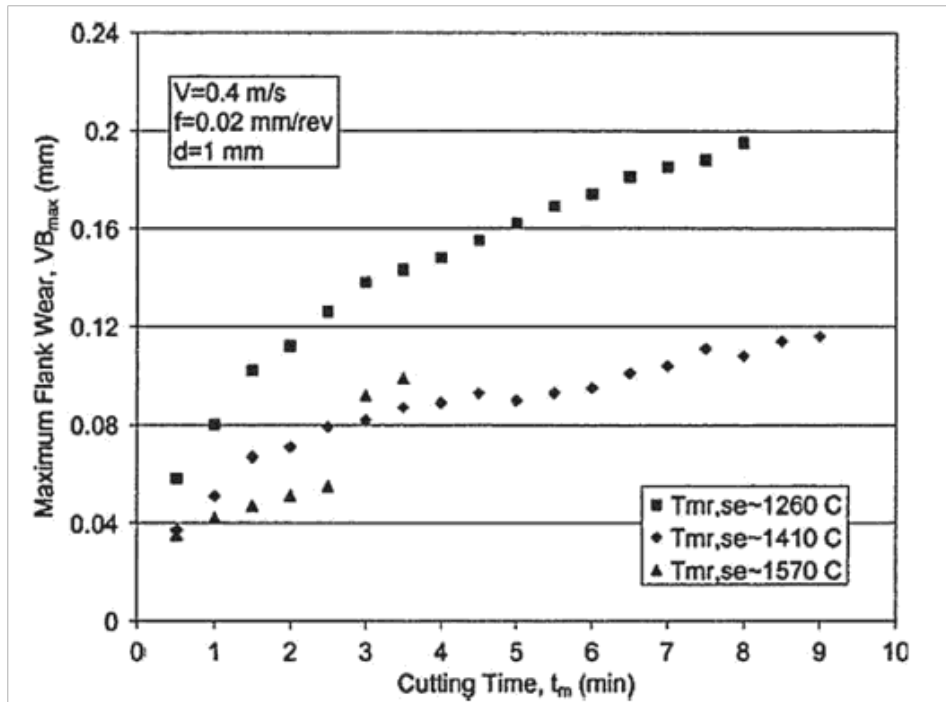


Figure 2.15: Flank wear vs. cutting time in laser assisted hard turning of silicon nitride [Lei et al. 2001].

Dumitrescu [Dumitrescu et al. 2006] investigated the tool wear of AISI D2 tool steel (60 HRC) with carbide inserts. It was observed that tool life doubled with laser-assisted machining. The modes of tool wear under conditions of conventional cutting comprised severe abrasive wear and large scale chipping of the cutting edge that eventually led to thermal damage and tool failure. Ding [Ding et al. 2010] studied the machined surface integrity in AISI 4130 steel machined by laser assisted hard turning process and observed that parts produced by laser-assisted process had surface finish (R_a) of <0.3 μ m.

Although these works have shown the capability of the approach to enhance the machinability of these materials, the process has certain limitations (discussed in Chapter 3) when it comes to practical implementation. In laser assisted hard turning process, the rate of cutting consummates the rate of pre-heating by the laser beam. The latter limitation often constrains the maximum cutting speeds, feeds and depths of cut that can be achieved in the process.

2.6 Modeling of Laser Based Process

2.6.1 Temperature Prediction due to Laser Irradiation

Carslaw and Jaeger [Carslaw et al. 1959] developed a semi-infinite analytical solution for a uniform heat source. The temperature under the laser beam was shown to decrease with the increasing velocity and increasing spot size. Higher velocity leads to shorter beam interaction time and larger spot size lowers the input heat intensity. Cline [Cline et al. 1977] developed a 3-D thermal model for a semi-infinite plate subjected to heat treatment by circular, Gaussian CO₂ laser beam. They pointed out that the temperature distribution of the moving heat source is asymmetric along the direction of the laser beam traverse. However their solution assumes that all the laser energy is absorbed at the surface of the target, which is appropriate only for metals and some semiconductors. The generalized time dependent solution developed by [Cline et al. 1977] was extended to elliptical beams, multi-layered structures, structures with temperature dependent thermal conductivity by [Nissim et al. 1980, Moody et al. 1982, Burgener et al. 1982].

Chen [Chen et al. 1983] investigated the temperature profile of semi-infinite slab with a scanning laser beam and demonstrated that there exists a critical velocity, given by the ratio of diffusivity to the beam radius, below which the effects of moving source become practically negligible. Sanders [Sanders et al. 1984] found a relation that exist

between the temperature rise produced by the absorption of scanning Gaussian laser beam by a uniform solid to two ratios: the ratio of scan speed to rate of thermal diffusion and the ratio of beam radius to absorption depth. The generalized integral solution was derived analytically, which was then used to find three approximated solutions – steady state solution (for small values of scan speed), energy density solution (for large values of scan speed), surface absorption solution.

Ion [Ion et al. 1992] used the analytical heat flow model proposed by [Ashby et al. 1984] to plot processing diagram for a range of continuous wave CO₂ laser treatments for metallic alloys. Galantucci [Galantucci et al. 1995, Galantucci et al. 1999] developed a transient numerical model based on finite element model to predict the temperature distribution for a given microstructure.

2.6.2 Kinetics

In laser transformation hardening, the metal surface to be hardened is heated by a high power laser beam until it reaches a phase transformation temperature followed by rapid quenching. Rapid heating followed by rapid quenching leads to laser transformation hardening.

Courtney and Steen [Courtney et al. 1979] investigated the laser heat treatment of EN8 steel using factorial design techniques varying laser intensity (laser power, P and beam diameter, D), and traverse speed, V . Based on the experimental data, an empirical relation that correlates depth of hardening to an empirical parameter P/\sqrt{DV} was proposed. Later, the experimental work by [Yang et al. 1990] on laser transformation hardening of tool steels suggested a correction to [Courtney et al. 1979] empirical parameter. They found that the case depth was correlated to P/\sqrt{V} . The empirical models provided a good starting point, however the model lacked theoretical understanding and cannot be extended to other materials.

Kou [Kou et al. 1983] developed a three dimensional finite difference model to predict the case depth in laser transformation hardening of AISI 1018 steel. In this work, a uniform distribution of heat intensity was provided by a CO₂ laser and case depth was based on a critical temperature.

The pioneering works of on laser transformation hardening of hypo-, and hyper-eutectoid steels by [Ashby et al. 1984], and [Li et al. 1986], respectively, provided mathematical model to predict the temperature and kinetic models to predict the hardness distribution. The 1-D kinetic model was based on the transformation of phases during heating (from ferrite, pearlite, cementite to martensite) and during rapid cooling (from martensite to ferrite, pearlite and cementite). Retained austenites were assumed negligible in this model. The approximated solution, which correlated well with the experimental values, was used to develop laser processing diagrams to show the relation between the scanning variables of Gaussian and uniform laser sources to the hardness and case depth. Davis [Davis et al. 1986] developed a theoretical model based on certain surface transformation conditions: (a) material must reach the austenitization temperature, (b) the material must remain above the austenitization temperature for an estimated 0.003 s for carbon diffusion, (c) the material is rapidly cooled (cooling rates of 10³ °C/s) to transform from austenite to martensite. The kinetic transformation model discussed so far was based on the maximum temperature reached during the thermal cycle and therefore, only case depth was of primary interest.

Li [Li et al. 1998] developed a thermo kinetic model that uses the thermal history predicted by finite element simulation. The reaction kinetics model predicts the austenite decomposition by an empirical formulation based on composition of phases and cooling rate. On the other hand, Patwa [Patwa et al. 2007] attempted to couple the kinetic model of [Ashby et al. 1984] with 3-D transient temperature numerical model of [Rozzi et al. 2000] to predict the laser scanning conditions that will produce maximum case depth. In that work, subsurface hardness of AISI 5150H steel subjected to CO₂ laser was obtained

at different depth values. Skvarenina [Skvarenina et al. 2006] extended the single pass laser hardening to predict the resulting microstructure. The austenite transformation, carbon diffusion and martensite formation were considered starting from a digitized micrograph of real material structure [Jacot et al. 1999].

Li et al. [Li et al. 1985] reported the presence of tempered region due to two overlapped scans of laser beam in case of high phosphorous cast iron. The hardness reduction was attributed to tempering and it was shown that the amount of tempering in the overlap region is dependent on the laser energy and the movement of the beam across the surface. This tempering, referred to as back tempering in the laser hardening literature, is undesirable in laser surface hardening.

Several works have been reported to simulate the back tempering. Lakhkar [Lakhkar et al. 2008] used volume fraction of the phases to predict the back tempering in laser hardening of AISI 4140. Tani [Tani et al. 2008] used integral transformation time to estimate the overheating temperatures in martensite re-austenization. The changes in hardening due to tempering were simulated by anisothermal formulation using Creusot-Loire empirical relation. Giorleo [Giorleo et al. 2011] used regressive analysis approach to model the back tempering. By correlating the hardness behavior of the tempered region to the maximum temperature induced at the tempering zone, an empirical law was proposed with an objective to efficiently select the process parameters for laser surface hardening. The objectives of these approaches were to select the processing condition for laser hardening such that the back tempering is minimized or avoided.

2.7 Summary

It is evident from the literature that thermally enhanced machining, in particular laser based machining, offers unique advantage to cut difficult-to-machine materials.

However the process has certain limitations when it comes to practical implementation. A cost-effective process that enhances the machinability and also increases the performance of the tool is required for turning difficult-to-machine hardened steels.

CHAPTER 3

LASER TEMPERING BASED HYBRID TURNING PROCESS

Cost-effective machining of materials such as bearing steels presents a significant challenge due to their high hardness. Machining of these materials is often characterized by high cutting forces and temperatures, and short tool lives. Thermal sources such as laser, plasma arc, etc. have been used as external heat sources to soften the workpiece prior to machining [Sun et al. 2010, Lei et al. 2007]. As the temperature is increased in the shear zone of the workpiece, there is a drop in the flow stress and the strain-hardening rate of the materials. From a machining standpoint, this thermal softening implies lower cutting forces and generally improved tool life or alternately a higher material removal rate without significantly diminishing tool life. These techniques have been used for machining hard ceramics, metals and metal matrix composites.

However, thermally enhanced hard turning processes such as laser assisted hard turning suffer from a number of constraints that limits its acceptance in practical applications. To overcome these limitations, a new two-step laser tempering based hybrid turning approach is proposed. This chapter introduces the laser tempering based hybrid turning approach and the experimental setup used to laser tempering the material. First, the limitations of the thermally enhanced hard turning processes, in particular laser-assisted hard turning process, are discussed.

3.1 Limitations of Thermally Enhanced Hard Turning Process

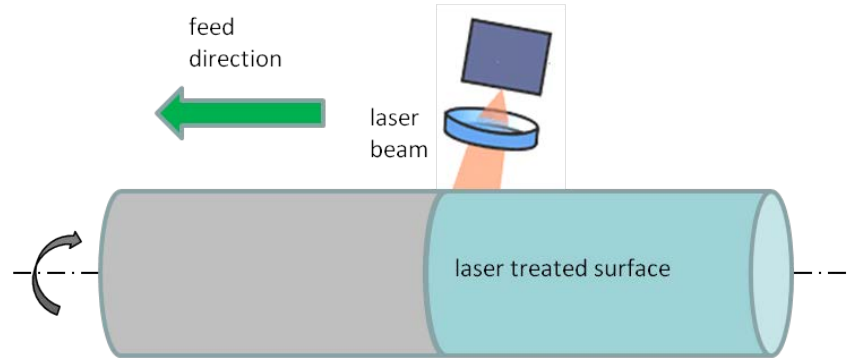
Although thermally enhanced machining processes have shown the capability to machine difficult-to-machine materials, they have number of limitations when it comes to practical implementation. The limitations include the following:

- The requirement of a high power laser (a few kW) to induce sufficient thermal softening in order to achieve practical material removal rates.
- A sufficient time is required by the laser source to heat the workpiece to higher temperatures. This constrains the maximum cutting speeds, feeds and depths of cut that can be achieved in the process.
- The heated workpiece (in most of the thermally enhanced machining processes) undergoes thermal expansion. Precise control of the cutting depth is therefore necessary as the heat starts to accumulate in the bulk of the material.
- Expensive tool materials that can withstand sufficiently high temperatures without losing their strength (e.g. CBN) are required for the process. Low conductive ceramic tools, that cannot withstand high temperatures, cannot be used.
- Inability to use cutting fluids in laser-assisted machining due to the simultaneous action of the cutting tool and heating by laser beam.
- All thermally enhanced machining processes introduce heat in front of the tool, which increases the tool-chip interface temperature. A tool that interacts with high temperature material can undergo premature degradation and accelerated diffusion and adhesion wear.
- Multiple passes are required for large material removal.
- The physical and safety challenges associated with integrating a laser into a machine tool are significant.
- The integration of laser source with the lathe reduces the throughput and operational efficiency, which are critical to mass production industries.

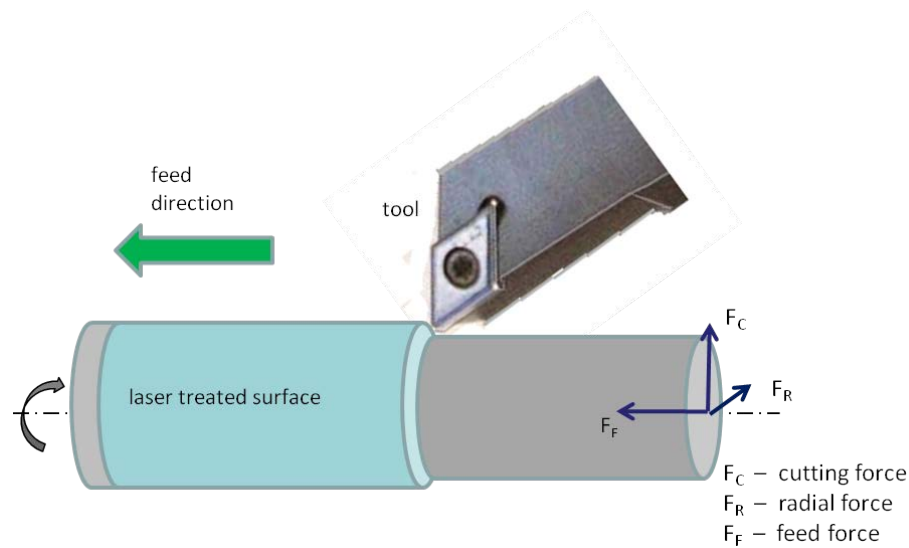
3.2 Process Description

To overcome the foregoing limitations of other laser based hard turning approaches, a new two-step laser tempering based hybrid turning approach is proposed. The laser tempering based hybrid turning process is made up of two decoupled steps

consisting of: (i) laser tempering of the workpiece surface to induce softening via microstructure alteration and therefore reduction in hardness over a pre-determined depth of workpiece, and (ii) machining of the laser tempered surface after it has cooled to room temperature. Figure 3.1 illustrates this approach. In the first step, the hardened workpiece surface is laser scanned (see Figure 3.1 (a)) in order to temper the material to a certain depth, thereby lowering its hardness over this depth. By appropriately controlling the laser scans, it is possible to produce a uniform, softer subsurface layer. The tempered subsurface region is subsequently removed by turning the part (see Figure 3.1 (b)) at practical feeds and speeds using relatively low cost ceramic tools in a subsequent machining pass. Alternatively, higher material removal rates can be utilized to remove the material using CBN tools without compromising tool life.



(a) Step 1: Laser treatment



(b) Step 2: Turning

Figure 3.1: Laser tempering based hybrid turning process.

3.2.1 Laser Tempering

The first step in the proposed process is to lower the hardness of the steel surface through a laser-tempering operation. This is accomplished by laser scanning the workpiece using overlapping passes. When the heat input exceeds the austenitization temperature (A_1), the workpiece surface undergoes transformation hardening (see Figure 3.2). The irradiated region in Figure 3.2 is harder than the workpiece hardness. Successive laser scans that overlap the previous scans (see Figure 3.3) temper the

previously hardened region to produce a softened subsurface. By appropriately controlling the laser scans, it is possible to produce a uniform, softer subsurface layer. Note that two metallurgical processes takes place in the softened region, (i) first, transformation hardening, followed by (ii) tempering due to heat from overlapping laser scans.

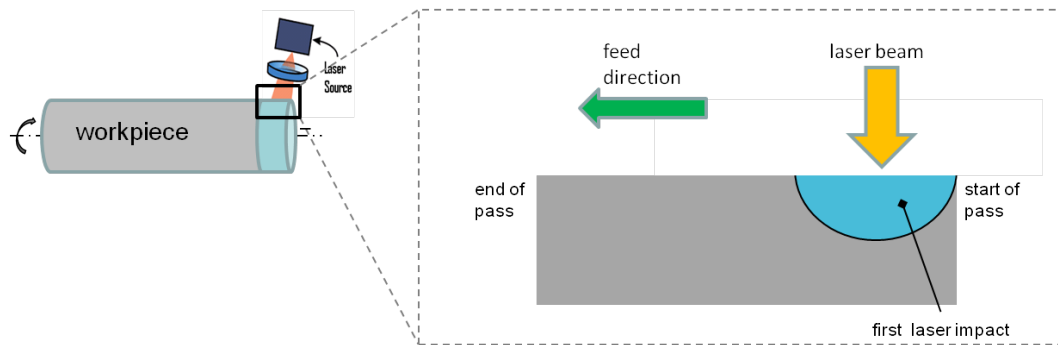


Figure 3.2: Illustration of non-overlapping laser scan in laser tempering based hybrid turning process.

3.2.1.1 Transformation hardening

A single non-overlapping scan of the laser beam with sufficient intensity is known to produce hardening of the steel surface. This is due to diffusionless martensitic phase transformation brought about by the rapid heating and quenching of the material. The latter is because the bulk of the material acts as a heat sink. This is the well-known process of laser hardening [Griffiths et al. 1987, Steen 1998, Akcan et al. 2002].

Laser hardening consists of an austenitization step followed by martensitic phase transformation. Austenitization is a high temperature diffusion-controlled phase transformation. Due to rapid heating, cementite dissolution starts at the phase interface between the elements in pearlite. Due to this, there is a concentration gradient in austenite, which initiates the carbon diffusion process. In order to maintain the equilibrium concentration, cementite and ferrite continually dissolve in the austenite matrix. At the end of the heating phase, austenite undergoes diffusion-less cooling phase

transformation because of the very fast cooling rate. At the end of the cooling phase, austenite transforms to martensite. The presence of a martensitic phase in the laser irradiated region causes the hardness of this region to be greater than the bulk material.

3.2.1.2 Tempering

Tempering occurs when successive laser scans overlap the hardened region produced by the previous scan. An overlap region is defined as the common area of two consecutive laser scans in the feed direction (see Figure 3.3). During tempering, carbon trapped in the martensite diffuses to produce a composition, which is a mixture of ferrite, cementite and pearlite.

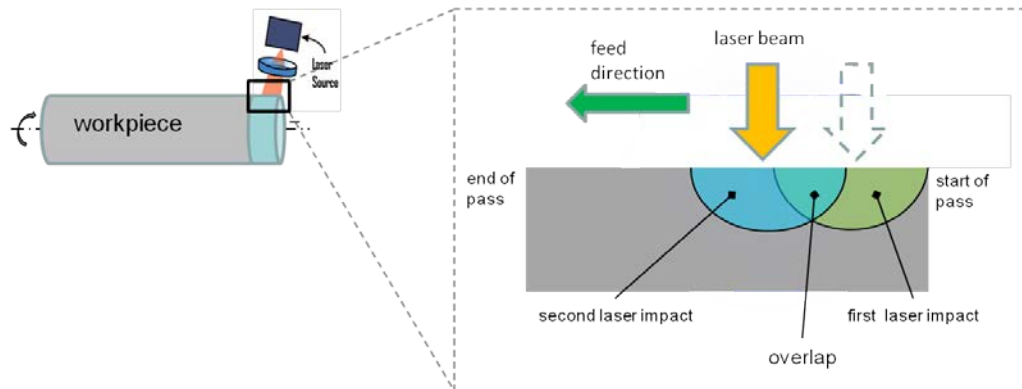


Figure 3.3: Illustration of overlapping laser scans in laser tempered hybrid turning process.

A portion of the input heat energy is transported via conduction to the region of the previous scan (denoted as first laser impact in Figure 3.3), which causes tempering if the induced temperature is below the phase transformation temperature (A_1). Furthermore, the heat affected region below the tempered zone (region immediately below the irradiated regions in Figure 3.3) is also tempered. Below the heat affected region is the bulk material that is unaffected by the heat input from the laser beam.

It can be visualized that, at the end of the pass, overlapping laser scans produces a tempered subsurface layer along the entire length of the laser pass. The subsurface tempering is dependent on input heat intensity, scan speed, extent of overlap, and thermal properties of the material.

3.2.2 Turning

The second step in the laser tempering based hybrid turning process is to remove the softened subsurface region by a cutting tool, as in conventional machining (Figure 3.4). At the end of the laser scan, a subsurface region of the workpiece is tempered (denoted as laser treated tempered region in Figure 3.4). The cutting tool removes the softened region to give the desired workpiece dimensions. The bulk of the material, which is not affected by laser treatment, retains its initial material properties.

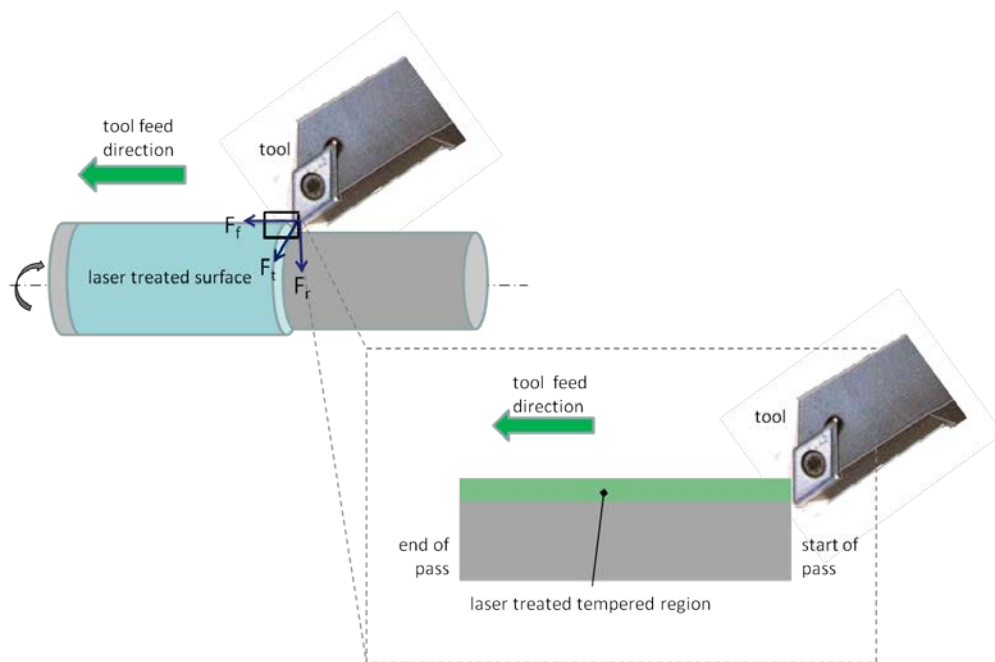


Figure 3.4: Illustration of turning in laser tempered hybrid turning process.

The key difference between the two laser based approaches – laser-assisted hard turning process (Figure 2.14), and laser tempering based hybrid turning process (Figure 3.1), is as follows. Laser-assisted hard turning is based on the softening characteristic of

the material at elevated temperatures. The laser beam and the workpiece are positioned such that heating caused by laser irradiation precedes the cutting tool by a specified short distance. The thermally softened irradiated region of the workpiece is removed by the cutting tool that follows the laser beam. In this process, the tool sees a heated workpiece material as it is being removed. On the other hand, the proposed laser tempering based hybrid turning process is based on the phase transformation characteristic of the material. A known depth of workpiece material is first tempered by overlapping laser scans. The tempered region is then removed, at room temperature, by a cutting tool in the subsequent pass.

3.2.3 Key Process Parameters

The proposed laser tempering based hybrid turning process is made up of two decoupled steps: (1) laser tempering, followed by (2) machining. The key process parameters in laser tempering are identified as: (i) heat input intensity (determined by laser power and beam spot size), (ii) laser beam energy profile (Gaussian, uniform, etc), (iii) scan speed and (iv) overlap ratio. The overlap is the ratio of the common area of two consecutive laser spots to the area of a single laser irradiated spot.

The key machining process parameters in the proposed process are similar to conventional hard turning: (i) cutting speed, v_c , expressed in m/min, (ii) Feed, f_c is expressed in distance (mm) that the tool advances per revolution of the spindle, (iii) depth of cut d_c (mm). The material removal rate (MRR) is defined as the volume of material that is removed per unit time. The material removal rate in turning (mm^3/min) is computed as,

$$MRR = v_c f_c d_c \quad (3.1)$$

The process responses of interest are, (i) tool life (in min), (ii) tool wear (μm), (iii) cutting forces, (iv) surface roughness, (v) the microstructure of the laser affected region, and (vi) hardness of the surface and the irradiated subsurface region.

3.3 Experimental Setup for Laser Tempering

3.3.1 Schematic of the Setup

The first step in laser tempering based hybrid process is to laser scan the hardened workpiece surface in order to temper the material to a certain depth. Figure 3.5 shows the experimental setup used for thermal softening the workpiece using the fiber-coupled diode laser.

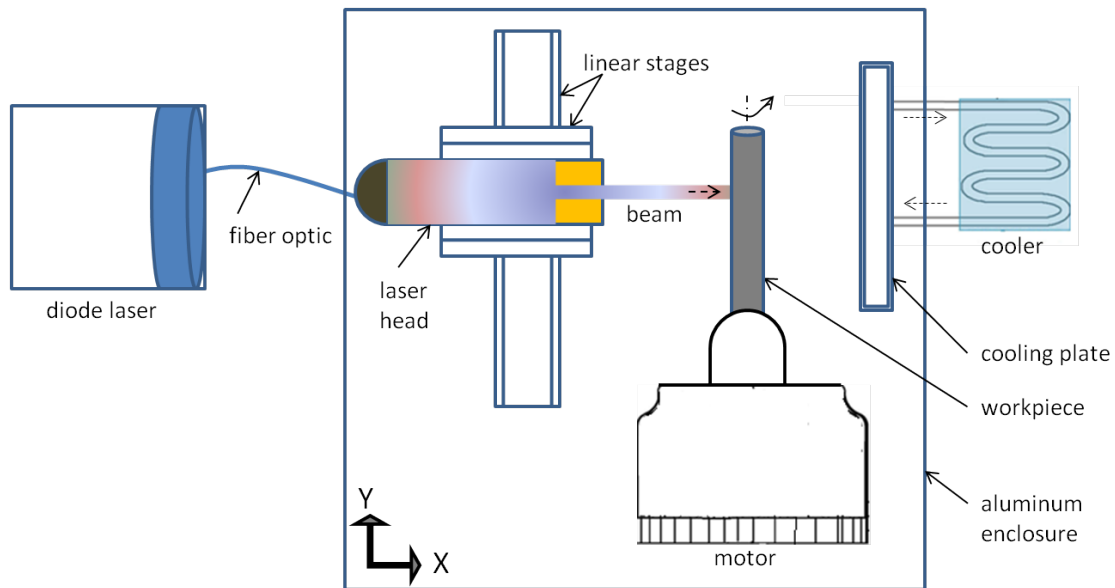


Figure 3.5: Schematic of the experimental setup.

A continuous wave, near Infrared (IR) 808 nm, laser beam is generated from a controllable laser high power (1 kW max) diode laser source. An optical fiber connects the output of the laser source to the laser head. The output of the laser head is a collimated 2 mm diameter laser beam. The laser head is mounted to a servo-controlled X-Y precision linear stage. The tangential movement of the laser head and its focal length adjustment are done using the X-Y precision linear stage.

The cylindrical workpiece is mounted in the rotating spindle. The laser head is positioned such that the laser beam center always strikes the centerline of the workpiece

and the convergent laser beam is always normal to the workpiece. The laser head is fed along the length of the workpiece during scanning.

A rectangular cooling plate is placed behind the clamped workpiece such that the cooling plate collects the laser beam not striking the workpiece. The rectangular cooling plate is continuously water cooled using a chiller.

A thick aluminum enclosure confines the laser radiation, both from the incident beam and the reflected beam, within the volume to protect the user from beam radiation.

3.3.2 Equipment for Laser Tempering

The two integral components for laser treatment are: (1) the laser diode system, and (2) the laser head. These two components are discussed below. Other components in the experiment setup (fiber optics, linear stages, electric drive, cooling system) are discussed in Appendix 8.1.1-8.1.4.

3.3.2.1 Laser Source:

Nuvonyx (Nuvonyx Inc.) ISL-1000M is a class IV laser diode system (see Figure 3.6) that combines micro-optics with a direct laser diodes to produce a single wavelength (808 ± 10 nm), laser beam at power levels up to 1 kW. The integrated laser system consists of ISL-1000M laser driver, laser assembly, and power supply. Table 4.1 lists the specification of the Nuvonyx laser ISL-1000M.

Diode laser systems provide power via semiconductors connected to a fiber based delivery system. The laser diode acts as a resonator cavity when stacked in one-or two dimensional arrays to produce laser beam of high power. The wavelength of the laser is dependent on the semiconductor material of the laser diode. The electric current provides the pump source for continuous production. The non-intermittent, high temporal stability laser beam is suitable for many manufacturing processes such as welding, brazing, soldering, cladding and soldering. In comparison to CO₂ laser, Nd: YAG, the efficiency of a diode laser is high.

An 808 ± 10 nm wavelength, low energy density, continuous wave (CW) laser beam is emitted from the fiber coupler at the rear of the Nuvonyx laser system. The Nuvonyx laser system has user interface connectors that provide convenient access for the user to all external connections to the laser controller including interlocks, external gate signals and external analog inputs. The interface display provided at the front of the laser system is used to set controlled inputs.

A bottled clean air (AIR ULTRA ZERO) is supplied as a purge gas to protect the laser system against (a) condensation, and (b) particulate matter. Condensation forms when the coolant temperature is less than the dew point of the surrounding air. Purged air reduces the potential for condensation by displacing the moisture-laden environmental air from the laser housing. Purged air supply creates a positive pressure inside the laser housing that prevents particulate matter from accumulating on the optical surfaces and electronic circuit boards.



Figure 3.6: Nuvonyx ISL-1000M laser system [Nuvonyx].

Table 3.1: Specification of Nuvonyx ISL-1000M laser system [Nuvonyx].

<i>system</i>	Nuvonyx ISL 1000M
<i>wavelength</i>	808 ± 10 nm
<i>numerical aperture</i>	0.22
<i>minimum pulse width</i>	250 ms
<i>duty cycle</i>	1-100 %
<i>max repetition rate</i>	1000 Hz
<i>max average output</i>	1 kW
<i>weight</i>	~200 Kg
<i>purge gas</i>	bottled-air, 5 psi.
<i>rated output operating current</i>	52 Amps.
<i>power supply</i>	208 V, 1-phase, 60 Hz

3.4.2.2 Laser Head

The Precitec YW50 laser head (Figure 3.7) is a high performance welding head that is coupled with the Nuvonyx diode laser through an optical fiber cable (see Appendix 8.1.1 for details on fiber cable). The laser beam from the fiber cable is first collimated. The collimated beam can be magnified or de-magnified by choosing appropriate focusing optics (see Figure 3.8). To ensure optimum beam quality at high power and efficient operation of the optics, operating temperature of the laser head should be kept within pre-defined limits. The laser head features temperature sensors to continuously monitor the operating temperature of the optics. The laser head is equipped with an internal water cooling system that continuously cools the collimating and focusing optics to keep the process conditions more homogenous.



Figure 3.7: Precitec laser head [courtesy: Precitec].

Table 3.2: Specification of Precitec YW50 [Precitec].

<i>system</i>	Precitec YW50 welding head
<i>max. laser Power</i>	8 kW
<i>free aperture</i>	48 mm
<i>weight</i>	5 Kg

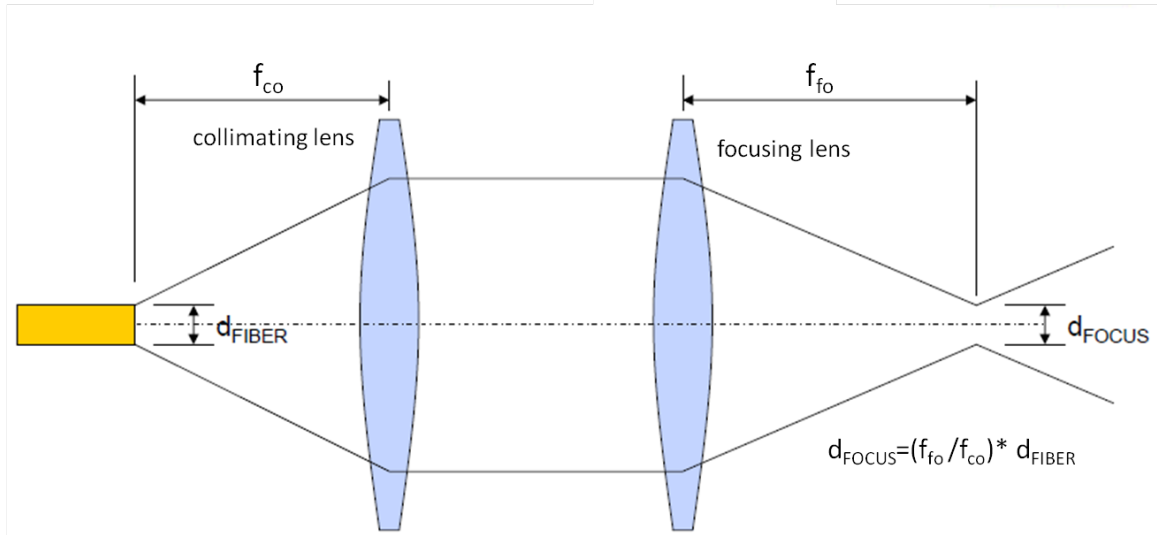


Figure 3.8: Schematic of laser head optics [Precitec].

An Optitemp chiller with R134a refrigerant is used to continuously cool the beam flow components in the Nuvonyx laser system and the optics in the laser head.

3.5.3 Layout of High Power Laser Lab

Figure 3.9 shows the layout of the high power laser lab built exclusively for laser treating the samples. The laser system utilizes two calibration constants, current monitor gain and current control gain, in order to correctly control and monitor the desired laser current. The calibration settings and the input power intensity is set from the interface display in Nuvonyx laser system. The experimental setup is placed in a thick aluminum enclosure, which is kept closed during operation. A telescopic sliding door at the front side of the aluminum enclosure provides the user access to the enclosed volume. A laser grade filter glass of optical density 7.0 is fitted to one of the sliding door. Sensors equipped on the sliding door prevent users from accidental view into the enclosed volume when the laser is armed. Safety compliance measures prescribed by American National Standard for Safe Use of Lasers [ANSI Z136.1] were ensured during the design and fabrication of the setup.

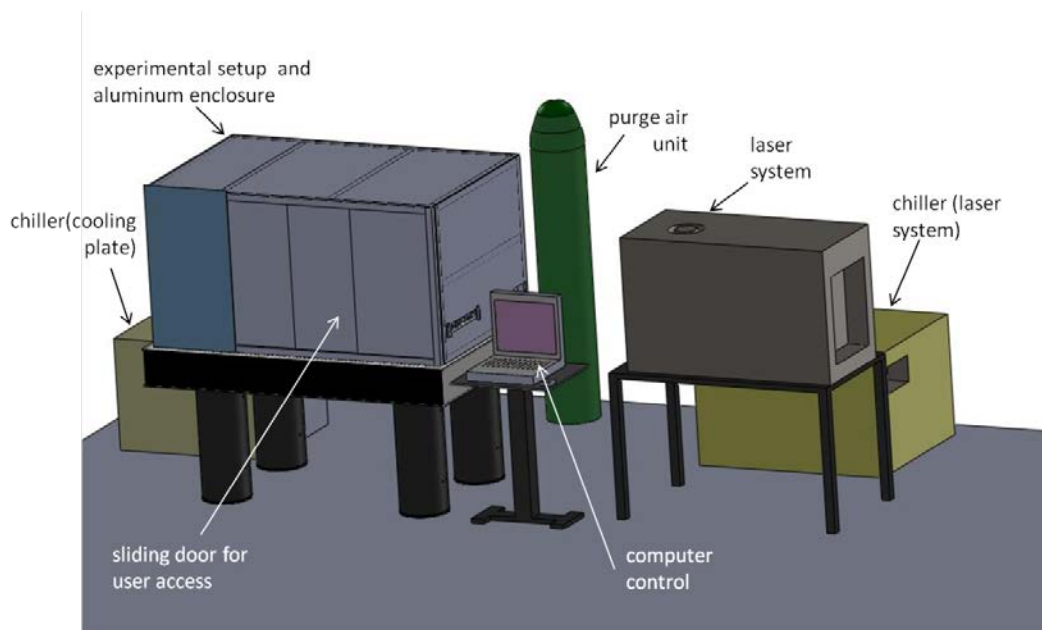


Figure 3.9: Laser treatment – overall layout (connecting cables, flow pipes are not shown).

Figure 3.10 shows the experimental set up in the enclosed volume of the aluminum enclosure. The output from the fiber coupler of the Nuvonyx laser system is carried to the laser head by a optical fiber cable. The output from the laser head is a multimodal, collimated, 2 mm spot size circular laser beam. The laser beam strikes the workpiece on the spindle that is set at a desired rotating speed. The laser head traverses along the length of the workpiece at a set speed for a set distance. The X-Y precision linear stages (for tangential feed) and the electric motor (for scan speed) are controlled by a computer, placed outside the thick aluminum enclosure.

The incident laser beam suffers from transmission loss (such as absorption loss, bending loss, insertion loss, and back reflection loss) in the optical fiber. Moisture in the fiber can absorb a portion of the beam energy causing absorption loss. Bending loss is due to the bent cable that disrupts the path of the beam. Insertion loss is due to the interconnector assembly at the ends. Back reflection loss is due to the beam reflection

that blocks the path of the beam travel. The total loss is typically 3.0-4.0 % and varies with the length of the fiber. An OPHIR thermal sensor was used to measure the output laser power of the incident beam. Figure 3.11 compares the power levels of the laser measured at the fiber coupler of the Nuvonyx laser system and that of the output beam from the laser head.

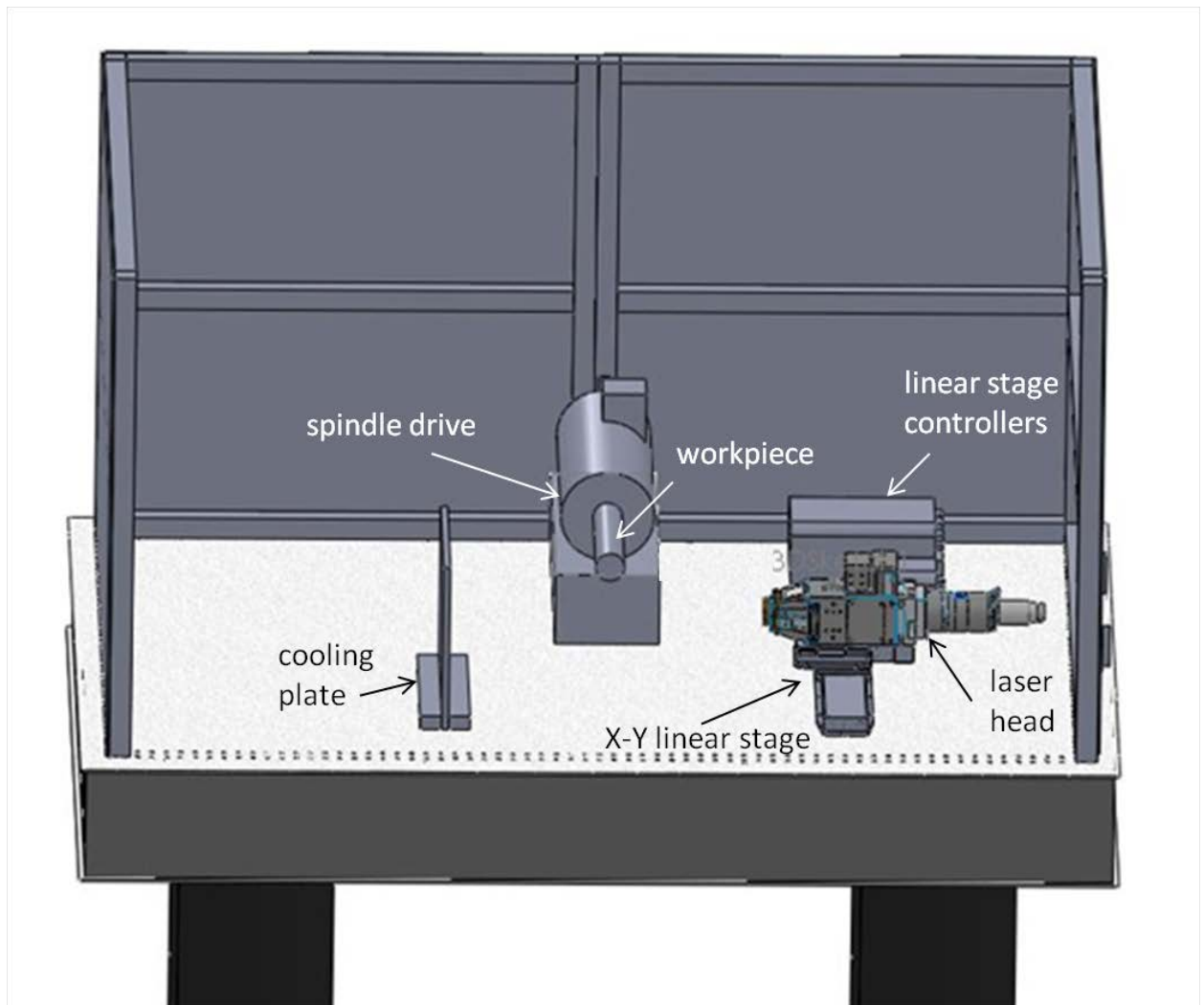


Figure 3.10: Laser treatment – experimental setup (connecting wires are not shown, front and top doors removed to show setup).

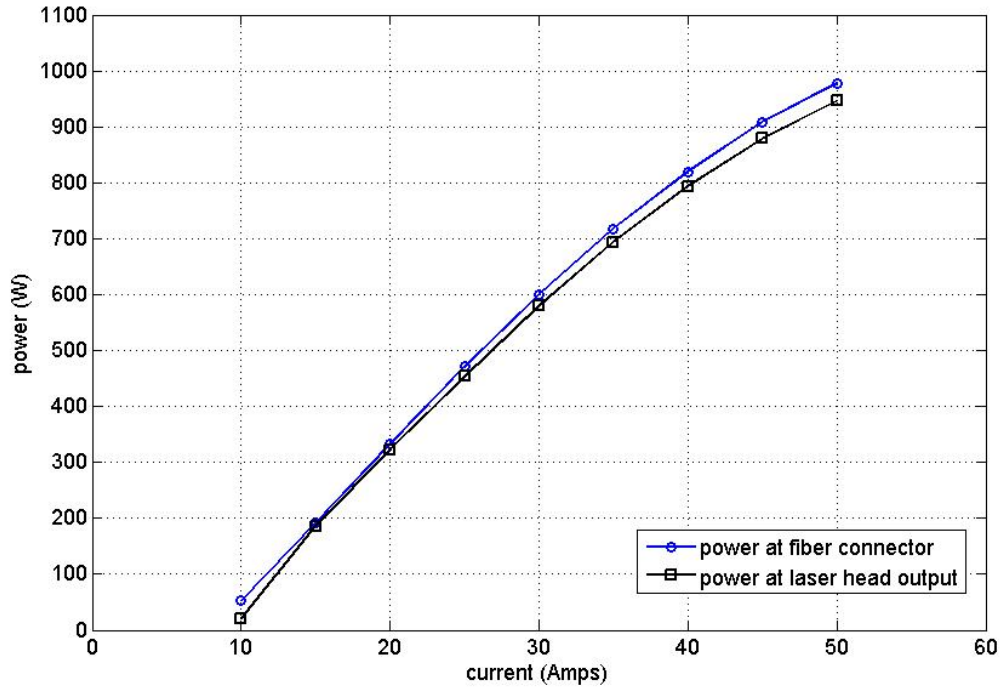


Figure 3.11: Laser system power levels.

3.4 Summary

In this chapter, the laser tempering based hybrid turning approach was introduced. The two-step process consists of first laser treating the hardened steel workpiece surface to induce tempering and therefore reduction in the material hardness over a certain depth. The second step consists of machining the softened layer at larger depths of cut. Then the experimental setup for the laser treatment was presented. In the next chapter, a thermo-kinetic model for laser-surface tempering is presented.

CHAPTER 4

LASER TEMPERING MODEL

In the previous chapter, laser tempering based hybrid turning process and the experimental setup was introduced. Laser tempering based hybrid turning process is made of two decoupled steps: (1) laser treating the workpiece, (2) machining the softened region of the tempered workpiece. An analytical model will aid the understanding of the processes in laser tempering based hybrid turning process and selecting the laser scanning parameters that will produce thermal softening for a known depth of subsurface layer in the workpiece.

In this chapter, a model is proposed to predict the hardness due to tempering during laser treatment. First, a three dimensional analytical model is used to evaluate the temperature field due to thermal cycles produced by laser irradiation. The predicted temperature histories are then fed to the phase change model to predict the surface and subsurface hardness for the selected laser processing conditions.

4.1 Introduction

Tempering is a process in which the hardened or normalized steel is usually heated below a critical temperature and subsequently cooled at a suitable rate to yield reduction in material hardness. The microstructures formed during tempering depend on the alloy composition and temperature fields, which in turn depends on the tempering temperature and time. Holloman and Jaffe [Holloman et al. 1945] proposed a tempering function that relates the resulting hardness of steel to tempering temperature and time. Zhang [Zhang et al. 2004] proposed a kinetic relation to describe the softening of steels during isothermal tempering of steels that can be used for predicting hardness in a tempering process. In addition, they showed that, for isothermal tempering of steels, there

is a sharp initial decrease in hardness, followed by a quasi-linear decrease that depends on the tempering temperature.

Laser tempering in the proposed hybrid process is not isothermal but has one or more thermal cycles (a thermal cycle is a heating phase followed by a cooling phase) with short interaction times. The tempering behavior under these conditions is difficult to explain using conventional transformation diagrams because the cooling rates and the temperature fields are not only time-variant, but also vary spatially. Previous works [Averbach et al. 1953, Speich et al. 1972] have studied the tempering in temperature controlled furnace heat treatments, which is not suitable for understanding material property changes in laser tempering. A computational model is therefore necessary to predict the evolution of surface and subsurface hardness in laser tempering.

Phase transformation characteristic of steels has been employed for case-hardening to improve surface hardness, fatigue strength, and wear resistance of the material. Several works [Ashby et al. 1984, Steen et al. 1979, Shiue et al. 1992] are available in literature for laser transformation hardening in low and medium carbon steels. In laser surface hardening, the metal surface is exposed to a high power laser beam until it reaches the phase transformation temperature (A_1) and is then rapidly quenched by the cooler bulk material when the laser source is removed. The rapid cooling rate leads to the formation of a hard martensitic phase. Overlapping laser scans are typically employed to produce a uniformly hardened surface. However, overlapping laser scans are known to temper the material in the overlap region. The extent of overlap, typically ranging from 5-15 %, causes tempering of the surface hardened by the previous laser scan. Devgun [Devgun et al. 1990] has shown the reduction in subsurface hardness in the overlapping scan during laser hardening. The hardness reduction was attributed to tempering and was shown that the amount of tempering in the overlap region is dependent on the laser energy and the movement of the beam across the surface. This tempering, referred to as back tempering in the laser hardening literature, is undesirable

in laser surface hardening. Several works have been reported to simulate back tempering, though the objective of their model is to efficiently select the process parameters for uniform laser surface hardening. A full laser tempering model has not been discussed in the literature.

Furthermore, only hypo-eutectoid steels have been the focus of studies reported on back tempering. This is quite understandable because low-strength, tempered steels are the ideal candidates for laser surface hardening.

4.2 Physical and Mathematical Description

Figure 4.1 shows a schematic of the laser tempering process. The key process parameters in laser tempering are identified as: (i) heat intensity (determined by laser power and beam spot size), (ii) laser beam energy profile (Gaussian, uniform, etc) (iii) scan speed, and (iv) overlap ratio. The overlap ratio is the ratio of the common area of two consecutive laser scans in the feed direction to the area of a single laser scan.

Laser heating of the workpiece (Figure 4.1 (a)) produces a thermal cycle that consists of heating and cooling phases. The heating phase produces a temperature field depending on the input heat energy, followed by a cooling phase caused by the bulk of the material, which acts as a heat sink resulting in rapid quenching of the irradiated workpiece (see Figure 4.1 (b)). A portion of the heat energy is retained in the workpiece at the end of the cooling phase. When the workpiece is scanned for its entire length, each point in the irradiated workpiece is exposed to one or more thermal cycles depending on the overlap (see Figure 4.1 (c)). An overlap region is the irradiated region that is common to two consecutive thermal cycles in the feed direction.

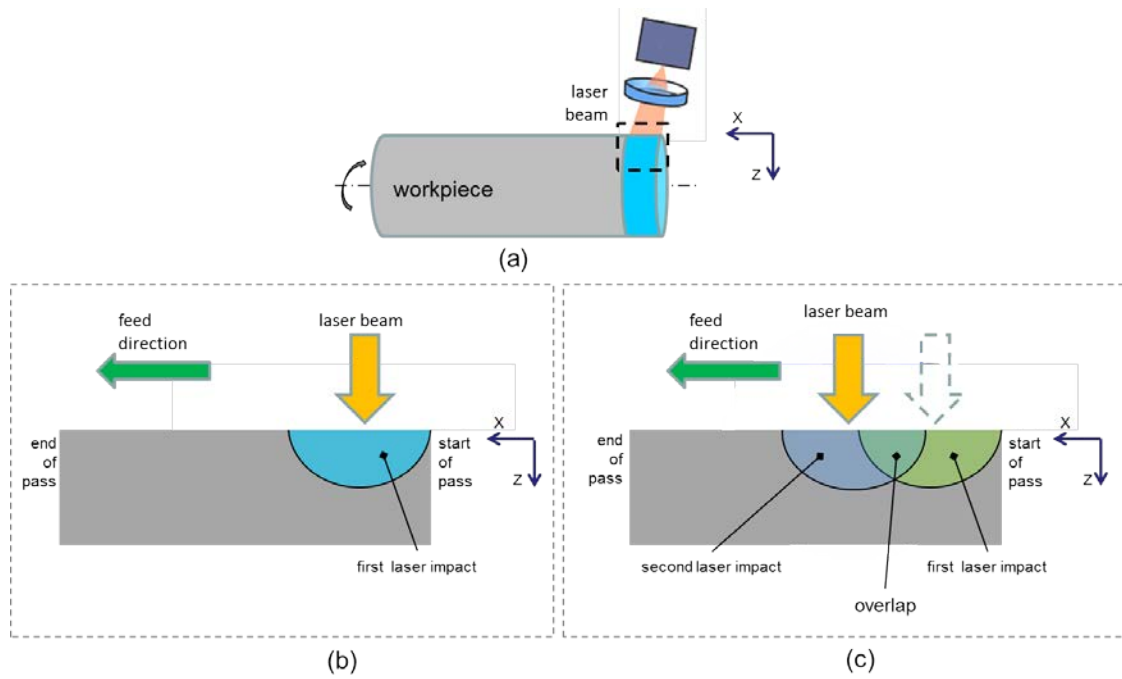


Figure 4.1: Schematic of laser tempering: (a) laser heating the workpiece, (b) laser transformation hardening, (c) laser tempering produced by overlapping scans ((b) and (c) are the longitudinal cross section of the irradiated subsurface region of the workpiece shown in (a)).

The initial microstructure of a hyper-eutectoid steel consists of a pearlite-ferrite matrix. In the heating phase of the thermal cycle in laser tempering, the microstructure transforms to austenite by cementite dissolution and outward carbon diffusion and homogenization when the temperature exceeds the austenitisation temperature (A_1). In the rapid cooling phase, the austenitic region transforms to martensite. When the martensitic region is subjected to an overlapping thermal cycle, the overlap region is tempered resulting in a softened phase consisting of a mixture of ferrite, cementite and martensite. In addition, depending on the thermal properties of the material, a portion of

the heat energy also conducts to the non-overlapped martensitic region of the first thermal cycle and the pearlite region below the irradiated region in Figure 4.1(c). By controlling the extent of overlap of successive thermal cycles and the thermal energy input by each thermal cycle, the amount of softening due to tempering and consequently, the resulting subsurface hardness can be controlled. If the thermal cycles are uniform throughout the scan length, the resulting subsurface microstructure will be uniform.

Unlike isothermal tempering, the temperature field in laser tempering is time-variant. Consequently, the resulting subsurface microstructure and hardness depend on the time-variant temperature field and corresponding cooling rate in each thermal cycle.

Therefore, the proposed laser tempering model (see Figure 4.2) consists of: (A) thermal model to predict the surface and subsurface temperatures, at any time instant t , and (B) a computational model to predict the hardness of the tempered subsurface.

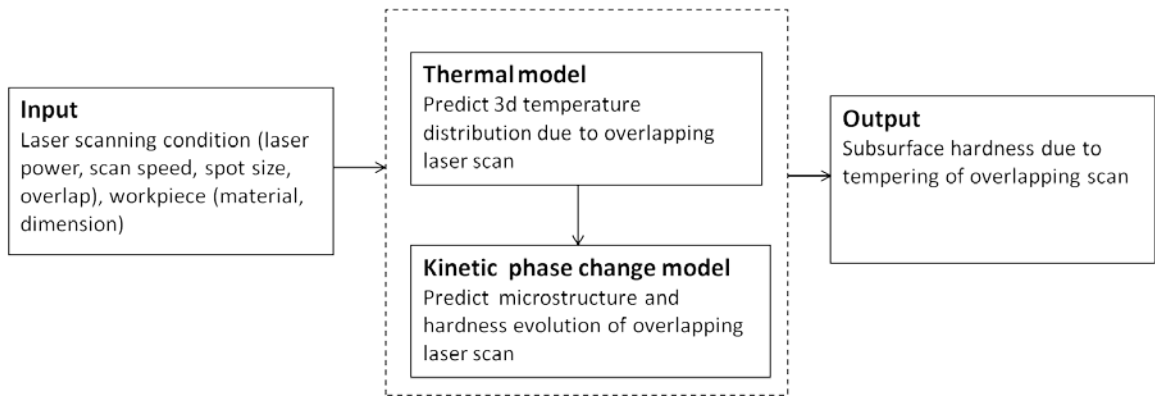


Figure 4.2: Block diagram representation of model.

4.2.1 Thermal Model

A laser beam moving at a scan speed V_y , generates a transient temperature field due to heat conduction, convection and radiation. The transient temperature field is computed from the solution of the following 3-D heat diffusion equation:

$$\begin{aligned} \frac{\partial}{\partial x} \left(k(T) \frac{\partial T}{\partial x} \right) + \frac{\partial}{\partial y} \left(k(T) \frac{\partial T}{\partial y} \right) + \frac{\partial}{\partial z} \left(k(T) \frac{\partial T}{\partial z} \right) + \dot{Q} = \rho C_p(T) \left(\frac{\partial T}{\partial t} \right) \\ + \rho C_p(T) V_y \left(\frac{\partial T}{\partial x} \right) \end{aligned} \quad (4.1)$$

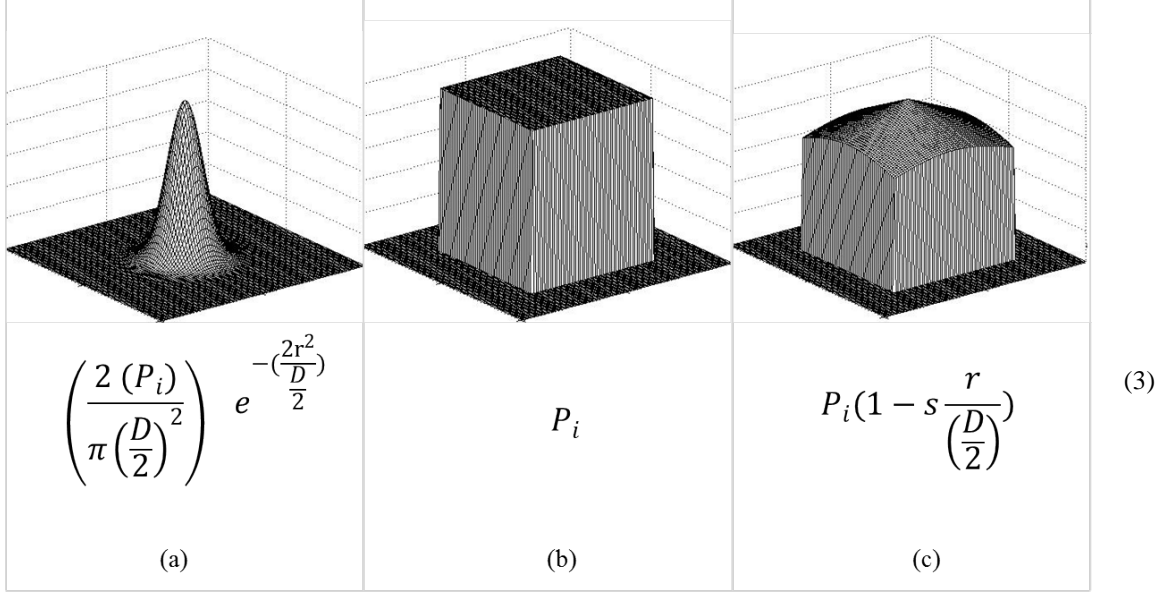
where ρ , $C_p(T)$, $k(T)$, and \dot{Q} are the density, specific heat, thermal conductivity, and rate of heat generation, respectively.

If P is the output laser power, the actual distribution of laser power intensity, $P_{a(x,y)}$, depending on the beam profile, is given in Table 4.1. Here, D is the laser spot diameter, P_i is the incident laser power, where $P_i = \eta P$ and η is the laser source efficiency, r is the Euclidean distance from the laser beam center given by, $r = \sqrt{x^2 + y^2}$, s is the difference between the incident power at the center and the incident power at the periphery of the irradiated spot. The radiation of heat from the laser-material interaction zone into the surrounding area is given by the Stefan-Boltzman's term. However, previous works have indicated that the radiation term is small as compared to the conduction and convection terms. In this work, the following lumped convection coefficient [Ferwin et al. 1999],

$$h = 2.4 \times 10^{-3} \epsilon T^{1.61} \quad (4.2)$$

where ϵ is the emissivity of the material, accounts for the combined convection and radiation losses.

Table 4.1: Energy distribution profile of laser beam. (a) Gaussian [Alda 2006], (b) uniform (top-hat), (c) tipped.



The model makes the following key assumptions:

- Ambient temperature $T_o = 27 \text{ }^\circ\text{C}$ is assumed as the initial temperature and is given by,

$$T(X, Y, Z, 0) = T_o. \quad (4.4)$$

- The workpiece surface boundary condition is given by,

$$k \frac{\partial T(X, Y, Z, t)}{\partial z} = \dot{Q} - h [T(X, Y, Z, t) - T_o]. \quad (4.5)$$

- The boundary condition for surfaces with convection and radiation heat losses is given by,

$$k \frac{\partial T(X, Y, Z, t)}{\partial N} = h [T(X, Y, Z, t) - T_o] \quad (4.6)$$

where N refers to the surface normal direction.

- The workpiece returns to the equilibrium temperature, T_o after the conclusion of the laser scans,

$$T(X, Y, Z, \infty) = T_o. \quad (4.7)$$

- No melting or vaporization of the workpiece occurs.

4.2.2 Tempering Model

Two modes of microstructural transformation take place: (i) ferrite/pearlite to martensite transformation when the temperature exceeds the austenitization temperature, and (ii) martensite to pearlite transformation when the temperature is below the austenitization temperature. The latter transformation results in tempering of the material. In addition, the non-martensitic pearlite region is also tempered by heat conduction.

The subsurface microstructural transformation at time t depends on the temperature $T(t)$, cooling rate $\left(\frac{dT(t)}{dt}\right)$, and the microstructure at time $(t - \Delta t)$, where Δt is the time between consecutive thermal cycles in the laser feed direction. The model, presented here, is based on the hardness model for hypereutectoid steels reported by [Li et al. 1986] and the tempering model proposed by [Zhang et al. 2004].

The resulting microstructure depends on atomic diffusion due to heat energy generated by laser irradiation. The kinetic strength of the laser energy at any time t is given by the Arrhenius rate equation,

$$I(t) = \int_0^{\infty} e^{-\left(\frac{Q}{RT(t)}\right)} dt = D_o e^{-(Q/RT(t))} \quad (4.8)$$

where $T(t)$ represents the temperature due to the heat cycle at time t , Q is the activation energy for the particular transformation, R is the universal gas constant, D_o is the pre-exponential for diffusion of carbon.

4.2.2.1 Pearlite to Martensite Transformation:

Martensitic transformation from the initial equilibrium microstructure at room temperature occurs in four stages: (a) pearlite colonies transform to austenite transformation, (b) ferrite to austenite transformation at high temperatures due to small carbon concentration in ferrite, (c) homogenization of austenite, and (d) austenite to martensite transformation that involves the sudden reorientation of C and Fe atoms from the face-centered cubic (fcc) solid solution of γ - Fe to a body-centered tetragonal (bct) solid solution of martensite. The first two stages are thermally activated during the heating phase and the last stage is a diffusionless, rate controlled process that occurs during the rapid cooling phase of the thermal cycle. Under rapid heating rates, carbon homogenization is assumed to be negligible [Fiorletta 1981].

When the temperature exceeds the A_1 temperature, the growth of austenite is initiated by the uniformly distributed spheroidized cementite matrix, which supplies carbon for the austenite to nucleate at the ferrite-cementite interface. The carbon diffusion from the cementite is dependent on the peak temperature in the heating phase. When the peak temperature exceeds the A_{CM} temperature, the cementite dissolves completely into the γ - Fe matrix. Equilibrium exists between the austenite-pearlite interfaces and therefore the carbon concentration can be obtained from the Fe - C phase diagram. This diffusion process is modeled by the invariant-size approximation detailed in [Li et al. 1986]. Under rapid cooling rates, the carbon atoms in γ - Fe are trapped inside the body-centered cubic (bcc) structure to form a body-centered tetragonal (bct) martensitic structure. The hardness of the transformed region is obtained from the rule of mixtures,

$$H = f_m * H_m + f_{ce} * H_{ce} + f_{ra} * H_{ra} + f_f * H_f \quad (4.9)$$

where the subscript m , ce , ra , f refer the carbide phases, martensite, cementite, retained austenite, and ferrite, respectively, H and f represent the hardness and volume fraction of the phases, respectively.

For hyper-eutectoid steels, the martensitic finish temperature (M_f) is close to the room temperature and therefore, a portion of austenite is retained in the phase transformed region. Previous works on hyper-eutectoid steels [Roberts 1953, Marder et al. 1967] have shown the presence of retained austenite (~9-10 % for steels with 1.0 % C) in martensitic transformation and have also shown an increase in retained austenite with initial carbon concentration. In addition, the phase transformed region has small quantities of ferrite and cementite.

In laser tempering, x-ray diffraction studies of laser treated samples involving additional thermal cycles (discussed in Chapter 5) show negligible retained austenite in the tempered overlap region. With each additional thermal cycle, any austenite retained from the previous thermal cycle undergoes martensitic transformation. Therefore, it is assumed here that the austenite with carbon concentration greater than a critical concentration (C_c) undergoes martensitic transformation. The instantaneous radius of the cementite particles (R_t^c) is given by,

$$R_t^c = r_e - \{2 * I(t) * \ln(1 + K) + (r_e - r_i)^2\}^{1/2} \quad (4.10)$$

where r_i is the radius of spheroidized carbide particle, and $2r_e$ is the spacing of adjacent cementite particles. The boundary of the region d_m , in which the carbon concentration exceeds the critical concentration value is obtained from the instantaneous radius of the cementite particles R_t^c , and Fick's second law as follows,

$$d_m = R_t^c + (r_e - R_t^c) \frac{\ln(K_c)}{\ln(1 + K)} \quad (4.11)$$

where $K = \left(\frac{C_\gamma^c - C_o}{C_c^\gamma - C_c^c}\right)$ is the supersaturation parameter and $K_c = \left(\frac{C_\gamma^c - C_c^\gamma}{C_c - C_c^\gamma}\right)$ is the critical carbon concentration factor. C_o is the carbon concentration in ferrite before laser

hardening, C_γ^c is the carbon content of the austenite in equilibrium with the cementite, C_c^Y is the carbon content in cementite in equilibrium with the austenite (see Figure 4.3).

The volume fraction of martensite produced is given by [Li et al. 1986],

$$f_m = \frac{1}{r_e} (d_m^3 - R_t^c)^3 \quad (4.12)$$

and the volume fraction of cementite in the diffusion field is given by [Li et al. 1986],

$$f_{ce} = \left(\frac{R_t^c}{r_e} \right)^3 \quad (4.13)$$

The hardness of martensite is given in terms of its carbon concentration as,

$$H_m = 1667C_m - 926C_m * C_m + 150, \quad (4.14)$$

where C_m is obtained from the mass conservation of carbon atoms,

$$C = C_m f_m + C_{ce} f_{ce} + C_f f_f, \quad (4.15)$$

and using the additive property of the volume fractions,

$$f_m + f_{ce} + f_f = 1. \quad (4.16)$$

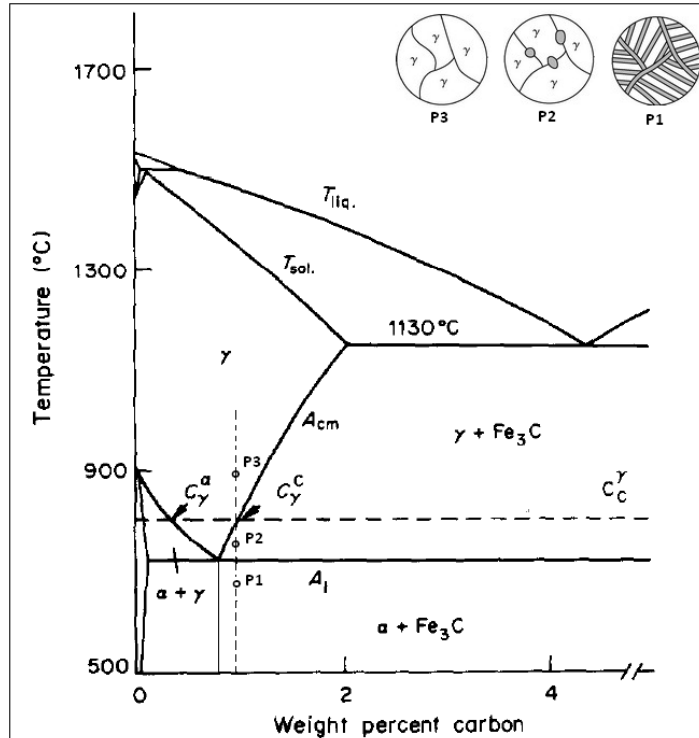


Figure 4.3: Fe-C diagram [Li et al. 1986].

The maximum solubility of carbon in austenite is 2.0 wt. % at 1130 °C and the ferrite solubility has a maximum of 0.02 wt. % at the phase transformation temperature. The hardness of cementite (H_{ce}) is 860 HV and the hardness of ferrite (H_f) is 150 HV.

4.2.2.2 Tempering due to Thermal Cycles:

The subsurface has: (a) a martensitic region formed due to laser heating and cooling, and (b) a non-martensitic region, which is the heat affected region adjacent to the martensitic region.

(a) Tempered Martensitic Region

Previous works [Cohen 1949, Balliett et al. 1976] have detailed the structural stages in tempering kinetics of martensitic hyper-eutectoid steels. Tempering starts by martensite decomposition into ferrite and transition ϵ -carbides ($Fe_{2,4}C$) at temperatures of 100-250 °C and the formation of tempered martensite and replacement of transition

carbides by ferrite and cementite (Fe_3C) at temperatures >250 °C. The hardness of the tempered layer is therefore obtained by using the rule of mixtures,

$$H = f_m * H_m + f_{ce} * H_{ce} + f_f * H_f + f_\epsilon * H_\epsilon, \quad (4.17)$$

Using mass conservation of carbon (C) atoms,

$$fC = f_m C_m + f_{ce} C_{ce} + f_f C_f + f_\epsilon C_\epsilon, \quad (4.18)$$

where f represents the volume fraction, the subscript ϵ represent the ϵ -carbide phase and the subscripts m, ce, f are as defined earlier. The hardness and volume fraction of the appropriate phases can be found based on the tempering stages.

Based on the earlier assumption that all austenite undergoes martensitic transformation, the mass balance of the martensitic region prior to tempering is obtained from

$$fC = f_m C_m \text{ or } C = C_m. \quad (4.19)$$

The Johnson-Mehl-Avrami continuous function for pearlite formation due to tempering temperature $T(t)$, is given by,

$$f_p(t) = 1 - \exp(-(I(t) * D_t * t)^m) \quad (4.20)$$

where m is the ageing component depending on the property of the material, D_t is the frequency factor, and $f_p(t)$ denotes the volume fraction of pearlites formed at time t . Consequently, the volume fraction of martensite is given by,

$$f_m(t) = f - f_p(t) \quad (4.21)$$

To account for the thermal cycles, the kinetic term in Equation 4.20 is differentiated as follows,

$$\frac{d}{dt} [I(t) * D_t * t] = D_t * I(t) \left[1 + t \left(\frac{Q}{RT^2} \right) \left(\frac{dT}{dt} \right) \right] \quad (4.22)$$

At temperatures between 100 and 250 °C, only ferrite and transition ϵ -carbides are formed. By solving, Equations 4.17, 4.21 and substituting, $f_p = f_f + f_\epsilon$, the following result is obtained,

$$f_f = f_p \left(\frac{C_m - C_\epsilon}{C_f - C_\epsilon} \right) \quad (4.23)$$

At temperatures >250 °C, ferrite and cementite are formed. Solving Equation 4.18, 4.21 and substituting, $f_p = f_f + f_{ce}$ the following result is obtained,

$$f_f = f_p \left(\frac{C_m - C_{ce}}{C_f - C_{ce}} \right) \quad (4.24)$$

Note that the carbon content of ϵ -carbide C_{ce} , is 8.22 wt%.

(b) Tempered Non-Martensitic Region

Zhang [Zhang et al. 2004] showed that, in tempering of steels, the structural changes, and consequently property changes, are thermally activated and therefore the tempering ratio $\tau_v(t)$ can be related to the Johnson-Mehl-Avrami function as follows,

$$\tau_v(t) = 1 - \exp(-(I_t(t) * D_t * t)^m) \quad (4.25)$$

where the empirical value D_t , and $I_t(t)$ represent frequency factor and activation energies for tempering, respectively. The tempering ratio (τ_v) defines the extent of diffusion of the unstable martensite to the quasi-equilibrium ferrite-cementite and is given by,

$$\tau_v(t) = \frac{H_v - H_o}{H_a - H_o} \quad (4.26)$$

where the subscript, v indicates any state between the as-quenched state (denoted by subscript o) and the annealed state (denoted by subscript a).

From Equations 4.25 and 4.26, the hardness at any time t is obtained as

$$H = H_o + \tau_v(t) * (H_a - H_o). \quad (4.27)$$

4.3 Implementation

In this section, properties of the workpiece material are described. Then, the approach to implementing the model is described.

4.3.1 Workpiece

The high-carbon, hyper-eutectoid AISI 52100 alloy steel is commonly used in many industrial applications such as bearing steel, power transmission components, etc and is used here as the test material. See Table 4.2 for chemical composition and nominal physical properties of AISI 52100.

Table 4.2: Chemical composition and physical properties of AISI 52100 steel.

Properties	Values
Chemical composition	<i>Fe</i> 97.0 % , <i>C</i> 0.90-1.05 % , <i>Cr</i> 1.35-1.65 % , <i>Mn</i> 0.25-0.45 % , <i>Si</i> 0.15-0.35 % , <i>Ni</i> < 0.30 %
Young's modulus (GPa)	210
Poisson ratio	0.3
Mass density (kg/m ³)	7853
Hardness, <i>H</i> (HRC)	~63
Melting point (°C)	~1420

Cylindrical bars of AISI 52100 of 38.1 mm (1.5 inches) diameter were through-hardened by holding at 829 °C (1525 °F) for 1.5 h, quenched in oil, then tempered at 163 °C (325 °F) for 2.0 h, which yielded a bulk tempered martensitic microstructure with a hardness of ~63 HRC. The work material bars were trued, centered and cleaned by machining a 1mm depth of cut from the outside surface.

The temperature dependent properties of AISI 52100 - yield strength, specific heat capacity, thermal conductivity, and coefficient of thermal expansion are shown in Figures 4.4 – 4.7 [Touloukian 1970, Podgornik et al. 2001, Guo et al. 2002, Gustavo 2002, Umbrello et al. 2004]. Figure 4.4 shows a significant drop in the yield strength after ~200-250°C. At temperatures >700 °C, the strength of the material exhibits small decrease with respect to the temperature, however the strength keeps decreasing as temperatures increase. The heat capacity and thermal conductivity changes dramatically with change in temperature (see Figure 4.5 and 4.6).

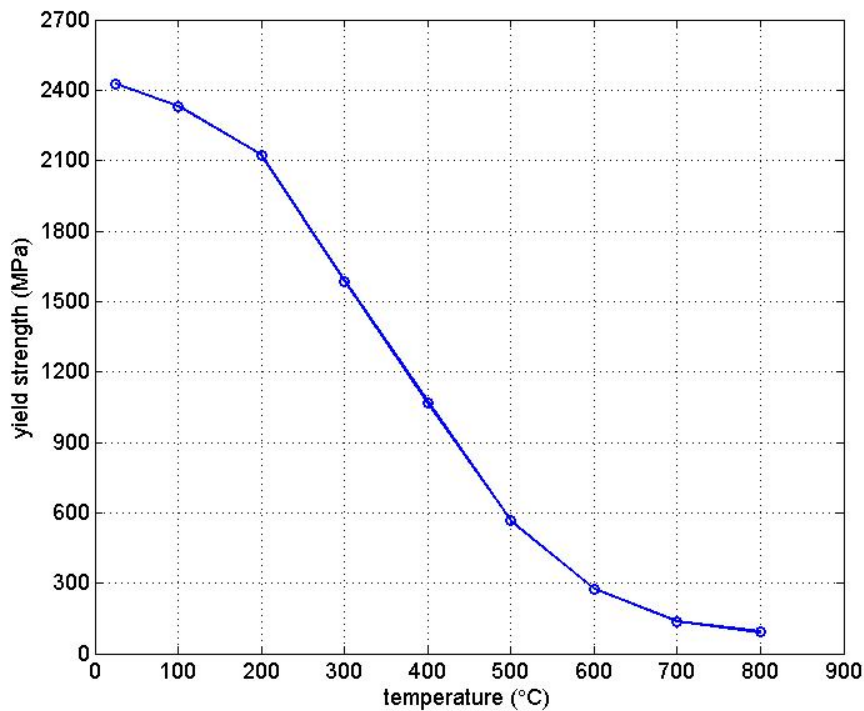


Figure 4.4: AISI 52100: yield strength vs. temperature [Gustavo 2002].

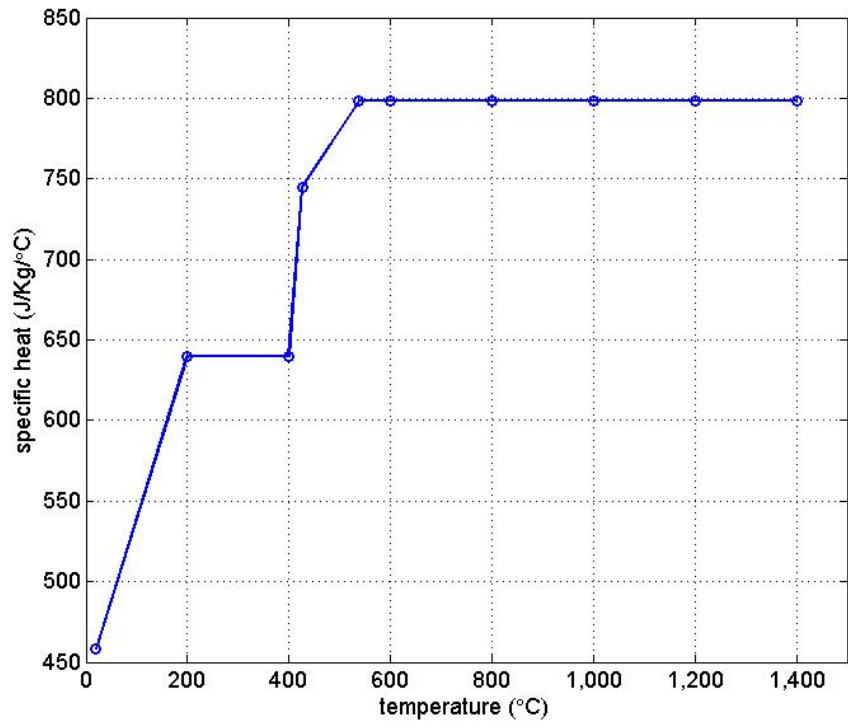


Figure 4.5: AISI 52100: specific heat vs. temperature [Touloukian 1970].

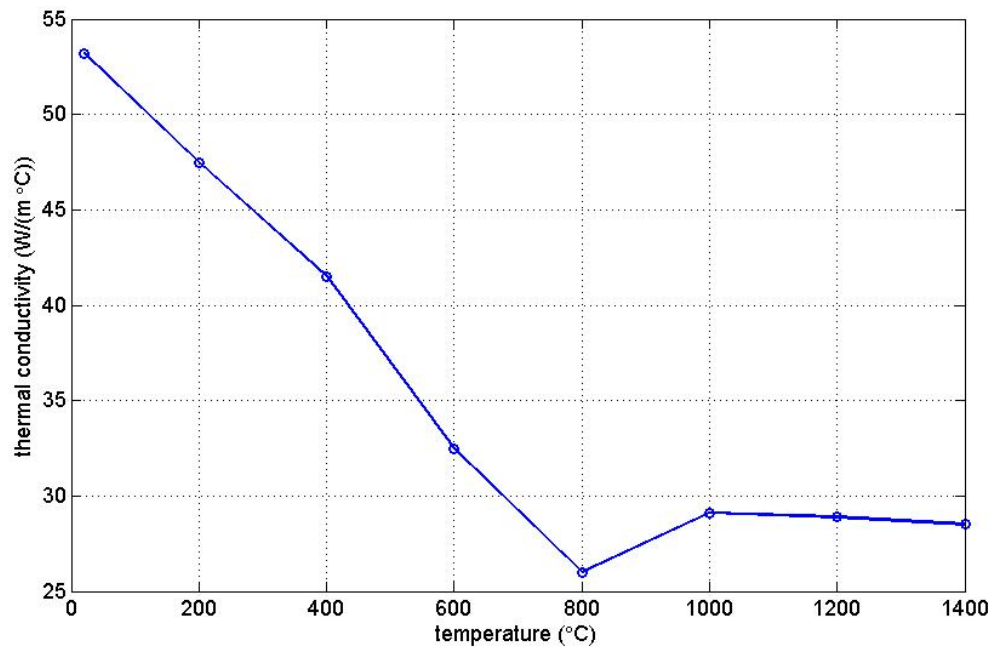


Figure 4.6: AISI 52100: thermal conductivity vs. temperature [Umbrello et al. 2004, Podgornik et al. 2001].

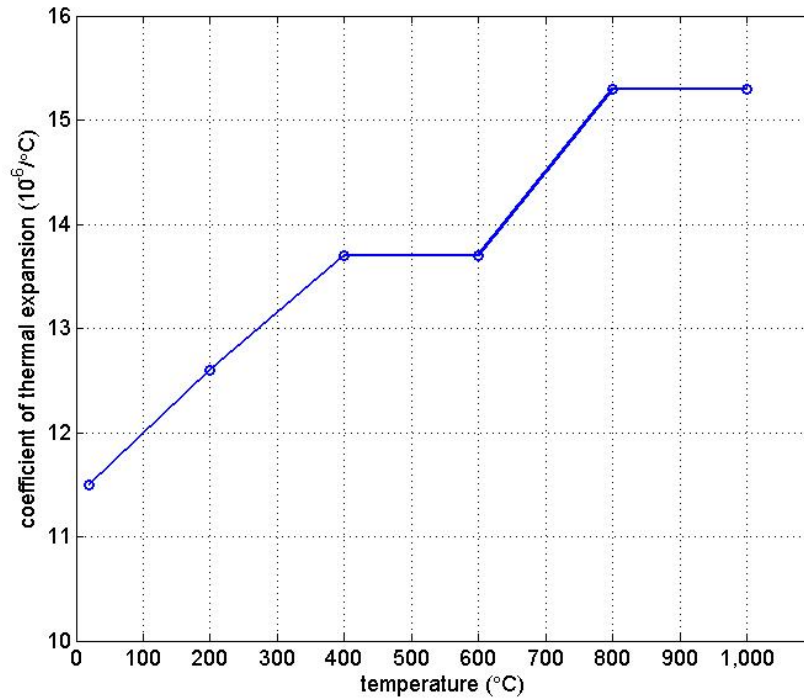


Figure 4.7: AISI 52100: coefficient of thermal expansion vs. temperature [Guo et al. 2002].

Bain and Paxton [Bain et al. 1961] have shown that the alloying elements have significant influence on the austenitic phase fields of hyper-eutectoid steels. The phase transformation temperatures (A_1 and A_{CM}), martensite start temperature (M_s) of AISI 52100 steel are obtained from the empirical relation derived as a function of its alloying constituents [Andrews 1965].

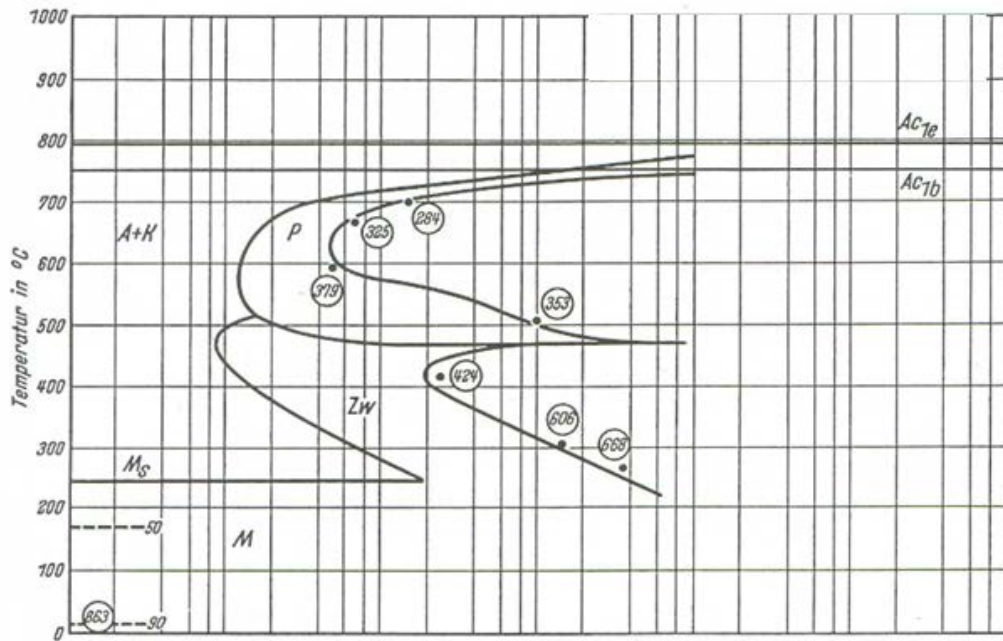
$$A_1(^{\circ}C) = 723 - (10.7 * Mn) + (16.9 * Cr) - (16.9 * Ni) + (29.1 * Si) + (290 * As) + (6.38 * W) \quad (4.28)$$

$$A_{CM}(^{\circ}C) = 910 - (25 * Mn) - (11 * Cr) - (20 * Cu) + (60 * Si) + (60 * Mo) + (40 * W) + (100 * V) + (700 * P) \quad (4.29)$$

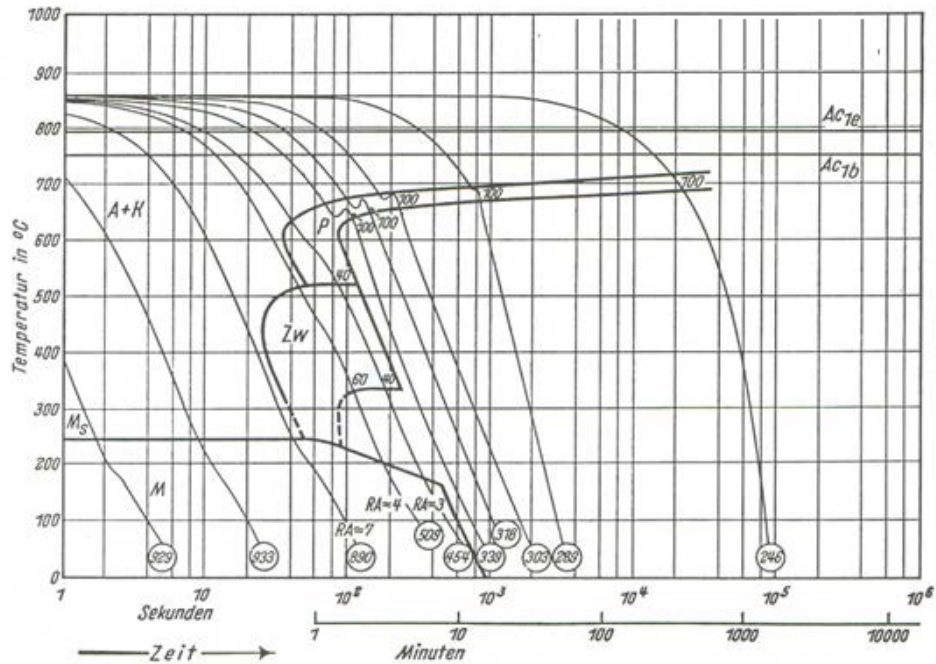
$$M_s(^{\circ}C) = 723 - (423 * C) - (30.4 * Mn) - (12.1 * Cr) - (17.7 * Ni) - (7.5 * Mo) \quad (4.30)$$

where the symbols C, Cu, Cr, Fe, As, Mo, Mn, Ni, Si, V, W represent the amount of alloy constituents in the hyper eutectoid AISI 52100 steel. It can be seen that the alloying elements depress the martensitic start temperature.

The rates of formation of different phases (pearlite, martensite) for isothermal tempering and at continuous cooling rates are self explanatory from the conventional transformation diagrams (see Figure 4.8) for AISI 52100.



(a)



(b)

Figure 4.8: Transformation diagram of AISI 52100 steel: (a) Time-Temperature Transformation, (b) Continuous Cooling Transformation. (A+K: Area for austenite and carbides, K: Area for carbide formation, P: Area for pearlite formation, O: Hardness in HV, Zw: Area for intermediate structure (bainite formation, M: Area for martensite formation, RA: Residual austenite, F: Area for ferrite formation, F+K: Area of nanlamellar eutectoids, Z: Cementite, 10Z: 10% Cementite, 1 & 2: refers to numbers on curves – percentage proportion of structure formed) [Voort 1991]

4.3.1 Modeling Procedure

For a given alloy, a relationship exists between the hardness and the thermal history that depends on the laser scanning condition. The proposed tempering model can be used to draw the relation between the laser processing parameters and resulting subsurface hardness distribution. The predicted hardness can be used to understand the influence of the scanning parameters to temper a desired depth of the subsurface region.

The cylindrical workpiece was modeled as a rectangular solid (see Figure 4.9), whose top surface represents the unwrapped surface of the cylinder. The width, depth, and length of the rectangular solid represent the circumferential length, radius, and the length of the cylindrical workpiece, respectively. The model has two assumptions: (a) the circumferential advection can be represented by a linear advection at a given linear speed, which is dictated by the rotational speed of the workpiece, (b) negligible thermal contribution due to the heat energy at the diametric end. The isotropic workpiece was modeled with temperature dependent material properties. Convection and radiation heat losses occur at the top surface and the two end surfaces of the cylindrical workpiece. In the model, the boundary condition of these surfaces was modeled using a lumped convection coefficient. The boundary condition of the other surfaces in the model was modeled as,

$$k(T) \frac{\partial T(X, Y, Z, t)}{\partial N} = 0 \quad (4.31)$$

where N refers to the normal direction to the surface.

The incident laser energy was input as a surface heat flux since the absorption of energy by metals extends to only a few microns from the surface. The heat flux traverses in the laser scanning direction for a distance equal to the circumferential length of the cylindrical workpiece. In this work, the laser beam path along the scanning direction is referred to as a ‘track’. Each track is subdivided into number of sectors based on the spotsize of the laser beam. Each sector of the track is subjected to a thermal load for a time period equal to the interaction time dictated by the scan speed (which is a function of spindle speed and the workpiece diameter). After each track, the laser beam returns to the initial track position and advances in the feed direction, by a distance equal to the feed. The process repeats for the entire duration of the scan.

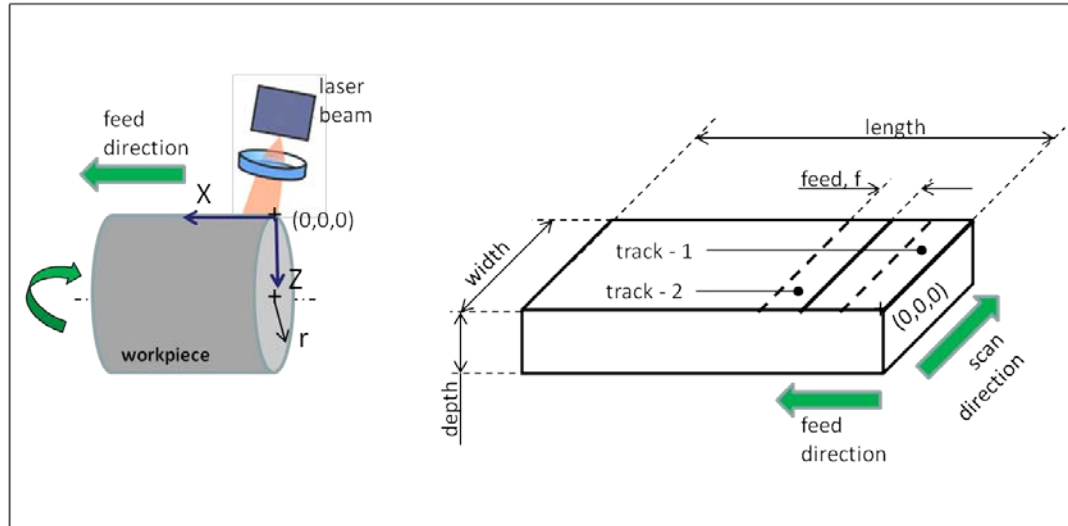


Figure 4.9: Schematic of the thermal model.

The temperature field was predicted using the finite element thermal model, developed in ANSYS v13.0. An eight node 3D thermal element (SOLID70) was used. To model the convection and radiation boundaries, surface elements (SURF152 and SURF153) were used. In order to achieve faster solution times, a 10 mm x 10 mm model was simulated. A three dimensional tipped distribution (Equation 4.3(c) in Table 4.1) was used to approximate the incident laser energy profile of the Nuvonyx laser source. The heat flux was determined by dividing the area of the spot into smaller elements and the calculating the heat flux at the center of each element. In the Y-direction, six divisions were found satisfactory based on the convergence test of nodal temperatures. Along the X-direction, the element size was dictated by the overlap ratio. In the Z-direction, fine mesh (20 μm) was used at the subsurface near the incident surface to accurately capture the temperature field and a coarse mesh (100 μm) was used at higher depths. A representative finite element model is shown in Figure 4.10. The amount of thermal energy of the interacting laser beam is dependent on the wavelength of the incident beam (808 nm) and the absorptivity of workpiece material. The model is validated for absorptivity.

The model inputs are the laser scanning conditions (laser power, scanning speed, spotsize, and overlap). The heat transfer equation (Equation 4.1) is then solved at each step till the solution converges. A contour plot of the temperature distribution is shown in Figure 4.11.

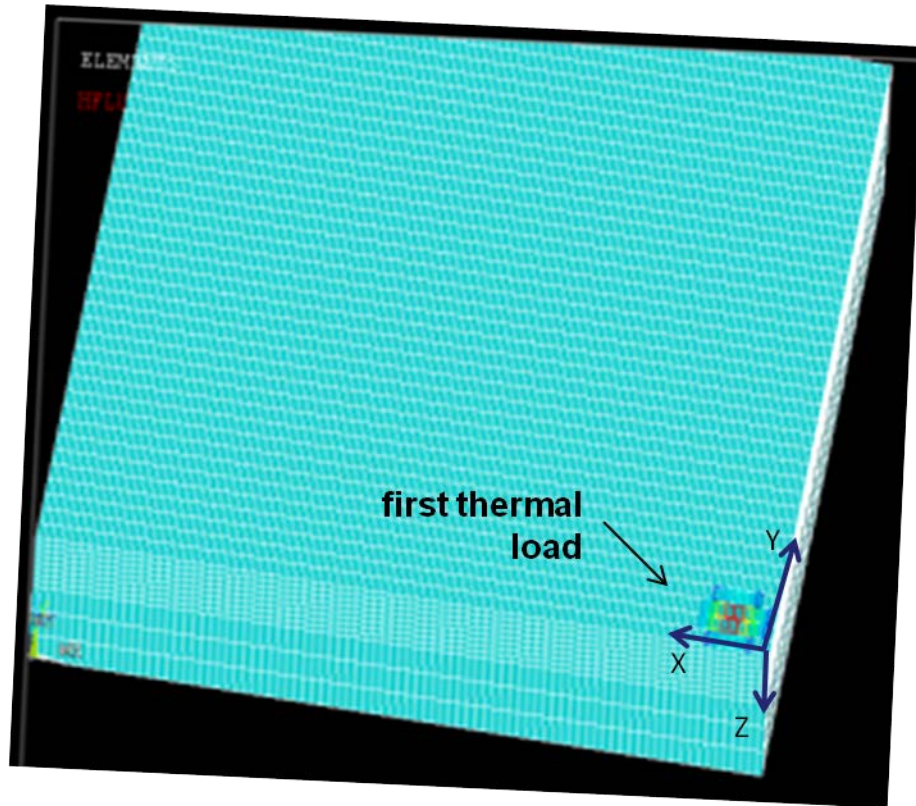
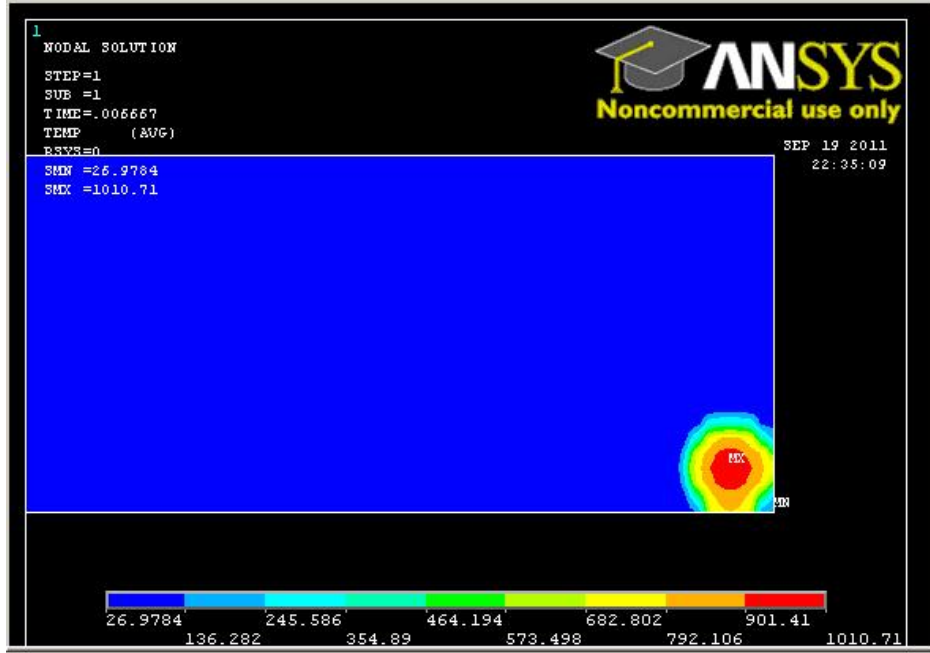
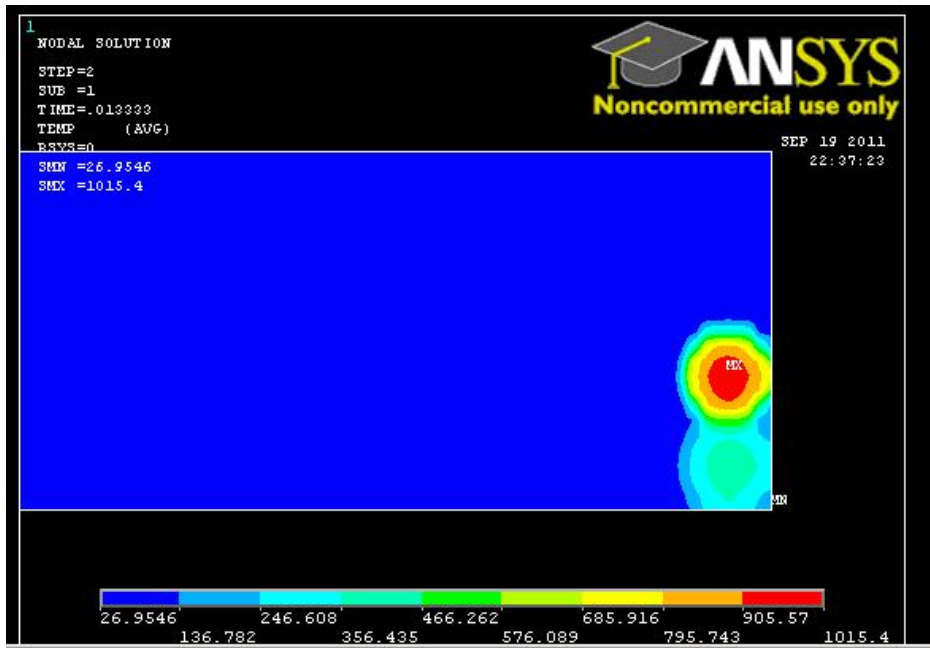


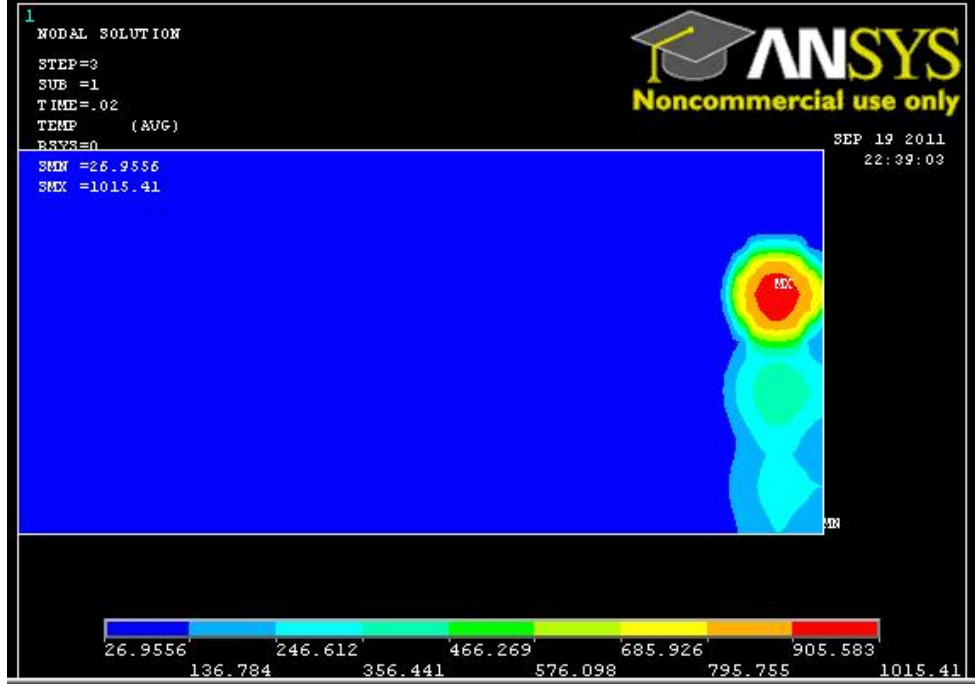
Figure 4.10: Finite element model, showing mesh, application of first thermal load.



(a)



(b)



(c)

Figure 4.11: Temperature distribution thermal model at time, $t =$ (a) t , (b) $(t + \Delta t)$, (c) $(t + 2\Delta t)$. (spot size: 2 mm, laser power: 694 W, scan speed: 17.95 m/min).

The predicted temperature history is then fed to the computational Matlab model to find the resulting subsurface hardness. The carbide particle radius r_i , and the spacing of the cementite particles $2r_e$ for the hyper-eutectoid steel with 1% C were assumed to be 0.4 μm and 1.6 μm respectively [Li et al. 1986]. The pre-exponential function for diffusion of carbon in austenite D_o , was assumed as $6 \times 10^{-5} \text{ m}^2 \text{ s}^{-1}$ [Smithells et al. 1967]. Using the [Hiller 1957] model for the TTT diagram, [Li et al. 1997] showed that the activation energy for reaction kinetics can be obtained from,

$$\frac{d}{dT} \left(\Delta T^n e^{-\left(\frac{Q}{RT_n}\right)} \right) = 0 \quad (32)$$

which leads to

$$Q = \left(\frac{nR}{\Delta T} \right) T_n^2 \quad (33)$$

where ΔT is the undercooling, T_n is the nose temperature obtained from CCT for AISI 52100 steel [Voort 1991] and the empirical exponent n is determined by the diffusion mechanism. Since the temperature is high enough for austenite nucleation, [Jacot et al. 1997] pointed that volume diffusion ($n=2$) is likely to occur during phase transformation. The median value of $Q = 208.85$ kJ/mol, obtained from the Equation 33 was used as the activation energy for the transformation kinetics.

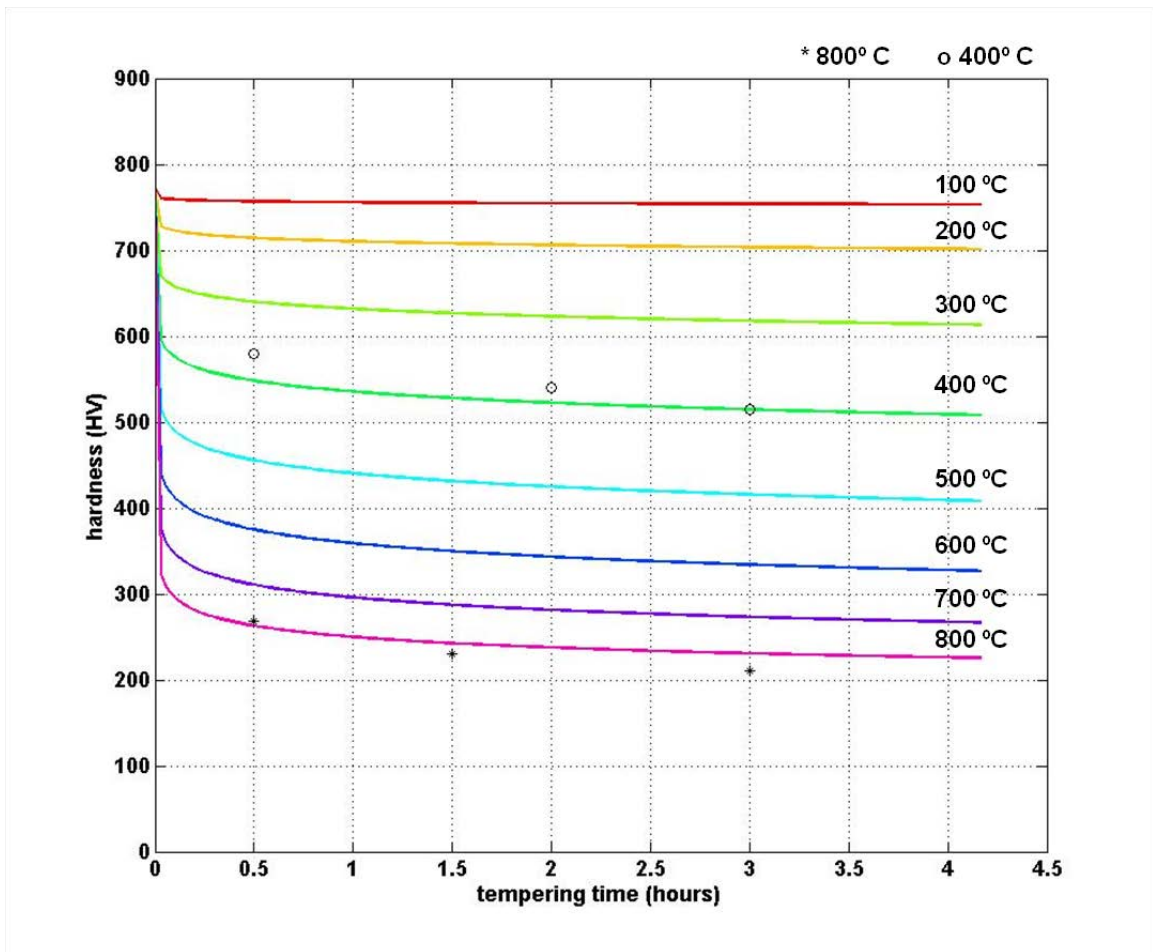


Figure 4.12: Isothermal tempering of AISI 52100 steel (Data from simulations are represented by continuous lines. Data from experiments are represented by points).

Isothermal tempering of AISI 52100 steel samples was conducted to determine the constants for the tempering model. Quarter circle samples of 8 mm thick were prepared and placed in the heating furnace at different periods of temperature and time. A constant heating rate of 0.24 °C/sec was used to reach the set temperature from the initial room temperature. At the tempering temperature, the sample was held for tempering time. Afterwards, the sample was water quenched. The average surface hardness of the sample was found from ten measurements. The tempered hardness was plotted against the tempering time as shown in Figure 4.12.

The values of m and D_t in Equation 4.25 were calibrated to match the measured tempered hardness obtained from experiments. The results from the simulations using the calibrated values of m and D_t are shown in Figure 4.12. In Table 4.3, the calibrated values of m , D_t for AISI 52100 are compared with values for comparable steels from [Hollomon et al. 1945]. The calibrated values closely matched the corresponding values for similar hyper-eutectoid steels.

Table 4.3: Comparison of constants with similar alloy steels.

	Alloy elements in steel	Activation energy Q (10^2 kJ mol$^{-1}$)	Ageing component, m	Frequency factor, D_t (10^8 sec$^{-1}$)
(AISI 52100)	1.0 % C, 1.45 % Cr, 0.35 % Mn, 0.23 % Si	2.0885	0.100	7.3
[Hollomon et al. 1945]	1.15 % C, 0.58 % Mn, 0.09 % Si	2.01238	0.122	0.711
[Hollomon et al. 1945]	0.98 % C, 0.30 % Mn, 0.30 % Si	2.01225	0.141	3.929

4.4 Summary

In this chapter, a tempering model was presented. The model is based on finite element analytical model to predict the temperature history, which is then used by the kinetic model to predict the subsurface hardness. The thermal model was implemented in finite element package and the kinetic model was modeled in Matlab. In the next chapter, the model will be calibrated using microstructural and phase analysis at different scanning conditions.

CHAPTER 5

MODEL VALIDATION

In the previous chapter, thermal model and kinetic phase change model were presented. The model is based on finite element analytical model to predict the temperature history, which is then used by kinetic model to predict the subsurface hardness. The key process parameters in laser-treatment are identified as: (i) heat input intensity (determined by laser power and beam spot size), (ii) laser beam energy profile (Gaussian, uniform, etc) (iii) scan rate and (iv) overlap ratio.

In this chapter, the model is first validated by microstructure analysis of AISI 52100 steel subjected to single, non-overlapping laser scans. The validated model is then used to analyze the influence of process parameters to temper the subsurface layer. In the following section, the microstructures and the composition of phases in the subsurface of a laser treated AISI 52100 steel samples subjected to laser scanning are evaluated. The experimental results from the model are compared with the values obtained from microstructure of the laser treated samples. Finally, the prediction of subsurface hardness at different laser treatment condition is presented.

5.1 Validation Procedure

The thermal model is first validated for absorptivity. A single, non-overlapping scan of high-powered laser beam strikes the workpiece surface to produce temperatures in excess of phase transformation temperature (A_1 temperature of the steel). When the volume of the irradiated region is negligible to the volume of the workpiece, phase transformational hardening occurs at the irradiated surface. The phase transformation in the workpiece is related to the temperature rise induced by the heat input from the laser beam. This property is used for validating the thermal model.

Figure 5.1 illustrates the cross-sectional view of steel irradiated by single laser scan. At the instant the laser beam strikes the workpiece, there is a rise in the surface temperature of the irradiated region which is proportional to the input heat intensity from the laser beam. Only a portion of heat energy is absorbed by the material and the rest is reflected. The absorptivity, defined as the ratio of the energy absorbed by the workpiece to the total available energy at the surface, is dependent on wavelength of the laser beam, laser beam/workpiece interaction time, and surface conditions of the workpiece. The energy absorbed at the surface is transferred to the neighboring region of the material. Based on thermal properties of the workpiece material, a thermal gradient exist in the subsurface and consequently, only a portion of the subsurface region is heated and leaving the rest of the material un-affected. The heated region, where the temperature exceeds phase transformation temperature, undergoes a phase transformation (pearlite to austenite). The phase transformed region and the heated region below the phase transformed region is subsequently cooled by the bulk of the material, which is at room temperature. During cooling, the phase transformation region undergoes additional phase transformation (austenite to martensite). In Figure 5.1, region **A - B - C** is the white martensitic region and the region **C - D** is the heated region that has not phase transformed. That is,

$$\mathbf{C - D: } T_o < T(t) < A_1 \quad (5.1)$$

The region below **D** is unaffected by the input heat from the laser beam.

A minimum interaction time of 10^{-2} s, a power density of $>10^3$ W/cm², and a traverse speed of 5-50 mm/s are required for transformation hardening of steels [Mazumder et al. 1984]. A melted and re-solidified zone is typically harder and therefore melting should be avoided. The bounding temperatures for transformation hardening are given by the phase transformation temperature of the material (A_1 temperature) on one

side and melting point of the material (T_{melt}) on the high side. Following conditions were used to validate the absorptivity of the model,

$$\begin{aligned} \mathbf{A, B:} & A_1 < T(t) < T_{melt} , \\ \mathbf{C:} & T(t) = A_1. \end{aligned} \tag{5.2}$$

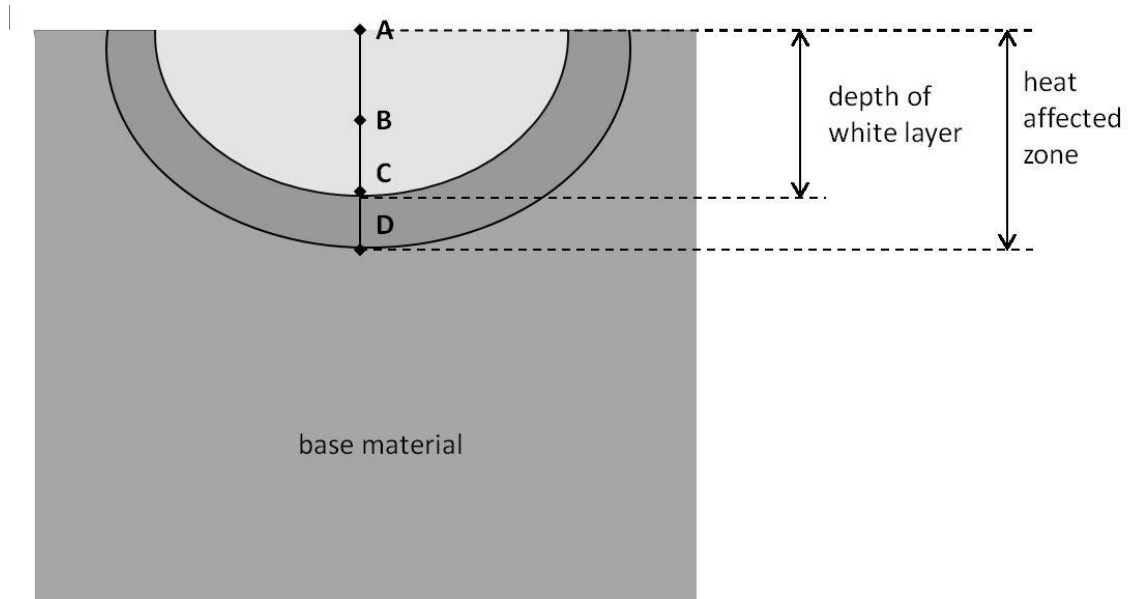


Figure 5.1: Illustration (front view of the longitudinal cross section of irradiated sample) of single, non-overlapping laser scan. (**A**, **B**, **C**, and **D** are defined by Equations 5.1 and 5.2).

The phase transformation temperature of AISI 52100 steel, obtained from Equation 4.28, is 747.8 °C and the melting point of AISI 52100 is given in Table 4.2.

5.2 Microstructure and Phase Analysis

The cylindrical AISI 52100 steel bars were subjected to single, non-overlapping laser scans and overlapping laser scans. The results from single, non-overlapping laser scans are presented prior to the case of overlapping laser scans. In each case, the laser tempered cylindrical bars were cut to size, mounted as 1 inch specimen in epoxy binder.

The specimen was polished using abrasive SiC discs grit 180, 240, 320 and 400 followed by 9, 3, and 1 μm diamond slurry. The samples were finally polished with 0.05 μm alumina suspensions and etched using a 2 % Nital solution (98 % alcohol, 2 % nitric acid). The etched sample was evaluated using a Leica DMRM compound microscope, Type 301-371.010 (for details, see Appendix 8.1.5).

5.2.1 Microstructural Analysis of Non-overlapping Laser Scans

Figure 5.2 shows the typical laser-hardened microstructure of a 52100 steel sample when exposed to a single non-overlapping scan of 800 W laser power, 2 mm spot size laser beam. Since the objective of this work is to induce only tempering of the hardened surface layer, the laser scanning conditions were chosen such that no melting took place. A spindle speed of 17.95 m/min did not produce melting at the surface. The circular laser spot produced a hemispherical shaped hardened zone as seen in Figure 5.2. A single non-overlapping pass of the laser beam of sufficient intensity is known to produce hardening of the steel surface due to martensitic phase transformation brought about by the rapid heating and quenching of the material. The bulk of the material acts as a heat sink and the cooling rate is sufficient to form the hard martensite.

The irradiated cross-section reveals three distinct regions: (1) a white layer, (2) a dark layer, and (3) the base material that is not influenced by the laser irradiation (see Figure 5.2). The white layer represents the phase transformed zone and the temperatures in this zone exceed the austenitization temperature of the steel at the instant when the laser beam strikes. After the laser beam moves past this austenitized region, it is rapidly quenched by the underlying bulk material, which is at room temperature. Also, a convective heat transfer takes place at the top surface of the part. This rapid heating and quenching cycle produces a diffusionless martensitic phase transformation in the material, which causes the hardness of this region to be greater than the bulk material. The dark layer below the phase transformed zone sees temperatures that are below the

austenitization temperature of the steel and consequently, this region experiences a tempering effect. The white layer and the dark layer together constitute the heat affected zone due to laser irradiation.

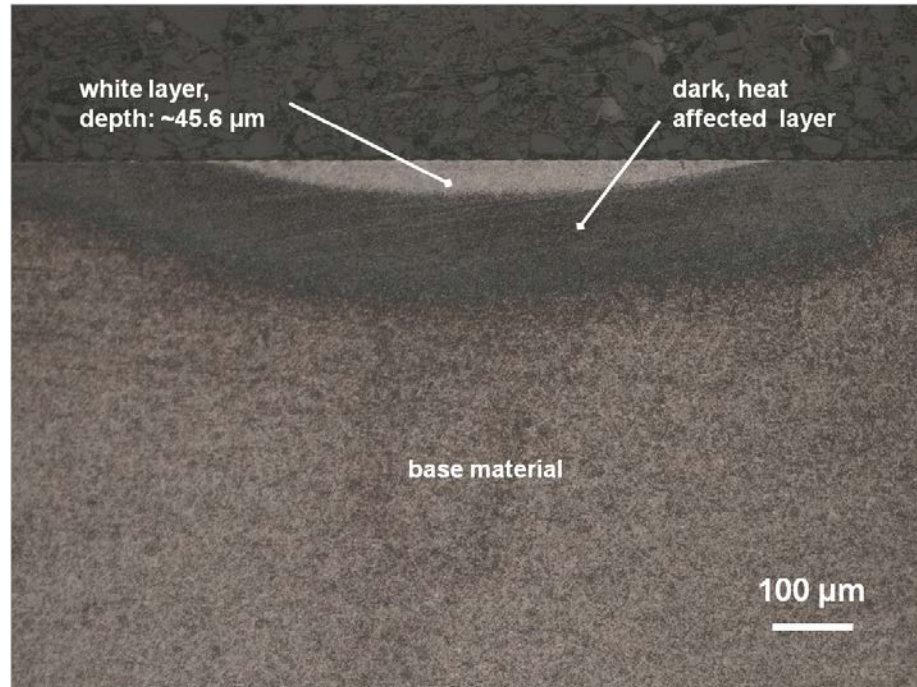


Figure 5.2: Microstructure (longitudinal cross-section of AISI 52100 steel sample) of a single non-overlapping laser scan (laser power: 800 W, spot size: 2 mm, scan rate: 17.95 m/min).

The model developed in Section 4.3 was validated as given in Section 5.1. A single, non-overlapping laser scan was simulated at 800 W laser power, 2 mm spot size, and 17.95 m/min scan speed) to model the microstructure shown in Figure 5.2. The absorptivity was varied until Equation 5.2 was satisfied. Figure 5.3 shows the simulated white layer depth of single, non-overlapping scans at different absorptivity values. A value of 35.7% (~36%) closely matched the white layer depth of 45.6 μm (shown as dotted line in Figure 5.3) obtained from microstructure.

Figure 5.4 shows the depth and the width of the white layer as a function of laser power at a constant scan speed of 17.95 m/min and a 2 mm spot size laser beam. It can be

seen that the depth and width of the white layer are proportional to the laser power. The microstructures are shown in Appendix 8.2. In addition, simulations were done using the model at different absorptivity values and each time, the predicted temperatures were compared with the measurements obtained from microstructural analysis using Equation 35. An absorptivity value of 36 % closely matched the white layer depths obtained from micrograph. The predicted depth and width of the white layer is shown in Figure 5.4. It can be seen that there is a good agreement between the predicted and measured values of depth of the white layer (see Figure 5.4(a)). At laser powers < 580 W, the workpiece temperature did not exceed the austenitization temperature and consequently, the depth and width of the white layer was negligible. The measured depth of the white layer remained constant at power > 879 W. However the model over-predicted the white layer depth by ~15 %. A good agreement was also obtained between the predicted and measured values of width of the white layer (see Figure 5.4(b)). At 793 W, the model over-predicted the width of white layer by ~22.02 %.

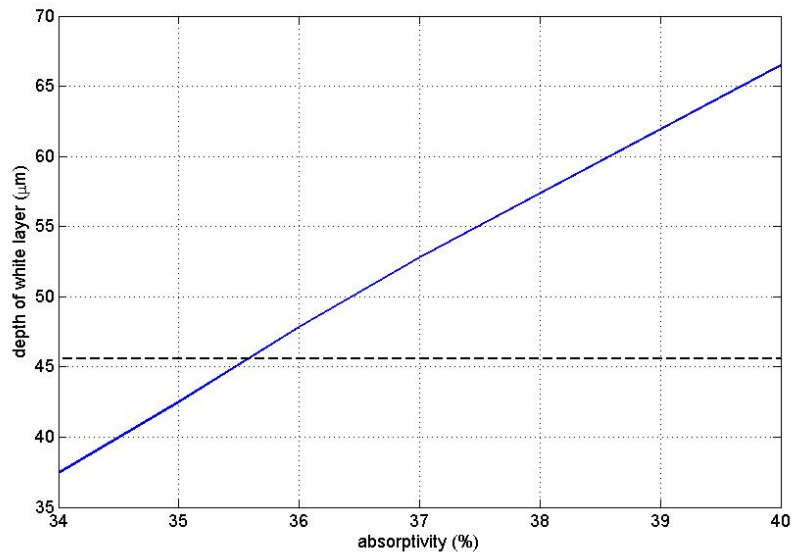
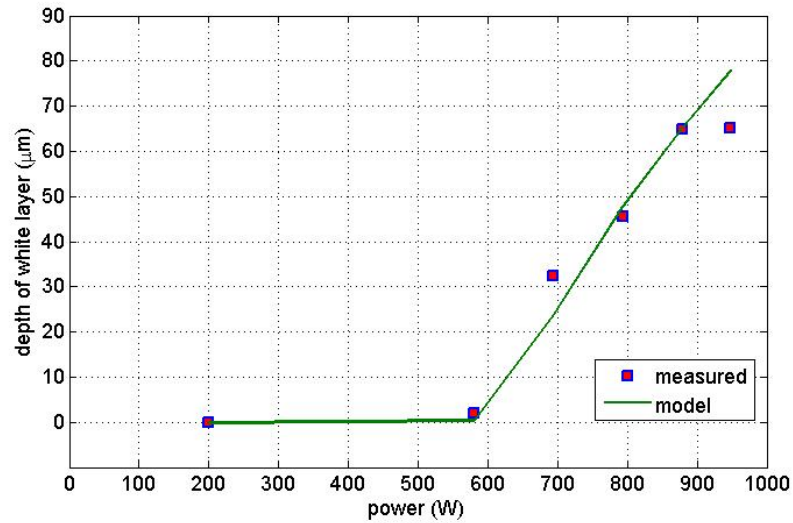
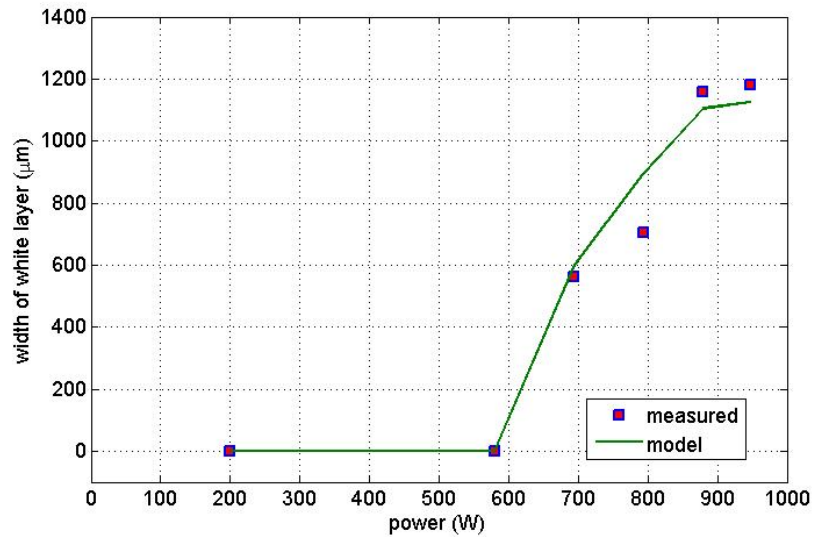


Figure 5.3: Absorptivity calibration of white layer depth in single, non-overlapping laser scan (AISI 52100, laser power: 800 W, spot size: 2 mm, scan speed: 17.95 m/min). Note:

Dotted line is shown to represent the target for selecting absorptivity value (model validation). The value $45.6 \mu\text{m}$ is from Figure 5.2.



(a)



(b)

Figure 5.4: White layer characterization as a function of laser power: (a) depth, and (b) width of white layer. (AISI 52100, spot size: 2 mm, scan speed: 17.95 m/min). For microstructures, see Figures 5.2 and Appendix 8.2. Data from simulation are plotted as continuous lines. Data from experiments are plotted as points.

5.2.2 Influence of Process Variables

The validated model was simulated to understand the effect of other process parameters - laser beam intensity, and scan speed.

Laser beam intensity is a function of incident spot size and laser beam power. In the experimental setup, the incident spot size is a fixed, 2 mm circular spot. The input heat intensity was therefore varied by changing the incident laser power. To study the influence of heat input intensity, scan speed was kept constant at 17.95 m/min. Figure 5.5 shows the simulated peak temperature in the subsurface at different intensity. As expected, the temperature is high at the surface and a thermal gradient was set in the subsurface depending on the surface temperature and thermal properties of the workpiece material. High laser power implies high beam intensity at the incident surface and consequently high temperature at the surface. Note that, the surface temperatures are below the melting point temperature of the material. At 800 W, the temperatures at the surface and a portion of subsurface region are above the phase transformation temperature (A_1) of the material. The hardness of this phase transformed region is more than the bulk material. At 500 W, the surface temperature is just below the phase transformation temperature and at 200 W, the surface and subsurface region are only heated. High laser power produces larger depth of phase transformed region.

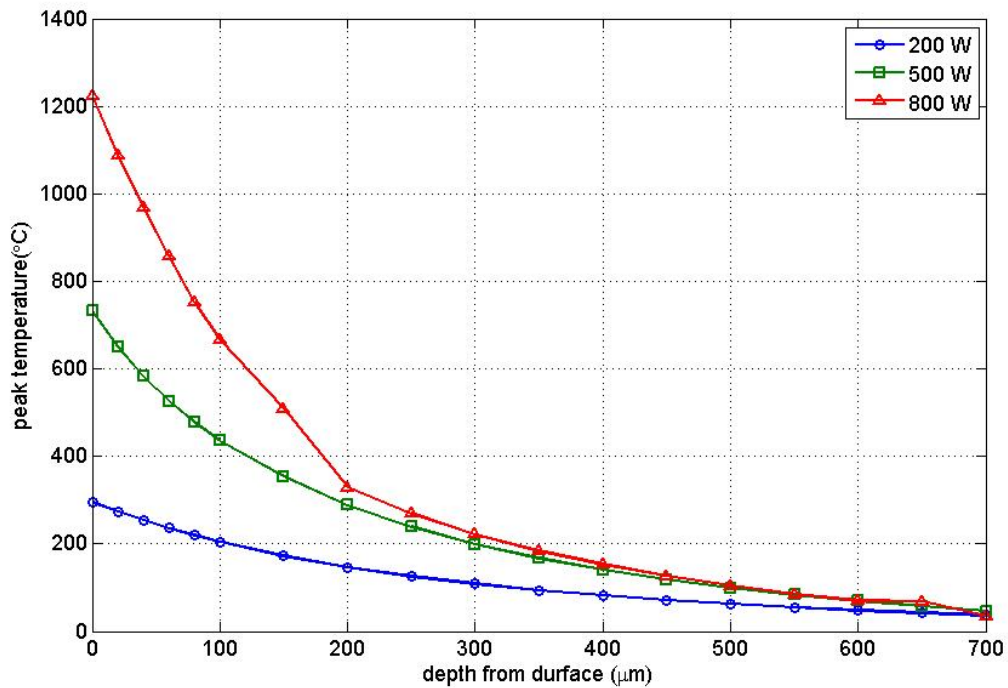


Figure 5.5: Simulated peak temperature (model) vs. depth from surface at different laser powers in single, non-overlapping scans. (spot size: 2 mm, scan speed: 17.95 m/min).

The effect of scan speed is now analyzed. It is enough to plot the peak surface temperature at different scan speeds. Figure 5.6 shows the simulated peak surface temperature at varying scan speeds. In the experimental setup, the minimum scan speed possible is 17.95 m/min. It can be seen that the increasing scan speeds will lead to lower surface temperature. Recall that the quantity of heat energy absorbed is dependent on the laser beam/workpiece interaction time, which is dictated by the scan speed. A slower scan speed has more interaction time, which leads to higher quantity of heat that will be absorbed and consequently, produces a higher surface temperature.

Summarizing, high laser power and slow scan speed produces large depth of phase transformed region.

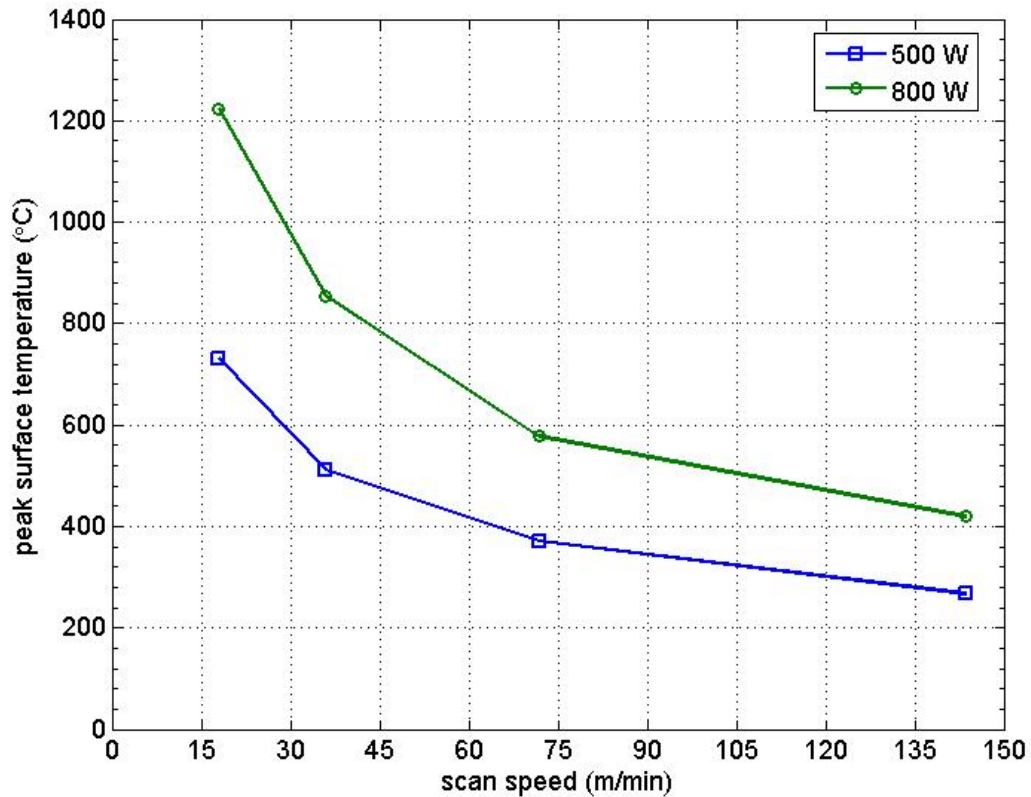


Figure 5.6: Peak surface temperature (model) vs. scan speed at different laser beam intensity in single, non-overlapping scans. (AISI 52100, spot size: 2 mm, scan speed: 17.95 m/min)

5.2.3 Microstructural Analysis of Overlapping Laser Scans

When the laser scans overlap each other, additional thermal energy is imparted to the overlap region. By modifying the overlap ratio, the amount of thermal energy imparted to the irradiated surface can be modified. Consequently, the hardness in the overlap region is lowered due to tempering. Figure 5.7 shows the tempered microstructure of a 52100 steel sample when exposed to overlapping laser scans at 800 W with 2 mm spot size and 17.95 m/min scan speed. The irradiated cross-section reveals three distinct regions: (1) a tempered white layer, (2) a dark layer, and (3) a base material that is unaffected by the overlapping laser scans.

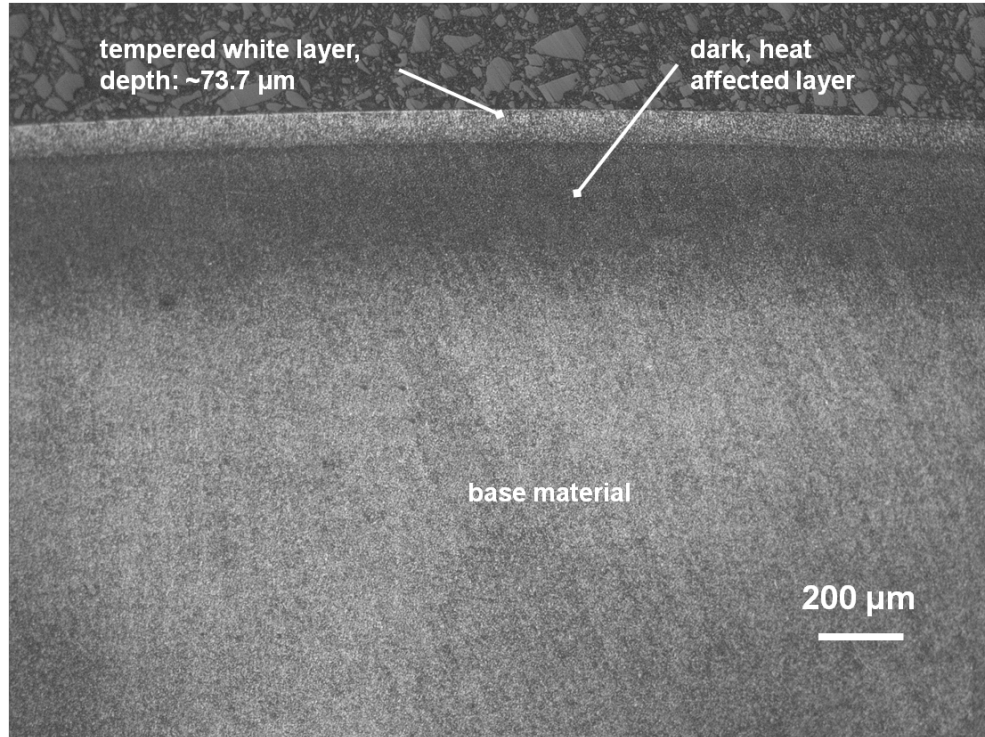


Figure 5.7: Microstructure (longitudinal cross-section of AISI 52100 steel sample) of overlapping laser scan (laser power: 800 W, spot size: 2 mm, scan speed: 17.95 m/min, overlap: 93.58%).

In the case of overlapping scans, the region, irradiated by the first laser scan, sees heat inputs from successive laser scans based on the extent of overlap. For a large overlap, number of heat input per unit length is more. With each heat input, the workpiece retains a portion of thermal energy resulting in an increase in the surface and subsurface temperatures. When the subsurface temperature rises above the austenitization temperature (A_1), phase transformation takes place at this depth to form a white layer, which is subsequently tempered by additional heat from the overlapping scans. The white layer seen in Figure 5.7 is a tempered region in contrast to the hardened white layer formed due to non-overlapping laser scans. This region is referred to as the ‘tempered white layer’, in order to differentiate it from the hardened white layer obtained with non-

overlapping laser scans. The tempered white layer is seen as white layer with dense dark spots superimposed.

The tempered white and dark layers together constitute the tempered region as a result of the overlapping scans. The number of heat inputs per unit length, the temperature rise due to successive heat inputs, the degree of tempering and consequently, the depth of tempering can be controlled by modifying the extent of overlap and the heat energy per overlapping scan. That is, the depth of the tempered region produced by the overlapping laser scans is a function of the input heat intensity, beam energy profile, scan speed and overlap.

Now, the effect of scan speed and overlap is analyzed at constant input heat intensity. Figures 5.7 and 5.8 show the tempered microstructure of a 52100 steel sample when exposed to overlapping laser scans at 800 W power, 93.58 % overlap, 2 mm spot size laser beam at two different scanning speeds, 17.95 m/min and 35.90 m/min respectively. At the 17.95 m/min scan speed, the irradiated cross-section of the workpiece had three distinct regions (see Figure 5.7). However, only two regions, dark layer and the base material, were seen at the 35.90 m/min scan speed (see Figure 5.8). Recall that the depth of hardened white layer in single non-overlapping scans decreases with the scan speed. Single, non overlapping scans at 800 W laser power, 2 mm spot size and with a scan speed of 35.90 m/min produced negligible white layer, suggesting that the austenitization temperature was not reached. A 93.58 % overlap of successive laser scans does not result in a surface temperature above the austenitization temperature and therefore no tempered white layer is seen (see Figure 5.8). Consequently, this resulted in a negligible tempered depth at 35.90 m/min in comparison to the 17.95 m/min scan speed.

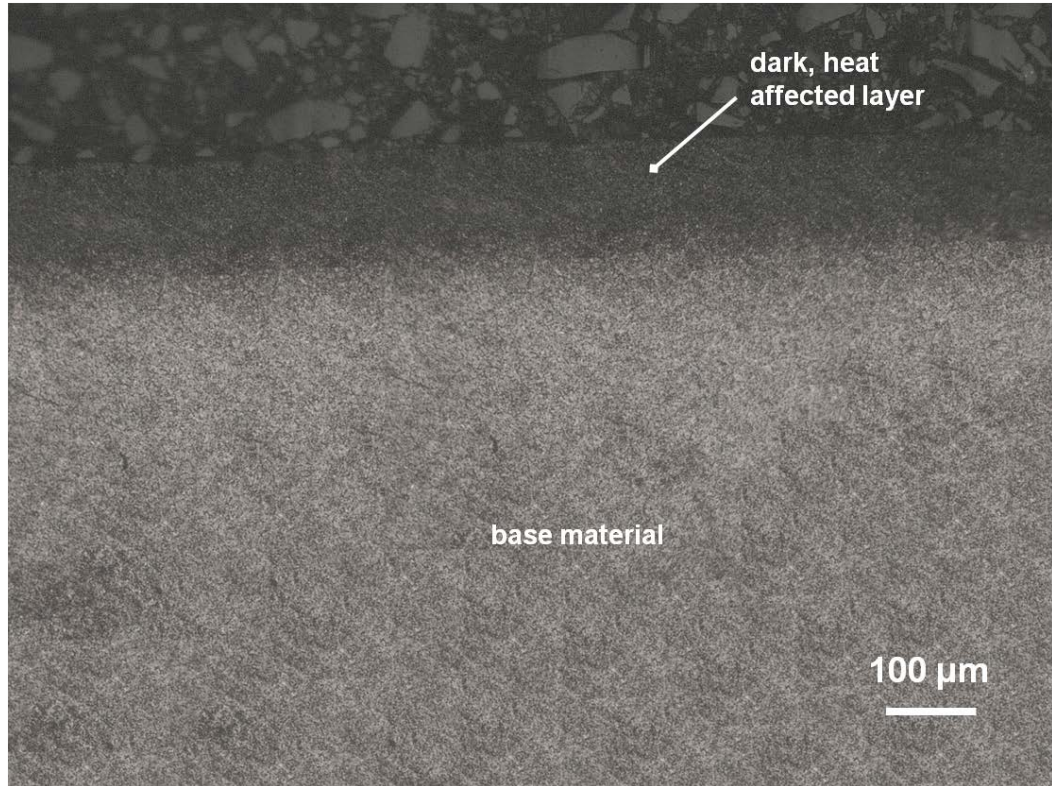


Figure 5.8: Microstructure (longitudinal cross-section of AISI 52100 steel sample) of overlapping laser scan (laser power: 800 W, spot size: 2 mm, scan speed: 35.90 m/min, overlap: 93.58 %).

Figures 5.7 and 5.9 show the tempered microstructure of a 52100 steel sample when exposed to an overlapping laser scans of 800 W power, 17.95 m/min scan speed, 2 mm spot size at different overlaps 93.58 % and 75.76 %, respectively. The irradiated cross-section of the workpiece reveals three distinct regions as mentioned before. However the depth of the tempered white layer and consequently, the depth of tempered region are different and depends on the overlap ratio. The depth of tempered white layer obtained with a 93.58 % overlap ratio is 73.7 μm , whereas the depth of the tempered white layer with a 76.27 % overlap ratio is 48.1 μm (see Figure 5.9). The depth of tempered white layer, at a given laser scan speed, is proportional to the overlap. Larger overlap produces higher temperatures resulting in a larger depth of tempered white layer.

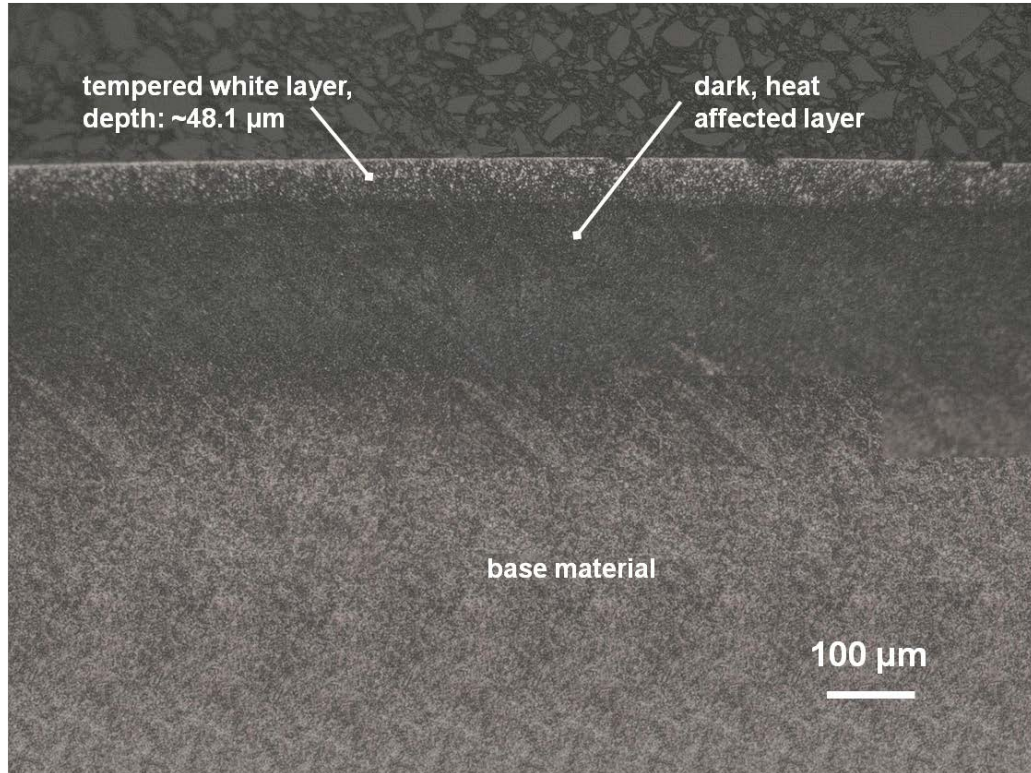


Figure 5.9: Microstructure (longitudinal cross-section of AISI 52100 steel sample) of overlapping laser scan (laser power: 800 W, spot size: 2 mm, scan speed: 17.95 m/min, overlap: 75.76 %).

It can be seen from Figure 5.10 that the depth of tempered white layer increases with overlap. Two simulations were carried out, one at a constant absorptivity and the other with absorptivity varying as a function of the surface temperature. Pantsar [Pantsar et al. 2004] showed that the absorptivity of the steel surface varies with the power and interaction time of the laser energy, and consequently with the surface temperature. Based on the absorptivity results for higher power with short interaction time reported by [Pantsar et al. 2004] and with the absorptivity validation in single non-overlapping scans carried out in this study, the absorptivity was assumed to vary linearly from room temperature (36 %) to the melting point temperature of the material (59 %). For larger overlaps, predictions from simulations with absorptivity as a function of temperature had

good agreement with the measured values obtained from micrograph. The surface temperature obtained in overlapping scans with larger overlap produced surface layer with higher percentage of oxides, resulting in absorptivity close to the assumed linear range. On the other hand, the formation of oxides was less in overlapping scans with smaller overlaps, resulting in lower absorption than the assumed linear range of absorptivity. As a result, the model over-predicted the depth of tempered white layer by about 18 %.

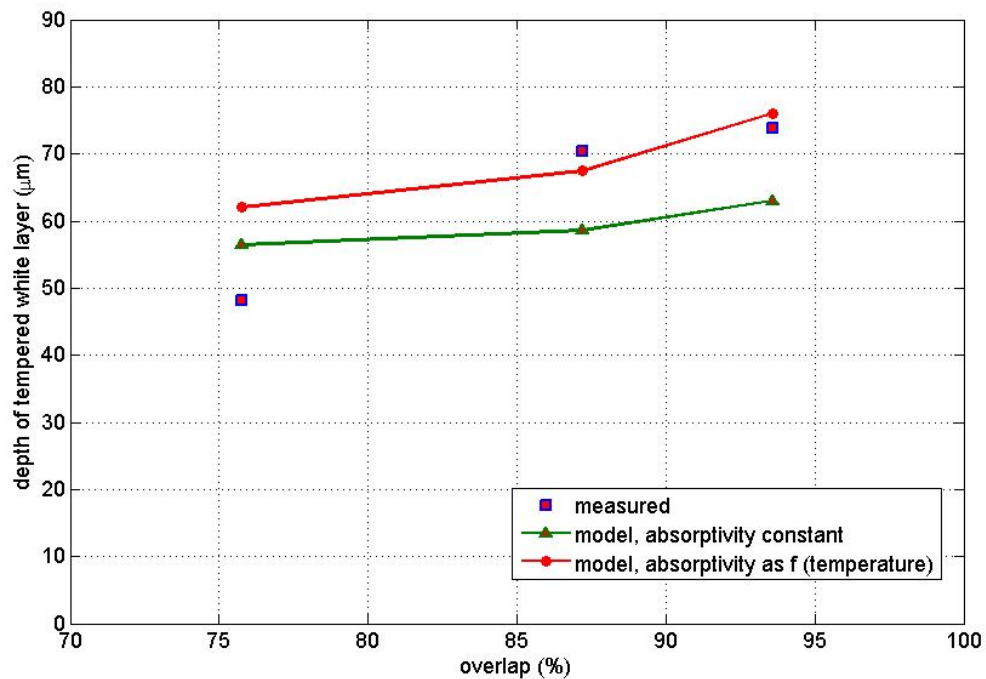


Figure 5.10: Depth of tempered white layer in overlapping laser scans as a function of overlap ratio (AISI 52100, laser power: 800 W, spot size: 2 mm, scan speed: 17.95 m/min). Data from simulations are represented by continuous lines with points. Data from experiments are represented by points.

The temperature field corresponding to the tempered white layer region is an indicator of the overall tempering in the workpiece due to laser scanning. For a given laser scanning condition, the tempered white layer is a region that has at least reached the

austenitization temperature. The depth of tempered white layer can be increased by appropriately choosing the laser scanning conditions. For example, at the selected laser power and scan speed, larger overlaps increase the surface temperature of the workpiece per overlapping scan. An increase in the surface temperature leads to rise in subsurface temperature and consequently, larger depth of tempered white layer. However, too high an overlap ratio causes the surface temperature to exceed the melting point of the workpiece and the hardness of the re-solidified region is higher than the tempered region. Thus, it is important to choose the overlap such that the temperature due to successive heat inputs does not exceed the melting temperature of the work material.

It is interesting that the minimum depth of tempered white layer in the overlapping scans is equal to the depth of the hardened white layer in single non-overlapping scans. A single, non-overlapping scan can be considered to be a special case of overlapping scans with 0 % overlap. Note that the depth of hardened white layer in single non-overlapping scans at 800 W laser beam and 2 mm spot size was 45.6 μm (see Figure 5.2). On the other hand, the maximum depth of the tempered white layer in overlapping scans is obtained by choosing an overlap ratio for which the maximum temperature due to successive heat input does not exceed the melting point of the material. That is, the depth of tempered white layer in overlapping scans ranges between the depth of hardened white layer in a single non-overlapping scan and the depth of white layer that is produced in overlapping scan that yields a surface temperature that is near the melting point of the material.

5.2.4 Phase Analysis of Overlapping Laser Scans

The objective of phase analysis is to evaluate the composition of subsurface phases present before and after laser treating the AISI 52100 steel samples. An overview of the phase analysis, experimental setup is provided in Appendix 8.3. Composition of phases in laser-treated samples were evaluated by x-ray diffraction patterns, obtained

using a monochromatic, PANalytical X'Pert Pro MPD (see Annexure 8.3.3) with Cu-K α radiation ($\lambda = 1.542 \text{ \AA}$), and with fixed slit incidence ($1/8$ divergence and soller slits) and diffracted optics. The voltage and current were set at 45 kV and 40 mA, respectively. AISI 52100 samples were placed in the stage such that the incoming beam from the x-ray source strikes the surface at some initial angle θ . The scan range was selected to be $30^\circ \leq 2\theta \leq 105^\circ$. (see Annexure 8.3.4) No distinction has been made between the ferrite and martensite phases because the theoretical X-ray diffraction patterns of these two phases are nearly the same [ASTM E975 – 03]. The integrated intensities (see Table 5.1) of the (110), (200), (211) and (220) peaks of ferrite and the (111), (200), (220), (311) and (222) peaks of austenite was used to determine the composition. The body centered cubic α -iron has a unit cell dimension of 2.8664 \AA and the face centered cubic γ -iron has a unit cell dimension of 3.60 \AA .

Table 5.1: Peak intensities and diffraction angle for α -iron and γ -iron.

	2θ	hkl	I(f)
α-iron	44.353	110	100
	64.527	200	11.6
	81.656	211	17.6
	98.038	220	4.6
	115.138	310	6.2
	135.215	222	1.6
γ- iron	43.279	111	100
	50.404	200	42.1
	74.054	220	17.5
	89.842	311	16.5
	95.042	222	4.5
	116.778	400	2.1
	136.262	331	6.7
	144.406	420	6.5

Four AISI 52100 steel samples of length 50.8 mm (2 inches) were used to study the composition of the phases in hardened steel. One sample was intended to be the

starting material, while the other three samples were laser-treated at a chosen laser scanning condition. An 800 W laser power, 2 mm spot size laser beam was used to treat the three laser-treated samples. Two scan speeds (17.95 m/min, 35.90 m/min) and two overlaps (93.58 %, 75.76 %) were selected to study the effect of scan speed and overlap to the compositional phases in the subsurface region. Of the three samples, the first sample was treated at 17.95 m/min scan speed and 93.58 % overlap. The other two samples were treated by changing either the scan speed or the overlap and keeping the other parameters same as the laser-treating conditions of the first sample. In order to reveal the subsurface phases, the laser-treated samples were grinded, using a sand paper, to a required depth.

In the original material, about two-third weight percentage of body-centered-cubic ferrite/martensite and one-third weight percentage of face-centered-cubic austenite were present (see Table 8.2).

Table 5.2: Composition of phases in hardened AISI 52100 steel (no laser treatment) from x-ray diffraction analysis.

	BCC (wt. %)	FCC (wt. %)	Ref.
Sample 1	67	33	Figure 8.3.5

In the laser-treated samples, phase transformation takes place in the subsurface region when the temperature exceeds the austenitization temperature. As expected, the composition of subsurface phases changed from the initial composition (see Table 5.2 and Table 5.3). Figure 5.11 shows the composition of phases in surface and subsurface of

the sample, which was laser-treated at 17.95 m/min scan speed and 93.58 % overlap. The patterns of phases were similar to the other laser scanning conditions.

The surface of the laser-treated samples had significant proportion of oxides. The proportion of the surface oxide layer was found larger at the laser scanning conditions that produced higher surface temperatures. In the 17.95 m/min scan speed, 93.58 % overlap case, the weight percentage of the surface oxide layer was ~52 %, whereas in the 35.90 m/min scan speed, 93.58 % overlap, the weight percentage of the surface oxide layer was ~19 %. Note that the surface temperature is less at higher scan speeds. In all the three samples, the oxide layer was very thin.

The three laser-treated samples had a thin layer (<10 μm) of retained austenite. In all the three laser-treated samples, the proportion of retained austenite was maximum at the surface and decreased to a negligible proportion (~1 %) within the thin subsurface layer. At the 17.95 m/min scan speed, 93.58 % overlap case (see Figure 5.11), retained austenite at ~7 μm depth was ~12.2 %. The proportion of the retained austenite in the surface was higher in the sample with larger volume of oxide layer. This is because the formation of oxide layer has slow down the austenite transformation to ferrite/martensite. Below the thin oxide layer and the thin retained austenite region, the tempered subsurface region is composed of ferrite/martensite and weak traces of retained austenite (~1 %). This is consistent with our earlier discussion that successive addition of heat from overlapping scans has tempered the hard martensite. Depending on the relative fraction of different phases (ferrite, martensite), there is variation in the hardness of the tempered subsurface region.

Table 5.3: Composition of phases in laser-treated AISI 52100 steel samples (laser power: 800 W, spot size: 2 mm).

(overlap %, scan speed m/min)	Depth from surface (μm)	BCC (wt. %)	FCC (wt. %)	Fe ₂ O ₃ (wt. %)	Fe ₃ O ₄ (wt. %)	Ref.
Sample L1 93.58 %, 17.95 m/min	0	18	30	30	22	Figure 8.3.6
	7	87.8	12.2	-	-	Figure 8.3.7
	42	99	1	-	-	Figure 8.3.8
	77	99	1	-	-	Figure 8.3.9
	109	99	1	-	-	Figure 8.3.10
	152	99	1	-	-	Figure 8.3.11
	242	99	1	-	-	Figure 8.3.12
	456	99	1	-	-	Figure 8.3.13
Sample L2 93.58 %, 35.90 m/min	0	74	7	-	19	Figure 8.3.14
	12	99	1	-	-	Figure 8.3.15
	27	99	1	-	-	Figure 8.3.16
Sample L3 75.76 %, 17.95 m/min	0	49	16	20	15	Figure 8.3.17
	11	98-99	1-2	-	-	Figure 8.3.18
	82	99	1	-	-	Figure 8.3.19

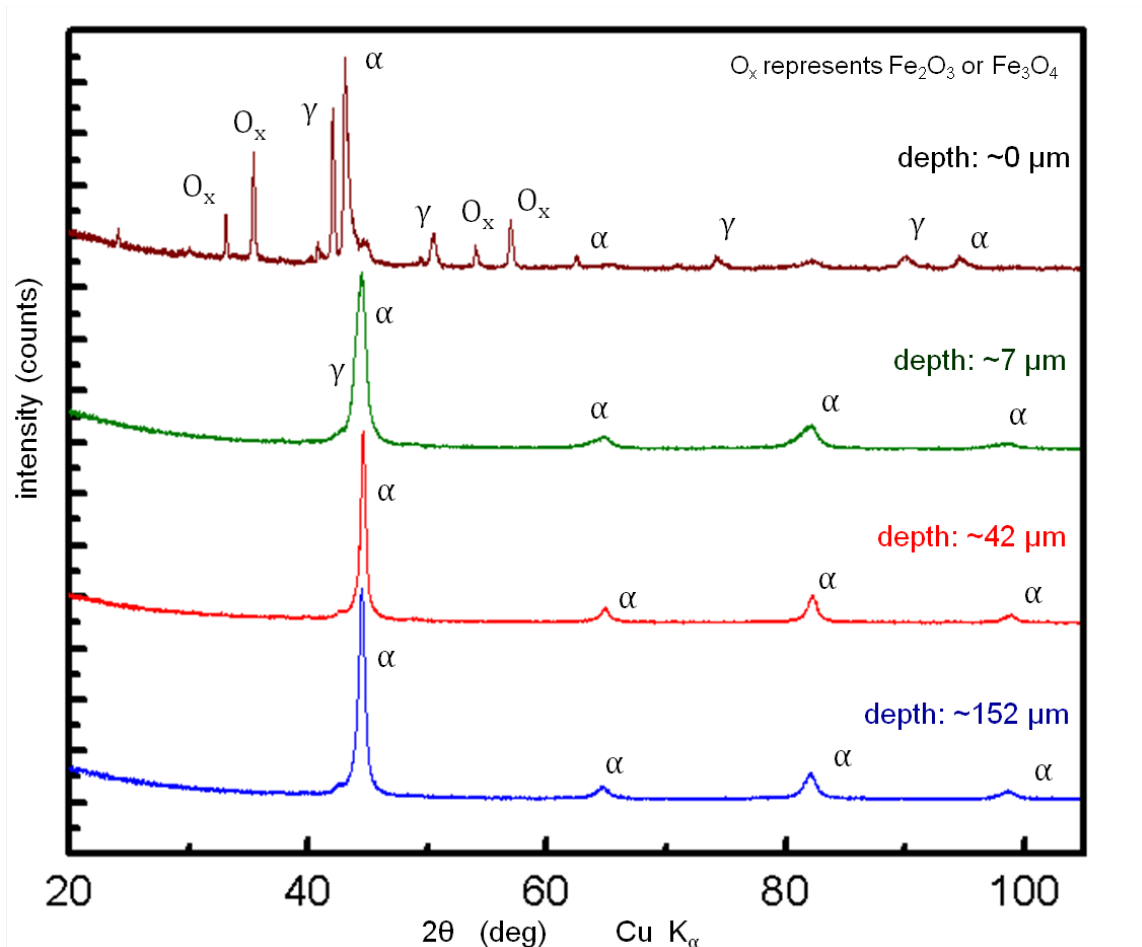


Figure 5.11: X-ray diffraction patterns of laser-treated AISI 52100 steel (laser power: 800 W, spot size: 2 mm, scan speed: 17.95 m/min, overlap: 93.58 %).

5.3 Prediction of Hardness

Figure 5.12 shows the hardness of AISI 52100 steel samples when exposed to an overlapping laser scans with varying scan speeds (17.95 m/min, 35.90 m/min) and overlap ratio (93.58 %, 87.22 %, 75.76 %). Laser-treated AISI 52100 samples were longitudinally sectioned to measure the subsurface hardness of irradiated region at different depths. The hardness was measured using a micro hardness tester at 500 gF load. In addition, simulations were done at selected laser scanning conditions to predict

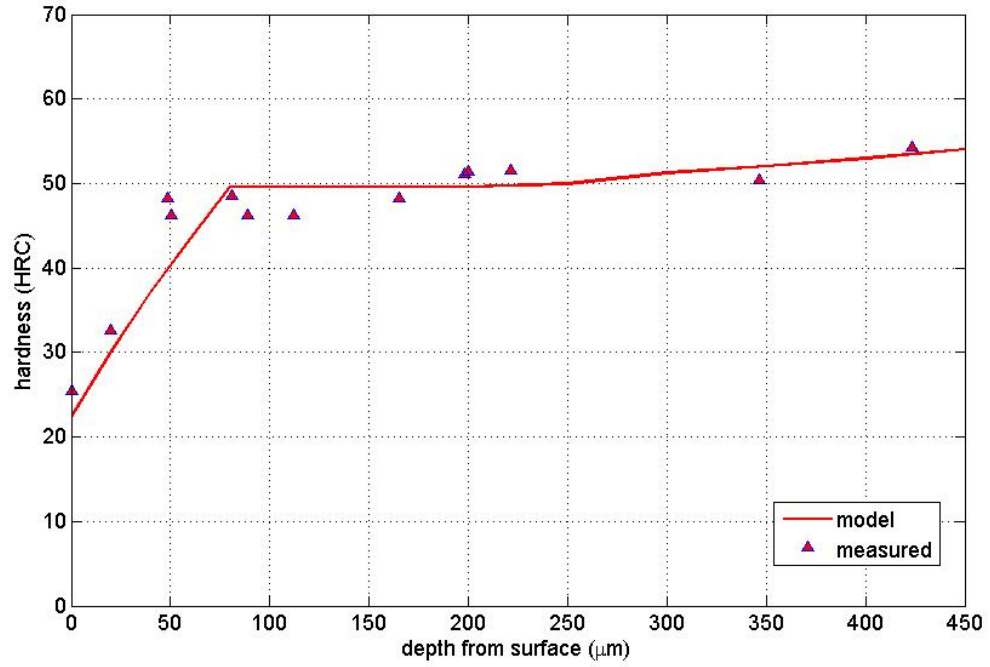
the subsurface hardness. Figure 5.12 compares the predicted hardness from the model with the measured values of hardness.

Figure 5.12 shows the effect of both scan speed and overlap on the subsurface hardness of tempered region. Four laser scanning conditions were chosen for laser-treating the samples: (a) 17.95 m/min, 93.58 % overlap, (b) 17.95 m/min, 87.22 % overlap, (c) 17.95 m/min, 75.76 % overlap, (d) 35.90 m/min, 93.58 % overlap. It can be seen that there is a good agreement between the measured and the simulated values for laser scanning conditions with 17.95 m/min scan speed. For the 35.90 m/min case, the model under-predicts the hardness by 10-20 %. This is due to the higher absorption rate assumed in the model. The surface temperature decreases with the scan speed. Consequently, the formation of oxides is reduced resulting in lower absorption rates than the assumed linear absorption range in the model. High absorptivity produced high subsurface temperatures that lead to more tempering in the model.

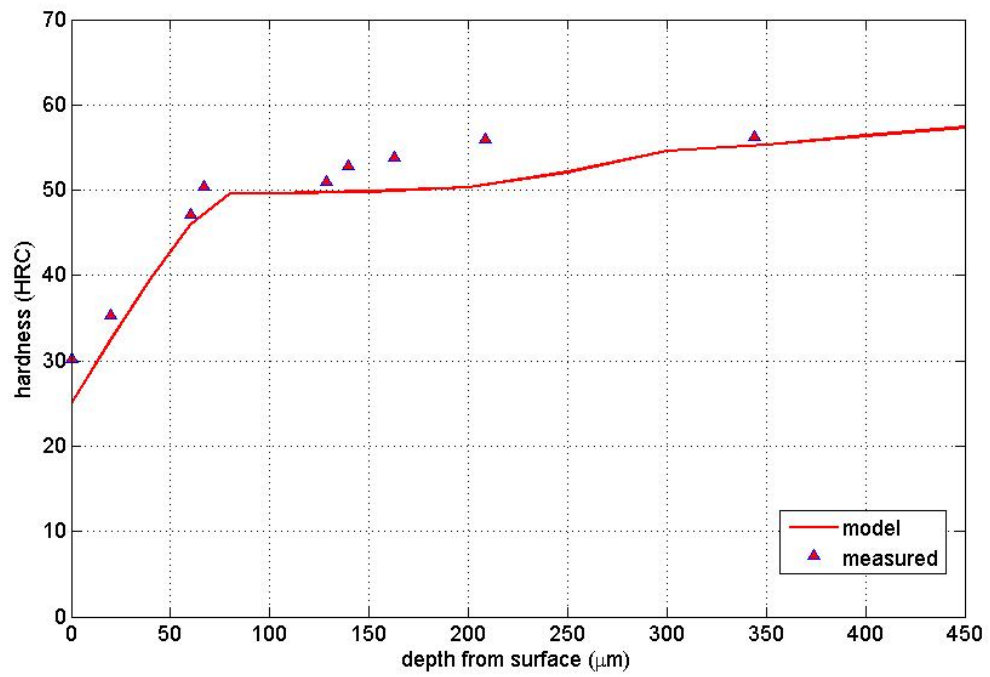
Two observations were made from the hardness measurements. First, at 17.95 m/min scan speed, the 93.58 % overlap ratio produced a larger depth of tempered layer compared to the other smaller overlap conditions. Recall that, at constant scan speed, the depth of tempered white layer increases with the overlap. On the other hand, at 93.58 % overlap, the 17.95 m/min scan speed produced a larger depth of tempering compared to the 35.90 m/min scan speed. Recall that the depth of tempered white layer was larger at the slower scan speed. As it was noted earlier, the depth of tempered white layer is an indicative measure of the depth of tempering in overlapping scans.

Furthermore, at a given heat input intensity and energy profile, larger overlaps and smaller scan speeds produce larger depths of subsurface tempering. At smaller scan speeds, the interaction time of heat input is more and therefore, more heat energy is absorbed. On the other hand, when the overlap is larger, the number of scans per unit length is larger. Heat energy is absorbed with each successive scans to cause additional tempering.

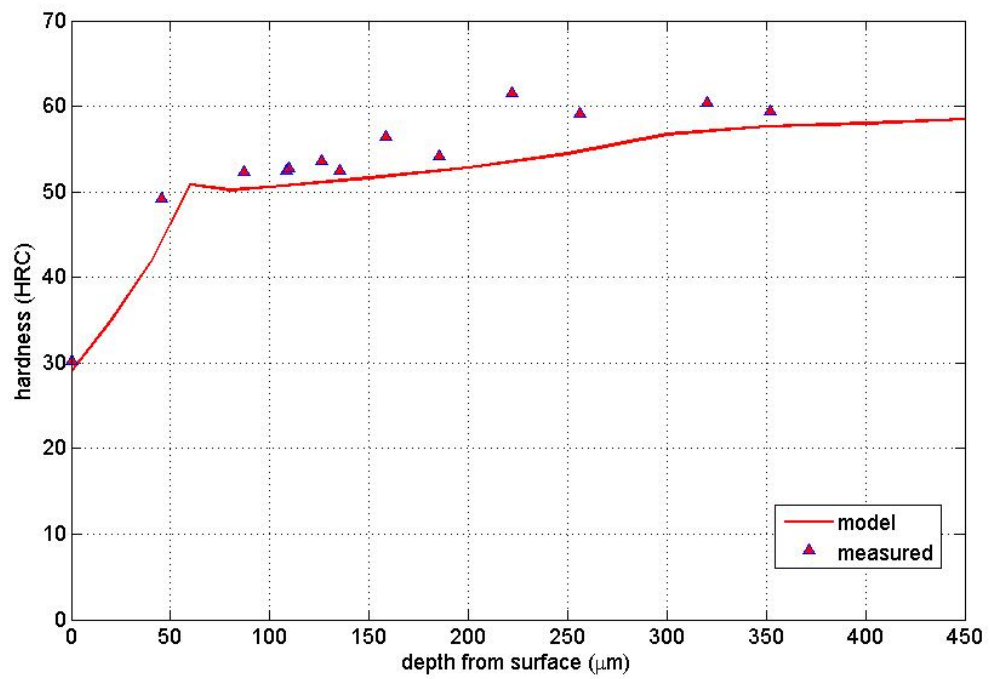
Finally, it is noted that it is possible to select the laser scanning condition that will produce a desired depth of tempering.



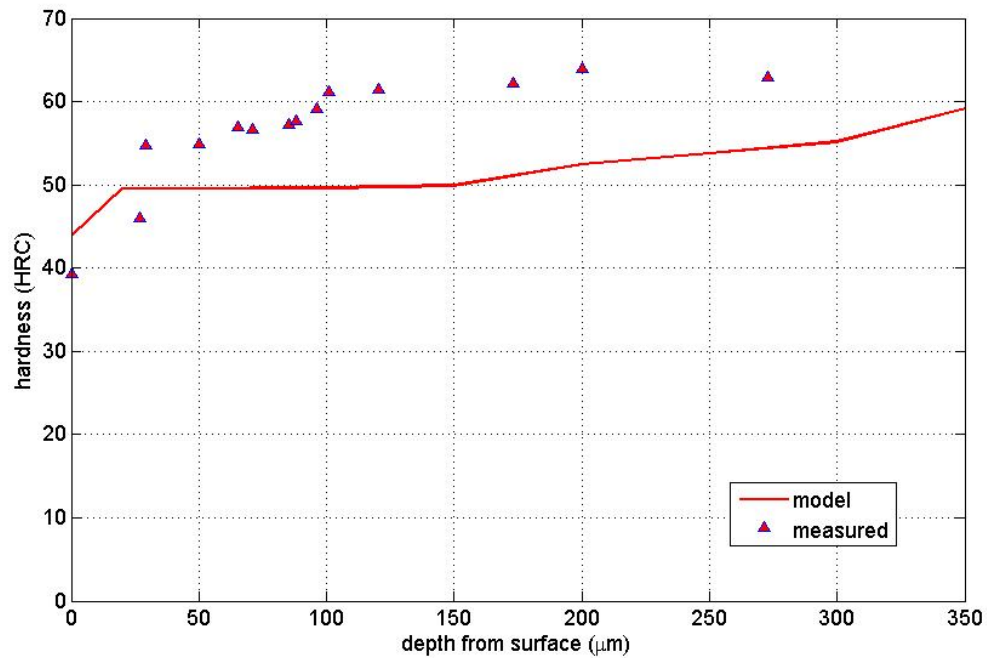
(a)



(b)



(c)



(d)

Figure 5.12: Surface and sub-surface hardness of longitudinal cross-section of AISI 52100 steel at laser scanning conditions: laser power: 800 W, spot size: 2 mm, and (a) overlap: 93.58 %, scan speed: 17.95 m/min (b) overlap: 87.22 %, scan speed: 17.95 m/min (c) overlap: 75.76 %, scan speed: 17.95 m/min (d) overlap: 93.58 % scan speed: 35.90 m/min. Data from simulation are plotted as continuous lines. Data from experiments are plotted as points.

5.4 Summary

The proposed laser tempering model was first validated. Then, the model was used to find the hardness of phase transformation region at different laser scanning conditions.

Microstructural analysis of the laser-treated AISI 52100 steel samples was presented to show the influence of laser scanning conditions to laser surface tempering. A tempered white layer forms in the subsurface region during overlapping scans. It was shown that at selected heat intensity, the depth and width of the tempered white layer is a

function of laser scanning condition. Larger overlaps and smaller scan speeds produce larger depths of tempered white layer. Finally, it was noted that the depth of tempered white layer is an indicator of the overall tempering in the workpiece. Phase analysis of the laser-treated AISI 52100 steel samples revealed that there is negligible retained austenite in the tempered subsurface region. A thin oxide layer was formed on the surface of the laser-treated specimen.

The results from the simulated model were compared with the measured values obtained from the laser treating the AISI 52100 steel at selected laser scanning condition. A good agreement was obtained between the proposed laser tempering model and the measured hardness of the tempered subsurface region. The model can be used to predict the subsurface tempered hardness for a selected laser scanning conditions or alternatively, predict the scanning conditions to produce a known depth of tempering.

CHAPTER 6

HARD TURNING APPLICATION

The second step in the laser tempering based hybrid turning process is to remove the softened subsurface region by a cutting tool. In the previous chapter, the thermo-kinetic model was demonstrated at different laser scanning conditions. In this chapter, the laser scanning parameters that yield the highest depth of tempered layer are obtained from the kinetic phase change model. Machining experiments are then performed to demonstrate the possibility of higher material removal rates and improved tool performance compared to the conventional hard turning process.

First, the experimental setup used for machining experiments is presented. In the following section, laser scanning conditions that yield larger depth of a tempered layer are identified from a phase change model discussed in Chapters 4, and 5. The selected laser parameters are used to treat the AISI 52100 samples and then machining experiments were conducted to compare the laser tempering based hybrid turning process with conventional hard turning. The tool wear performance of CBN tools, as well as low cost ceramic tools are compared in machining of hardened AISI 52100 steel (~63 HRC). In addition, cutting forces, and machined surface finish are compared for the laser tempering based hybrid turning and conventional hard turning processes.

6.1 Experimental Work

6.1.1 Cutting Tool

Two cutting tool materials were used in this work. One of the tool materials was a mixed alumina ceramic, (Kennametal KY1615 grade) with the following geometry: CNGA 432 with an 80° insert angle, -5° rake angle, -5° clearance angle, and 0.2 mm nose radius. The other tool material was the Cubic Boron Nitride (Kennametal KD050 grade)

with the following geometry: CNGA 432 with an 80° insert angle, -5° rake angle, -5° clearance angle and 0.8 mm nose radius. The nomenclatures for the two inserts are noted in Table 6.1. The inserts were held by the tool holder, Kennametal MCGNL-124B (see Appendix 8.1.7).

Table 6.1: Kennametal CBN and ceramic turning inserts - nomenclature [Kennametal].

	CBN tool, Kennametal KD050 grade (see Figure 6.1)	Ceramic tool, Kennametal KY1615 grade (see Figure 6.2)
C	insert shape: diamond (rhombic) with 80° included angle	
N	insert relief angle: 0°	
G	tolerance class of the insert inscribed circle thickness.	
A	insert has a cylindrical hole at the center. (hole size: 0.203")	
4	size of inscribed circle: 1/2"	
3	insert thickness: 3/16"	
2	defines the cutting point configuration (corner radius: 1/32 ")	
S	negative land and hone	
04	width of T-land: 0.004"	
20	T-land angle: 20	
D	two sided mini-tip	
	uncoated, no chip breakers	

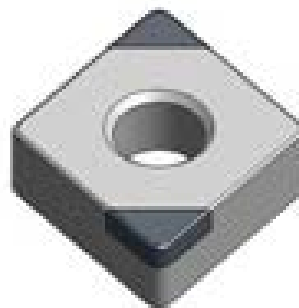


Figure 6.1: Kennametal CBN double-tipped turning insert [Kennametal]. Two cutting edges on the top side.

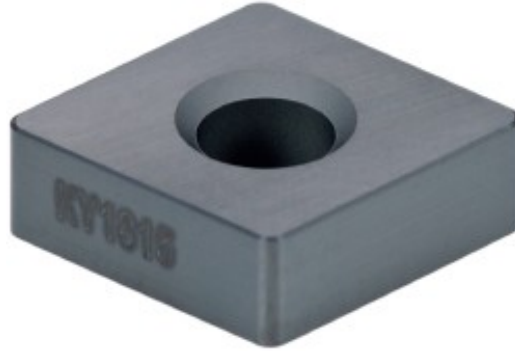


Figure 6.2: Kennametal ceramic turning insert [Kennametal]. Two cutting edges each side - top and bottom.

6.1.2 Experimental Setup

Figure 6.3 shows the experimental setup used for machining the laser treated workpiece. For comparison, the hardened steel workpiece without laser-treatment was also machined under identical conditions. Figure 6.3 is the front view of the rigid CNC lathe Hardinge T-42SP (for details, see Appendix 8.1.6).

A Kistler force dynamometer Type 9257B (for details, see Appendix 8.1.8) connected to the data acquisition system, records the cutting forces. A Kistler connecting cable Type 1687B5 connects the dynamometer to a three axis Kistler 5010 dual mode amplifier that converts the dynamometer output signal into a voltage signal. The sensitivity of the dynamometer-dual charge amplifier was set to 7.93 pC/N, 7.93 pC/N, and 3.73 pC/N for x, y, and z axis, respectively. The charge amplifier gain was set to 50 N/volt. The charge amplifiers contained a 180 kHz low pass filter that filters the output voltage signal. The data was sampled at a frequency of 1000 Hz. The frequency of the low pass filter is significantly above the sampling frequency of the acquisition system.

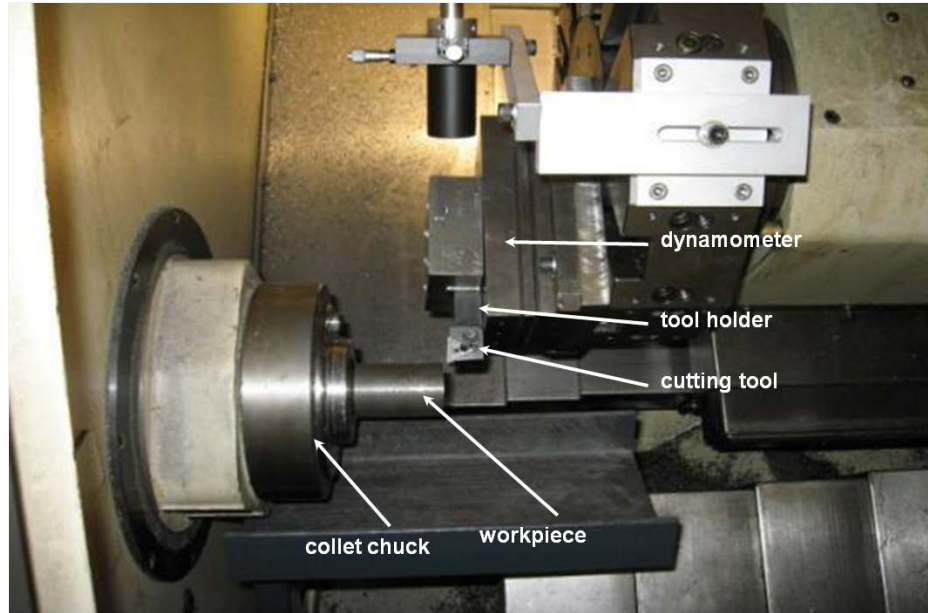


Figure 6.3: Experimental setup for turning (front view).

Tool wear was evaluated using a Leica microscope (for details, see Appendix 8.1.5). The micrographs shown in this paper were obtained from the workpiece surface, mounted as a 1 inch specimen in epoxy binder. The specimen was polished and etched using a 2 % Nital solution and observed in the Leica microscope.

Surface analysis on a machined sample was done using the Zygo NewView 200 (for details, see Appendix 8.1.8) and evaluated using the Metropro data acquisition software. The NewView 200 is a non-contact, 3D imaging surface structure analyzer that uses a white light interferometry technique to evaluate the exposed the workpiece surface. The generated profile is analyzed and visualized by the Metropro data acquisition software. The repeatability of the Zygo NewView 200 is 0.1 nm Rq.

6.2 Process Parameter Selection

6.2.1 Laser Tempering Process Parameters

The first step in the laser tempering based hybrid turning process is to lower the hardness of the steel surface through a laser tempering operation, which is accomplished

by laser scanning the workpiece using overlapping passes. By appropriately selecting the laser scanning parameters, a pre-determined depth of subsurface material can be tempered.

In order to select the process parameters for laser tempering, the model developed and validated in Chapters 4, and 5 was used. The laser intensity was kept constant by choosing a laser power of 800 W and a spot size of 2 mm. Simulations were performed keeping in mind the operating range of the experimental setup. The lowest laser scan speed possible in the experimental setup is 17.95 m/min. The scanning parameters that yielded the largest depth of tempering were selected. A larger depth of tempering implies a larger depth of material that can be removed by the tool.

Figure 6.4 shows the predicted subsurface hardness for different combinations of scan speed and overlap. It can be seen that larger overlaps and smaller scan speeds produce a larger depth of subsurface tempering. At the selected laser intensity and lowest scan speed, overlaps greater than 93.58 % produced surface melting. For the given heat input intensity, a 17.95 m/min scan speed and 93.58 % overlap produced the largest depth of tempering. In order to demonstrate higher material removal rates in the laser tempering based hybrid turning process, a scan speed of 17.95 m/min and 93.58 % overlap was chosen for laser tempering the 52100 hardened steel.

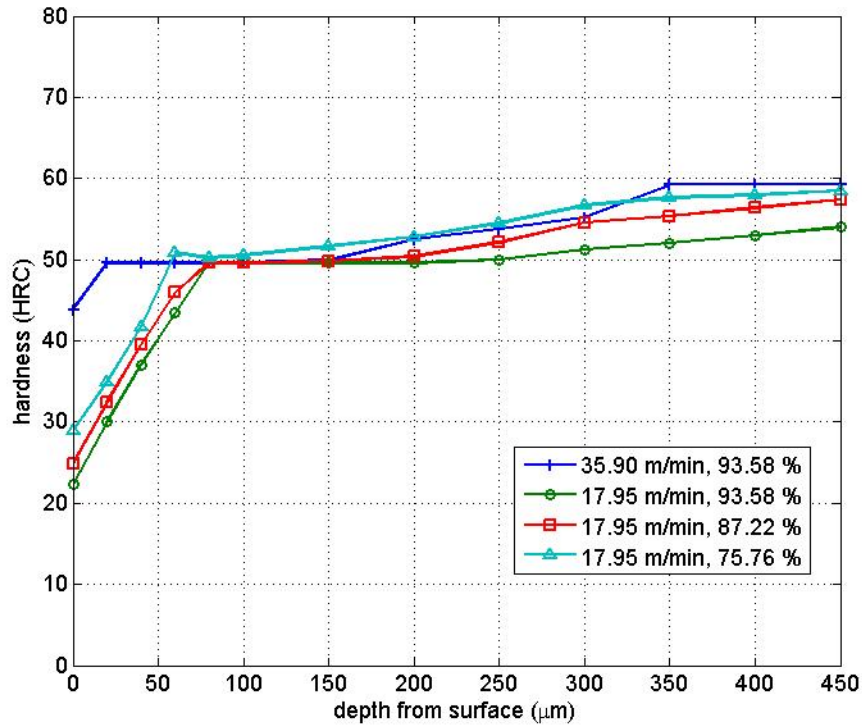


Figure 6.4: Predicted hardness vs. depth from surface for varying scan speeds (m/min) and overlap ratios (%) at constant laser intensity (laser power: 800 W, spot size: 2 mm).

6.2.2 Machining Parameters

In this work, the cutting speed and cutting depth were chosen to demonstrate a higher material removal rate in the laser tempering based hybrid turning process, while the feed was kept constant at 0.10 mm/rev. The selected laser scanning condition produced softening up to a depth of 0.3 mm. A maximum cutting speed of 130 m/min was selected based on the manufacturer’s recommendations for the cutting tool. Conventional hard turning, where the sample is not laser-treated, was also carried out under similar cutting conditions in order to compare the process with laser tempering based hybrid turning.

Three experiments were conducted to compare the laser tempering based hybrid turning with conventional hard turning. The first experiment (Expt. 1 in Table 6.2) demonstrates that CBN tools exhibit a longer life in laser tempering based hybrid turning over that in conventional hard turning. In addition, a cutting speed of 180 m/min was used to evaluate the tool performance at high material removal rates. The second and third experiment (Expts. 2 and 3 in Table 6.2) were intended to demonstrate the potential savings in tooling cost with laser tempering based hybrid turning process. Specifically, the behavior of the ceramic tool in the laser tempering based hybrid turning process is compared with the behavior of CBN tool in conventional hard turning to show the possibility that a low cost ceramic tool can potentially replace the CBN tool without comprising tool life or material removal rate.

Table 6.2: Experiment matrix.

Expt.	Cutting tool	Process (Conv: conventional hard turning; LT: laser tempering based hybrid turning)	Feed (mm/rev)	Cutting speed (m/min)	Cutting depth (mm)
1	CBN	LT	0.10	180	0.3
	CBN	Conv	0.10	180	0.3
2	ceramic	LT	0.10	130	0.3
	CBN	Conv	0.10	130	0.3
3	ceramic	LT	0.10	130	0.2
	CBN	Conv	0.10	130	0.2

6.3 Experimental Procedure

Two AISI 52100 cylindrical bars, one for each process, were considered for each experiment. In the laser tempering based hybrid turning process, the workpiece was first laser-treated (see Figure 6.5) to produce a tempered subsurface region, which was subsequently turned.

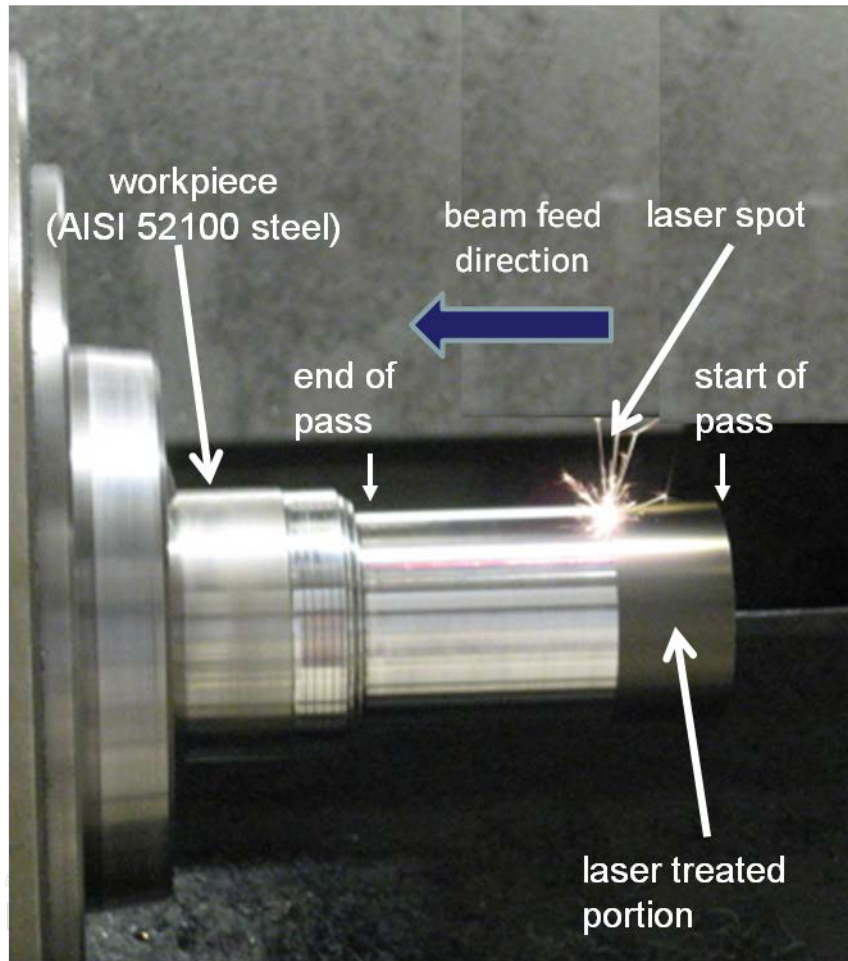


Figure 6.5: Laser treatment of AISI 52100 steel workpiece.

Single pass, dry turning experiments were conducted to compare the laser tempering based hybrid turning process with conventional hard turning. The length of each machining pass was kept between 50.8 and 76.2 mm (2 and 3 inches). The turning experiments, were conducted at room temperature. In the laser tempering based hybrid turning process, after each pass, the workpiece was machined to a sufficient depth, such that the effect of previous laser scans was removed and the hardness verified to be equal to the original surface hardness.

Figures 6.6 and 6.7 show the rake face of CBN and ceramic tools, respectively, prior to the machining experiments.

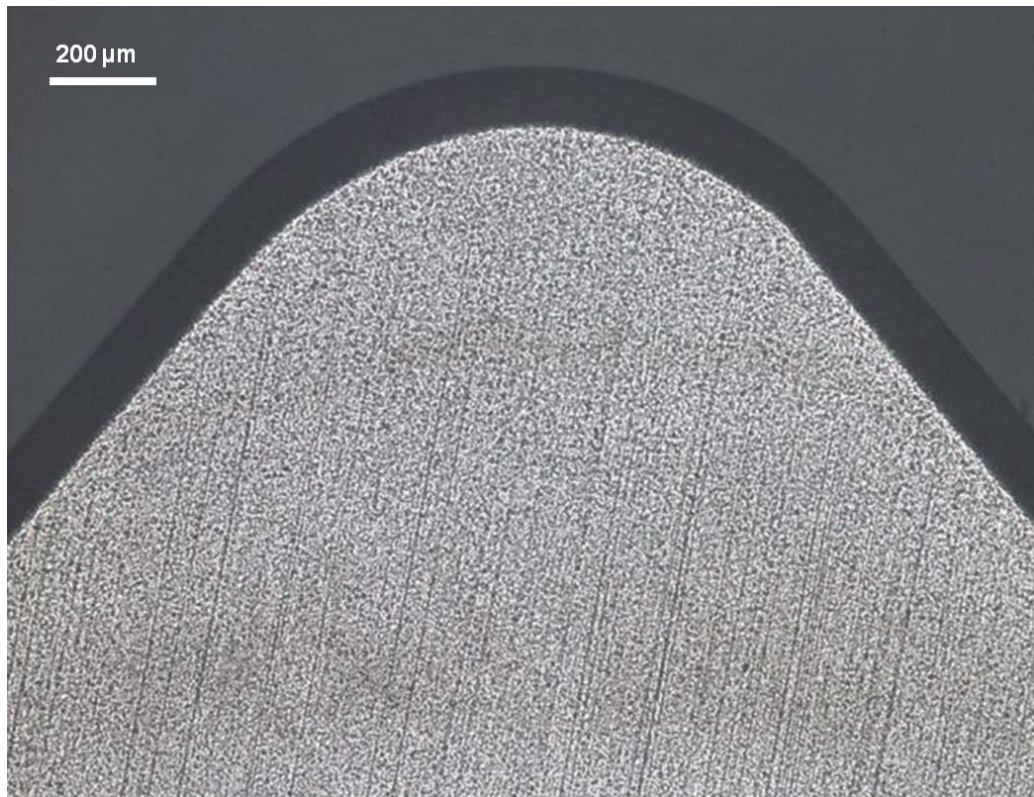


Figure 6.6: Rake face of CBN tool (top view).

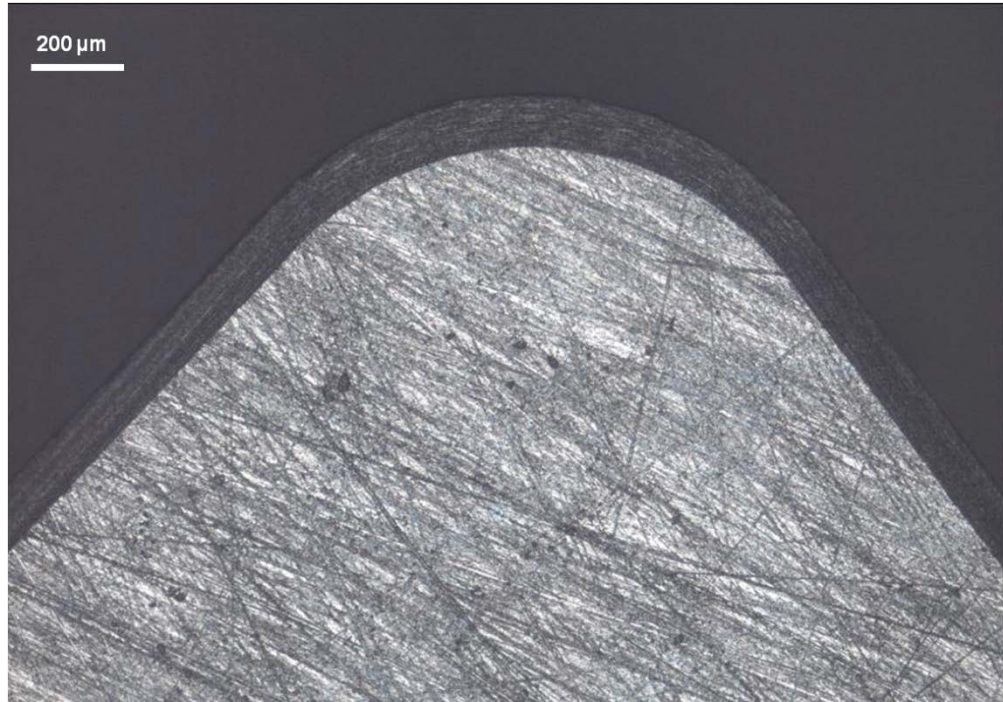


Figure 6.7: Rake face of ceramic tool (top view).

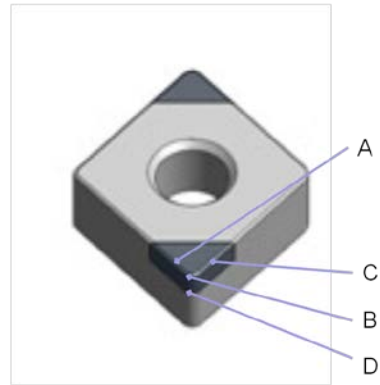
6.3.1 Machinability Metrics

In each experiment in Table 6.2, tool wear, cutting force, and surface finish were the measured responses for comparing the two process variants. The progression of the first two responses is compared. For the third response, the finish produced by the new tool, i.e., after the first machining pass, is compared.

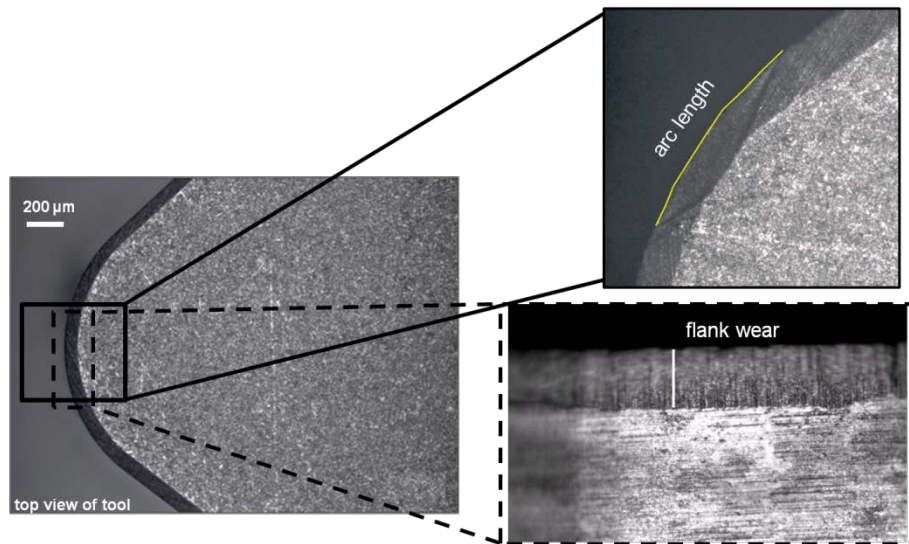
Tool wear was characterized by two parameters: arc length (arc A-B-C in Figure 6.8(a)) and flank wear (line B-D in Figure 6.8(a)). Arc length is a measure of the length of the wear curve on the rake face and around the insert nose. A minimum of fifteen measurements were made along the perimeter of the wear region (see Figure 6.8(b)). For each experiment, tool wear curves for the arc length and mean flank wear are plotted vs. time. The standard deviation bar represents the variation of these measurements after each pass along the width of the measured region.

The radial and tangential forces were recorded for each machining pass and their average values are reported in this work. A representative profile of the cutting forces is

shown in Figure 6.9. Average force value is the average of the force values in the tool/workpiece engagement time.



(a)



(b)

Figure 6.8: Tool wear characterization: arc length and flank wear

(a) illustration, (b) representative tool wear.

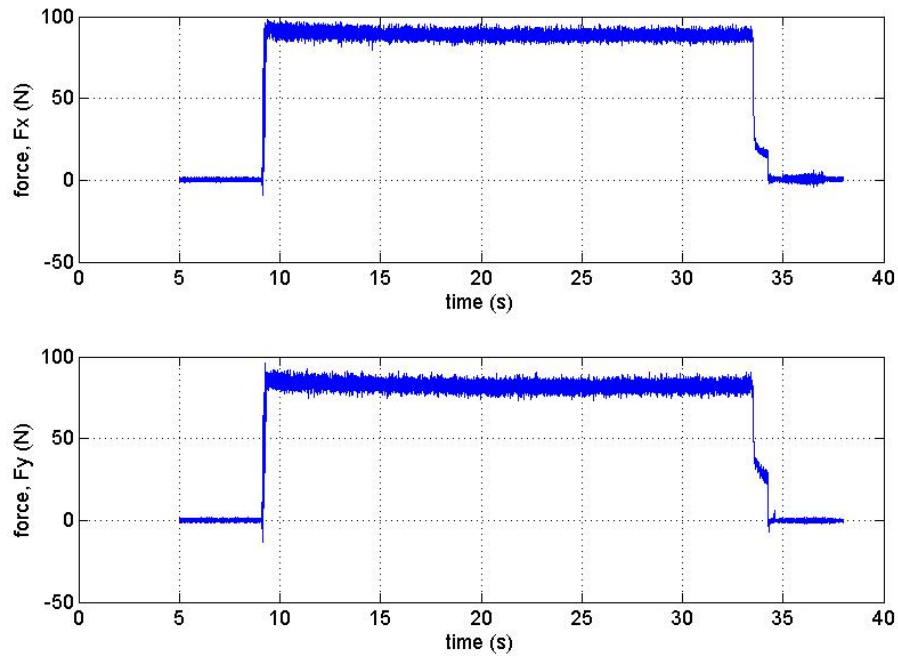


Figure 6.9: Representative cutting force profiles.

The surface of the machined workpiece was analyzed using the NewView200 surface analyzer. Surface roughness values were recorded at ten locations around the circumference of each machined workpiece to assess the variability of the surface roughness in the two approaches. A representative surface profile and the surface roughness parameters are shown in Figure 6.10 and Table 6.3, respectively. In this work, the surface roughness parameter (R_a) and peak-to-valley height parameter (R_t) were compared for the surface of the laser treated sample with the conventional process. The values correspond to the machined surface finish produced by the tool after the first machining pass.

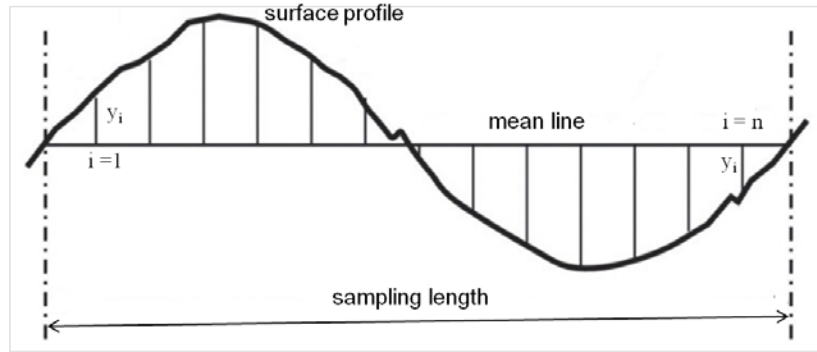


Figure 6.10: Representation of surface roughness profile.

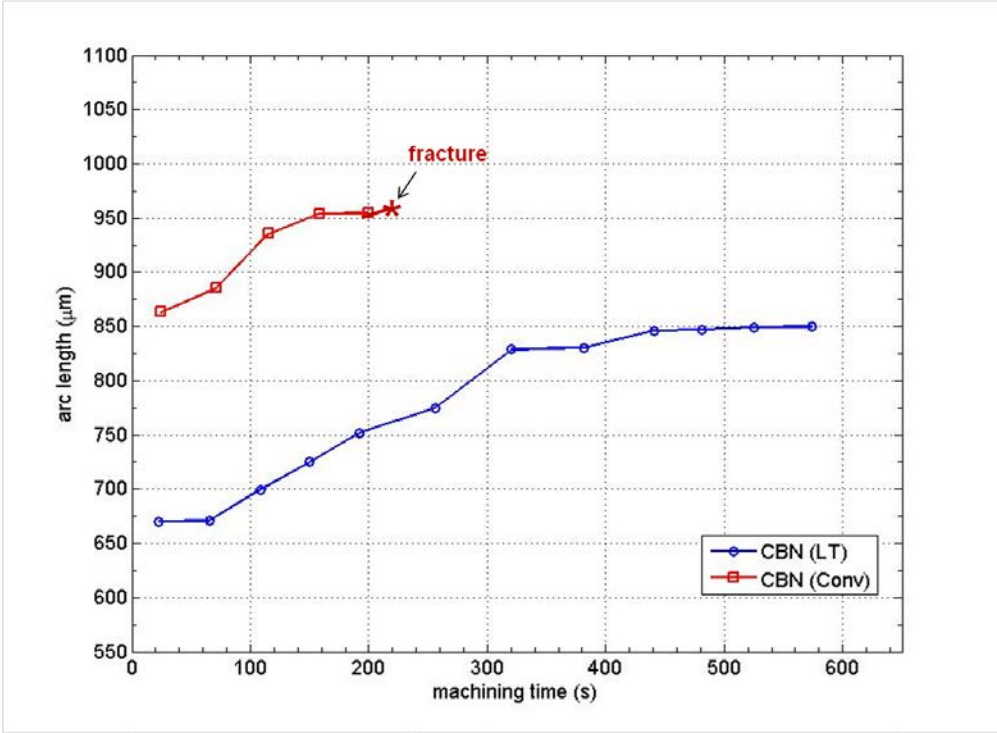
Table 6.3: Surface roughness parameters [Zygo].

Surface roughness parameter	Roughness parameter description	Formula (y_i as noted in Figure 6.7)
R_a	arithmetic average of absolute values	$R_a = \frac{1}{n} \sum_{i=1}^n y_i $
R_{rms} or R_q	root mean squared	$R_{rms} = \sqrt{\frac{1}{n} \sum_{i=1}^n y_i^2}$
R_p	maximum peak height	$R_p = \max y_i$
R_v	maximum valley depth	$R_v = \min y_i$
R_{p-v} or R_t	peak-to-valley height	$R_t = R_p - R_v$
R_z	average of peak-to-valley height over a samples, s over a sampling length	$R_z = \frac{1}{s} \sum_{i=1}^s R_{t_i} $
R_{sk}	skewness	$R_{sk} = \frac{1}{nR_{rms}^3} \sum_{i=1}^n y_i^3$
R_{ku}	kurtosis	$R_{sk} = \frac{1}{nR_{rms}^4} \sum_{i=1}^n y_i^4$

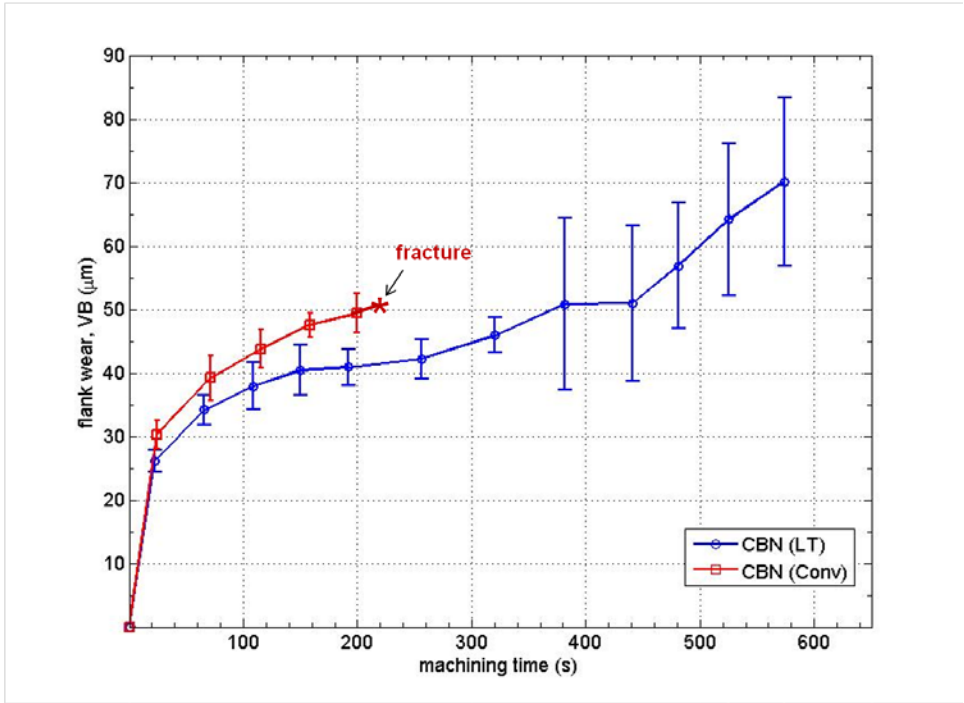
6.4 Results and Discussion

6.4.1 Tool Wear

Figure 6.11 compares the wear progression of the CBN tool, in Expt. 1, in the laser tempering based hybrid turning process and the conventional hard turning processes for Expt. 1. The CBN tool in the laser tempering based hybrid turning case shows reduced arc length of wear around the tool nose (see Figure 6.11(a)) and flank wear (see Figure 6.11(b)). The initial arc length in the conventional hard turning was $\sim 863.3 \mu\text{m}$, about 30 % more than the initial arc length in the laser tempered case. It is also noted that the arc length of wear in the CBN tool in laser tempering based hybrid turning after 526 s of machining was less than the initial arc length of wear in the CBN tool in conventional hard turning. The CBN tool in conventional hard turning fractured after ~ 235 s, while the CBN tool did not fail even after ~ 526 s of cutting. At the instant of tool failure in conventional hard turning, the mean flank wear of the tool in laser tempering based hybrid turning was less.



(a)

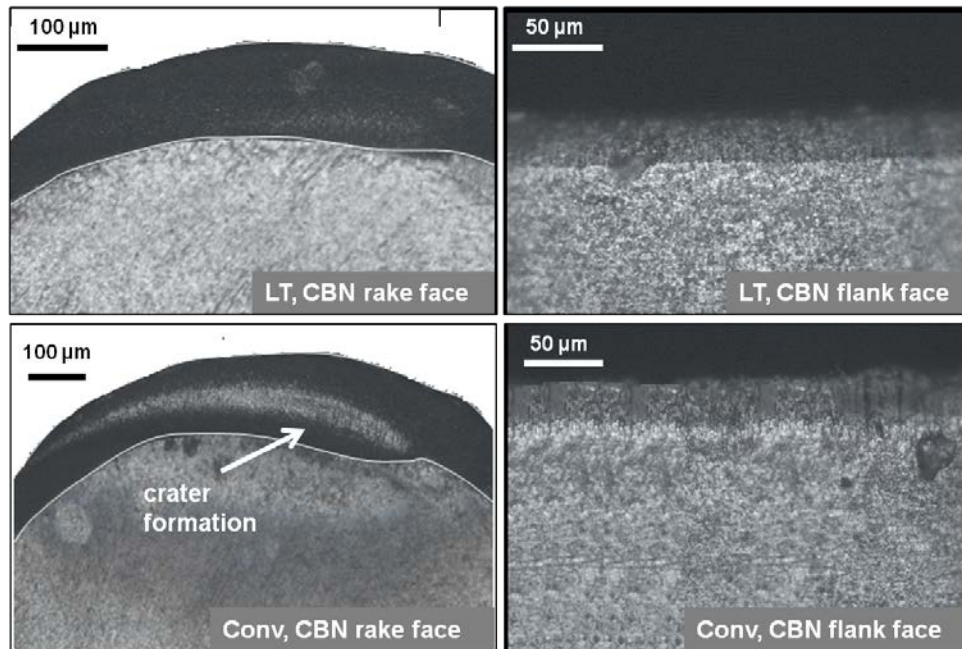


(b)

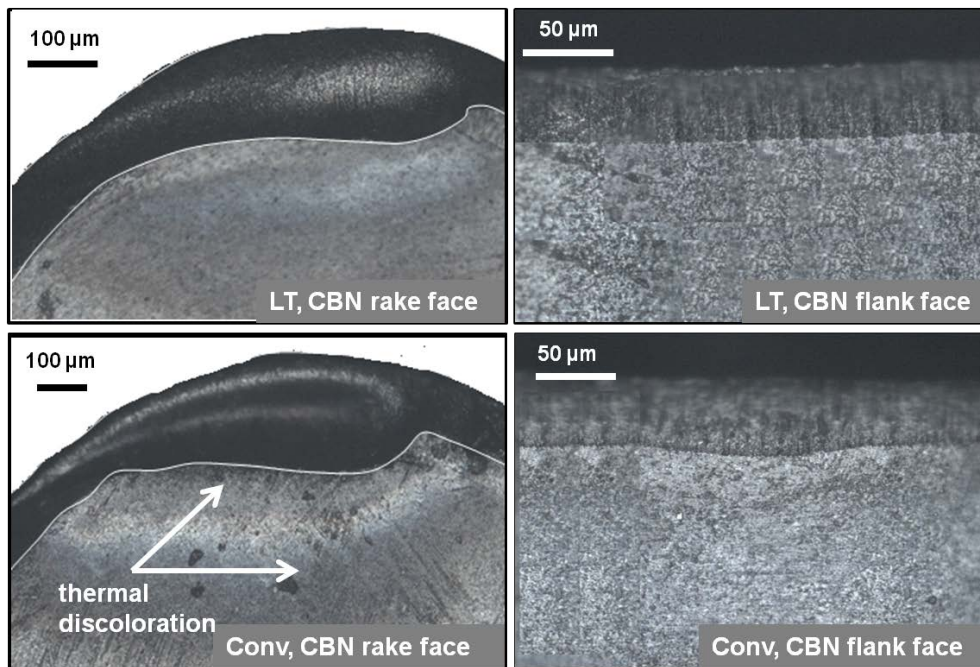
Figure 6.11: CBN tool wear (a. arc length, b. flank wear) progression in laser tempering based hybrid turning (LT) and conventional hard turning (Conv). Error bars represent 1 std. dev. of the wear measurements. (depth of cut: 0.3 mm, cutting speed: 180 m/min, feed: 0.10 mm/rev).

Figure 6.12 compares the CBN tool condition in laser tempering based hybrid turning with conventional hard turning at various time instants. It can be clearly seen (see Figure 6.12(a)) that a crater forms on the rake face much earlier in the conventional hard turning because of the higher hardness. Additionally, thermal discoloration (see Figure 6.12(b)) is seen on the rake face of the CBN tool in conventional hard turning case most likely due to high cutting temperatures. In conventional hard turning, the wear of the tool continues at a higher rate in each machining pass leading to catastrophic failure through fracture. The fractured CBN tool in the conventional hard turning process is shown in Figure 6.12(c). This was also evident from the measurements of arc length of wear around the tool nose (see Figure 6.11(a)).

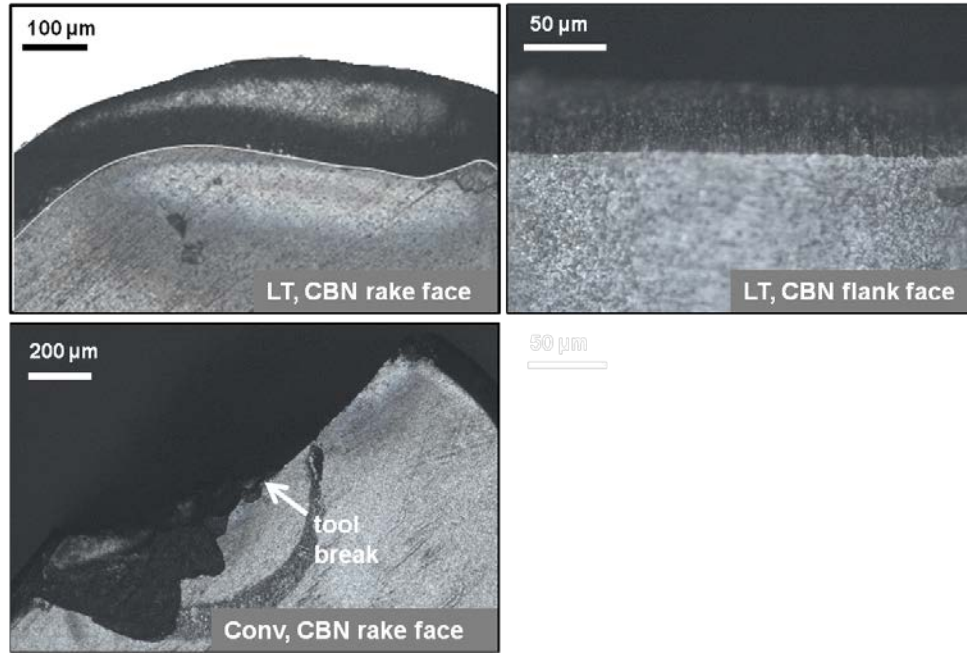
Figure 6.13 shows the CBN tool in laser tempering based hybrid turning, which exhibited more gradual wear than the conventional case, even after 526 s of machining.



(a)



(b)



(c)

Figure 6.12: CBN tool wear in laser tempering based hybrid turning (LT) and conventional hard turning (Conv) after (a) ~22 s, (b) ~151 s, (c) ~235 s, of machining. (depth of cut: 0.3 mm, cutting speed: 180 m/min, feed: 0.10 mm/rev).

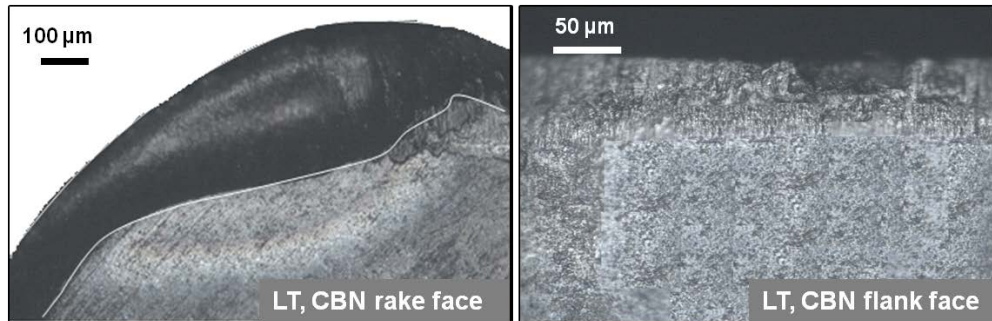


Figure 6.13: CBN tool wear in laser tempering based hybrid turning (LT) after 526 s of machining (depth of cut: 0.3 mm, cutting speed: 180 m/min, feed: 0.10 mm/rev).

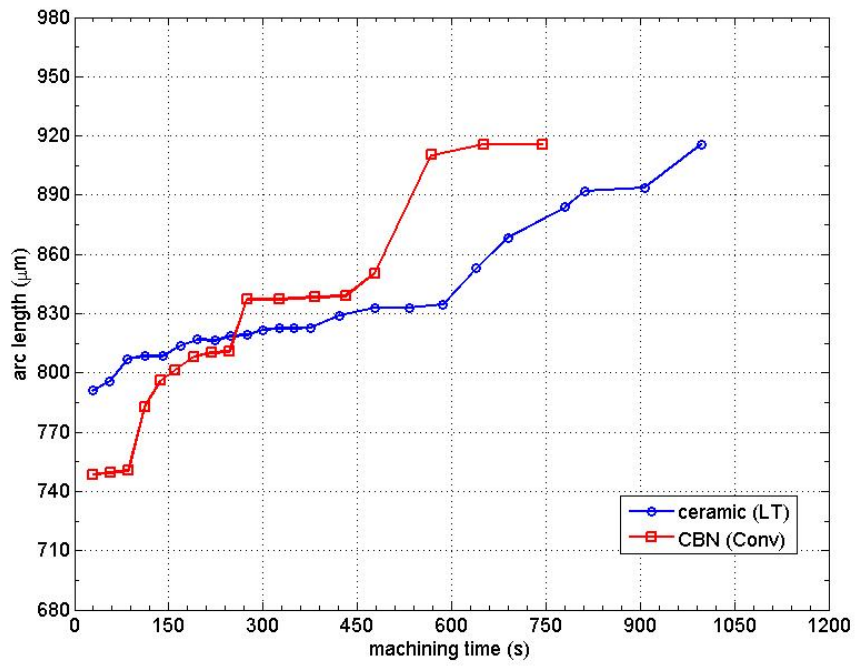
Note that Expt. 1 used a cutting speed and depth that was higher than the values recommended by the tool manufacturer. This shows that higher material removal ratlaser tempering without compromising tool life.

In Expts. 2 and 3, a low cost ceramic (Al_2O_3) tool was used to machine the laser tempered workpiece. This was done to investigate the possibility of replacing the expensive CBN tool in hard turning and thereby lowering the cost of the cutting process.

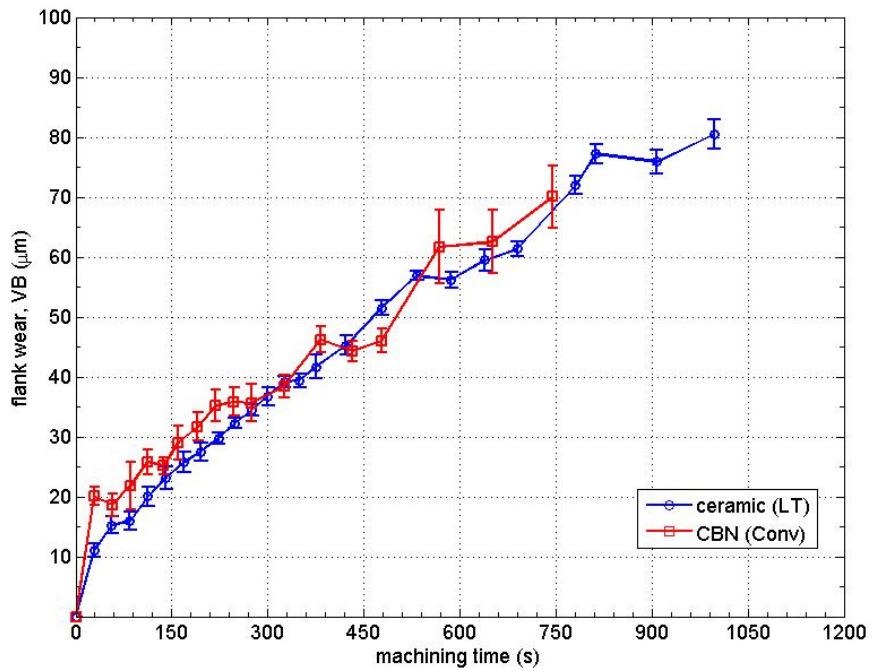
Note that a cutting speed of 130 m/min and a feed of 0.10 mm/rev were chosen based on the initial experiments and also in reference to the cutting conditions recommended by the tool manufacturer. Two depths of cut, 0.2 mm and 0.3 mm, were used in the experiments. For each depth of cut, tool wear in the laser tempering based hybrid process is compared to the performance of the CBN tools in the conventional process.

Figure 6.14 compares the tool wear progression for the ceramic tool in the laser tempering based hybrid turning process in comparison to the CBN tool in the conventional process. Figure 6.14(a) shows the progression of the arc length of wear around the tool nose. Though the ceramic tool in the laser tempering based hybrid case started with a somewhat higher initial arc length around the tool nose, the rate of progression of the arc length was smaller than the CBN tool. It can be seen that the rate of tool wear progression for the CBN tool is non-uniform and overtakes the wear of the ceramic tool as the test progresses.

Both tools show comparable flank wear (see Figure 6.14(b)). However, it can be seen that the mean flank wear width is more uniform for the ceramic tool in the laser tempering based hybrid turning case than for the CBN tool in the conventional hard turning case (see the 1σ error bars in Figure 6.14(b)). In addition, it can be seen that the wear progression for the ceramic tool is slightly less erratic than the CBN tool in the conventional process.



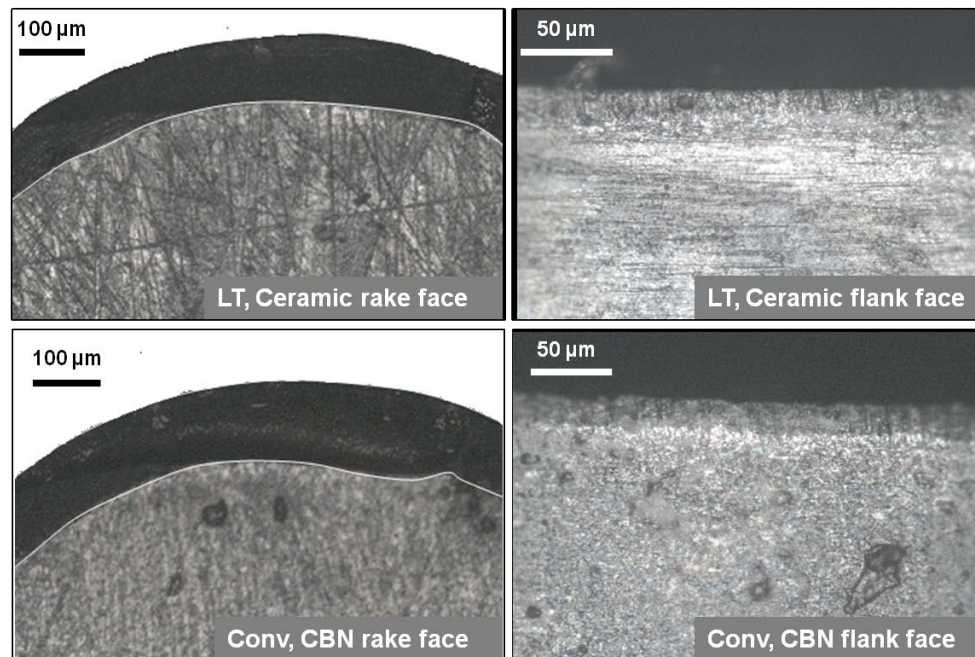
(a)



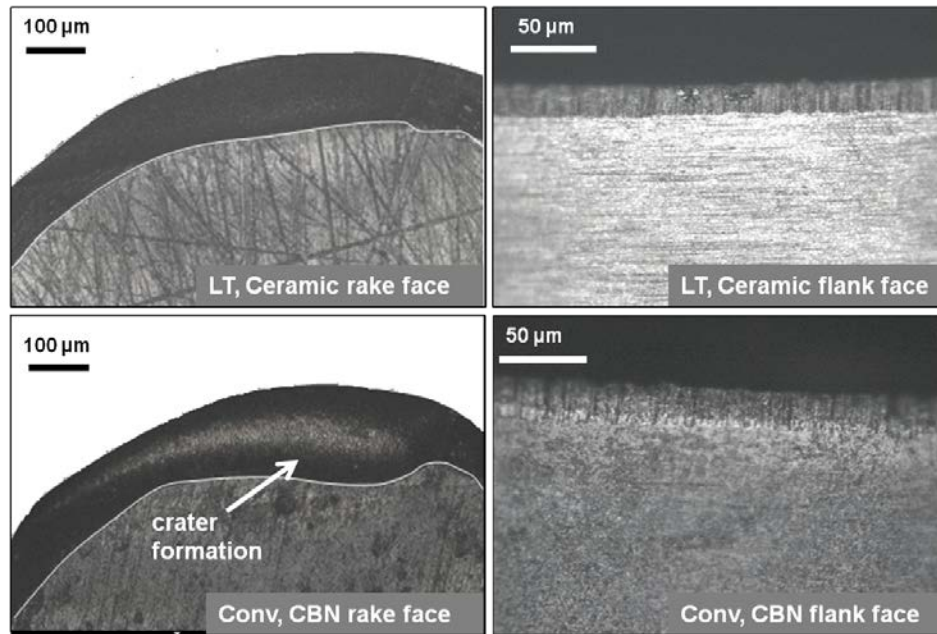
(b)

Figure 6.14: Tool wear (a. arc length, b. flank wear) progression in laser tempering based hybrid turning (LT) and in conventional hard turning (Conv). Error bars represent 1 std. dev. of the wear measurements. (depth of cut: 0.3 mm, cutting speed: 130 m/min, feed: 0.10 mm/rev).

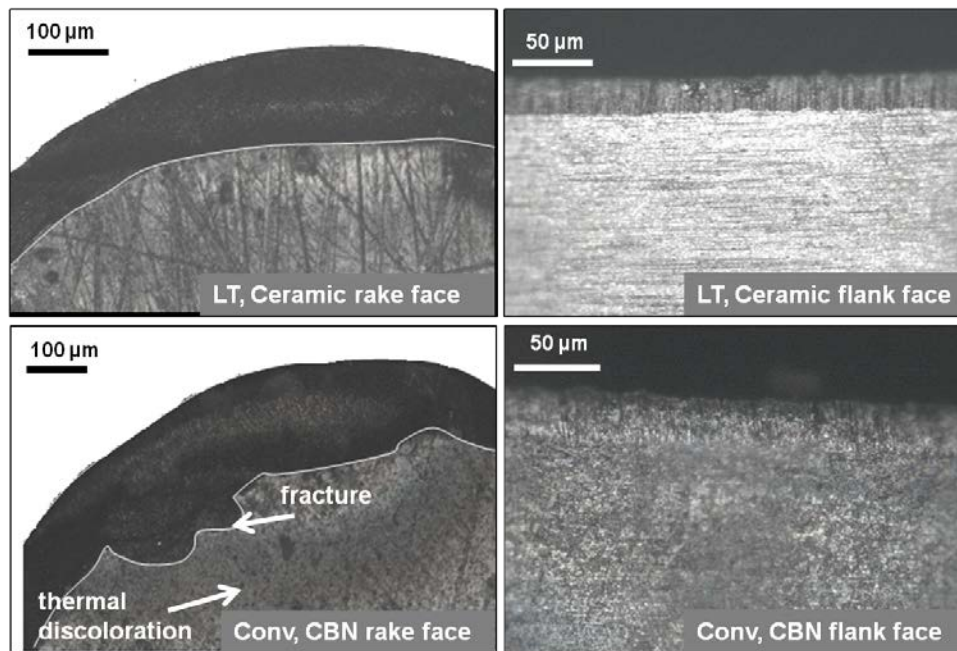
Figure 6.15 compares the condition of the ceramic and CBN tools at various stages of machining. In the conventional process, the CBN tool developed a crater on the rake face (see Figures 6.15(a) and (b)) early in the process, which was followed by initial fracture at ~115 s (see Figure 6.15(c)) and extensive fracture at ~170 s (see figure 6.15 (d)). Figure 6.16 shows the ceramic tool condition after ~639 s of machining.



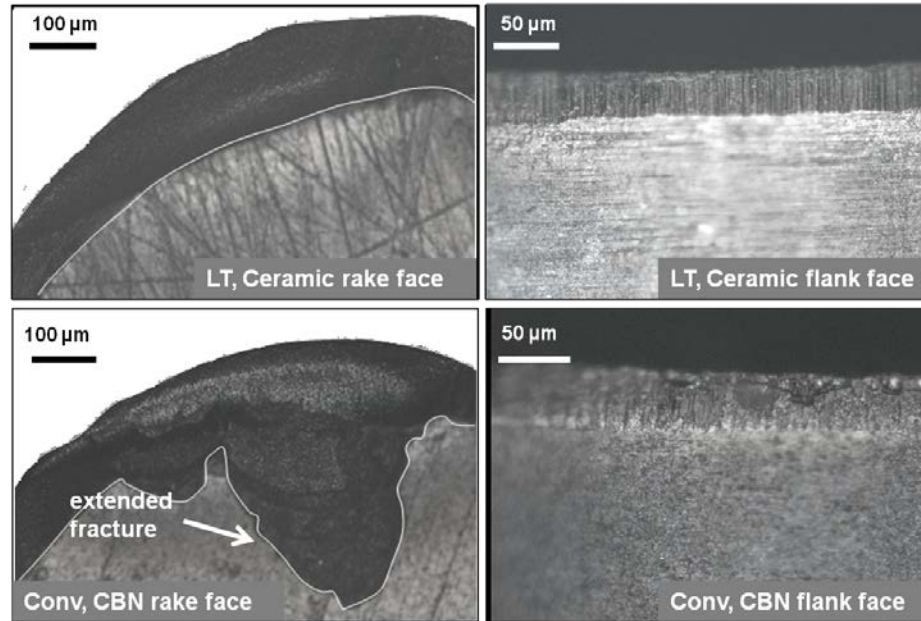
(a)



(b)



(c)



(d)

Figure 6.15: Ceramic tool wear in laser tempering based hybrid turning (LT) and CBN tool wear in conventional hard turning (Conv): (a) ~29 s, (b) ~84 s, (c) ~115 s, (d) ~170 s, of machining. (depth of cut: 0.3 mm, cutting speed: 130 m/min, feed: 0.10 mm/rev).

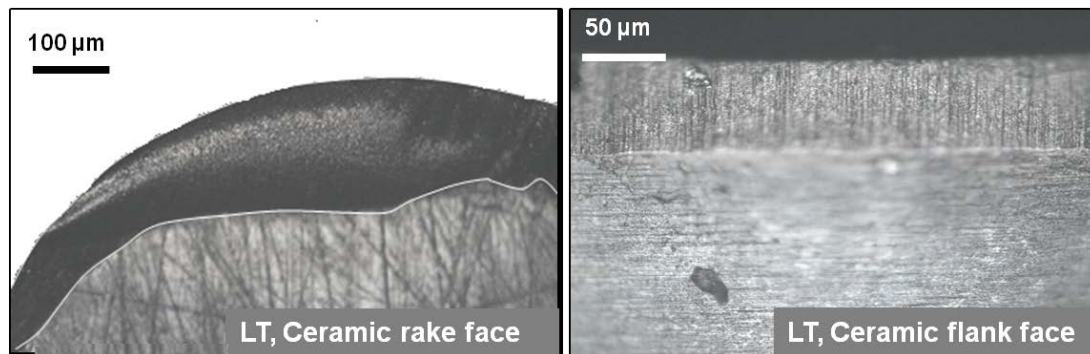


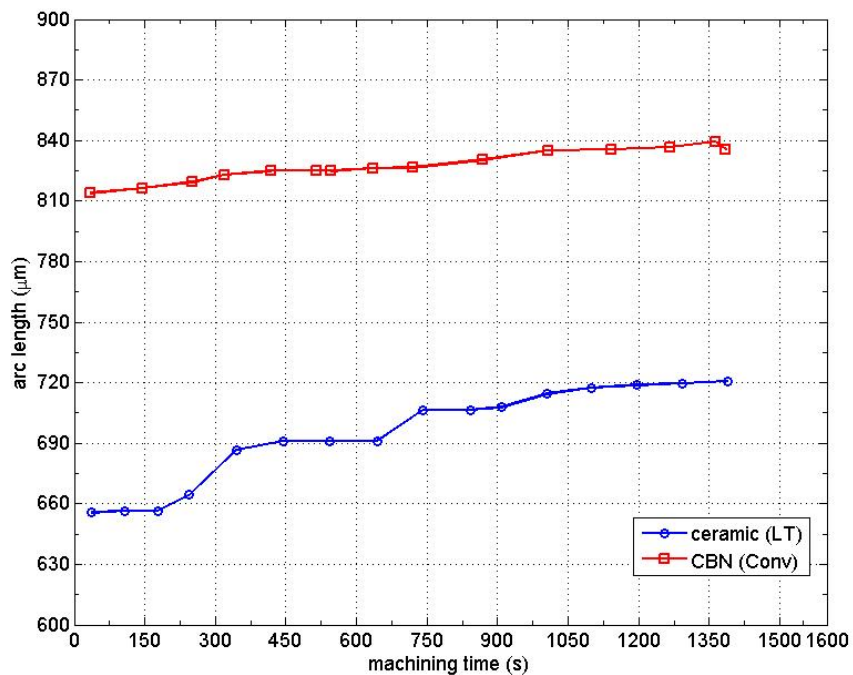
Figure 6.16: Ceramic tool wear in laser tempering based hybrid turning (LT) after ~639 s of machining. (depth of cut: 0.3 mm, cutting speed: 130 m/min, feed: 0.10 mm/rev).

Figure 6.17 compares the wear curves for the two tool materials in Expt. 3, which has a lower depth of cut (0.2 mm) than Expt. 2. Other experimental conditions including

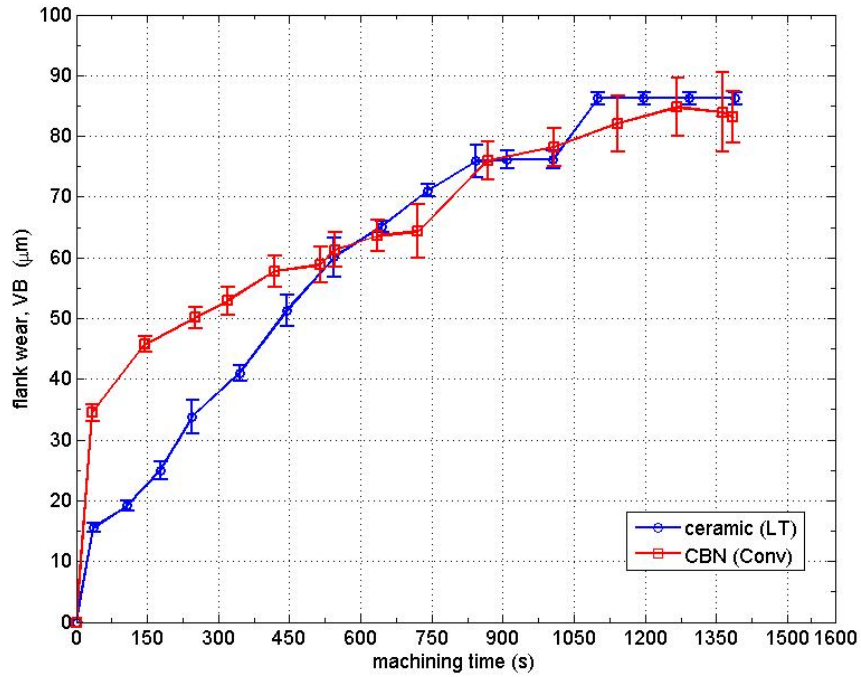
the depth of laser tempering are the same as in Expt. 2. It can be seen from Figure 6.17(a) that the arc length around the tool nose is smaller for the ceramic tool in the laser tempered case compared to the CBN tool in the conventional case. The flank wear behavior (Figure 6.17(b)) for the ceramic tool is lower than the CBN tool till ~600 s, after which it exceeds the CBN tool wear.

Figure 6.18 compares the images of the ceramic tool in the laser tempering based hybrid process with the condition of the CBN tool in the conventional hard turning at various stages of machining.

Summarizing, three important observations are noted in regards to laser tempering based hybrid turning process: (i) higher material removal rates due to softened material in the cutting zone which lowers the cutting forces (discussed in the following section) and consequently, the cutting temperatures, (ii) improved tool life due to uniform and gradual wear along the flank and the nose of the cutting tool, and (iii) the low-cost ceramic tools can potentially replace the CBN tools without compromising the material removal rates.

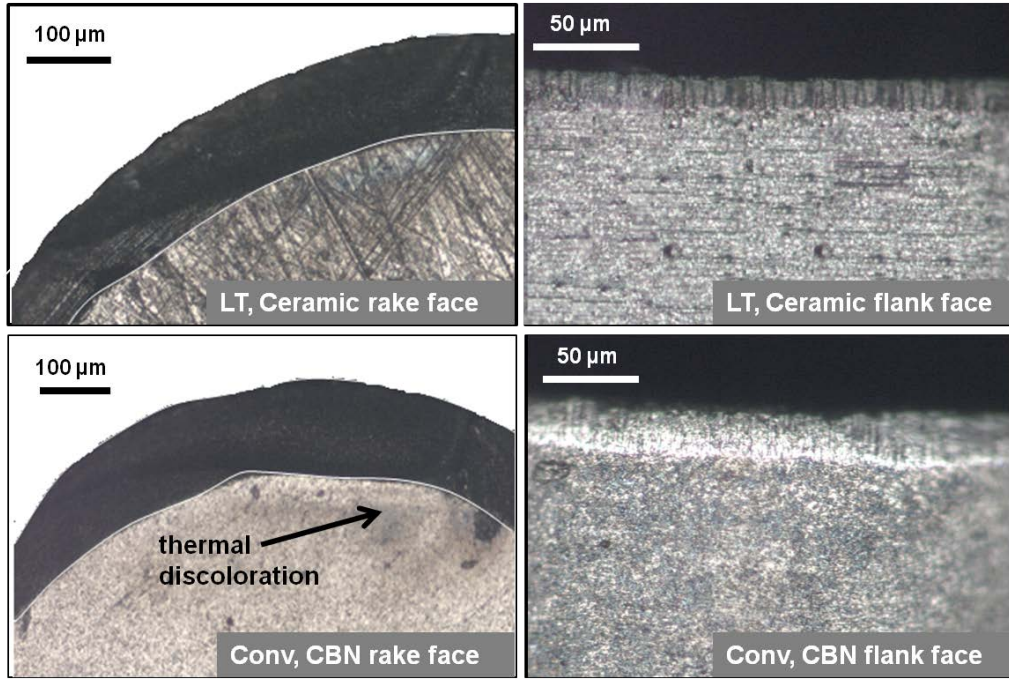


(a)

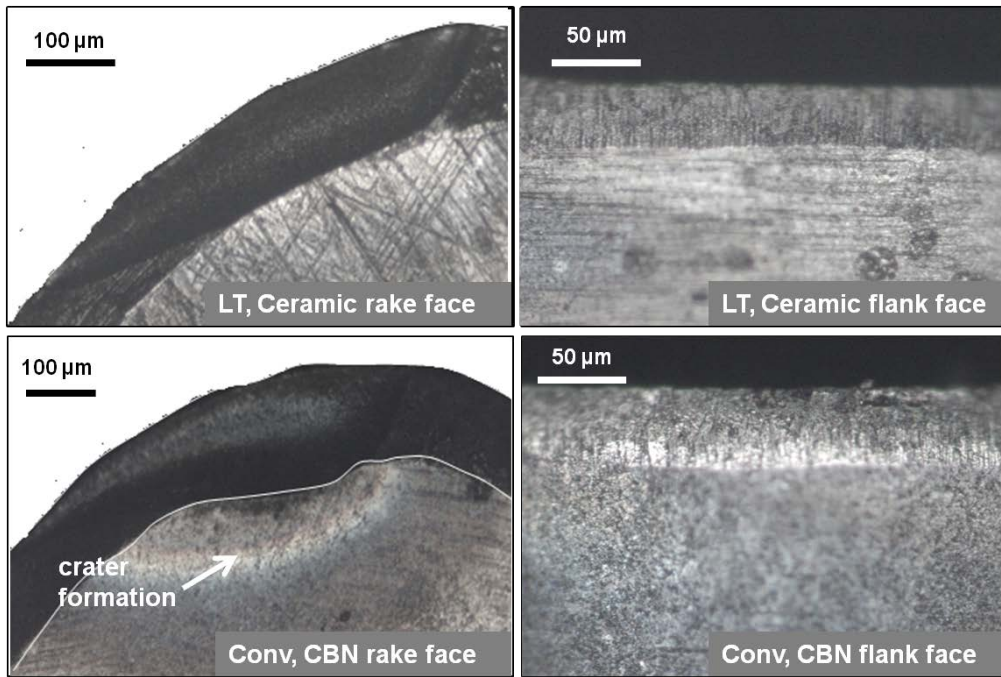


(b)

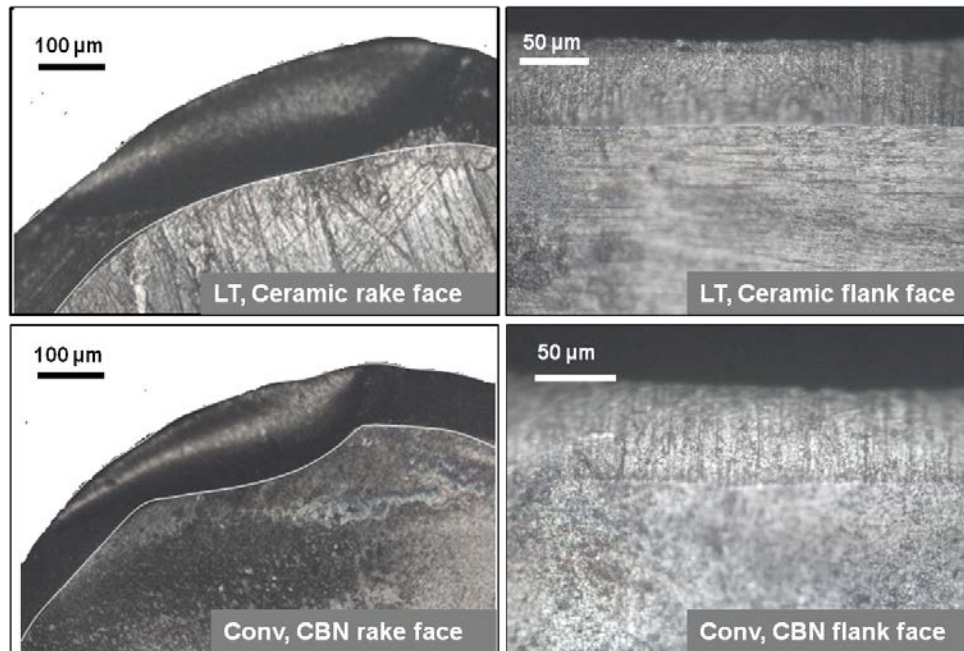
Figure 6.17: Tool wear (a. arc length, b. flank wear) progression in laser tempering based hybrid turning (LT) and conventional hard turning (Conv). Error bars represent 1 std. dev. of the wear measurements. (depth of cut: 0.2 mm, cutting speed: 130 m/min, feed: 0.10 mm/rev).



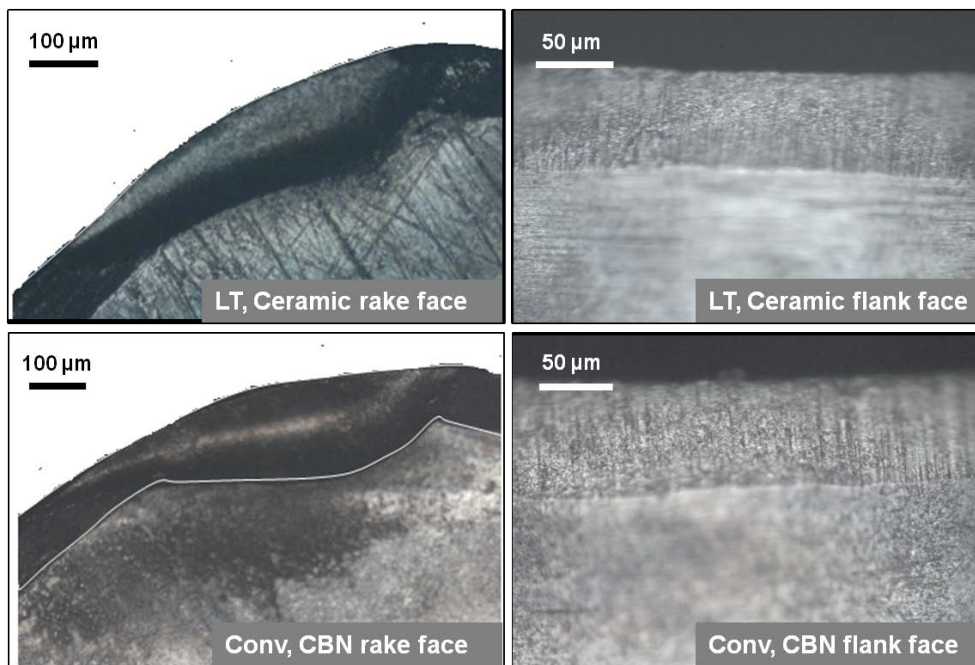
(a)



(b)



(c)



(d)

Figure 6.18: Ceramic tool wear in laser tempering based hybrid turning (LT) and CBN tool wear in conventional hard turning (Conv): (a) ~25 s, (b) ~245 s, (c) ~643 s, (d) ~1264 s, of machining. (depth of cut: 0.2 mm, cutting speed: 130 m/min, feed: 0.10 mm/rev).

6.4.2 Cutting Forces

The radial and tangential forces were averaged over the length of each machining pass. Figures 6.19 and 6.20 show the progression of the average tangential and radial forces in the three experiments. Figure 6.19 compares the cutting forces in Expt. 1 for both the process variants. It can be clearly seen that the forces are lower in the laser tempering based hybrid case than in the conventional hard turning process. This confirms the reduction in hardness of the material due to laser tempering. Similar observations can be made in the force results for Expts. 2 and 3 (see Figure 6.20).

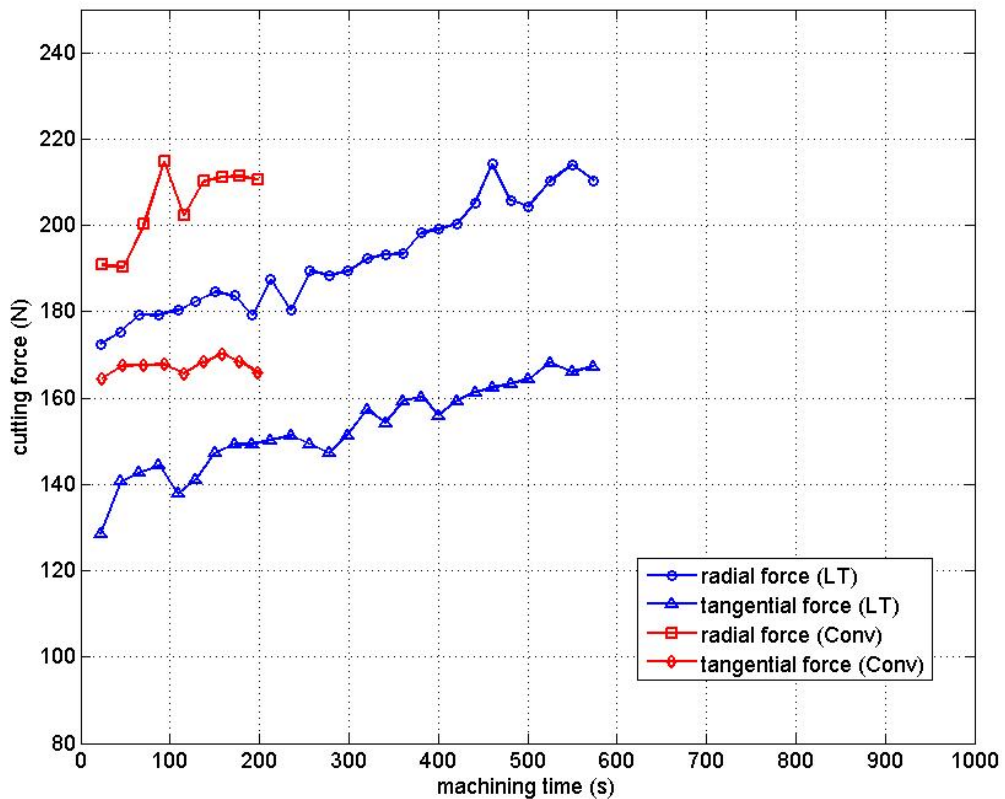
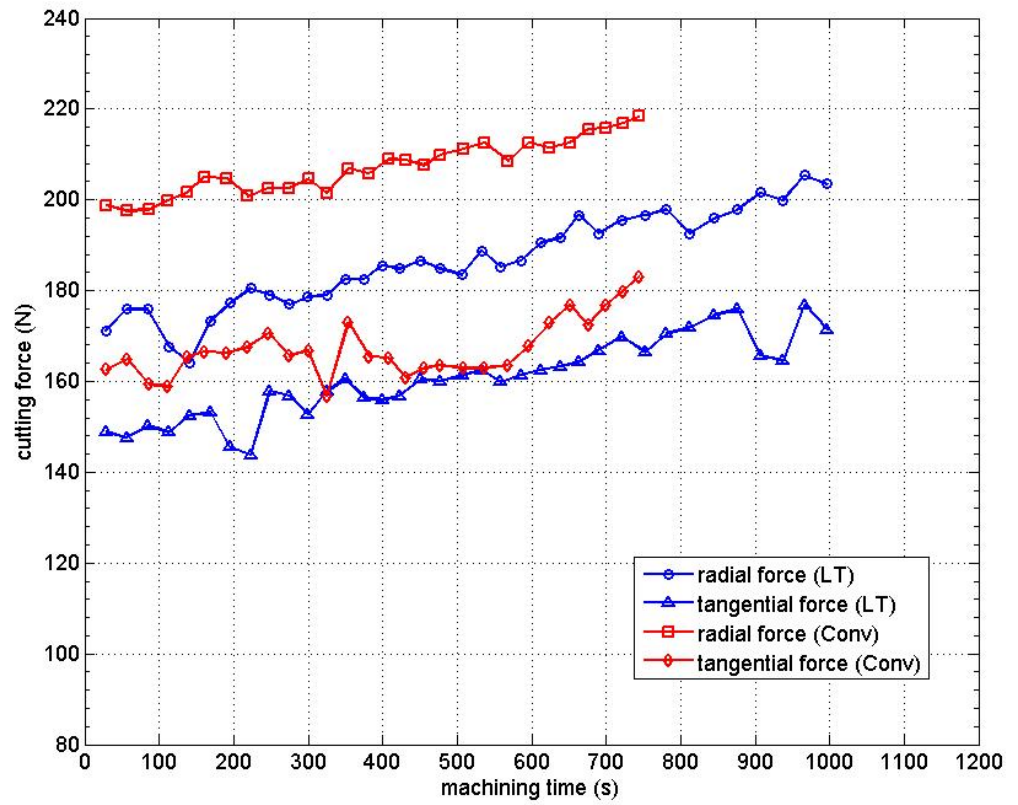
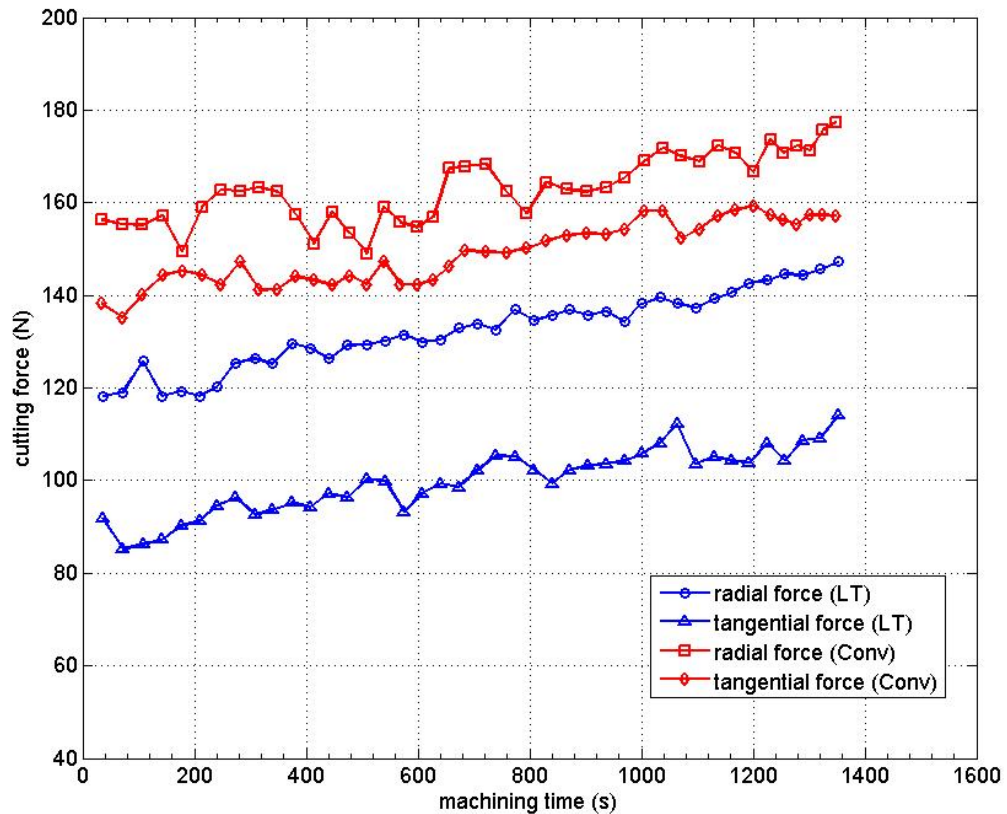


Figure 6.19: Progression of cutting forces in Expt. 1 - depth of cut: 0.3 mm, cutting speed: 180 m/min, feed: 0.10 mm/rev (Conv: conventional hard turning with CBN tool, LT: laser tempering based hybrid turning with CBN tool).



(a)



(b)

Figure 6.20: Progression of cutting forces in Expts. 2 and 3. (a) depth of cut: 0.3 mm, cutting speed: 130 m/min, feed: 0.10 mm/rev, (b) depth of cut: 0.2 mm, cutting speed: 130 m/min, feed: 0.10 mm/rev (Conv: conventional hard turning with CBN tool , LT: laser tempering based hybrid turning with ceramic tool).

6.4.3 Surface Finish

Figure 6.21 compares the surface finish of the two processes in Expt. 1. Recall that in this experiment, CBN tool was used in both the processes. The average surface roughness height R_a in laser tempered hybrid turning process was $0.25 \mu\text{m}$, which is slightly better than the $0.31 \mu\text{m}$ observed in the conventional process. In addition, the peak-to-valley roughness height, R_t for the laser tempering based hybrid case is much lower than the conventional case indicating a smoother surface.

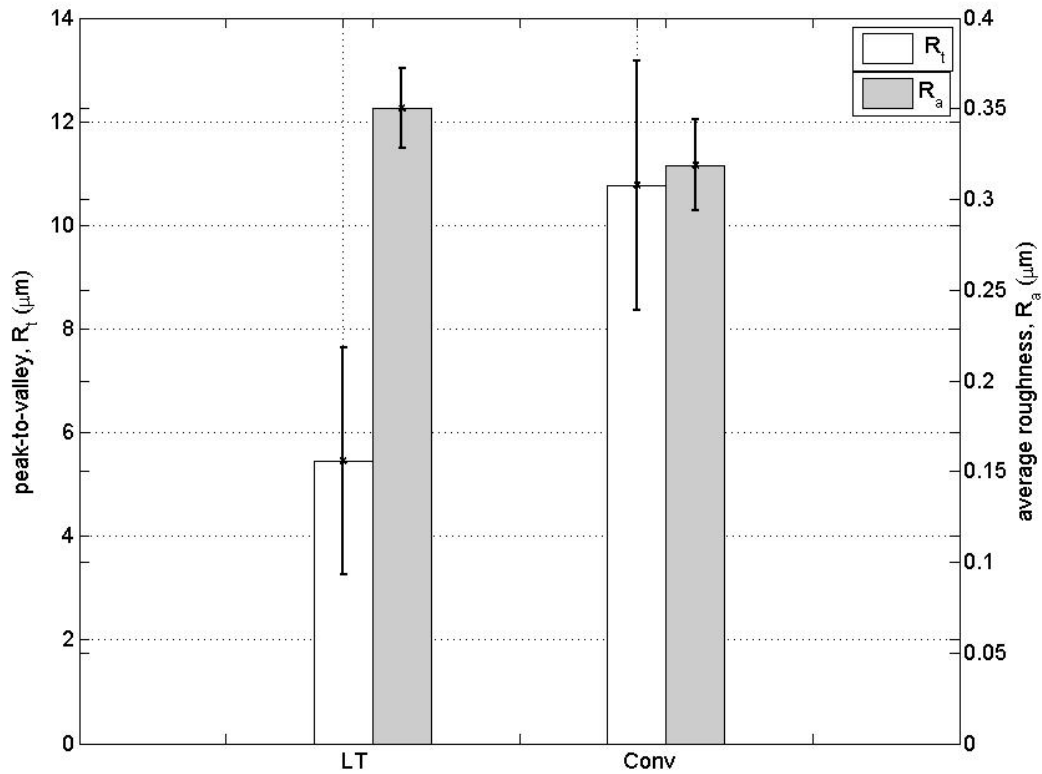


Figure 6.21: Machined surface roughness (R_a and R_t) in Expt. 1- cutting speed: 180 m/min, feed: 0.10 mm/rev, depth of cut: 0.3 mm. Error bars represent 1 std. dev. of the measurements. (Conv: conventional hard turning with CBN tool, LT: laser tempering based hybrid turning with ceramic tool)

Figures 6.22 compares the surface finish results obtained for the process variants in Expts. 2 and 3. Recall that in these experiments, a ceramic tool was used in the laser tempered process while a CBN tool was used in the conventional process. In Expt. 2, the average surface roughness height R_a in laser tempered hybrid turning process was $\sim 0.25 \mu\text{m}$, which is slightly better than the $\sim 0.3 \mu\text{m}$ observed in the conventional process. Similar observations were seen in Expt. 3 (see Figure 6.22). In both experiments, the laser tempered process produced a lower peak-to-valley roughness height. In Expt. 3, the

surface finish obtained in the laser tempered process had ~50 % lower peak-to-valley height than that obtained in the conventional process.

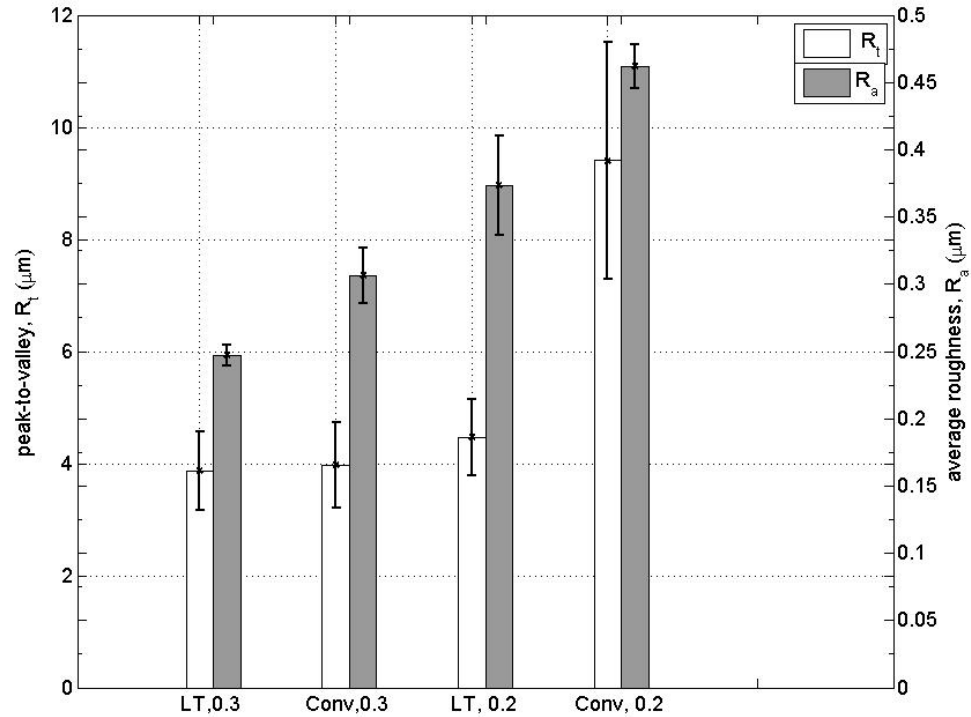


Figure 6.22: Surface roughness (R_a and R_t) results in Expts. 2 and 3 - cutting speed: 130 m/min, feed: 0.10 mm/rev. Error bars represent 1 std. dev. of the measurements. (Conv: conventional hard turning with CBN tool, LT: laser tempering based hybrid turning with ceramic tool, 0.3: 0.3 mm depth of cut, 0.2: 0.2 mm depth of cut)

6.5 Summary

The advantage of laser tempering hybrid turning in comparison with the conventional machining was presented using the results obtained from the experiments. The experimental results show potential benefits in tool life and tooling cost for the laser tempering based hybrid turning process over the conventional hard turning process. The results clearly show that the two-step laser tempering based hybrid turning process yields

reduced cutting forces, lower and more uniform tool wear, and consequently improved tool life. It was also shown that the laser tempered workpiece machined with ceramic tool had lower peak-to-valley roughness height than the CBN tool in the conventional process.

CHAPTER 7

CONCLUSIONS AND RECOMMENDATIONS

The goal of this thesis was to investigate the possibility of using laser treatment to enhance the machinability of hardened steel surfaces using low cost tooling. The goal was achieved by introducing a new two-step laser based hybrid process for machining hardened steels. First, a phase change model was developed to predict the subsurface hardness of a laser-treated hyper-eutectoid steel (AISI 52100). The model was used to aid the selection of laser scanning conditions that yield a large depth of tempered region in the through-hardened steel. Cubic Boron Nitride (CBN) tools, as well as low cost ceramic tools, were used to machine the tempered region. For comparison, the conventional hard turning process was also carried out under the same cutting conditions. The results of the machining experiments showed higher material removal rates and longer cutting tool life in the laser tempering based hybrid turning process. The key conclusions of from the work are summarized and finally, possible avenues of future research are discussed.

7.1 Conclusions

7.1.1 Laser Tempering Based Hybrid Process

- The work presented a new two-step laser tempering based hybrid turning process for increasing the productivity and lowering the tooling cost in machining of hardened steel. The two-step process consists of first laser treating the hardened steel workpiece surface to induce tempering and thereby reduction in the material hardness over a certain depth. The second step consists of machining the softened layer by a CBN or ceramic cutting tool.

7.1.2 Microstructural Analysis

AISI 52100 steel samples were laser treated at selected laser scanning conditions. The microstructures of the laser-treated AISI 52100 samples were evaluated to study the hardness of the tempered subsurface layer in the workpiece and to study the influence of laser scanning conditions to laser surface tempering. The key conclusions are:

- The irradiated cross-section reveals three distinct regions: (1) a tempered white layer, (2) a dark layer, and (3) a base material that is unaffected by the overlapping laser scans.
- The tempered white layer, and the heat affected tempered region adjacent to the tempered white layer together constitute the tempered subsurface region. The heat affected region is tempered due to heat conduction.

7.1.2.1 Tempered White Layer

- A ‘tempered white layer’ is formed in the subsurface region of the workpiece due to overlapping of laser scans. When heat from a single, non-overlapping laser beam raises the temperature of the subsurface region above the phase transformation temperature of the material, hardened white layer is formed. The additional heat from an overlapping laser beam, tempers the white layer to form a tempered white layer.
- For a selected heat input intensity and beam energy profile, following observations were noted:
 - (1) The depth of the tempered white layer and consequently the depth of tempered region is a function of the laser scanning condition. Larger overlaps and smaller scan speeds produce a thicker tempered white layer.
 - (2) The depth of tempered white layer ranges between the depth of hardened white layer in a single non-overlapping scan and the depth of white layer that is produced in a overlapping scan that yields a surface temperature that is near the melting point of the material.

- (3) The hardness of the tempered white layer is lowest at the workpiece surface and increases along its depth. The subsurface hardness of the tempered region is a function of the laser scanning condition.
- (4) The depth of tempered white layer region is an indicator of the overall depth of tempering in the workpiece. A tempered white layer is the phase transformed region that has subsequently tempered. Large depth of tempered white layer signifies that the temperature at that depth has reached the phase transformation temperature. Phase transformation temperatures at a higher depth lead to larger depths of tempered subsurface region.

7.1.3 Phase Analysis

Laser-treated AISI 52100 samples were evaluated using an x-ray diffractometer to study the composition of phases in the tempered region.

- A thin surface layer (<10 μm) of the laser treated samples is composed of oxides and retained austenite. The tendency for formation of the surface oxide layer increases with temperature, which is a function of the laser scanning conditions. The proportion of retained austenite decreases along the depth to a negligible proportion (~1 %) within the thin subsurface layer.
- The tempered region below the thin surface oxide layer is composed of ferrite and martensite and weak traces of retained austenite (~1 %). With each additional thermal cycle, any austenite retained from the previous thermal cycle undergoes martensitic transformation, which is subsequently tempered.

7.1.4 Laser Surface Tempering Model

- A tempering model to predict the subsurface hardness of hyper-eutectoid steels subjected to thermal cycles from a laser beam was presented. The laser tempering model consists of a thermal model that predicts the surface and subsurface

temperatures at a given laser scanning condition and a phase change model that uses the temperatures from the thermal model to predict the hardness of the tempered subsurface region.

- The hardness predicted by the simulated model was compared with the measured values obtained from the laser treated AISI 52100 steel at select laser scanning conditions. Good agreement was achieved between the experimental and simulated values of the hardness.

7.1.5 Machining Experiments

Machining experiments were carried out to show that the laser tempering based hybrid turning process is an effective process. A effective process provides higher material removal rate and increases the performance of the tool without deteriorating the machined surface. Machinability metrics used in this experiment were progression of tool wear and cutting forces, and surface finish. Machinability metrics of the laser tempering based hybrid turning process was compared with those for the conventional hard turning process to show the advantages of the former process.

7.1.5.1 Higher Material Removal Rate

- The laser tempering based hybrid turning process is a decoupled process that allows practical cutting speeds and feeds during turning. In addition, a larger depth of cut can be employed by appropriately selecting the laser scanning conditions. Practical cutting speeds, feeds, and larger cutting depths imply a higher material removal rate per pass.

7.1.5.2 Cutting Performance

- In laser tempering based hybrid turning process, the cutting forces are reduced and consequently, the wear of the tool is reduced. The CBN tool showed improved tool life in comparison to the CBN tool in the conventional hard turning process.

- In laser tempering based hybrid turning process, the tempered material in the cutting zone requires only a ceramic tool to remove the softened region, instead of the conventional CBN tool used in hard turning. The tool wear and cutting forces exhibited by the low-cost ceramic tool in the laser tempering based hybrid turning process were compared with the more expensive CBN tool in conventional hard turning and yielded the following results:
 - (1) Experimental tool wear studies at cutting conditions that yield a higher material removal rate suggest a potential tool life advantage of the CBN tool in laser tempering based hybrid turning. Furthermore, the possibility of using low cost ceramic tools in place of CBN tools, without compromising the material removal rates was investigated. Ceramic tools show a wear performance that is comparable to the CBN tool.
 - (2) The cutting forces in the laser tempering based hybrid turning process were found to be much lower than in the conventional hard turning process.

7.1.5.3 Surface Roughness

- Surfaces of the laser-treated workpiece, machined with the ceramic tool had lower peak-to-valleys, R_t than that produced by the CBN tool in the conventional hard turning process. The surface roughness parameter R_a of the machined surfaces produced by the ceramic tool in the laser tempering based hybrid turning process was slightly better than the R_a value produced by the CBN tool in the conventional hard turning process.

The experimental results show potential benefits in tool life and tooling cost for the laser tempering based hybrid turning process over the conventional hard turning process. It should also be pointed out that simultaneous laser-assisted hard turning (as documented in the literature) is limited in its material removal rate efficiency to induce

adequate thermal softening of the material. Consequently, it is argued that the two-step laser tempered hybrid turning process examined in this paper provides significant productivity and tooling cost advantages over the conventional hard turning process.

7.2 Recommendations

7.2.1 Laser Surface Tempering Model

- A linear range of absorptivity values was assumed in the model for all laser scanning conditions. Detailed investigations of the surface energy absorption for various scanning conditions will improve the performance of the model in predicting the subsurface temperatures.
- The model needs to be investigated for tempering of other hardened materials.

7.2.2 Laser Tempering based Hybrid Process

- The laser based hybrid process needs to be evaluated for other hardened alloy steels, tool steels and other difficult-to-machine materials.
- The applicability of the process to other manufacturing process(es) such as drilling needs to be investigated.
- In order to economically justify the process, a complete economic analysis of the process for a specific component needs to be carried out and compared to the conventional hard turning process economics.

APPENDIX

8.1 Equipments

8.1.1 Optical Fiber

An optical fiber (Figure 8.1.1 & Table 8.1.1) provides the passage for the laser beam from fiber connector end of the laser system to the laser head. The fiber core, fiber clad, jacket layer, fiber coupler connector, laser head connector make the fiber cable system. The core is the transparent silica through which the incoming beam travels. The clad is a glass sheath that surrounds the core. The cladding acts like a mirror, reflecting light back into the core (total internal reflection). The jacket protectively covers the fiber core and the clad. The laser beam is focused onto the input side of the optical fiber with an angle less than the numerical aperture of the fiber and with a focal spot smaller than the core of the fiber.



Figure 8.1.1: Fiber optics system.

Table 8.1.1: Specifications of fiber optics system [Precitec].

<i>mean power</i>	max. 5 kW
<i>peak power</i>	max. 50 kW, 1 ms pulse length
<i>fiber eccentricity (input side)</i>	<20 μm input side
<i>fiber eccentricity (output side)</i>	<40 μm input side
<i>output angle at incoupling angle 10 mrad</i>	<100 mrad
<i>angular deviation</i>	<15 mrad
<i>weight</i>	0.08 kg/m

8.1.2 X-Y Precision Linear Stages

Newmark NLS4 series X-Y precision linear stage (see Figure 8.1.2) was used to traverse the laser head along the length of the workpiece. A stepper controller guides the 0.250 inch/rev pitch lead screw in the X-stage and a servo controller with an encoder feedback mechanism guides the 1/16 inch/rev pitch lead screw in the Y-stage. Table 8.1.2 lists the specifications of the X-Y linear stage.



Figure 8.1.2: X-Y precision linear stage [courtesy: Newmark systems].

Table 8.1.2: Specifications of linear stage [Newmark systems].

<i>travel</i>	2.0 inches along x-axis, 12.0 inches along y-axis
<i>resolution</i>	x: 0.13 μm @ 50,000 steps/rev motor resolution y: 1.60 μm @ 4,000 counts/rev encoder resolution
<i>maximum load</i>	50 lbs (horizontal), 15 lbs (vertical), 40 lbs (side)
<i>repeatability bidirectional</i>	5.0 μm
<i>weight</i>	~14 lbs
<i>travel speed</i>	25 mm/sec

8.1.3 Spindle and Electric Drive

A spindle coupled to the Reliance GV3000 electric drive (see Figure 8.1.3) rotates the cylindrical workpiece at a set speed. The GV3000/SE AC drive is a pulse-drive-modulated drive to precisely control motor speed in both directions. The flux vector control regulation provides high dynamic response. The serial port on the drive is intended to communicate to a PC using Reliance CS3000 software.



Figure 8.1.3: Motor drive [courtesy: Reliance Electric].

8.1.4 Cooling System

The cooling system consists of a cooling plate and an affinity F-series chiller. The internally fabricated cooling plate consists of copper tubes routed between sandwiched

aluminum plates. The temperature controlled affinity chiller continuously cools the water to the set temperature that is circulated in the copper tubes.

8.1.5 Leica DMRM Microscope

Microstructures were evaluated using a Leica DMRM microscope (See Figure 8.1.4 and Table 8.1.3).



Figure 8.1.4: Leica DMRM microscope [courtesy: Leica Microsystems].

Table 8.1.3: Specifications of Leica microscope [Leica Microsystems].

<i>type</i>	Leica DMRM Type 301-371.010
<i>stage traversing range</i>	25 mm
<i>load capacity</i>	4 Kg
<i>X-Y stage drive</i>	coarse/fine, manually controllable
<i>objective lens</i>	plan 5x/0.15 BD-D 12.2, plan 10x/0.30 BD -/D 11.0, plan 20x/0.50 BD 0/D 1.27 plan 50x/0.80 BD 0/D 0.5

8.1.6 Hardinge Conquest T42SP Lathe

Hardinge Conquest T42SP (see Figure 8.1.5) is a two axis (X-Z) super precision Computer Numerical Control (CNC) lathe with an overall axis repeatability of 0.76 μm . The machine is mounted on a 2200 kg HARCRETE polymer composite base for vibration isolation. Table 8.1.5 lists the specification of the Hardinge Conquest T42SP lathe.



Figure 8.1.5: Hardinge Conquest CNC lathe [courtesy: Hardinge Inc.].

Table 8.1.4: Specifications of Hardinge Conquest lathe [Hardinge Inc.].

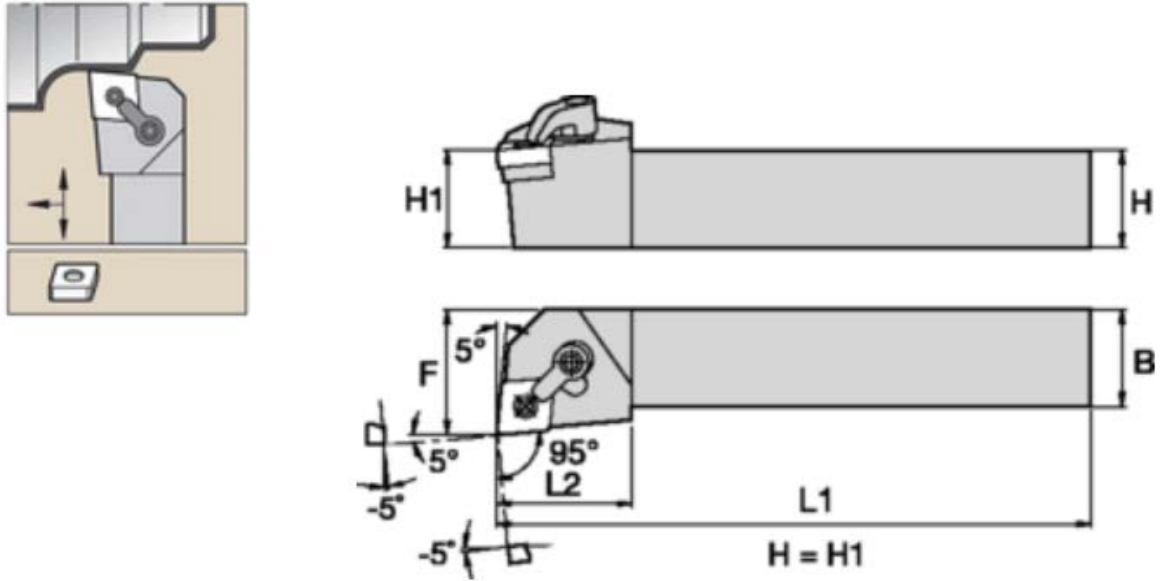
<i>System</i>	Hardinge Conquest T42SP
<i>Spindle configuration</i>	
<i>spindle speed</i>	50-5000 rpm; 1 rpm steps
<i>drive motor</i>	7.5 kW (10 HP) AC
<i>torque rating @ 1250 rpm</i>	57 N-m (42 ft-lb)
<i>collet configuration</i>	16C collet ANSI A2-5" spindle nose, max. through capacity: 1.625"
<i>Carriage and cross slide configuration</i>	
<i>swing over bed</i>	538.5 mm (21.2 in)
<i>max. distance spindle face to turret face</i>	355.6 mm (14.0 in)
<i>max. x-axis travel</i>	134.9 mm (5.31 in)
<i>max. z-axis travel</i>	13.8 in
<i>rapid traverse rate (x-axis)</i>	12 m/min (472 ipm)
<i>rapid traverse rate (z-axis)</i>	16 m/min (630 ipm)
<i>Turret stations (nos.)</i>	12
<i>Inspection specifications</i>	
<i>part roundness</i>	0.40 μm (15 μin)
<i>part surface finish</i>	0.20 μm (8 μin)
<i>overall axis repeatability</i>	0.76 μm (30 μin)
<i>turret indexing repeatability</i>	1.27 μm (50 μin)
<i>Dimensions</i>	104 in x 72 in x 68 in

8.1.7 Tool Holder

Kennametal MCGNL-124B tool holder (see Figure 8.1.6) was used to hold the inserts. The tool holder geometry is given in Figure 8.1.7.



Figure 8.1.6: Kennametal MCGNL-124B tool holder [courtesy: Kennametal]



shank height, H	shank width, B	overall length, L1	L2	F	insert holding
0.75"	0.75"	4.50"	1.25"	1.0"	method: top and hole clamping lockpin KL46, 3/32" hex clamp screw STC20, 1/8"

Figure 8.1.7: Kennametal MCGNL-124B tool geometry [Kennametal].

8.1.8 Cutting Force Dynamometer

Kistler Force dynamometer Type 9257B (see Figure 8.1.8) is a compact, high resolution, high natural frequency, three-component force dynamometer. The Type 9257B dynamometer can measure both dynamic and quasi-static force measurements. Table 8.1.6 lists the specification of the Kistler force dynamometer Type 9257B.

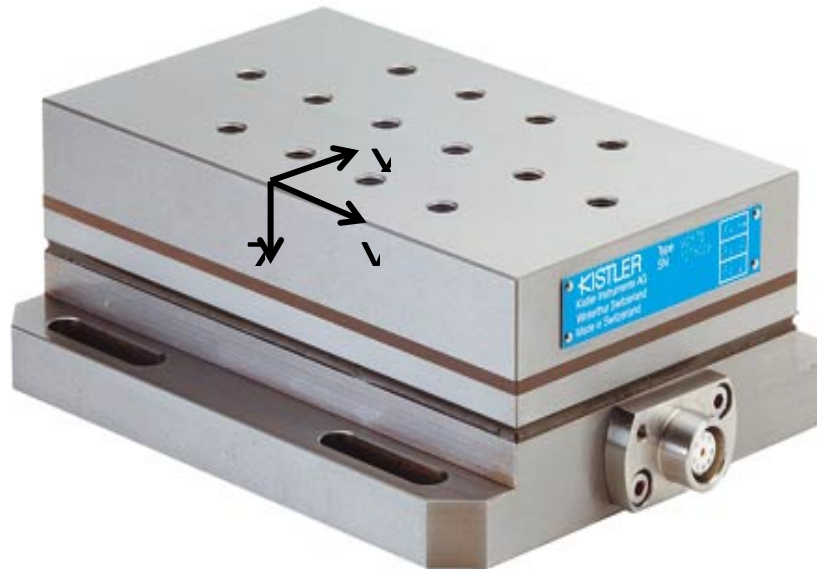


Figure 8.1.8: Kistler force dynamometer [courtesy: Kistler].

Table 8.1.5: Specifications of Kistler force dynamometer [Kistler].

<i>system</i>	Kistler Type 9257B
<i>measuring range F_x, F_y, F_z</i>	$\pm 0.1 - 5$ kN
<i>sensitivity</i>	$F_x, F_y : \sim 7.5$ pC/N ; $F_z : \sim 3.7$ pC/N
<i>natural frequency</i>	$f_{n_x} : \sim 2.3$ kHz ; $f_{n_y} : \sim 3.5$ kHz
<i>dimension</i>	170 mm x 100 mm x 60 mm
<i>mass</i>	7.3 kg

8.1.9 Zygo NewView 200

The Zygo NewView 200 is a high-resolution, non-contact, non-destructive, 3-D imaging surface structure analyzer. It provides both imaged surface details of test parts and accurate measurements to characterize the surface. The NewView uses scanning white light interferometry to image and measure the topography of exposed surface. Table 8.1.6 lists the specification of the Zygo NewView 200.

The two major parts to the NewView system (see Figure 8.1.9) are: the microscope with illuminator optics and the computer. Microscope combines optical microscopy and interferometry to provide the raw data needed for imaging and for surface structure analysis. The device utilizes the pairing of a highly precise vertical scanning transducer and a camera to generate the three-dimensional image of exposed surface of the sample. This is achieved by using the fringes produced by the optical path difference between the reference and the reflection beam. The processed data is fed to the MetroPro software, which provides the three-dimensional image of the surface topography. The entire setup is placed in a vibration isolation table to minimize errors from external sources.

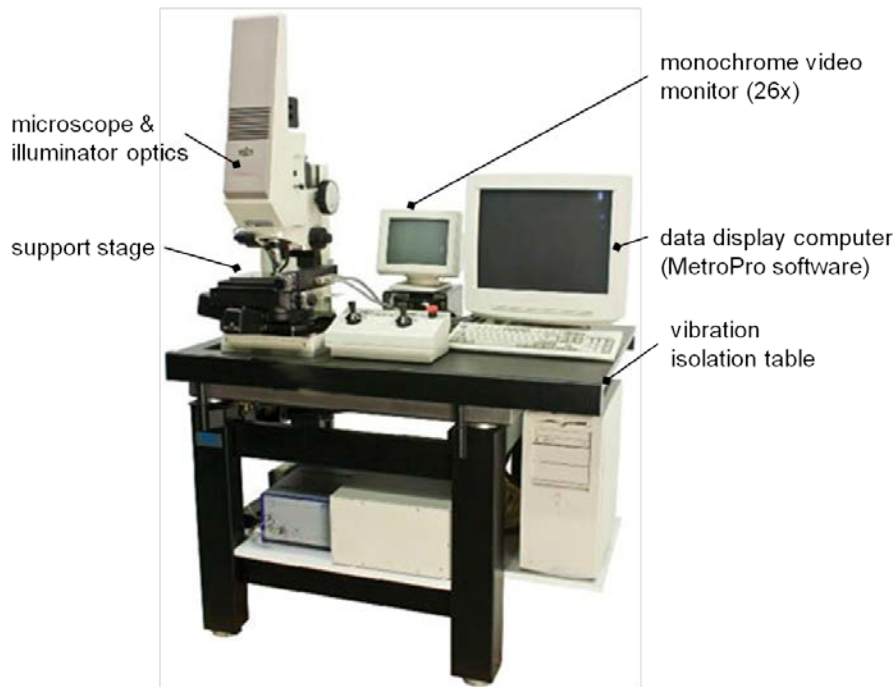


Figure 8.1.9: Zygo NewView200 setup [courtesy: Zygo]

Table 8.1.6: Specifications for Zygo NewView200 [Zygo].

<i>system</i>	Zygo NewView 200
<i>measurement repeatability</i>	0.3 nm Rq
<i>max. part dimension</i>	150 mm x 150mm x 100 mm
<i>performance</i>	vertical resolution: 0.1 nm, max. vertical step height: 100 μ m
<i>vertical travel</i>	130 mm
<i>camera resolution</i>	640 x 480

The concept of interferometry can be best explained with the help of Figure 8.1.10. Interferometry is a traditional technique in which a pattern of bright and dark lines (fringes) result from an optical path difference between a reference and a sample beam. The incoming light is split inside an interferometer, one beam going to an internal high quality reference surface and the other to the sample placed on instrument table. The reflected beam recombines inside the interferometer, undergoing constructive and destructive interference and producing the light and dark fringe pattern.

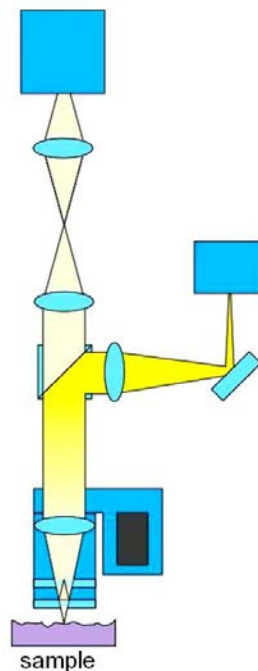


Figure 8.1.10: Principle of interferometry - Zygo NewView200 [Zygo].

8.2 Micrographs of Tempered Subsurface Region

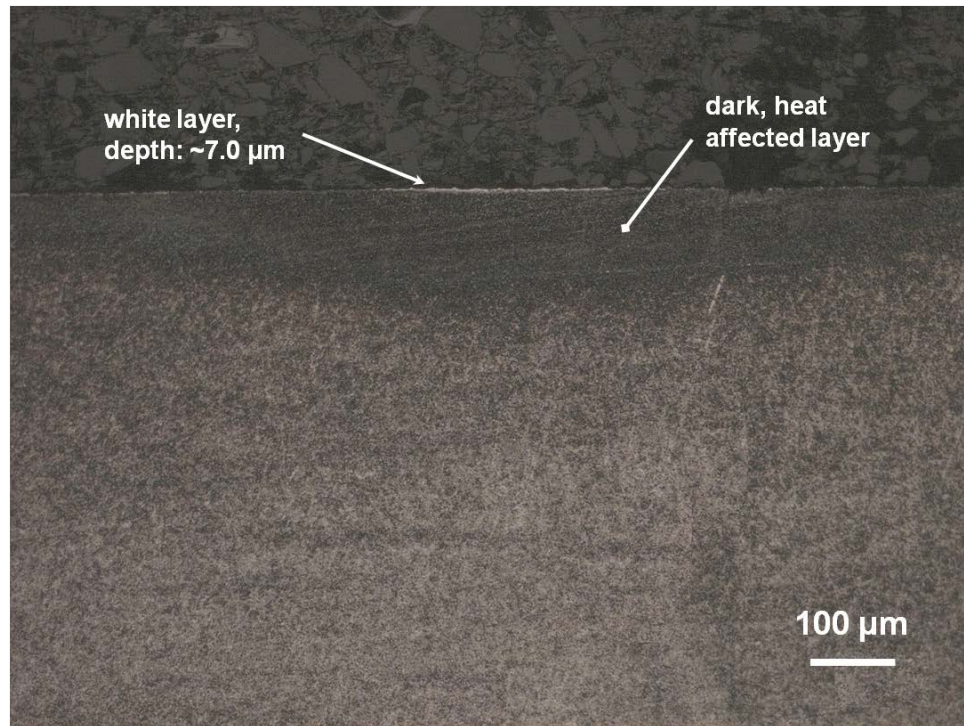


Figure 8.2.1: Microstructure (longitudinal cross-section) of AISI 52100 steel samples after a single, non-overlapping laser scan (laser power: 580 W, spot size: 2 mm, scan rate: 17.95 m/min).

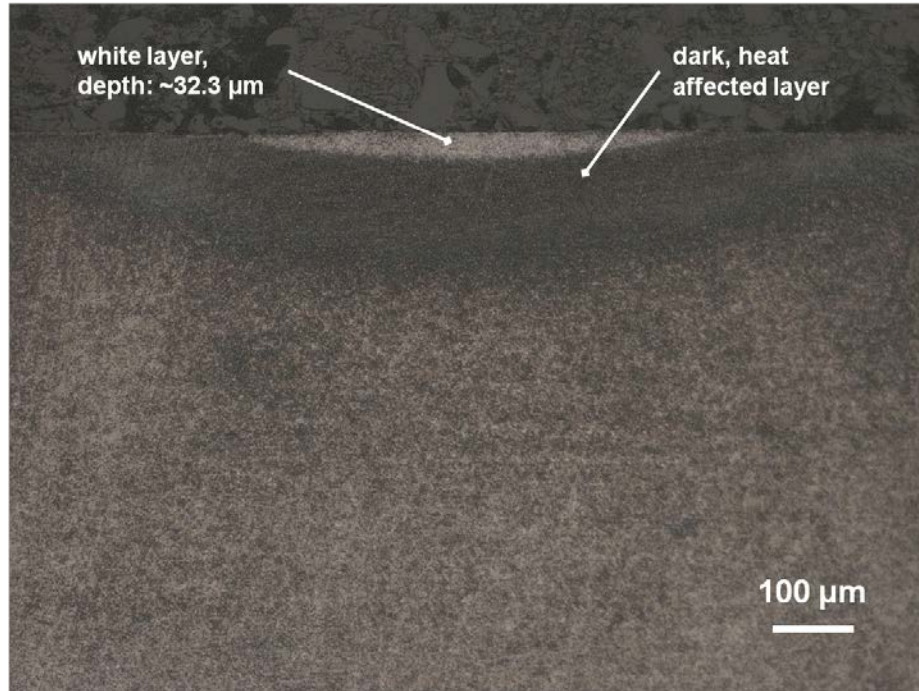


Figure 8.2.2: Microstructure (longitudinal cross-section) of AISI 52100 steel samples after a single, non-overlapping laser scan (laser power: 694 W, spot size: 2 mm, scan rate: 17.95 m/min).

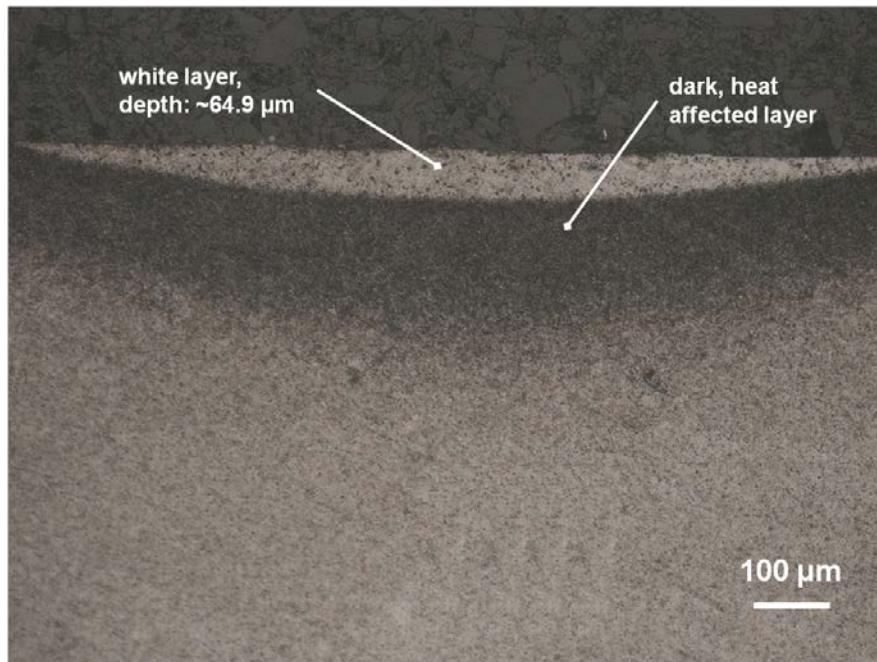


Figure 8.2.3: Microstructure (longitudinal cross-section) of AISI 52100 steel samples after a single, non-overlapping laser scan (laser power: 879 W, spot size: 2 mm, scan rate: 17.95 m/min).

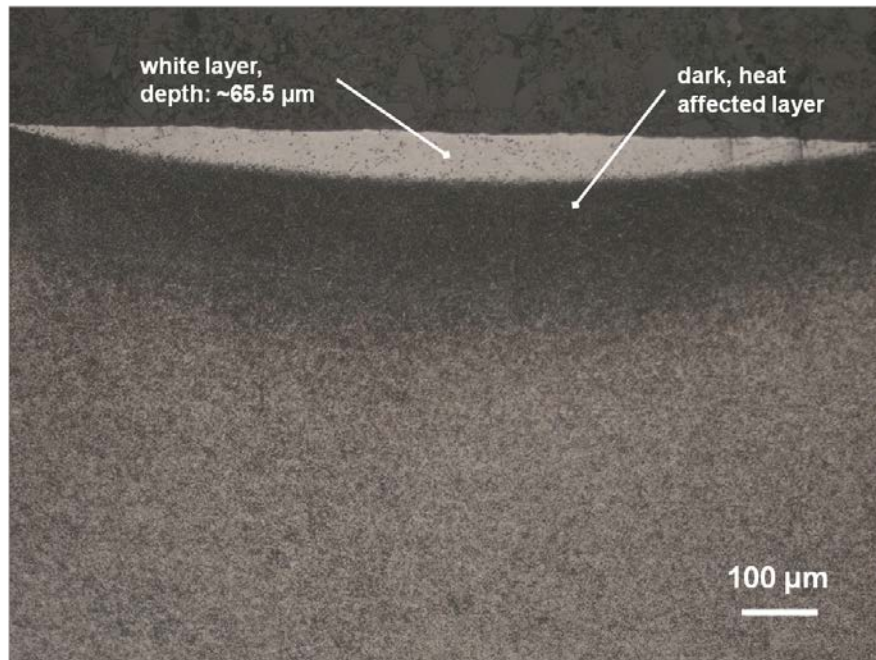


Figure 8.2.4: Microstructure (longitudinal cross-section) of AISI 52100 steel samples after a single, non-overlapping laser scan (laser power: 947 W, spot size: 2 mm, scan rate: 17.95 m/min).

8.3 Composition of Phases Using X-ray Diffraction

8.3.1 Objective

The objective of phase analysis is to evaluate the composition of subsurface phases present before and after laser treating the AISI 52100 steel sample. The results of the phase analysis will aid the kinetic phase change model that uses the volume fraction of different phases to predict the subsurface hardness. X-ray diffraction technique was used to study the composition of the phases.

8.3.2 Overview

The two essentials for a diffraction analysis are: (1) a wave motion that is capable of interference (x-rays), and (2) a set of periodically arranged scattering centers (the atoms of a crystal) [Cullity 1956].

A crystalline material consists of periodic three-dimensional arrangement of unit cell into a lattice. A unit cell, the smallest volume element, contains one or more atoms in a fixed arrangement. The crystal lattice parameters of the unit cell are the lengths a , b , c and the angles between the lattice lengths α , β , γ (see Figure 8.3.1) Crystalline materials consist of plane of atoms that are spaced at a interplanar distance, d .

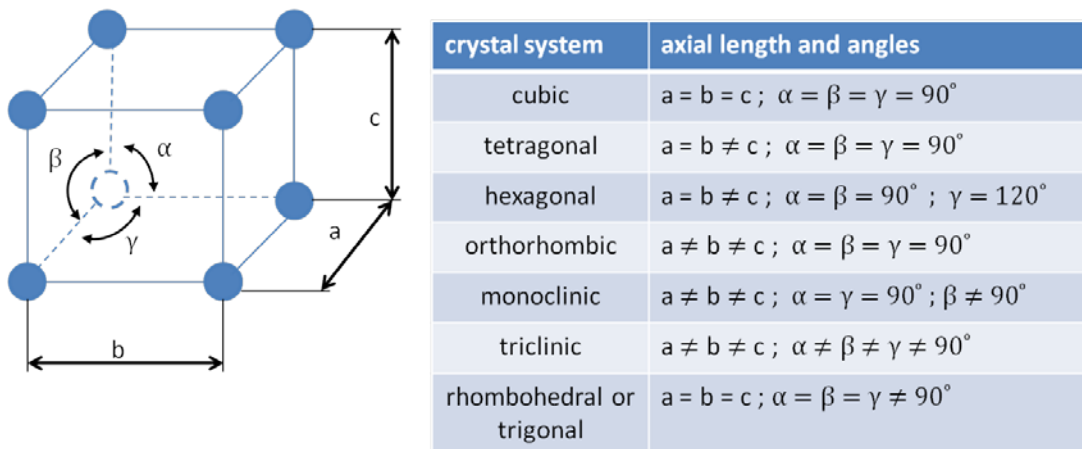


Figure 8.3.1: Left: Unit cell in crystalline material, Right: definition of crystal structure [Cullity 1956].

X-rays are produced when high speed electrons collide with a metal target in a sealed chamber. Most of the kinetic energy of the striking electrons is converted to heat energy and a portion of it is transformed to x-rays. When x-rays strike the surface of a crystal (see Figure 8.3.2 (a)), the incident beam is partially scattered by atoms. The part of the x-ray that is not scattered passes through to the next layer of atoms, at an interplanar spacing d , where again part of the x-ray is scattered and part passes through to the next layer. When an incoming x-ray beam (AB and DE in Figure 8.3.2 (a)) strike the atom, the electrons around the atom start to oscillate with the same frequency as the incoming beam. The in-phase, parallel, incident rays, AB and DE, make an angle θ with the surface and penetrate to a depth depending on the frequency. X-rays strike the surface and are reflected (beams BC and EF) from the surface at the same angle θ . The interference of the reflected beam produces a diffracted beam that is either constructive or destructive. If the beams diffracted by two different layers are in phase, constructive interference occurs and the diffraction pattern shows a peak. On the other hand, if the beams are out of phase, destructive interference occurs and there is no peak (see Figure 8.3.2(b)). Since the atoms are arranged periodically on a lattice, the rays scattered by them have definite phase relation between them. Destructive interference occurs in most directions of scattering, but constructive interference occurs in few directions to produce diffracted beam.

The electrons which are stopped in one impact (beam A-B in Figure 8.3.2(a)) will give rise to photons of maximum energy, i.e., to x-rays of minimum wavelength. Due to the rapid deceleration of one or more electrons, a continuous spectrum of radiation of many wavelengths is produced. The wavelengths produced are characteristic of the target metal used and they are referred as the characteristic lines, denoted as K , L , M , etc in the order of increasing wavelength. The longer wavelength lines are easily absorbed and therefore, X-ray diffraction analysis uses the K characteristic lines. There are several lines in the K set, but only the three strongest lines ($K_{\alpha 1}$, $K_{\alpha 2}$, $K_{\beta 1}$) are observed in the

normal diffraction work. The wavelengths of the components $K_{\alpha 1}$, $K_{\alpha 2}$ are so close that they are not resolved as separate lines, but as a single line, referred to as the K_{α} line. The high intensity K_{α} lines are very narrow and sharp.

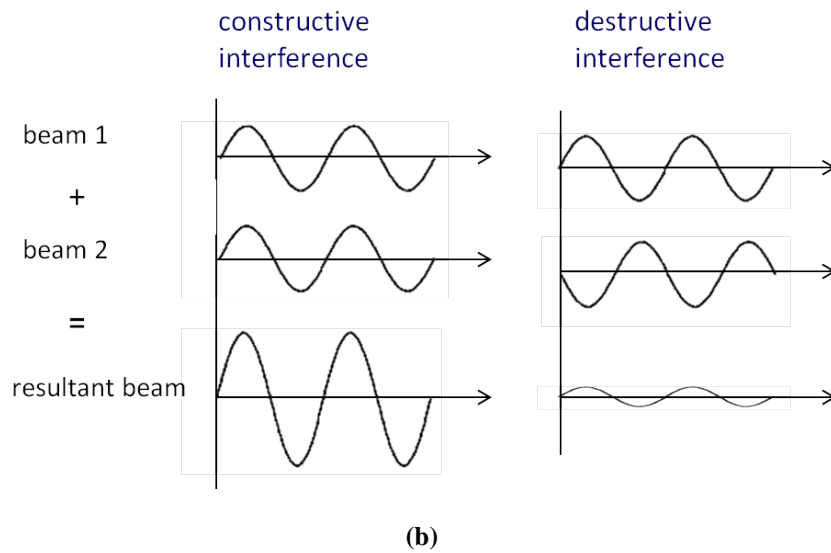
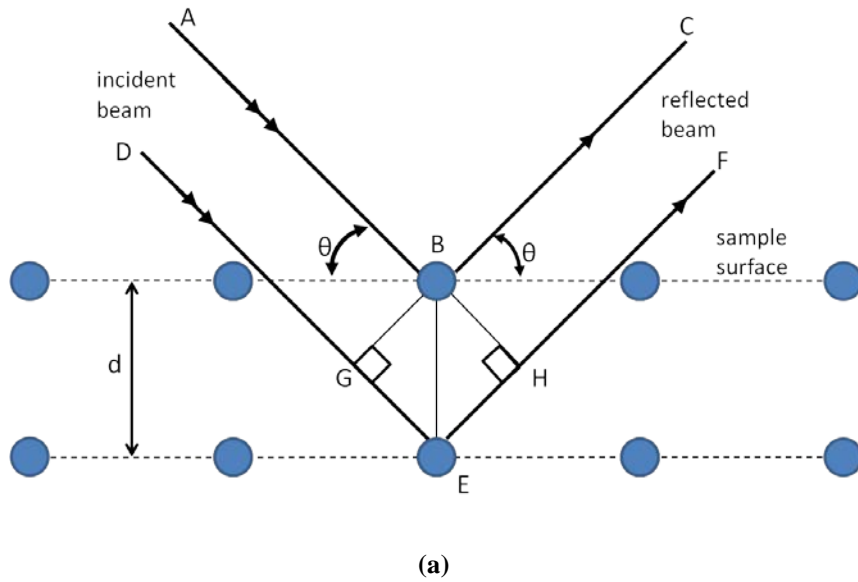


Figure 8.3.2 (a) Diffraction of x-rays in crystalline material [Cullity 1956], (b) Beam interference patterns [Cullity 1956].

In order for an x-ray to diffract the sample, the inter-planar spacing ‘ d ’ between the atom layers must be an integer multiple of the radiation wavelength (Bragg’s law). If λ is the wavelength of the incident x-ray and n_b is any integer, the path difference (see figure 8.3.2(a)) is given by,

$$n_b\lambda = GE + EH, \quad (8.3.1)$$

Substituting, $GE = EH = d (\sin \theta)$, yields

$$n_b\lambda = 2d (\sin \theta), \quad (8.3.2)$$

X-ray diffraction can be done using a single crystal or polycrystalline applications. The former is used to evaluate the molecular structure of the compounds and the latter is used for finger print identification of various crystalline surfaces.

8.3.3 Equipment

XRD patterns of AISI 52100 steel samples were collected using a monochromatic, PANalytical X’Pert Pro MPD (see Figure 8.3.3) with Cu- K_α radiation ($\lambda = 1.540 \text{ \AA}$), and with a fixed slit incidence ($1/8$ divergence and soller slits) and diffracted optics. Table 8.3.1 lists the specification of PANalytical X’Pert Pro MPD.



Figure 8.3.3: PANalytical X'Pert Pro MPD [courtesy: PANalytical].

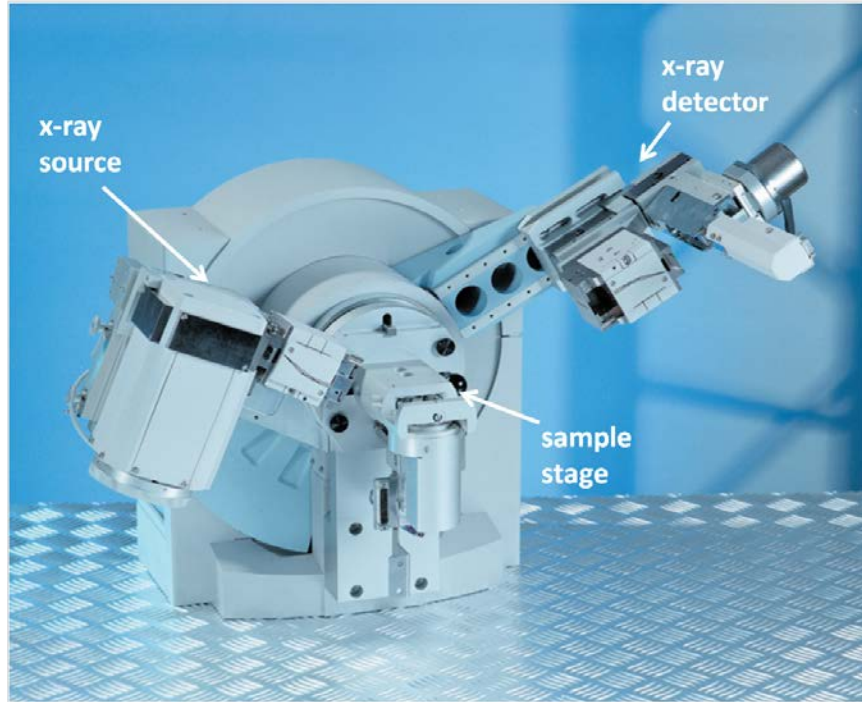
Table 8.3.1: Specifications of x-ray diffractometer [PANalytical].

<i>equipment</i>	PANalytical X'Pert Pro MPD
<i>power</i>	1.8 kW, 45 kV, 40 mA
<i>radiation</i>	Cu ($\lambda=1.5406 \text{ \AA}$)
<i>receiving slit acceptance</i>	1/8 divergence slit & soller slit
<i>source to specimen distance</i>	240 mm

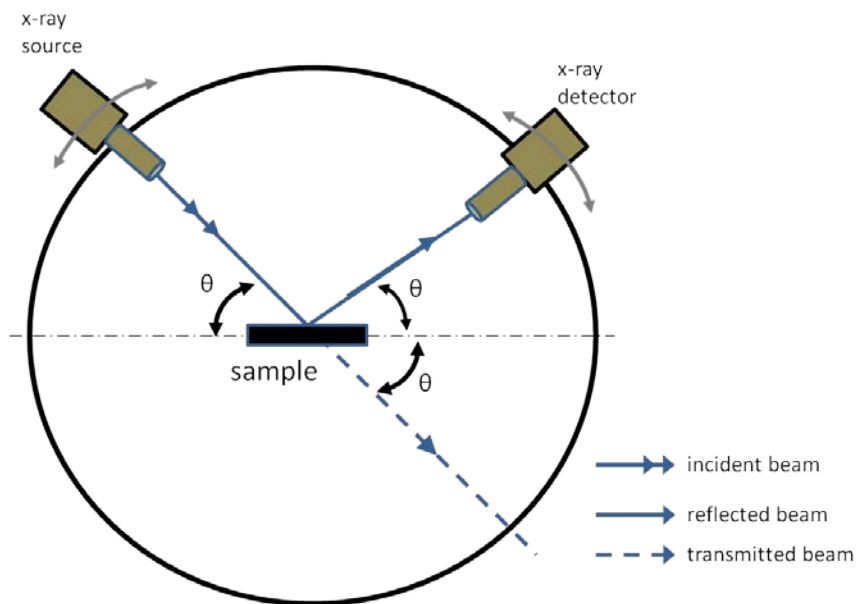
8.3.4 Experimental Procedure

A powder X-ray diffractometer consists of an x-ray source, an x-ray detector and a sample stage (see Figure 8.3.4 (a)). Samples were placed in the sample stage such that the incoming beam from the x-ray source strikes the surface of the sample. The x-ray source generates x-rays, while the detector collects the beam that is reflected by the sample. The

source emits radiation in all directions. In order to enhance the beam focus to the sample, the divergence in the direction along the line of focus is to be adjusted. This is done by passing the incident beam through a soller slit, which contains a set of closely spaced thin metal plates. Afterwards, the x-ray source is positioned such that the incoming beam is focused on the sample at some initial angle θ . The angle between the diffracted beam and the transmitted beam is always 2θ (see Figure 8.3.4(b)), which is referred to as the diffraction angle. The scan range was selected to be $30^\circ \leq 2\theta \leq 105^\circ$. No peak of interest outside this range existed. The voltage and current were set at 45 kV and 40 mA respectively. The X-ray counts at each step are saved to a file on the computer. The diffraction pattern due to interference is characteristic of the structure. In powder x-ray diffraction, the diffraction pattern represents the bulk material of the crystalline surface. Since most materials have unique diffraction patterns, compounds can be identified by using a database of diffraction patterns. Once finished, the data were evaluated using Rietveld analysis. The Rietveld analysis is a least squares approach to refine a theoretical line profile until it matches the measured profile. The data is then processed by the Highscore Plus software to plot intensity peaks against the diffraction angle 2θ .



(a)



(b)

Figure 8.3.4: (a) Goniometer of PANalytical X'Pert Pro MPD, (b) Schematic of the goniometer [PANalytical].

8.3.5 Diffraction Patterns

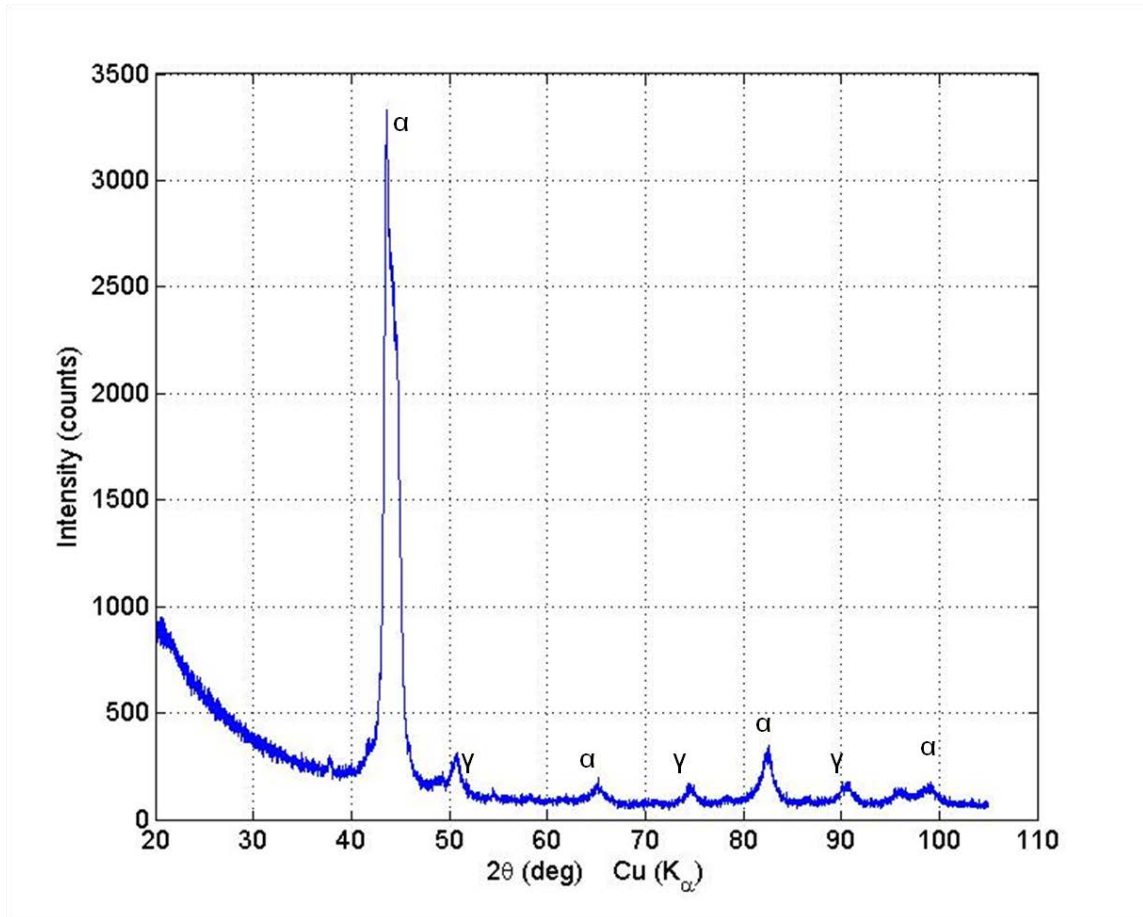


Figure 8.3.5: X-ray diffraction patterns of hardened AISI 52100 steel sample (~63 HRC), no laser treatment.

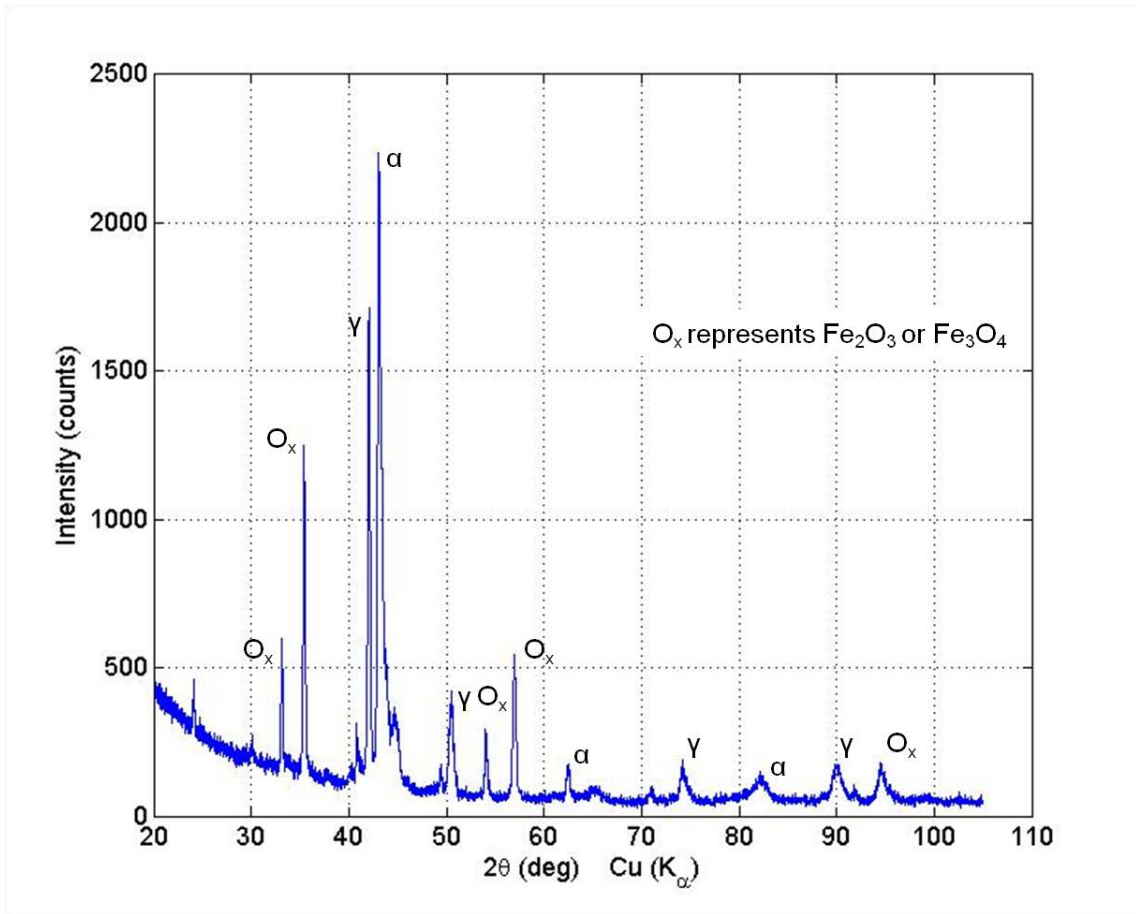


Figure 8.3.6: X-ray diffraction patterns of laser-treated AISI 52100 steel sample - depth from surface: 0 μm (laser power: 800 W, scan speed: 17.95 m/min, overlap: 93.58 %)

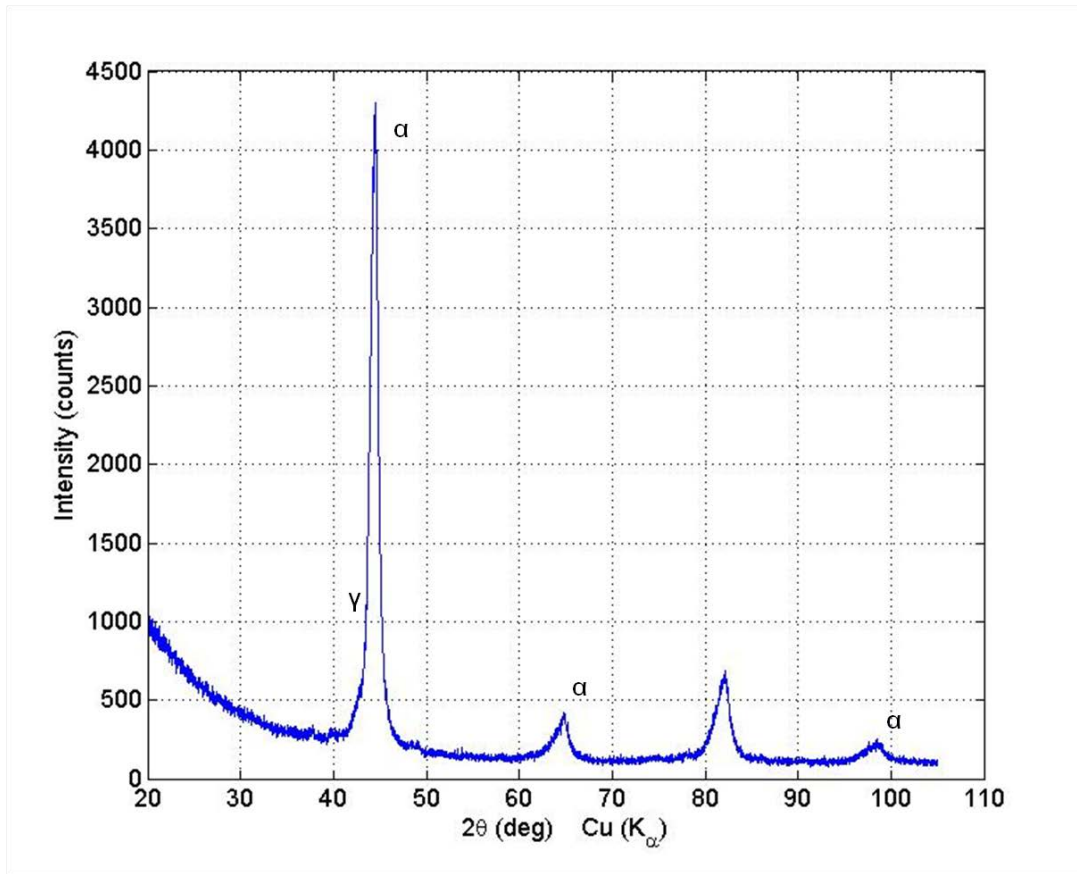


Figure 8.3.7: X-ray diffraction patterns of laser-treated AISI 52100 steel sample - depth from surface: $\sim 7 \mu\text{m}$ (laser power: 800 W, scan speed: 17.95 m/min, overlap: 93.58 %).

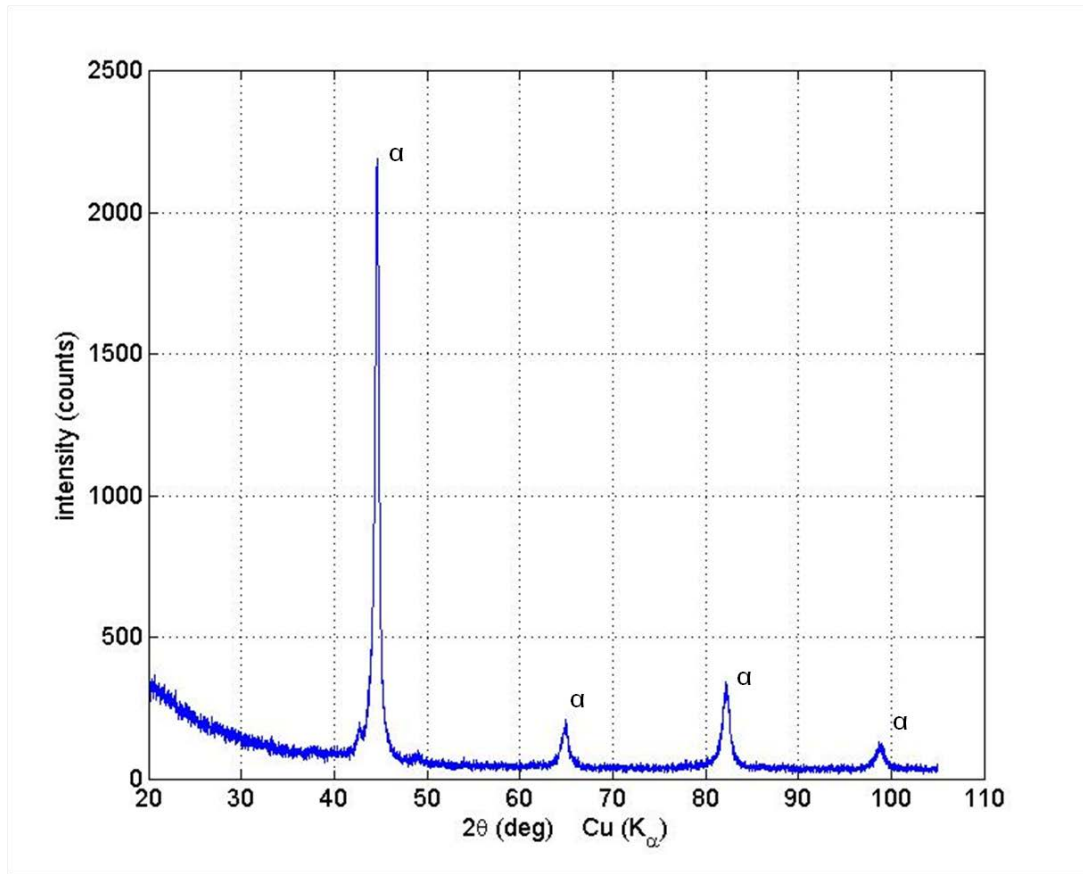


Figure 8.3.8: X-ray diffraction patterns of laser-treated AISI 52100 steel sample - depth from surface: $\sim 42 \mu\text{m}$ (laser power: 800 W, scan speed: 17.95 m/min, overlap: 93.58 %).

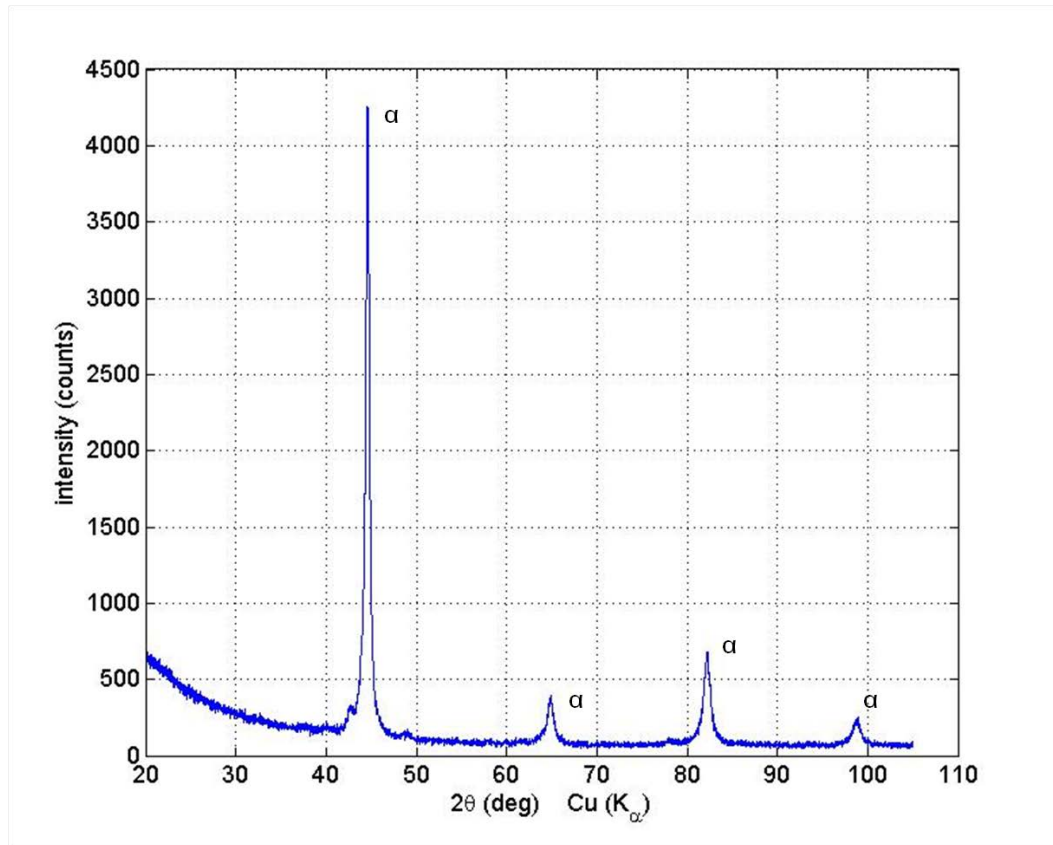


Figure 8.3.9: X-ray diffraction patterns of laser-treated AISI 52100 steel sample - depth from surface: $\sim 77 \mu\text{m}$ (laser power: 800 W, scan speed: 17.95 m/min, overlap: 93.58 %).

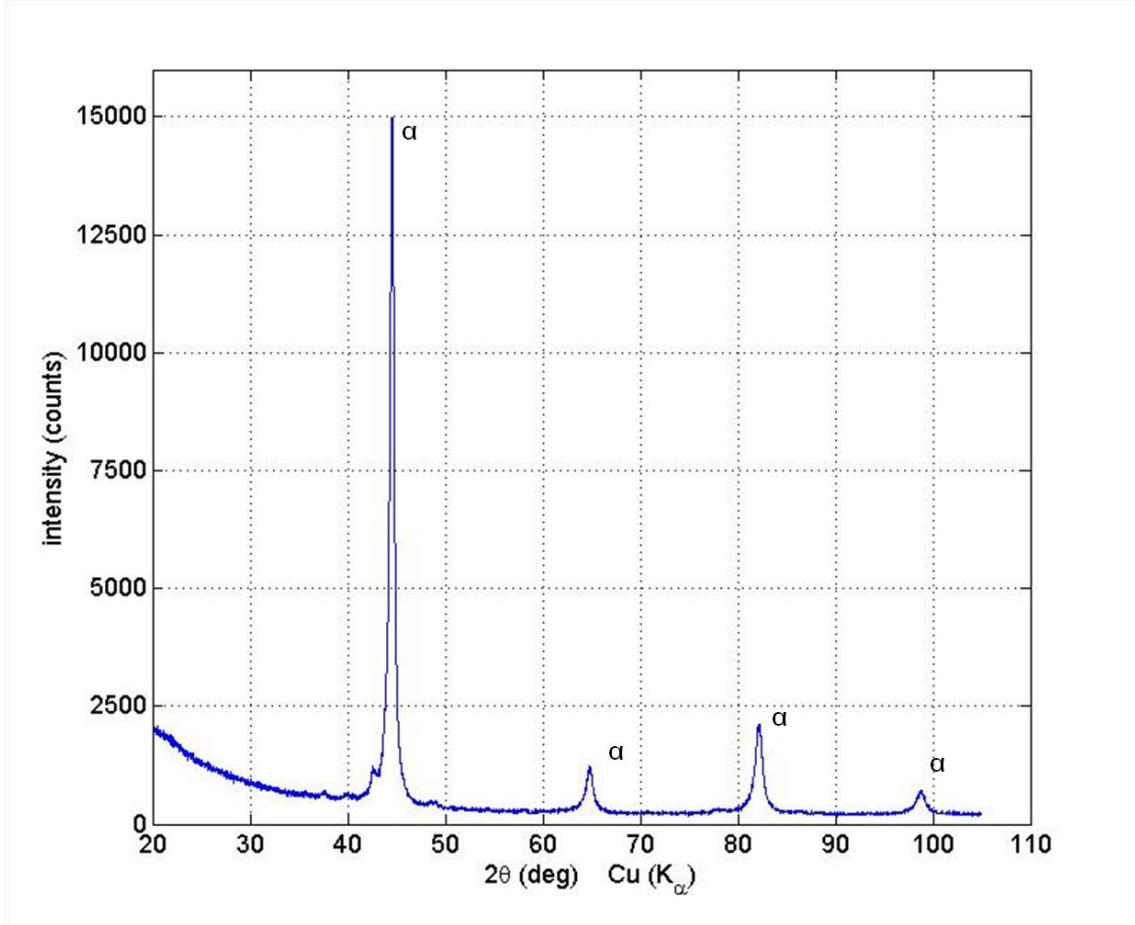


Figure 8.3.10: X-ray diffraction patterns of laser-treated AISI 52100 steel sample - depth from surface: ~109 μm (laser power: 800 W, scan speed: 17.95 m/min, overlap: 93.58 %)

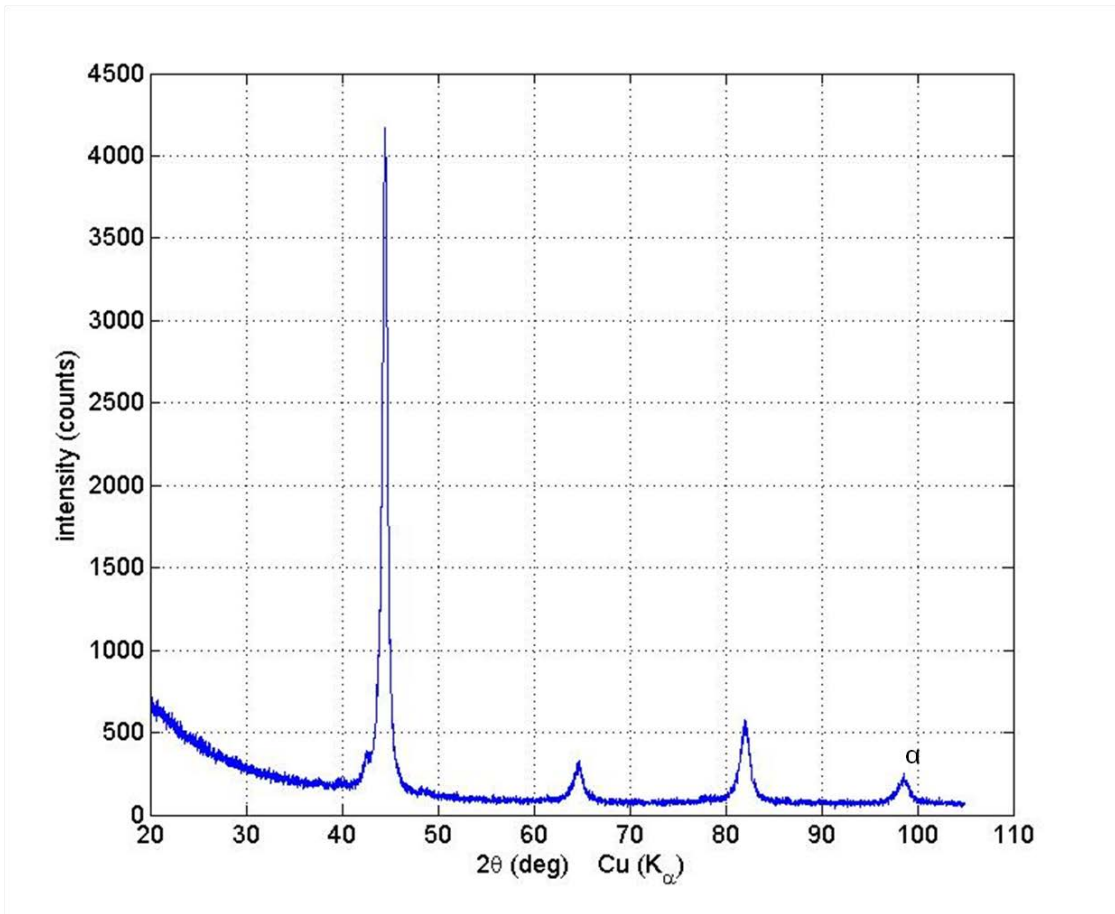


Figure 8.3.11: X-ray diffraction patterns of laser-treated AISI 52100 steel sample - depth from surface: $\sim 152 \mu\text{m}$ (laser power: 800 W, scan speed: 17.95 m/min, overlap: 93.58 %).

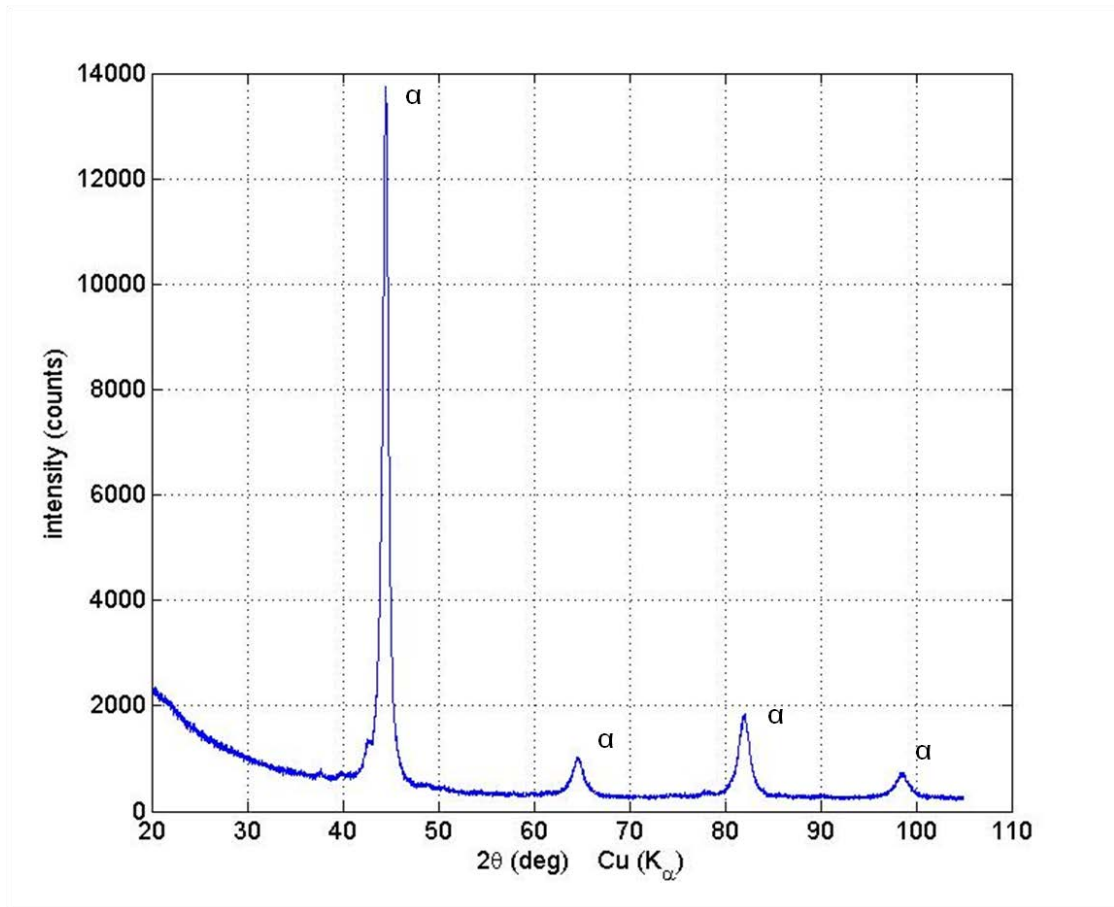


Figure 8.3.12: X-ray diffraction patterns of laser-treated AISI 52100 steel sample - depth from surface: ~242 μm (laser power: 800 W, scan speed: 17.95 m/min, overlap: 93.58 %)

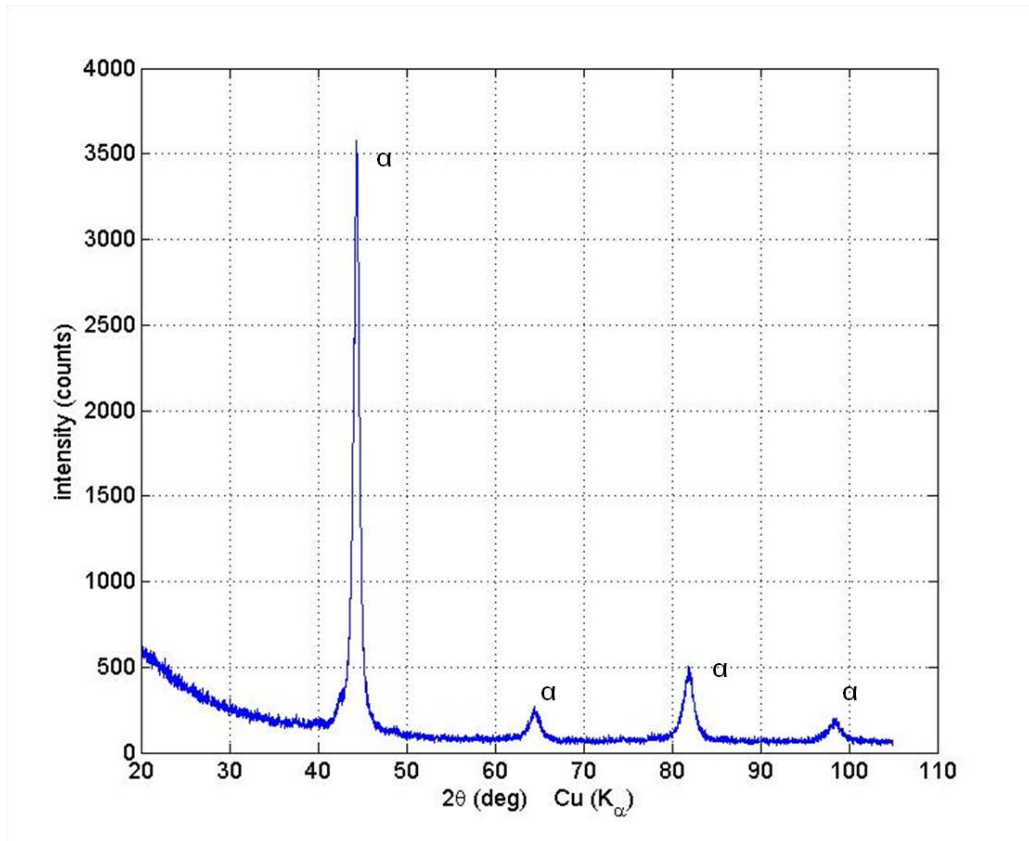


Figure 8.3.13: X-ray diffraction patterns of laser-treated AISI 52100 steel sample - depth from surface: ~456 μm (laser power: 800 W, scan speed: 17.95 m/min, overlap: 93.58 %).

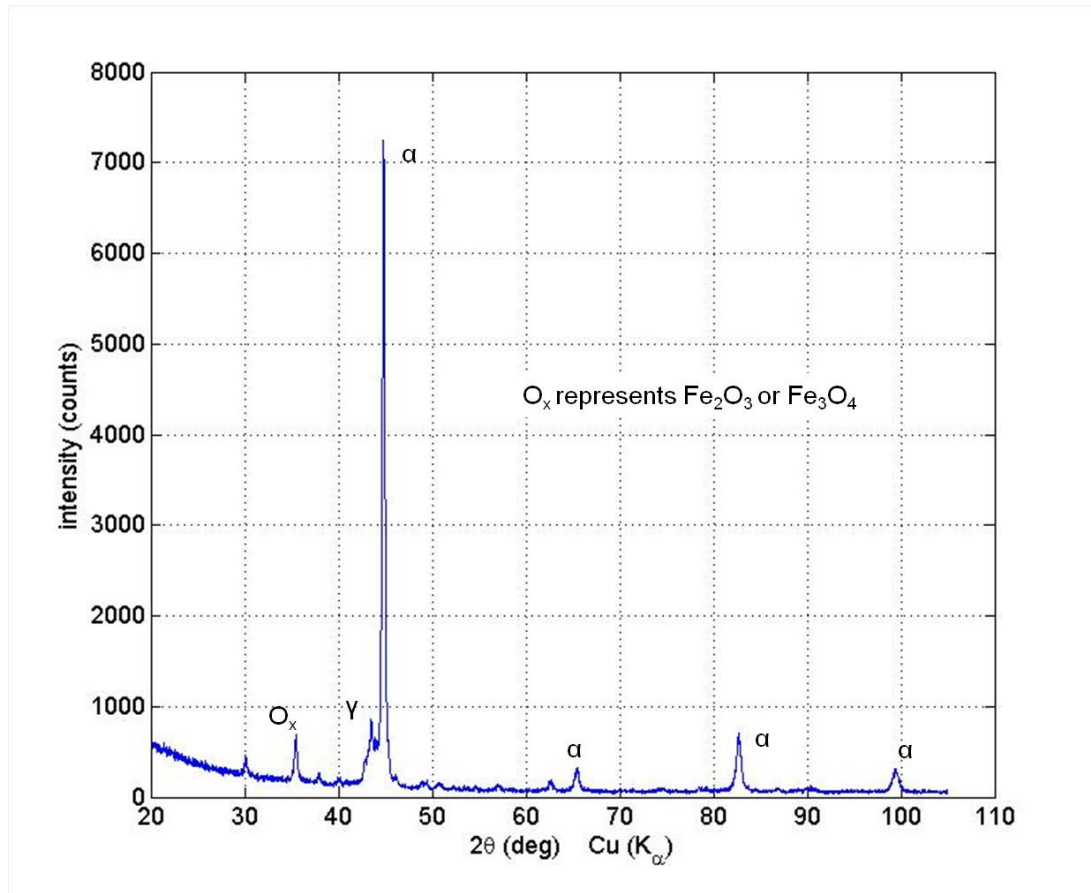


Figure 8.3.14: X-ray diffraction patterns of laser-treated AISI 52100 steel sample - depth from surface: ~0 μm (laser power: 800 W, scan speed: 35.90 m/min, overlap: 93.58 %)

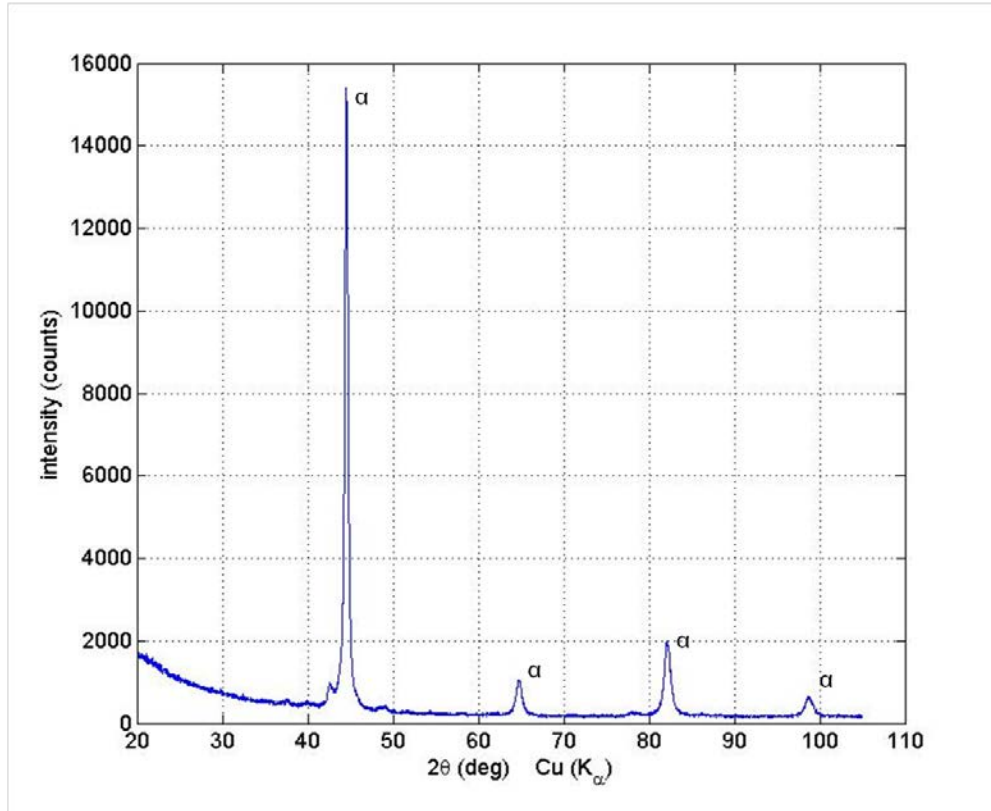


Figure 8.3.15: X-ray diffraction patterns of laser-treated AISI 52100 steel sample - depth from surface: $\sim 12 \mu\text{m}$ (laser power: 800 W, scan speed: 35.90 m/min, overlap: 93.58 %).

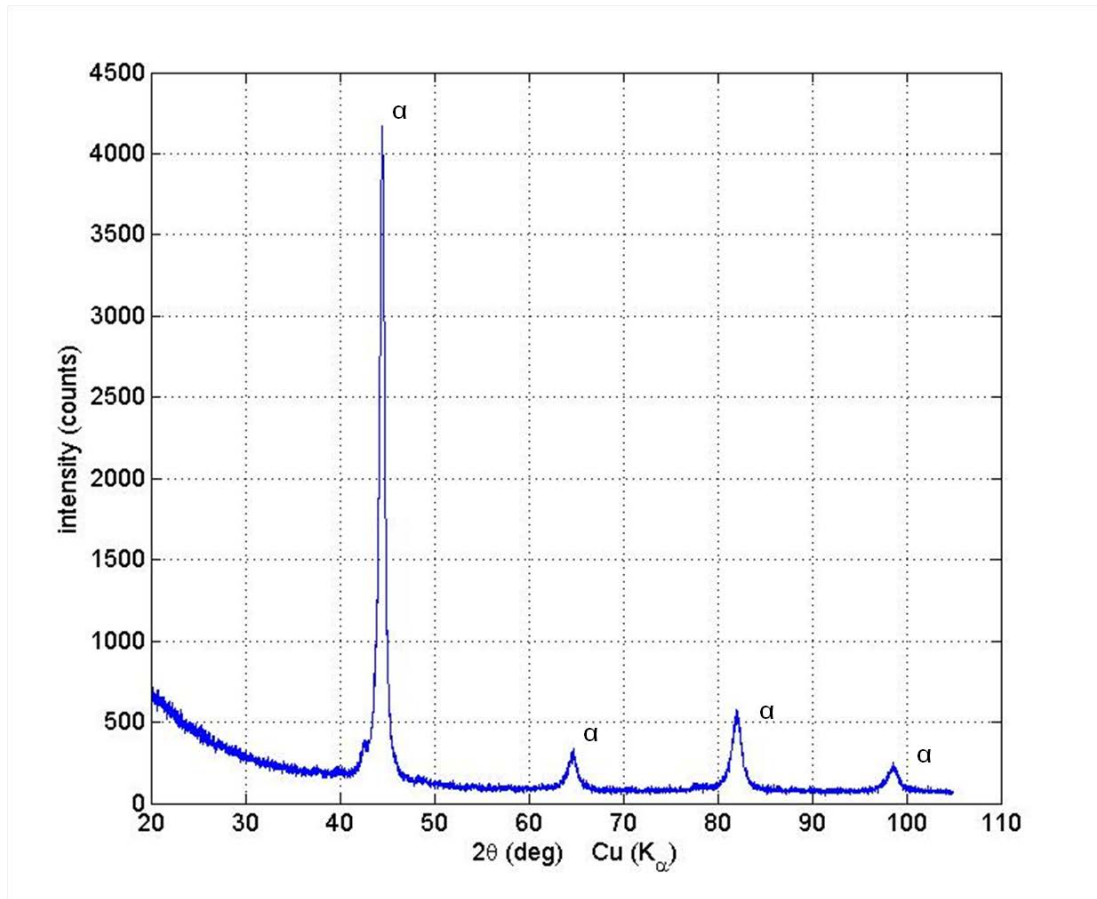


Figure 8.3.16: X-ray diffraction patterns of laser-treated AISI 52100 steel sample - depth from surface: $\sim 27 \mu\text{m}$ (laser power: 800 W, scan speed: 35.90 m/min, overlap: 93.58 %).

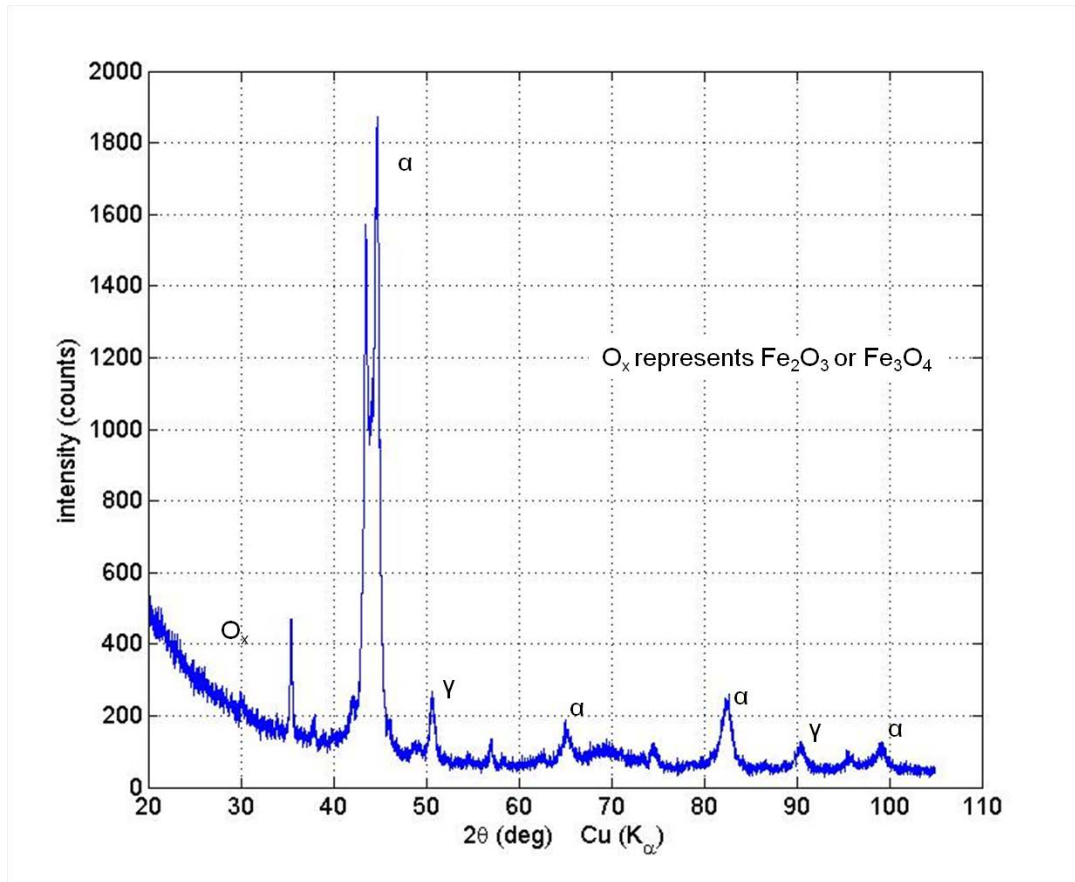


Figure 8.3.17: X-ray diffraction patterns of laser-treated AISI 52100 steel sample - depth from surface: ~0 μm (laser power: 800 W, scan speed: 17.95 m/min, overlap: 75.76 %).

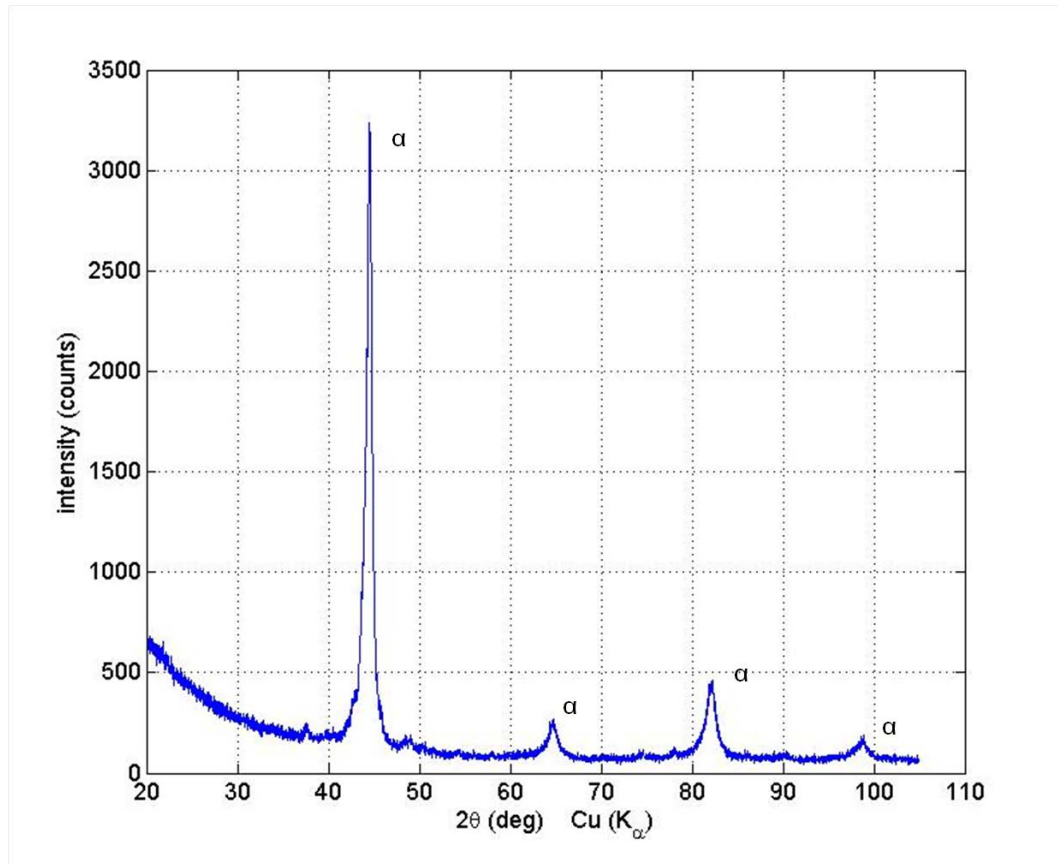


Figure 8.3.18: X-ray diffraction patterns of laser-treated AISI 52100 steel sample - depth from surface: $\sim 11 \mu\text{m}$ (laser power: 800 W, scan speed: 17.95 m/min, overlap: 75.76 %).

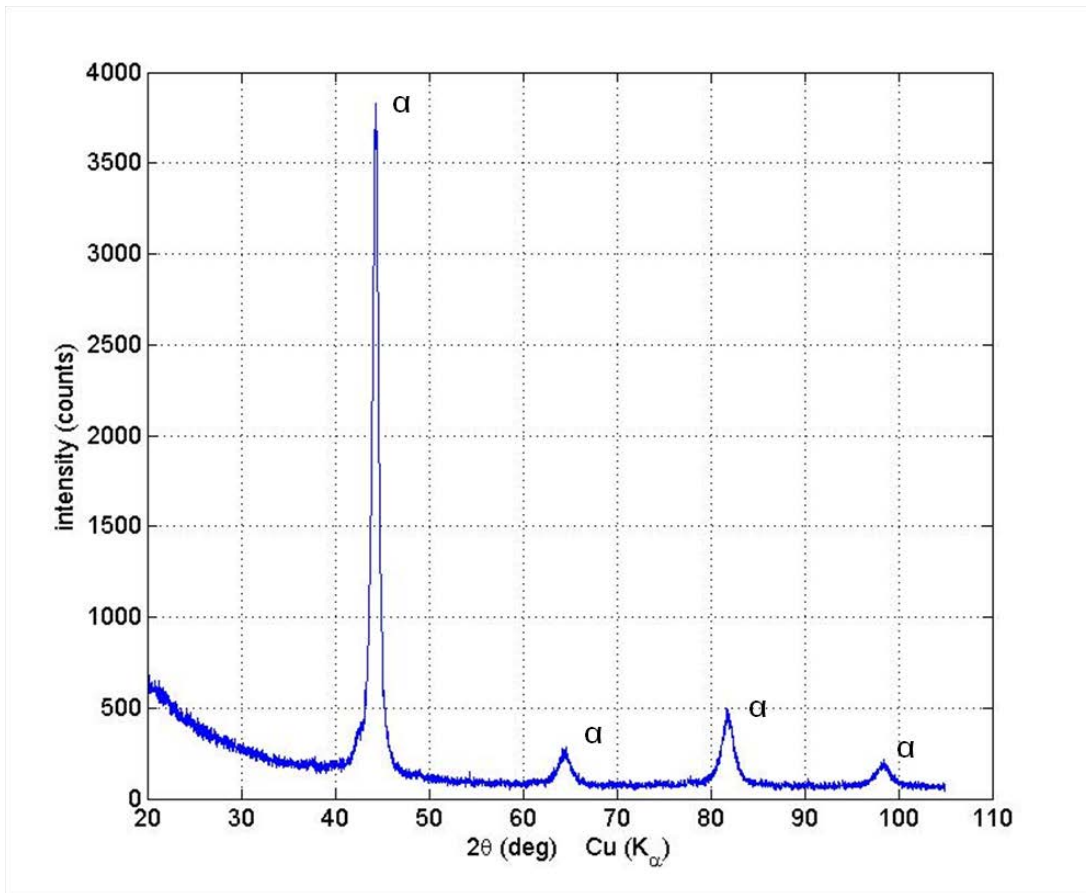


Figure 8.3.19: X-ray diffraction patterns of laser-treated AISI 52100 steel sample - depth from surface: $\sim 82 \mu\text{m}$ (laser power: 800 W, scan speed: 17.95 m/min, overlap: 75.76 %).

CHAPTER 9

REFERENCES

Abrao, A. M., Wise, M. L. H., Aspinwall, D. K., 1995a, Tool wear, cutting forces and temperature evaluation when turning hardened bearing steel using PCBN and ceramic tool materials, Intl. MATADOR Conf., pp.209-216

Abrao, A. M., Wise, M. L. H., Aspinwall, D. K., 1995b, Tool life and workpiece surface integrity evaluations when machining hardened AISI 52100 steels with conventional ceramic and PCBN tool materials, SME technical paper, MR95-159, pp.1-9

AISI (American Iron and Steel Institute), *www.steel.org*

Akcan, S., Shah, S., Moylan, S. P., Chhabra, P. N., Chandraseksar, S., Yang, H. T. Y., 2002, Formation of white layers in steels by machining and their characteristics, Metall. Mater. Transactions A, 33A, pp. 1245–1254

Alda, J., 2006, Laser and Gaussian beam propagation and transformation, Encyclopaedia of Optical Engineering, Marcel Dekker Inc.

American National Standard, 1985, Tool life testing with single-point turning tools, ANSI/ASME B94.55M-1985, ASME, New York

Anderson, M., Patwa, R., Shin, Y. C., 2006, Laser-assisted machining of Inconel 718 with an economic analysis, International Journal Mach. Tools Manufacturing, 46, pp. 1879–1891

Anderson, M., Shin, Y. C., 2006, Laser-assisted machining of an austenitic stainless steel: P550, Proceedings of the Institution of Mechanical Engineers—Part B: JEM – 2006, pp. 2055–2067

Andrews, K. W., 1965, Empirical formulae for the calculation of some transformation temperatures, JISI, vol. 203, 1965, pp.721-727

American National Standard for Safe Use of Lasers, ANSI Z136.1, American National Standards Institute, Washington DC

Armarego, E. J. A., Brown, R. H., 1969, The machining of metals, Prentice-hall Inc., Englewood Cliffs, NJ, USA

Armitage, K., 2005, Laser assisted machining of high chromium white cast iron, Thesis for Master of Engineering, Swinburne University of Technology, 2005

Arsecularatne, J. A., Zhang, L. C., Montross, C., Mathew, P., 2006, On machining of AISI-D2 steel with PCBN tools, *Journal of Materials Processing Technology* 171, pp. 244–269

ASTM International, Standard: E975-03, 2008, Standard practice for x-ray determination of retained austenite in steel with near random crystallographic orientation

Ashby, M. F., Easterling, K. E., 1984, Transformation hardening of steel surfaces by laser beams – part I. hypo-eutectoid steels, *Acta. Metallurgica* 32 (11), pp.1935-1948

Avrami, M., 1939, Kinetics of phase change. I General theory, *Jour. Chem. Phys.*, 7, pp. 1103–1112

Balliett, A.T., Krauss, G., 1976, Fine Structure and the early stages of tempering in the martensite of an Fe-1.22 C alloy, *Metallurgical and Materials Transactions A*, vol. 7, n 2, pp. 318-320

Barry, J., Byrne, G., 2001, Cutting tool wear in the machining of hardened steels Part II: cubic boron nitride cutting tool wear, *Wear* 247, pp. 152–160

Bass, M., Beck, D., Copley, S. M., 1978, Laser assisted machining. SPIE, 4th European Electro-Optics Conference, vol. 164, pp. 233–240

Barnes, J. E., Shin, Y. C., Brandt, M., Sun, S., 2009, High speed machining of titanium alloys, *Materials Science Forum* 618–619, pp. 159–163

Barnes, S., Pashby, I. R., Mok, D. K., 1996, The effect of workpiece temperature on the machinability of an aluminum/SiC MMC, *Journal of Manufacturing Science and Engineering, Transactions of the ASME* 118, pp. 422–427

Bhattacharyya, S. K., Aspinwall, D. K., 1981, Aspect of machinability using polycrystalline diamond and CBN compact tooling, ASM, Metals park, OH

Boothroyd, G., Eagle, J. M., and Chisholm, A. W. J., 1967, Effect of tool flank wear on the temperatures generated during metal cutting, *Proc. 8th Int. Machine Tool Design and Research Conf.*, pp. 667–680

Bowman, K. J., Pfefferkorn, F. E., Shin, Y. C., 2002, Recrystallization textures during laser-assisted machining of zirconia ceramics, *Materials Science Forum* 408–412, pp.1669–1674

- Brandt, G., Gerendas, A., Mikus, M., 1990, Wear mechanisms of ceramic cutting tools when machining ferrous and non-ferrous alloys, *Journal of European Ceramic Society*, vol. 6, pp. 273-290
- Brandt, G., 1986, Flank and crater wear mechanisms of alumina based cutting tools when machining steel, *Wear* 112, pp.39-56
- Brandt, G., 1999, Ceramic cutting tools, state of the art and development trends, *Mater. Technol.*; vol. 14: pp. 17–22
- Burgener, M. L., Reedy, R. E., 1982, *Journal of Appl. Phys.* 53, 4357
- Carius, A., Rigby, P., 1995, PCBN turns the hard stuff, *Cutting Tool Engineering*. 47, 4, pp. 24-32
- Carlsaw, H. S., Jaeger, J. C., 1959, *Conduction of heat in solids*, Oxford, University press, Oxford, UK
- Chang, C., Kuo, C., 2007, Evaluation of surface roughness in LAM of aluminum oxide ceramics with Taguchi method, *International Journal of Machine Tools and Manufacturing* 47, pp.141–147
- Chang, C. W., Kuo, C. P., 2007, An investigation of laser-assisted machining of Al_2O_3 ceramics planning, *International Journal of Machine Tools and Manufacturing* 47, pp. 452–461
- Chou, Y., Barash, M. M., 1995, Review on hard turning and CBN cutting tools, SME technical paper, *Proceedings of the 1st International Machining and Grinding Conference*, MR95-214, pp. 951-962
- Chou, K. Y., Evans, J. C., 1997, Tool wear mechanism in continuous cutting of hardened tool steels, *Wear* 212, pp.59-65
- Chou, K. Y., Evans, J. C., 1997, Cubic boron nitride tool wear in interrupted hard cutting. *Wear* 225:234–24
- Choudhury, I. A., El-Baradi, M. A., 1998, Machinability of nickel-based superalloys: a general review , *Journal of Materials Processing Technology* 77 pp. 278–284
- Chryssolouris, G., 1982, Turning of hardened steels using CBN tools, *Journal of Appl. Metalwork*, 2, pp.100-106
- Chryssolouris, G., Bredt, J., Kordas, S., Wilson, E., 1988, Theoretical aspects of a laser machine tool, *ASME Journal of Engineering for Industry*, vol. 110, pp. 65 - 70

- Chryssolouris, G., 1991, Laser machining: theory and practice, SpringerVerlag, New York, USA
- Claussen, N., 1985, Material Science and Engineering, vol. 71, 1985, pp. 23-38
- Cline, H. E., Anthony, T. R., 1997, Treating and melting material with a scanning laser or electron beam, Journal of Appl. Phys. 48(9), pp. 3895–3900
- Courtney, C., Steen, W. M., 1979, Laser surface treatment of EN8 steel using a 2 kW CO₂ laser, Met. Technol., vol. 6, (12), pp. 456-462
- Cohen, M., Trans ASM 1949, vol. 41, pp.35-94
- Colding, N.B., 1980, Coated Cutting Tools, SME Cutting tools clinic, Issue - March 1980
- Cullity, B. D., 1956, Elements of x-ray diffraction, Addition-Wesley publishing company Inc., Massachussets, USA
- Dandekar, C. R., Shin, Y. C., Barnes, J., 2010, Machinability improvement of titanium alloy (Ti-6Al-4V) via LAM and hybrid machining, International Journal of Machine Tools and Manufacture, vol. 50, pp. 174–182
- Davis, M., Kapadia, P., Dowden, S., Steen, W. M., Courtney, C. H. G., 1986, Heat hardening of metal surfaces with a scanning laser beam, Jour. of Appl. Phys., vol. 19, pp.1981-1997
- Dawson, T. G., Kurfess, T. R., 2000, An investigation of tool wear and surface quality in hard turning, Transactions of the North American Manufacturing Research Institution of SME, vol. 28, pp. 215-220
- Devgun, M. S., Molian, P. A., 1990, Experimental study of laser heat-treated bearing steel, Journal of Materials Processing Technology, pp. 41-54
- Ding, H., Shin, Y. C., 2010, Laser-assisted machining of hardened steel parts with surface integrity analysis, International Journal of Machine Tools and Manufacture, vol. 50, pp. 106–114
- Diniz, A. E., Oliveria, A. J., 2008, Hard turning of interrupted surfaces using CBN tools, Journal of Material Process Technology, 195, pp. 275-281
- Ducker Worldwide, International report 2009, Aluminum association, Auto and Light Truck Group

- Dumitrescu, P., Koshy, P., Stenekes, J., Elbestawi, M. A., 2006, High-power diode laser assisted hard turning of AISI D2 tool steel, *Intl. Journal of Machine Tools and Manufacture*, vol. 46, Issue 15, Dec 2006, pp. 2009-2016
- Edwards, R., 1993, *Cutting tools*, The Institute of Materials, The University Press, Cambridge.
- Evans, C., 1991, Cryogenic diamond turning of stainless steels, *Ann. CIRP* 40 (1), pp. 571-575
- El-Gallab, M., Sklad, M., 1998, Machining of Al/SiC particulate metal–matrix composites, Part I: Tool performance, *Journal of Materials Processing Technology*, 83, pp. 151–158
- Farhat, Z. N., 2003, Wear mechanism of CBN cutting tool during high-speed machining of mould steel, *Mater. Sci. Eng. A361*, pp. 100–110
- Fiorletta, C., 1981, Electron Beam heat treating in *Metals Hand Book*, 9th edition, ASM, Metals park, OH, vol. 4, pp. 518-521
- Freist, B., Haferkamp, H., Laurinat, A., Louis, H., 1989, American Water Jet Conference - Aug 29-31 1989, Toronto, Canada, pp. 191-204
- Frewin, M. R., Scott, D. A., 1999, Finite element model of pulsed laser welding, *Welding Journal*, 78(1), pp. 15S- 22S
- Galantucci, L. M., Tricarico, L., 1995, Transient numerical analysis of laser heat treatment using FEM, *Manufacturing Systems*, 24/2, pp. 165-181
- Galantucci, L. M., Tricarico, L., 1999, An experimental and numerical study on the influence of not uniform beam energy distribution in laser steel hardening, *CIRP Annals - Manufacturing Technology*, vol. 48, issue 1, pp. 155-158
- G. E. Superabrasives product literature, 1997, Hard turning with tools made with BZN 8100 compacts, General Electric.
- Germain, G., Lebrun, J. L., Morel F., Morel, A., 2007, Machinability and surface integrity for a bearing steel and a titanium allot in laser assisted machining, *Lasers in Eng.*, vol. 17, pp. 329-344
- Germain, G., Lebrun, J. L., Braham-Bouchnak, T., Bellett, D., Auger, S., 2008, Laser-assisted machining of Inconel 718 with carbide and ceramic inserts, *International Journal of Materials Forming* (suppl. 1), pp. 523–526

Giorleo, L., Previtali, B., Semeraro, Q., 2011, Modeling of back tempering in laser hardening, Intl. Journal Adv. Manuf. Technol., vol. 54, pp. 969–977

Gratias, J.F., Fan, L.J., Marot, G., Cohen, G.P., Moisan, A., 1993, Proposition of a method to optimize the machining of XC42 steel with laser assistance, CIRP Annals 42, pp. 115–118

Groover, M.P., 2007, Fundamentals of Modern Manufacturing, 3rd edition (2007), John Wiley & Sons, Inc.

Griffiths, B.J., 1987, Mechanisms of white layer generation with reference to machining and deformation processes, ASME: Jour. Tribol., vol. 109, pp. 525–530

Guo, Y., Liu, C., 2002, 3D FEA modeling of hard turning, Journal of Manufacturing Science and Engineering, vol. 124, no. 2, pp. 189-199

Gustavo A Toledo Garcia, 2002, High temperature compression testing of hardened steels for plasticity behavior modeling, MS Thesis, Mechanical Engineering, Georgia Institute of Technology, Atlanta, GA

Hahn, R., Schultze, P., 1993, Ultrasonic machining of glass and ceramics, The American Ceramic Society Bulletin, vol. 72, n8, pp.611-630

Hardinge Conquest lathe T42SP operational manual

Hasan, R. (Sumitomo Electric Carbide Inc., Mt. Prospect, IL), 1998, Why are you still Grinding?, Manufacturing Engineering, Issue: feb 1998, pp. 76-80.

Hillert, M., Nilsson, K., Törndahl, L. E., 1971, Effect of alloying elements on the formation of austenite and dissolution of cementite, Journal of Iron Steel Inst., vol. 209, n. 1, pp. 49-66

Hillert, M., 1957, Jernkot Ann., vol. 141, pp. 557-585

Hollomon, J., Jaffe, L., 1945, Time–temperature relations in tempering steel, Trans. AIME, 162, pp. 223–249

Incopera, F. P., 2002, Introduction to Heat Transfer, 4th edition, Wiley, Newyork, USA

ISO 3685:1993, Tool-life testing with single-point turning tools, 2nd edition, pp.12

Jacot, A., Rappaz, M., 1997, A two-dimensional diffusional model for the prediction of phase transformation: application to austenization and homogenization of hypoeutectoid Fe-C steels, *Acta Mater.*, 45 (2), pp. 575-585

Jacot, A., Rappaz, M., 1999, A combined model for the description of austenitization, homogenization and grain growth in hypo-eutectoid Fe-C steel during heating, *Acta Mater.*, 47(5), pp. 1645-1651.

Jacot, A., Rappaz, M., Reed, R. C., 1997, Modeling of re-austenitization from the pearlite structure in steel, *Acta Metallurgica Inc.*, vol. 46, issue 11, pp. 3949-3962

Jang, D. Y., Watkins, T. R., Kozaczek, K. J., Hubbard, C. R., Cavin, O. B., 1996, Surface residual stresses in machined austenitic stainless steel, *Wear*, 1, vol. 194, pp. 168-173

Jau, B. M., Copley, S. M., Bass, M., 1980, Laser assisted machining, SME technical paper MR80-846, pp. 1-15

Jeon, Y., Pfefferkorn, F., 2008, Effect of laser preheating the workpiece on micro end milling of metals, *Journal of Manufacturing Science and Engineering, Transactions of the ASME* 130 011004-1-9

Johnson, W., Mehl, R., 1939, Reaction kinetics in processes of nucleation and growth, *American Institute of Mining and Metallurgical Engineers - Transactions*, vol. 135, pp. 416-442

Johnson, W., 1967, Cutting with tools having a rounded edge: some theoretical considerations, *Annals of the C.I.R.P.*, vol. XIV, pp. 315 - 319

Kainth, G. S., Dey, B. K., 1980, Experimental investigation into tool life and temperature during hot machining of EN-24 steels, *Bulletin Cercle Etudes des Metaux*, vol. 14, n11, pp. 22.1-22.7

Kalpakjian, S., Schmidt, S. R., 2001, *Manufacturing Engineering and Technology*, 4th edition, Prentice Hall Publications

Kannan, S., Kishawy, H. A., 2008, Tribological aspects of machining aluminum metal matrix composites, *Journal of Materials Processing Technology* 198 pp. 399-406

Kennametal Turning Inserts Catalog, 1993, Kennametal Corp. USA

Kim, S., 1994, Material properties of ceramic cutting tools, *Key Eng. Mater.* 96 pp. 33-80

Klimanko, S. A., Mukovoz, Y. A., Polonsky, L. G., 1996, Advanced ceramic tools for machining application-II, Key Eng. Mater. 114, pp. 1–63

Klocke, F., Bergs, T., 1997, Laser-assisted turning of advanced ceramics, Proc. SPIE, 3102, pp. 120–130

Kobayashi, S., Thomsen, E. G., 1960, The role of friction in metal cutting, ASME Journal of Engineering for Industry, vol. 82, pp. 324–332

König, W., Zaboklicki, A. K., 1993, Laser-assisted hot machining of ceramics and composite materials, International conference on machining of advanced materials, vol. 847, NIST Special Publication, Gaithersburg, MD, pp. 455–463

Konig, W., Cronjager, L., Spur, G., Tonshoff, H., Vigneau, M., Zdeblick, W., 1990, Machining of new materials, Annals of the CIRP, 39 (2), pp. 673–681

Konig, W., Klinger, M., Link, R., 1990, Machining hard materials with geometrically defined cutting edges - field of applications and limitations, Annals of the CIRP, vol. 39/1, pp. 61-64

Klueh, R. L., Harries, D. R., 2001, High chromium ferritic and martensitic steels for nuclear applications, ASTM International, West Conshohocken, Pennsylvania, USA

Kou, S., Sun, D. K., Lee, Y. P., 1983, A fundamental study of laser transformation hardening, Metall. Trans., A 14, pp. 643-653

LAI International, www.laico.com

Lakhkar, R.S., Shin, Y. C., Krane, M. J. M., 2008, Predictive modeling of multi-track laser hardening of AISI 4140 steel, Materials Science and Engineering A, v 480, n 1-2, pp. 209-217

Lange, F. F., 1982, Journal of Material Science, vol. 17, n1, 1982, pp.225-234

Lax, M., 1977, Temperature rise induced by a laser beam, Journal of Appl. Phys., vol. 48 (9), pp. 3919-3924

Lee, T. C., Lau, W. S., 1991, Material. Manuf. Processes, vol.6, n4, pp. 635-648

Leidinger, D., Penz, A., Schuocker, D., 1995, Improved manufacturing processes with high power lasers, Infrared Phys. Technol., vol. 36, no. 1, pp.251-266

- Lei, S., Shin, Y. C., Incropera, F. P., 2001, Experimental investigation of thermo-mechanical characteristics in laser assisted machining of silicon nitride ceramics, *Journal of Manufacturing Science and Engineering, Transactions of the ASME* 123, pp. 639–646
- Lei, S., Pfefferkorn, F. E., 2007, A review of thermally assisted machining, *Proceedings of the ASME international conference on manufacturing science and engineering, Atlanta, GA*, pp. 1–12
- Lement B. S., Averbach B. L., Cohen, M., 1954, Microstructural changes on tempering iron-carbon alloys, *ASM Transactions*, vol. 46, pp. 851-881
- Liang, S., 2006, Technology assessment on current advanced research projects in the area of hard turning, *The Association of Manufacturing Technology 2006*
- Liu, C. R., Barash, M. M., 1982, Variables governing patterns of mechanical residual stress in a machined surface, *Journal of Engineering for Industry*, vol. 104, pp. 257-264
- Long, Y., Huang, Y., 2010, Combined effects of flank and crater wear on cutting force modeling in orthogonal machining – part 1: model development, *Machining Science and Technology*, 14 pp. 1-23.
- Li, Z., Zheng, Q., Li, J., Hu, W., Wang, H., Tian, H., 1985, Laser surface treatment of high-phosphorus cast iron. *Journal of Appl. Phys* 58, pp. 3860–3864
- Li, W. B., Ashby, M. F., Easterling, K.E., 1986, Laser transformation hardening of steel - II hyper-eutectoid steels, *Acta Metallurgica* 34 (8), pp.1533-1548
- Li, V. M., Niebuhr, David V., Meekisho, Lemmy, L., Atteridge, David G., 1997, A computational model for prediction of steel hardenability, *Metallurgical and Material Transactions B.*, vol. 28, pp.661-672
- Mamalis, A. G., Kundrak, J., Horvath, M., 2002, Wear and Tool Life of CBN Cutting Tools, *Intl. Journal Adv. Manuf. Technol.* 20: pp.475–479
- Manna, A., Bhattacharyya, B., 2002, A study on different tooling systems during machining of Al/SiC-MMC, *Journal of Materials Processing Technology* 123, pp. 476–482
- Marder, A. R., Krauss, G., 1967, The morphology of martensite in iron-carbon alloys, *Trans ASM*, vol. 60, pp.651-660
- Mazumder, J., 1983, Laser heat treatment: the state of the art, *Jour. of Metals*, pp.18-26

- Madhavulu, G., Ahmed, B., 1994, Hot machining process for improved metal removal rates in turning operations, *Journal of Materials Processing Technology* 44 pp. 199–206
- Mehl, R. F, Hagel, W. C., 1956, The austenite: pearlite reaction, *Progress in metal physics*, Ed.: Chalmers, B., and King, R., vol. 6, Pergamon Press, New York, pp.74-134
- Mital, A., Mehta, M., 1988, Surface finish prediction models for fine turning, *International Journal of Production Research*, vol. 26, No. 12, pp.1861-1876
- Moody, J. E., Hendel, R. H., 1982, *J. Appl. Phys.* 53, 4364
- Nakayama, K., Arai, M., Kanda, T., 1988, *Machining Characteristics of Hard Materials*, CIRP Ann., 37~11, pp. 89–92
- Narukati, N., Yamane, Y., 1979, Tool wear and cutting temperature of CBN tools in machining of hardened steels, *Annals of CIRP*, vol. (28)(1), pp. 23-28
- Nissim, Y.I., Lietoila, A., Gold, R. B., Gibbons, J. F., 1980, *J. Appl. Phys.* 51, 274
- NIST (National Institute of Science and Technology, USA), October 2000, <http://jazz.nist.gov/atpcf/prjbriefs/prjbrief.cfm?ProjectNumber=00-00-4143>
- Novak, J. W., Shin, Y. C., Incopera, F. P., 1995, Assessment of plasma enhanced machining of improved machinability of Inconel 718, *Journal of Manufacturing Science and Engineering*, vol. 119, pp.125-129
- Nuvonyx Inc., Nuvonyx-ISL 1000M operating manual
- Ohse, R. W., 1988, Laser application in high temperature materials, *Pure and Appl. Chem.*, vol. 60, No.3, pp. 309-322
- Ozel, T., 2005, Predictive modeling of surface roughness and tool wear in hard turning using regression and neural networks, *International Journal of Machine Tools and Manufacture*, vol. 45, n4-5, pp. 467-479
- PANanalytical Incorporations, X-ray diffractometer reference manual
- Pantsar, H., Kujanpaa, V., 2003, Diode laser beam absorption in laser transformation hardening of low alloy steel, *Journal of Laser Application*, vol. 16, Issue 3, pp.147-153
- Patwa, R., Shin, Y.C., 2007, Predictive modeling of laser hardening of AISI 5150H steels, *Intl. Journal of Machine Tools and Manufacture* 47, pp. 307-320

Petrofes, N. F., Gadalla, A. M., 1988, Electrical discharge machining of advanced ceramics, *Ceramic bulletin*, vol.67, n6, pp.1048-1052

Pfefferkorn, F. E., Shin, Y. C., Incropera, F. P., Tian, Y., 2004, Laser-assisted machining of magnesia-partially-stabilized zirconia, *Journal of Manufacturing Science and Engineering, Transactions of the ASME* 126, pp.42–51

Podgornik, B., Kalin, M., Vizintin, J., Vodopivec, F., 2001, Microstructural changes and contact temperatures during fretting in steel-steel contact, *ASME*, vol. 123, Issue 4, pp. 670-675

Poulachon, G., Bandyopadhyay, B. P., Jawahir, I. S., 2001, Tool wear mechanisms in hard turning with PCBN tools, *Wear* 250, pp. 576 – 586

Poulachon, G., Pheulpin, S., Seguin, E., Bandyopadhyay, B. P., Jawahir, I. S., 2003, The influence of the microstructure of hardened tool steel workpiece on the wear of PCBN cutting tools, *International Journal of Machine Tools and Manufacture*, 43, pp. 139–144

Pramanik, A., Zhang, L.C., Arsecularatne, J. A., 2008, Machining of metal matrix composites: effect of ceramic particles on residual stress, surface roughness and chip formation, *International Journal of Machine Tools and Manufacture* 48, pp. 1613–1625

Precitec Inc., *Laser optics resource manual*

Precitec Inc., *Laser Head YW50, Operating manual*

Raghavan, S., Hashimoto, F., Melkote, S., 2011, Efficient Machining of Hardened AISI 52100 Steel Using a Laser-based Hybrid Process, *Proceedings of NAMRI/SME*, vol. 39, pp. 224-232

Rajagopal, S., Plankenhorn, D. J., Hill, V. L., 1982, Machining aerospace alloys with the aid of 15 kW laser, *Journal of Applied Metalworking*, Issue 2(3), pp.170-184

Roberts C. S., Averbach, B.L., Cohen, M., 1953, The mechanism and kinetics of first stage of tempering, *ASM Transactions*, vol. 45, pp.576-604

Roberts C.S., 1953, Effect of carbon on the volume fractions and lattice parameters of retained austenite and martensite, *Trans AIME*, vol. 197, pp. 203-204

Rodriguez, C. J. C., 2009, Cutting edge preparation of precision cutting tools by applying micro-abrasive jet machining and brushing, *Dissertation, Universitat Kassel, Germany*

Rozzi, J. C., Pfefferkorn, F. E., Incropera, F. P., Shin, Y.C., 2000, Transient three dimensional heat transfer model for the laser assisted machining of silicon nitride: I- Comparison of predictions with measured surface temperature histories, Intl. Journal of Heat and Mass Transfer 43, pp. 1409-1424

Sandvik, 2005, C-1040:069 ENG/01 product brochure,
www2.coromant.sandvik.com/coromant/pdf/Hard.../C-1040-069.pdf

Samant, A. N., Dahotre, N. B., 2009, Laser machining of structural ceramics- a review, Journal of the European Ceramic Society 29, pp. 969–993

Scintag Incorporations, X-ray diffraction reference manual and catalogue.

Shi, B., Attia, H., Vargas, R., Tavakoli, S., 2008, Numerical and experimental investigation of laser-assisted machining of Inconel 718, Machining Science and Technology 12, pp. 498–513

Shintani, K., Fujimura, Y., 1987, Effective use of CBN tool in fine cutting (continuous and intermittent turning), Proceedings of the international conference on strategies for automation of machining: materials and processes - May 1987, Orlando, FL, pp. 117–126

Shiue, R. K., Chen, C., 1992, Laser transformation hardening of tempered 4340 steel, Metallurgical Transactions A, 23 A (1), pp. 163-170

Silva, L. R., Abrao, A. M., 1999, Machining of the hardened AISI 4340 steel using ceramic and PCBN tooling, Sci. Eng. Jour., vol. 8, pp. 85–92

Sin, H., Saka, N., Suh, N. P., 1979, Abrasive wear mechanisms and the grit size effect, Wear 55, pp.163-190

Skvarenina, S., Shin, Y. C., 2006, Laser-assisted machining of compacted graphite iron, International Journal of Machine Tools and Manufacture, 46, pp. 7–17

Smithey, D. W., Kapoor, S. G., DeVor, R. E., 2001, A new mechanistic model for predicting worn tool cutting forces, Machining Science and Technology, 5, pp. 23–42

Steel and the national Defense – 2007 U.S. steel industry analysis report, SSINA public release

Steen, W. M., 1998, Laser material processing, Edition II, Springer-Verlag London Limited, UK

Steen, W. M., Courtney, C. H. G., 1979, Surface heat treatment of EN 8 steel using a 2 kW continuous-wave CO₂ laser, *Metals Technology* - Dec 1979, pp. 456–46

Stephenson, D. A., Agapiou, J. S., 1996. *Metal Cutting theory and practice*, 1st Edition, Marcel Dekker, New York, USA

Stephenson, D. A., Agapiou, J. S., 2006, *Metal cutting theory and practice*, 2nd edition, Taylor & Francis group, Boca Raton, FL, USA

Sun, S., Brandt, M., Dargusch, M. S., 2010, Thermally enhanced machining of hard-to-machine materials—A review, *International Journal of Machine Tools & Manufacture* 50, Issue 8, pp. 663–680

Tani, G., Orazi, L., Fortunato, A., 2008, Prediction of hypo eutectoid steel softening due to tempering phenomena in laser surface hardening, *CIRP Annals - Manufacturing Technology*, v 57, n1, pp. 209-212

Thangaraj, A. R., Weinmann, K. J., 1992, On the wear mechanisms and cutting performance of silicon carbide whisker reinforced alumina, *J. Eng. Ind.*, 114, pp. 301–308

Takatsu, S., Shimoda, H., Otan, K., 1983, Effect of CBN content on cutting performance of PCBN tools, *International Journal of Refract. Hard Met.* 12, pp.175-178

Thiele, J. D., Melkote, S. N., 1999, Effect of cutting edge geometry and workpiece hardness on surface generation in the finish hard turning of AISI 52100 steel, *Journal Mater. Process. Technol.*, 94 (2), pp. 216– 226

Thiele, J. D., Melkote, S. N., Reascoe, R. A., Watkins, T. R., 2000, Effects of cutting edge geometry and workpiece hardness on surface residual stresses in finish hard turning of AISI 52100 steel, *ASME Journal of Manufacturing Sci. Eng.* 122, pp. 467-479

Thomsen, E. G., MacDonald, A. G., Kobayashi, S., 1962, Flank friction studies with carbide tools reveal sublayer plastic flow, *J. Eng. Ind.*, 84, pp. 53–62

Tian, Y., Shin, Y. C., 2007, Laser-assisted burnishing of metals, *International Journal of Machine Tools and Manufacture*, 47, pp. 14–22

Tonshoff, H., Wobker, H. S., Brandt, D., 1995, Hard turning – Influences on the workpiece properties, *Transactions of NAMRI/SME*, vol. 23, pp.215-220

Tool materials, Edition 2005, ASM International, Materials Park, OH, USA

Tooling and Production, 2009 cutting tools survey, Nelson Publishing Inc., Nokomis, FL, USA

Trent, E., Wright, P., 2000, Metal Cutting, 4th edition, Boston, Oxford, Butterworth/Heinemann, Oxford

Trigger, K. J., Chao, B. T., 1956, The mechanism of crater wear of cemented carbide tools, Trans. ASME, 78, pp. 1119–1126

Umbrello, D., Hua, J., Shivpuri, R., 2004, Hardness-based flow stress and fracture models for numerical simulation of hard machining AISI 52100, Journal of Bearing Steel Material Science and Engineering, vol. A 374, pp. 90-100

Voort, G. V., 1991, Atlas of Time-Temperature Diagrams for irons and steels, pp.127, ASM International, Materials Park, OH

Westkamper, E., 1995, Grinding assisted by Nd:YAG lasers, CIRP Annals 44, pp. 317–320

Waldorf, D. J., DeVor, R. E., Kapoor, S. G., 1998, A slip-line field for ploughing during orthogonal cutting. Transaction of ASME, Journal of Manufacturing Science and Engineering, 120, pp. 693–699

Wang, J. Y., Liu, C. R., 1999, The effect of tool flank wear on the heat transfer, thermal damage and cutting mechanics in finish hard turning. Annals of the CIRP, 48, pp. 53–58

Wang, Z. Y., Rajurkar, K. P., Fan, J., Lei, S., Shin, Y. C., Petrescu, G., 2003, Hybrid machining of Inconel 718, International Journal of Machine Tools and Manufacture 43 pp. 1391–1396

Xiao, H., 1990, Wear behavior and wear mechanism of ceramic tools in machining steel, Wear, 139, pp.439-451

Yang, L. J., Jana, S., Tam, S. C., 1990, Laser transformation hardening of tool steel specimens, Journal of Materials Processing Technology, vol. 21, pp. 119-130

Yang, N., Brandt, M., Sun, S., 2009, Numerical and experimental investigation of the heat-affected zone in a laser assisted machining of Ti6Al4V alloy process, Materials Science Forum 618-619, pp. 143–146

Zhang, E. C., Shin, Y. C., 2002, A novel laser-assisted truing and dressing technique for vitrified CBN wheels, International Journal of Machine Tools and Manufacture, vol. 42, pp. 825–835

Zhang, Z., Delagnes, D., Bernhart, G., 2004, Microstructure evolution of hot-work tool steels during tempering and definition of a kinetic law based on hardness measurements, *Materials Science and Engineering: A*, vol. 380, issues 1-2, 25, August 2004, pp. 222-230

Zhou, J. M., Walter, H., Andersson, M., Stahl, J.E., 2003, Effect of chamfer angle on wear of PCBN cutting tool, *Int. Journal of Mach. Tools Manuf.*, vol. 43, pp. 301–305

Zhu, Z. C., Wang, W. Z., Yi, S. L., 1994, The austenized transformation in laser, *Chinese Journal of Laser*, A21, pp. 846 -851

Zygo New View 200 reference manual, Zygo Corp.

[This page is intentionally left blank]